Development of Procedures for Real-Time Hybrid Simulation and Testing of a Buckling-Restrained Braced Structure

Robin William Carr Malloy
St Hugh's College
University of Oxford

A thesis submitted for the degree of

Doctor of Philosophy

Trinity 2018

Abstract

In real-time hybrid simulation (RTHS), a simulated structure is split into two substructures: one being a physical specimen, and the other a numerical model of the rest of the structure. These are connected in a real-time feedback loop to simulate the dynamic response of the combined structure. An issue in RTHS is the delay in the response of the servo-hydraulic actuators applying the displacements which can destabilise the feedback loop. The delay can vary significantly during the simulation, predominantly due to nonlinearity of the tested specimen.

This thesis presents work developing and testing RTHS procedures, which are used to simulate buildings fitted with buckling-restrained braces (BRBs) as the physical substructure. An improved version of the well-known Adaptive Time Series (ATS) delay compensator is presented, retaining the performance of the original but significantly improving its computational efficiency. An online stiffness simulator is then presented which ensures stable force feedback using a continually updated numerical model of the BRB response. Accuracy is further improved by correcting for rig flexure using feedback from encoders measuring the BRB extension. Finally, a numerical model of the BRB is created which is then used in a multi-degree-of-freedom model.

The performance of the modified ATS compensator and rig flexure correction was demonstrated through predefined displacement tests, achieving excellent displacement accuracy. This was combined with a single-degree-of-freedom numerical substructure and the stiffness simulator to form a RTHS system showing excellent accuracy and stability up to high frequencies – the compensator adapting effectively to changes in delay caused by yielding. A multi-degree-of-freedom numerical substructure was then implemented to simulate the nonlinear response of realistic structures designed to Eurocode 8. Finally, the system was applied to RTHS with a viscoelastic damper, demonstrating the versatility of the adaptive system.

Acknowledgements

I am extremely grateful to my supervisors, Professor Anthony Blakeborough and Professor Martin Williams, for their patient guidance, expert advice and continual support throughout my project. I am especially indebted to Professor Blakeborough for the substantial time and effort he dedicated to supporting me through the toughest parts of my work – well in excess of what anyone could expect of a supervisor.

I am grateful to the Engineering and Physical Sciences Research Council (EPSRC) and the EU FP7 SERIES (grant no. 227887) for the funding which supported this project, and to Start Seismic Europe Ltd for providing the BRB for testing.

I am grateful to Clive Baker for his assistance and patience in the lab, and to Christos for allowing me use of his test rig to obtain additional results. I am grateful for the friendship and camaraderie I have received from all those who I am fortunate enough to call friends. I want to thank Giuseppe for the coffee breaks, Helder for the after-work drinks, Anna for the moral support and Dani for ensuring I was never hungry.

My especial gratitude goes to my parents for their continual and unconditional support, and for always believing in me. Everything I have achieved, I owe to them.

Contents

Abstract i
Acknowledgements ii
Contents iii
1. Introduction 1
2. Seismic Design and Supplemental Energy Dissipation 9
2.1. Earthquake Resistant Design to Eurocode 8 9
2.1.1. Seismic Design Codes 9
2.1.2. Performance Levels 10
2.1.3. Combinations of Actions 11
2.1.4. Determining the Seismic Action 13
2.1.5. Capacity Design Rules 14
2.1.6. Methods of Analysis 16
2.2. Structural Analysis 24
2.2.1. Finite Element Analysis 24
2.2.2. Modal Analysis 24
2.2.3. Modelling Inherent Damping 27
2.3. Supplemental Energy Dissipation Devices 31
2.3.1. Rate-dependent devices 32
2.3.2. Rate-independent devices 33
2.3.3. Equivalent Viscous Damping 35
2.3.4. Estimating damping from structural response 36
2.4. Buckling-Restrained Braces 37
2.4.1. BRB Principle of Operation 37
2.4.2. History of BRBs and Current Applications 38
2.4.3. Incorporation of BRBs in Design Codes 39
2.4.4. Extending Eurocode Rules to BRBFs 41
2.4.5. Sample BRB Tested in this Project 43
2.4.6. BRB Design Displacement 45
3. Real-Time Hybrid Simulation and Laboratory Setup 47
3.1. Overview of Hybrid Simulation 47

3.2. Alternatives to Real-Time Hybrid Simulation 48
3.3. History of Hybrid Testing 50
3.4. Obstacles to Real-Time Hybrid Simulation 53
3.5. Test Rig and Laboratory Setup 54
3.5.1. Actuators and Power 54
3.5.2. Transducers 56
3.5.3. Controller 58
3.5.4. dSpace® Board 58
3.5.5. Data Acquisition 60
3.6. Conclusion 62
4. Stability and Accuracy of Actuation 63
4.1. Stability of the RTHS Feedback Loop 63
4.1.1. Sources of Instability 63
4.1.2. Actuation Delay and Amplitude Error 64
4.1.3. The Destabilising Effect of Actuation Delay 65
4.1.4. Conditions Affecting Stability in the Presence of Actuation Delay 68
4.2. Inner Control Loop and Actuation Delay 69
4.2.1. The PID Controller 69
4.2.2. Effect of PID Parameters on Stability and Delay 71
4.2.3. Measuring Actuation Delay 73
4.3. Delay Compensation 76
4.3.1. Aims of Delay Compensation 76
4.3.2. Constant Delay Methods 77
4.3.3. Pre-Recorded Delay Estimates 81
4.3.4. Adaptive Compensation Methods 82
4.4. Proposed Modification to ATS Compensator 90
4.4.1. Advantages of Modified System 90
4.4.2. Derivation of Modified ATS Equations 91
4.4.3. Implementation of the mATS Compensator 93
4.4.4. Effective Time Window 95
4.4.5. Initialisation of mATS compensator 96
4.5. Compensating for Compliance of the Test Rig 97
4.5.1. The Issue of Rig Flexibility 97
4.5.2. Method of Correcting for Rig Flexibility 98

4.5.3. Accounting for Two Actuator System 99
4.5.4. Combining Rig Flexibility Correction with the Delay Compensation 101
4.5.5. Rig Flexibility Correction Considerations 102
4.5.6. Measuring Actuation Quality 105
4.6. Small Displacement Open-Loop Testing 105
4.6.1. Predefined Displacement Testing 105
4.6.2. Effect of Time Window on Compensator Coefficients 108
4.6.3. Control of Actuator Displacements 108
4.6.4. Sample Open-Loop Test Results 110
4.6.5. Open-Loop Cyclic Test at 0.5Hz 111
4.6.6. Open-Loop Cyclic Test at 5Hz 115
4.6.7. Open-Loop Cyclic Test with Realistic Predefined Displacement 118
4.6.8. Open-Loop Tests with Different Delays 121
4.6.9. Discussion 123
4.7. Large Displacement Open-Loop Testing 125
4.7.1. Large Displacement Pre-Defined Displacement 125
4.7.2. Results of Large Displacement Open-Loop Test 125
4.7.3. Discussion 130
4.8. Summary 131
5. Single-Degree-of-Freedom Hybrid Testing 132
5.1. Substructuring Overview 132
5.2. Numerical Substructure 133
5.2.1. Single-Degree-of-Freedom Model 133
5.2.2. Selection of Numerical Substructure Properties 134
5.2.3. Time Dilation 135
5.2.4. Earthquake Ground Motions 136
5.3. Integration Algorithm 137
5.3.1. Integration Algorithm Properties 137
5.3.2. Integration Timestep and Controller Timestep 139
5.3.3. Newmark Family of Methods 140
5.3.4. Central Difference Method 142
5.3.5. Runge-Kutta Methods 142
5.3.6. Unconditionally Stable Explicit Methods 144
5.3.7. Selected Algorithm 146

5.4. Stiffness Simulator 147
5.4.1. Ensuring Stable Force Feedback 147
5.4.2. Stiffness Simulator Equations 150
5.4.3. Stiffness Simulator Initial Coefficients 153
5.4.4. Testing Stiffness Simulator 154
5.5. Free Vibration Hybrid Testing 159
5.5.1. Initial Excitation 159
5.5.2. Free Vibration Response 160
5.5.3. Conclusions 164
5.6. High Frequency RTHS Testing 164
5.6.1. Stability at High Frequencies 164
5.6.2. RTHS of 10Hz Structure 165
5.6.3. RTHS of 15Hz Structure 172
5.7. Large Displacement SDOF Hybrid Testing 174
5.7.1. RTHS of a 1Hz SDOF Structure with Numerical Stiffness 174
5.7.2. RTHS of a 1Hz SDOF Structure with No Numerical Stiffness 177
5.7.3. RTHS of a 4Hz SDOF Structure 179
5.8. Maximum Displacement SDOF Hybrid Simulations 183
5.8.1. Northridge 183
5.8.2. El Centro 185
5.8.3. Kalamata 187
5.9. Conclusion 189
6. Multi-Degree-of-Freedom Hybrid Testing 190
6.1. Numerical Modelling of BRBs 190
6.1.1. Candidate BRB Models 191
6.1.2. Optimisation of Model Parameters 191
6.1.3. Model 1 – Bilinear Model 193
6.1.4. Model 2 – Multilinear Model 195
6.1.5. Model 3 – Menegotto-Pinto Model 197
6.1.6. Model 4 – Ramberg-Osgood Model 199
6.1.7. Model 5 – Bouc-Wen Model 199
6.1.8. Comparison of Models 201
6.1.9. Scaling of BRB Model 204
6.2. Design of Numerical Substructures 206

6.2.1. Structural form 206
6.2.2. MRF-BRBF Dual Structure 206
6.2.3. BRBF Structure 209
6.3. Numerical Substructure 215
6.3.1. MDOF Model 215
6.3.2. Modal Model of MRF-BRBF Dual Structure 215
6.3.3. Modal Model of BRBF Structure 217
6.3.4. Integration algorithm 217
6.3.5. Coordinate Transformation 218
6.4. Hybrid Simulation of Dual MRF-BRBF Structure 219
6.4.1. Description of tests 219
6.4.2. Results 219
6.5. Large Displacement Hybrid Simulation of BRBF Structure 223
6.5.1. Description of tests 223
6.5.2. Results 224
6.5. Hybrid Simulation with Viscoelastic Damper 227
6.5.1. Application to Other Physical Substructures 227
6.5.2. Viscoelastic Test Setup 227
6.5.3. Viscoelastic Test Results 230
6.6. Conclusion 235
7. Conclusion 236
7.1. Outcomes 236
7.2. Future Work 238
8. References 239
Appendix A – Ground Motion Records 246

List of Abbreviations

ADC – Analogue-to-digital converter

ATS – Adaptive time series (compensator)

BRB – Buckling-restrained brace

BRBF – Buckling-restrained braced frame

CBF – Concentrically braced frame

DAC – Digital-to-analogue converter

DL – Damage limitation

DOF – Degree-of-freedom

EBF – Eccentrically braced frame

ID(R) – Interstorey drift (ratio)

mATS – Modified Adaptive time series (compensator)

MDOF – Multi-degree-of-freedom

MRF – Moment-resisting frame

NLTH – Nonlinear time history (analysis)

PsD – Pseudo-dynamic (testing)

RTHS – Real-time hybrid simulation

SDOF – Single-degree-of-freedom

ULS – Ultimate limit state

VE – Viscoelastic

1. Introduction

A significant proportion of the world's population lives in potential earthquake areas. Structural collapse and the associated loss of life are common after severe earthquakes in regions without fully developed or enforced seismic codes, as shown by the 2010 Haiti earthquake which is believed to have claimed over a hundred thousand lives [1]. Stringent modern seismic codes and appropriate regulations enforcing them can be effective at the primary goal of seismic engineering: preserving life safety by preventing structural collapse and allowing safe evacuation. However, the costs of returning the structure to operation are often extensive [2].

A crucial property in seismic engineering is ductility. This is the ability of a material to deform beyond its elastic limit and undergo significant plastic deformation prior to fracture. In steel structures, ductility can be provided by the axial yielding of steel bracing or formation of plastic hinges in frame members, while in reinforced concrete structures it comes from axial yielding of the steel reinforcing bars. Ductile member behaviour is vital to maintaining structural integrity in the presence of the significant deformations an earthquake can induce and can help redistribute loads through the structure. A significant consequence of ductile yielding is energy dissipation from the structure during motion and hence a reduction in seismic demands. Modern seismic codes [3] [4] make use of this energy dissipation to allow the structure to be designed for smaller loads by ensuring global ductile behaviour is achieved, whilst ensuring the deflections can be accommodated by preventing premature brittle failures.

A natural extension of the philosophy of using beneficial energy dissipation to reduce seismic demands is to introduce devices into the structure which have the specific purpose of dissipating energy during structural motion, referred to as *dampers*. A variety of damper types exist, using a variety of mechanisms for converting the kinetic energy of the structure into heat, e.g. fluid orificing, movement through viscous fluid, deformation of viscoelastic solids, yielding of metals or frictional sliding [5]. The

idea is that the dampers will dissipate energy which would otherwise have to be dissipated through yielding of structural elements, thereby reducing or eliminating damage to the main structure. The dampers are designed either to survive the earthquake undamaged or to be easily (and cheaply) replaceable after the earthquake. While dampers add an additional construction cost, they can lead to savings in other areas, e.g. by allowing the use of smaller section members and allowing smaller foundations to be used due to the reduced base shear. Dampers can also reduce damage to non-structural elements, the reduced costs associated with repair and downtime of the building, should an earthquake occur, justifying an increased initial investment. As well as being used in the design of new structures to achieve superior seismic performance, dampers have also been used in the retrofit of many existing structures. By increasing energy dissipation, they can be used to reduce the seismic demands to a level the existing structure can withstand, which in many cases can be more practical than attempting to strengthen the structure to resist the original demands. The benefits of supplemental dampers have been widely demonstrated through experimental and analytical research [6], and their use continues to grow, particularly in the USA and Japan. However, there is a delay in the uptake of new devices due to the time taken for them to be incorporated in design codes, for design practices to become established and for confidence in the new technology to develop.

The damper tested in this project is a buckling-restrained brace (BRB) which uses yielding of steel as its energy dissipation mechanism. BRBs consist of an axially loaded steel core encased in a casing which provides lateral restraint to prevent buckling of the core under axial compression, while a debonding layer prevents axial loads from being transferred to the casing. The preclusion of buckling causes the core to yield in compression, as well as in tension, producing approximately symmetrical behaviour. This ability to undergo stable yielding in both directions results in highly ductile behaviour giving significant energy dissipation capacity during an earthquake. BRBs have been used in Japan, where they were first developed by Nippon Steel, since 1987 and in the USA since 1999 [7]. They have recently seen their first few implementations in Europe, but simplified design approaches for buckling-restrained braced frames (BRBFs) do not appear in the current European seismic design code (Eurocode

8 [3]) – it seems likely that they will appear in the next version, which could initiate a large increase in their uptake in the high seismicity regions of Europe.

Any novel earthquake protection device must undergo testing to determine its properties and validate its performance before it can be implemented in structures. In addition, the behaviour of the structure in which the devices are installed must be simulated to ensure performance objectives are achieved. Hybrid simulation has the potential to be an extremely useful and efficient tool for carrying out such testing. In a hybrid simulation, the structure is divided into two subsystems: a physical substructure and a numerical substructure. The physical substructure consists of the key component or subassembly of interest in the structure being modelled, which is tested at full or large scale. The remainder of the structure forms the numerical substructure which is modelled numerically on a computer. The two subsystems are connected in a feedback loop so as to simulate the response of the combined structure. The structural equations of motion are integrated on the computer while actuators apply the required displacement or force to the physical substructure, and transducers measure the response of the device (force or displacement) which is fed back into the numerical substructure.

In a hybrid simulation, the duration of the test is divided into discrete intervals called timesteps. During each timestep, a numerical algorithm solves the equations of motion to determine the displacements of the structure at the end of the timestep. The resulting displacement calculated across the physical substructure is applied to the specimen by actuators, and the force resulting from this applied displacement is measured and fed back into the numerical substructure where it is treated as an external force in the integration of the equations of motion for the next timestep. This process is repeated until the simulation is complete. This describes a system operating under displacement control of the actuation system, which is by far the most common method. However, it could alternatively be implemented under force control, in which case the numerical substructure would calculate the force to be applied to the physical substructure and it is the resulting displacement that would be fed back.

Providing the numerical part of the hybrid simulation is accurate, and equilibrium and compatibility between the two substructures are ensured (i.e. the correct displacements are applied to the device and the force accurately measured, or vice versa), this allows the device to be tested under as realistic a loading situation as possible, with the effect of the device on the structural response directly taken into account. The alternative way to test the device under such realistic conditions is shake table testing, where the whole structure, including its full mass, is constructed on a movable base which has the earthquake ground motion applied to it by actuators in real-time, while transducers measure the structural response. However, this requires large, expensive testing equipment and facilities, in addition to the cost of constructing the entire structure. There are few facilities capable of testing large structures at full-scale, so scaling of the sample structure must usually be resorted to. When a particular component is of interest, scaling the component will increase the uncertainty in its response, or may not even be possible. Hybrid testing with substructuring therefore has clear benefits for testing novel damping devices since it allows the component of interest to be tested at full-scale, or close to full-scale, without requiring the remainder of the structure or its mass to be physically constructed. The size of equipment and facilities required to perform these tests is therefore much smaller and more widely available. The numerical substructure generally consists of conventional materials and forms of construction for which the properties are known, and suitable constitutive models and modelling procedures are well established. While the concept of hybrid testing with substructuring is relatively straightforward, there are a number of difficulties to be overcome to ensure the quality of the test.

A major limitation on the hybrid simulation procedure has been the rate at which the test can be performed, which is restricted by multiple factors [8]. For much of the history of hybrid testing it has therefore been necessary to carry out tests at reduced rates with non-continuous loading, referred to as pseudo-dynamic (PsD) testing. Limitations on computing power, combined with the small timestep necessary to ensure stability of the integration algorithm, prevented all of the calculations necessary for the integration to be completed within the time interval assumed in the model. In addition, the limited dynamic ability of the actuators prevented the velocities assumed in the simulation from being

achieved. The displacements therefore had to be applied more slowly than assumed in the simulation. Once the integration algorithm had calculated the displacements for the next timestep, the integration would pause while the required displacement was applied to the physical substructure. Once this displacement had been achieved by the actuators, the resulting force measured by the transducers would be fed back to the numerical substructure and the next step of the integration would begin.

A clear problem with this approach is its inability to capture any rate-dependent properties of the physical substructure. This can be acceptable when testing components with a predominantly displacement-dependent response, but many devices currently of interest have a highly rate-dependent response. In viscous or viscoelastic dampers, for example, it is the velocity across the device which is responsible for its energy dissipation. It is therefore highly desirable to have a system capable of testing in real-time – that is, continuous testing in which the velocity across the physical substructure matching that assumed in the numerical substructure. The rapid increase in computing power and speed means that integrating the equations of motion in real-time is now a possibility in many cases, although it is far from a trivial problem and the efficiency of the numerical integration is still a significant consideration. At the same time, improvements in actuator technology have made it possible to apply loads at the rates likely to be experienced during earthquake induced motion. The key impediment to performing real-time hybrid simulation (RTHS) that remains is the actuation delay – that is, the time it takes for the actuators to achieve the requested displacement once it has received the command signal from the computer. This was not an issue with PsD since the system would wait for the required displacement to be achieved before proceeding with the integration. While the use of higher specification dynamic actuators and optimisation of the actuator controllers can minimise this delay, it cannot be removed completely due to the inherent characteristics of the actuation and control systems. The delay this introduces in the feedback loop has a destabilising effect which adds energy to the system, equivalent to having negative damping [9]. The significance of this destabilising effect depends on the size of the delay in relation to the natural frequencies of the structure being modelled, as well as the type of device being tested. Unfortunately, the natural frequencies experienced in most

building structures are of an order that the actuation delays experienced in hydraulic actuation systems will be large enough to compromise the accuracy of the hybrid simulation significantly, if not destabilise it completely.

Since this was identified during early investigations into RTHS in the early 1990s, researchers have been exploring methods of compensating for actuation delay to allow accurate RTHS to be successfully performed [10]. Compensating for actuation delay first requires an estimate of the delay size, and then an extrapolation procedure that predicts what the target displacement to be applied to the physical substructure will be a time equal to the delay size in the future. This extrapolated signal is then sent as the command to the actuator controller instead of the current target displacement so as to cancel out the delay as far as possible. Tests in this project confirm the findings of Darby et al. [11] that the size of the delay can vary significantly during a hybrid simulation, mainly due to nonlinearity of the component forming the physical substructure, as well as it not being known in advance of testing on a new device. These both demonstrate the need for adaptive delay compensation, that is, a compensator which varies the extrapolation time in accordance with a continually updated estimate of the current delay. Systems for achieving adaptive delay compensation which have been proposed and demonstrated in the literature include the Darby Estimator [11] and Adaptive Times Series (ATS) Compensator [12].

The key outcome of this project is a system capable of performing stable, accurate hybrid simulations, with substructuring, in real-time with a highly nonlinear physical substructure. A BRB has been used as the physical substructure in this project, but the testing system has been designed with the intention that it should be possible to apply it to any type of device. This is demonstrated at the end of the project when the system is applied to a different type of device: a viscoelastic damper. The ATS compensator is shown to be effective at compensating for actuation delays and providing a stable feedback loop. In addition, unlike most delay compensation methods, it further improves accuracy by correcting for amplitude errors, where the actuator displacements overshoot or undershoot the target values. However, it is also found to require a significant amount of computation and processing during each

timestep. The number of computations and operations that can be performed per timestep in a real-time simulation, for a given processor, are limited by the size of the integration timestep which must be small enough to ensure stability of the integration. Therefore, the more processing required by the delay compensator, the less is available for integrating the numerical substructure, reducing the structural complexity, such as number of degrees-of-freedom (DOFs), which can be simulated. In this project, a modification to the ATS has been tested which operates on the same principle, but with greatly reduced computational demand. Through extensive testing, the modified ATS (mATS) compensator is demonstrated to provide actuation quality which is as good as or better than that of the original, and the importance of the parameters defining the compensator have been investigated.

Another novel component included in the RTHS system is an online stiffness simulator. This produces a continually updated model of the current stiffness of the physical substructure which provides smooth, continuous force feedback tracking that of the physical substructure. This provides stability by extrapolating the force feedback to correct for any actuation error which remains, while maximising accuracy by using a continually updated estimate of the stiffness for the extrapolation.

An additional issue affecting actuation quality is the flexibility of the components of the test rig, since deflection occurring in the rig due to the applied forces causes a disparity between the displacement of the actuators and the deflection of the physical substructure. To ensure the target displacements are accurately applied, a method for compensating for rig compliance is incorporated into the system and shown to be effective. This also deals with the additional complexity caused by the rig layout, which uses two actuators in parallel, by constraining the displacements of the actuators to be the same.

The chapters of this thesis are arranged as follows:

- *Chapter 2* gives a background to seismic design within the framework of the Eurocode standards. It introduces BRBs and their potential implementation in this design context. This is used in the design of two steel frame structures which are simulated using RTHS in Chapter 6. The first consists of a moment-resisting frame (MRF) to which BRBs are added as supplemental dampers, while the

second consists of a BRB frame (BRBF) in which the BRBs form the main lateral load resisting system.

- *Chapter 3* provides a background to RTHS and a review of previous research into hybrid simulation. It describes the key components of a RTHS system, the obstacles which must be overcome to achieve a stable, accurate simulation, and the laboratory setup used in this project.
- *Chapter 4* deals with the problem of providing high quality actuation. It explains the deleterious effect an actuation delay can have on the stability of the system and reviews a selection of compensation methods proposed and tested in the literature. A modified version of the ATS compensator is proposed and the equations defining the compensator are derived, along with a method for compensating for compliance of the test rig. The resulting control system is applied to open-loop (predefined displacement) testing of a BRB where the performance of the system is investigated for small and large displacements, and at low and high frequencies.
- *Chapter 5* describes the implementation of a single-degree-of-freedom (SDOF) numerical substructure and introduces the stiffness simulator. These are combined with the work of Chapter 4 to create the complete RTHS feedback loop and the performance of the system is tested.
- *Chapter 6* extends the RTHS system to simulate a multi-degree-of-freedom (MDOF) structure. Suitable steel structures for simulation were designed with reference to the Eurocode 8 seismic design code and numerical models implemented as the numerical substructure. As the simulated structures contain multiple BRBs, but facilities were only available to test one at a time, a numerical model was fitted to the results of earlier tests and used to model the BRBs not forming the physical substructure. The accuracy and stability of the system is demonstrated for the hybrid simulation of realistic structures under realistic levels of seismic demand. The results demonstrate the performance of BRBs under realistic seismic loading conditions and their ability to undergo many large-displacement yielding cycles with considerable reserves of ductility. As a final demonstration of the versatility of the RTHS system, results are presented of its successful application to RTHS with a viscoelastic damper as the physical substructure.

2. Seismic Design and Supplemental Energy Dissipation

2.1. Earthquake Resistant Design to Eurocode 8

2.1.1. Seismic Design Codes

Using conventional forms of construction, it is rarely economical to design a structure to remain elastic during a strong earthquake. Modern design codes therefore make use of ductility to dissipate energy and reduce the seismic forces. Here this approach will be elucidated with reference to the Eurocodes [3], [13]–[15]. These are a set of ten standards governing structural design which provide harmonisation of technical specifications between 34 European countries. These standards are summarised in Figure 2.1, where those used in this project are shaded, the most important being *Eurocode 8: Design of structures for earthquake resistance — Part 1: General rules, seismic actions and rules for buildings (EN 1998-1)* [3]. In the USA, seismic design is governed by the standard *ASCE 7-16 Minimum Design Loads and Associated Criteria for Buildings and Other Structures* [16], which is incorporated into the International Building Code [4] by reference. This code (approved in 2016) is of interest as it incorporates specific rules for buckling-restrained braced frames (BRBFs) which the current version of Eurocode 8 (approved in 2004) does not. This section gives an overview of the key aspects of

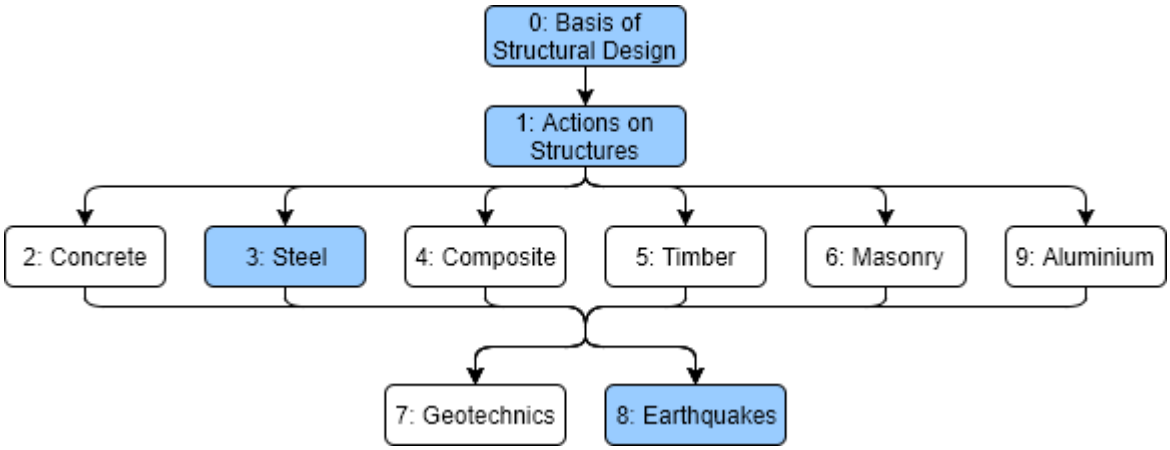

Figure 2.1 – Summary of Eurocode standards (EN1990-EN1999) for structural design

performing the seismic design of a steel building structure in accordance with Eurocode 8 [3] and the methods of analysis available to the engineer, which will be used to design structures to be simulated in the RTHS testing presented in Chapter 6.

2.1.2. Performance Levels

Eurocode 8 [3] specifies that two performance levels are considered:

1. No-Collapse performance level (*life safety*): the structure must maintain full vertical load bearing capacity after an earthquake with a 475-year return period (the *ULS action*) with sufficient residual lateral strength and stiffness to protect life during aftershocks.

2. Damage Limitation performance level: the cost of damage and limitations of use of the structure after an earthquake with a 95-year return period (the *damage limitation action*) should not be disproportionately high in comparison with the cost of the structure.

The first is achieved using "capacity design" where it is ensured that the *ductility demand* (the maximum ductility experienced by the structure during the earthquake) is exceeded by the *ductility supply* (the maximum ductility that the structure can sustain without failure). A "hierarchy of resistance" is employed to ensure that the intended ductile modes occur before brittle modes can form, e.g. flexural strengths should be significantly lower than shear strengths and 'soft-storey' behaviour must be prevented. The regions expected to undergo ductile yielding are referred to as *dissipative zones*.

The second performance level is considered to be achieved if the peak interstorey drift ratios (IDRs) under the *damage limitation action* fall within allowable limits. The interstorey drift, d_r, in each storey is defined as the relative displacement between adjacent floors. This is divided by the storey height, h, to obtain the IDR, d_r/h, which is limited to the following values:

- 0.5% for buildings having non-structural elements of brittle materials attached to the structure;

- 0.75% for buildings having ductile non-structural elements;

- 1.0% for buildings having non-structural elements fixed in a way so as not to interfere with structural deformations or without non-structural elements.

Non-structural elements are components of the building which do not form part of the load carrying system such as cladding, partition walls, suspended ceilings and utilities. In calculating these deflections, Eurocode 8 assumes that the *damage limitation* ground motion is simply a scaled version of that due to the *ULS seismic action*. The recommended value of the reduction factor, ν, is 0.5 for buildings of ordinary importance. Note that the damage to some non-structural elements (such as suspended ceilings, desktop electronics and air handling units) is more dependent on acceleration than displacements. Eurocode 8 requires the effect of accelerations on individual non-structural elements to be considered where failure of the element might cause risk to persons or affect the main structure or services of critical facilities; however, it does not apply direct limits on the accelerations of the structure itself [3].

Some projects require more onerous performance requirements be achieved, notably structures important for civil protection must have sufficient strength and stiffness to maintain the function of vital services after a seismic event with an appropriate return period. Alternatively, building owners may impose more onerous performance requirement on the design due to a consideration of total life costs of the structure. The increased construction costs required to improve seismic performance can be justified by the reduction in repair costs and downtime of the building should an earthquake occur.

2.1.3. Combinations of Actions

Eurocode 0 [13] specifies how actions are to be combined using a partial factor approach. For verifying the resistance of the structure to non-seismic actions, the following combination is specified:

$$\sum_{j\geq 1} \gamma_{G,j} G_{k,j} \text{ "+" } \gamma_Q Q_{k,1} \text{ "+" } \sum_{i>1} \gamma_{Q,i} \psi_{0,i} Q_{k,i} \qquad 2\text{-}1$$

where $G_{k,j}$ are the set of permanent actions, $Q_{k,1}$ is the leading variable action, $Q_{k,i}$ $(i > 1)$ are the accompanying variable actions, and the symbol "+" is used to mean “in combination with”. The partial

safety factor for permanent actions, $\gamma_{G,j}$, is taken as 1.35 (or 1.0 if the action is favourable) while that for variable actions, $\gamma_{Q,i}$, is taken as 1.5 (or 0.0 if favourable). The combination factor, $\psi_{0,i}$, for the characteristic combination accounts for the improbability of the accompanying actions taking their peak values at the same instant as the leading action does, taking the value of 0.7 for imposed loads, 0.5 for wind loads and 0.6 for temperature induced loads. The structure must be verified against all possible combinations (i.e. with each variable action taken as leading action in turn), with the actions $G_{k,j}$ and $Q_{k,i}$ being determined in accordance with Eurocode 1 [14]. The designer must then verify that the resistances of the structural members and connections, calculated in accordance with Eurocode 3 [15], exceed the action effects resulting from these combinations.

Structures to be built in seismically active regions must also be verified against the seismic combination:

$$\sum_{j\geq 1} G_{k,j} \text{ " + " } A_{Ed} \text{" + " } \sum_{i\geq 1} \psi_{2,i} Q_{k,i} \qquad 2\text{-}2$$

where the design seismic action A_{Ed} is determined in accordance with Eurocode 8 [3]. Due to the extreme but infrequent nature of a seismic loading event, the partial safety factors are reduced to 1.0 and the combination factor, $\psi_{2,i}$, for the quasi-permanent combination is used in place of $\psi_{0,i}$, which takes the value of 0.3 for imposed actions (except at the roof where it is 0.0), and 0.0 for wind or temperature induced actions. As well as providing rules for determining the design seismic action, Eurocode 8 also provides specific design rules to ensure that the capacity design requirements mentioned above are met. In addition, each Eurocode part is accompanied by a National Annex for the country where the structure is to be constructed which specifies the values of parameters and approaches to be used for instances where national choice is permitted. Importantly, the national annex to Eurocode 8 will specify the level of seismicity to be designed for which is generally presented by a seismic hazard map specifying the peak ground acceleration, a_{gR}, to be used for structures within each seismic region.

2.1.4. Determining the Seismic Action

Eurocode 8 specifies the design seismic action in terms of an *elastic ground acceleration response spectrum*. An elastic response spectrum is a plot of the peak acceleration, S_e, occurring in an elastic single-degree-of-freedom (SDOF) structure in response to the ground motion against the natural period, T, of the structure. The elastic response spectrum of the design seismic action is therefore intended to provide an envelope of possible earthquakes having the specified return period (usually 475 years). The shape of the response spectrum is illustrated in Figure 2.2 and is defined by the periods T_B, T_C and T_D which delimit the four branches of the spectrum. The magnitude depends on the design ground acceleration, a_g, which is given by:

$$a_g = \gamma_I a_{gR} \qquad 2\text{-}3$$

where a_{gR} is the peak ground acceleration on type A ground (depending on the seismic region) and γ_I is the importance factor (depending on the building's intended purpose). The influence of local ground conditions is accounted for by multiplying the accelerations by a soil factor, S, depending on the type of ground on which the building is to be located. The elastic response spectrum defined by Eurocode 8 assumes inherent damping ζ of 5% which accounts for energy dissipated by the main structure during motion through multiple sources (e.g. friction between surfaces), although an additional factor, η, can be applied to take approximate account of an inherent damping level which differs from this.

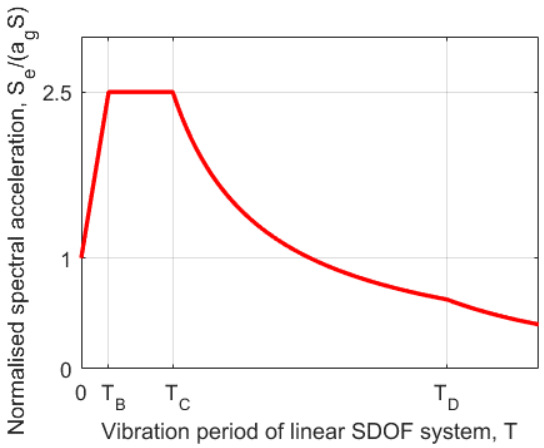

Figure 2.2 – Eurocode 8 Elastic Response Spectrum

2.1.5. Capacity Design Rules

Capacity design is used to ensure that the distribution of material and element properties is such that dissipative zones, where yielding is to occur, form where intended. The location of the dissipative zones depends upon the structural type which is defined based on the method for resisting loads. In moment-resisting frames (MRFs) the dissipative zones are created by plastic hinges forming in the beams (and in the columns at the base of the structure). In concentrically braced frames (CBFs) the dissipative elements are the braces which are expected to yield in tension. In eccentrically braced frames (EBFs) the dissipative zones form in elements or parts of elements called seismic links which yield in shear and/or bending due to the line of action of the bracing being offset with respect to the frame. To ensure the hierarchy of resistance is achieved in light of possible material overstrengths, non-dissipative elements (e.g. the columns) are verified against an increased set of design actions given by:

$$N_{Ed} = N_{Ed,G} + 1.1\gamma_{ov}\Omega N_{Ed,E} \quad \text{2-4(a)}$$

$$M_{Ed} = M_{Ed,G} + 1.1\gamma_{ov}\Omega M_{Ed,E} \quad \text{2-4(b)}$$

$$V_{Ed} = V_{Ed,G} + 1.1\gamma_{ov}\Omega V_{Ed,E} \quad \text{2-4(c)}$$

where $N_{Ed,G}$, $M_{Ed,G}$ and $V_{Ed,G}$ are the compression force, bending moment and shear force in the elements due to the non-seismic actions; $N_{Ed,E}$, $M_{Ed,E}$ and $V_{Ed,E}$ are the compression force, bending moment and shear force in the elements due to the design seismic action; and γ_{ov} is the overstrength factor accounting for the possibility that the actual yield strength of the steel in dissipative zones exceeds the nominal value. For MRFs, Ω is the minimum value of $\Omega_i = M_{pl,Rd,i}/M_{Ed,i}$ of all beams, i, in which dissipative zones are located, where $M_{pl,Rd}$ is the plastic moment of resistance at each plastic hinge location. For CBFs, Ω is the minimum value of $\Omega_i = N_{pl,Rd,i}/N_{Ed,i}$ of all braces, i, where $N_{pl,Rd}$ is the plastic resistance of the brace in tension.

To ensure that the full plastic moment can be achieved in the beams (or beam-column connections) in a MRF, it must be verified that $V_{Ed} \leq 0.5V_{pl,Rd}$ where $V_{pl,Rd}$ is the design shear resistance of the beam and V_{Ed} is the shear force generated when the full plastic moments have been reached at both ends

of the beam – beyond this value the moment of resistance would be reduced by the presence of the shear force. Connections must also be verified against this worst-case combination and must be capable of accommodating the rotation required for the plastic hinge to form.

To ensure global ductile behaviour the formation of soft stories, where deformations are concentrated within a single storey, must be avoided due to the excessive local ductility demands this imposes on the columns, as shown in Figure 2.3(a). In MRFs, this is done by ensuring "weak beam / strong column" behaviour at any connection of a beam to a primary column to ensure plastic hinges form in beams before they form in columns, as shown in Figure 2.3(b). To achieve this the sum of the moments of resistance, M_{Rc}, of the columns framing the joint must be at least 1.3 times the sum of the moments of resistance, M_{Rb}, of the beams framing the joint:

$$\sum M_{Rc} \geq 1.3 \sum M_{Rb} \qquad 2\text{-}5$$

To ensure ductility is distributed over the height of the structure in CBFs, as shown in Figure 2.3(c), a restriction is applied on the allowable variation of the overstrength factor, Ω_i, between the braces in tension in the structure:

$$\max(\Omega_i) \leq 1.25 \min(\Omega_i) \qquad 2\text{-}6$$

This aims to ensure ductility demands aren't excessively concentrated in the braces of a single storey. Since the braces in compression will buckle, they can be assumed to provide no lateral resistance in simplified analysis (apart from in chevron bracing where they are included in the model, but with a reduced buckling strength). Eurocode 8 therefore requires that the horizontal projection of the bracing providing resistance in each direction must not differ significantly within each storey to provide similar behaviour in both directions.

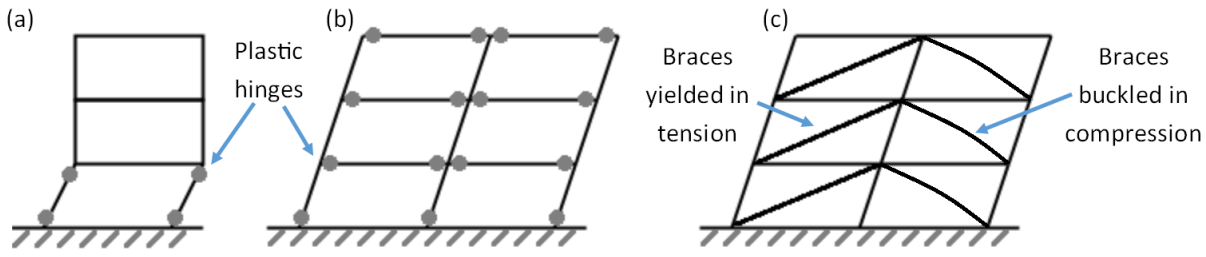

Figure 2.3 – (a) Soft storey mechanism; (b) target mechanism for MRFs; (c) target mechanism for CBFs

2.1.6. Methods of Analysis

Having defined the seismic action, one of the four methods of analysis allowed by Eurocode 8 must be used to determine the action effects. These consist of two linear-elastic methods: *the lateral force method of analysis* and the *modal response spectrum analysis*; and two non-linear methods: *nonlinear static (pushover) analysis* and *nonlinear time history (dynamic) analysis*.

The linear-elastic methods account for the significant non-linear plastic behaviour expected during the design seismic action by the application of a behaviour factor, q, which depends on the structural type (the method of transferring lateral loads to the foundations) and its ductility class. For example, for steel structures of ductility class medium (DCM), q is taken as 4 for MRFs, CBFs with diagonal bracing and EBFs, while for CBFs with chevron bracing q is taken as 2. Higher values of q are permitted if the structure is designed for high ductility (DCH) which depend on the overstrength ratio α_u/α_1 where α_1 is the multiplier which must be applied to the seismic action to first reach the plastic resistance in any member and α_u is the multiplier which must be applied to the seismic action to form sufficient plastic hinges to cause overall instability of the structure. In this case, q is increased to $5\alpha_u/\alpha_1$ for MRFs and EBFs, $4\alpha_u/\alpha_1$ for combined MRFs with concentric bracing and to 2.5 for CBFs with chevron bracing but remains at 4 for CBFs with diagonal bracing. To use these higher values, stricter limits are placed on the section classes that may be used (only class 1 sections can be used for dissipative elements, rather than class 1 or class 2 for DCM) and the connections must be designed to provide a larger rotation capacity for plastic hinge regions. The default values of α_u/α_1 (which can be used if analysis to determine the actual value of α_u/α_1 are not performed) are 1.2 for single bay multistorey MRFs and for EBFs, and 1.3 for MRFs with multiple moment resisting bays per storey. The maximum value of α_u/α_1 allowed by the code is 1.6 (even if analysis, such as pushover analysis, gives a higher value), so that the maximum value q can take under any circumstances is 8.

Ductile yielding reduces the forces experienced by the structure while increasing the deflections, hence the acceleration of the elastic response spectrum is divided by q (for $T > T_B$) to obtain the *design*

response spectrum illustrated in Figure 2.4. Using equivalent linear analysis, the design spectrum is used to determine the loads to apply to the structural model and the design displacements, d_s, are obtained by multiplying the computed elastic displacements, d_e, due to these loads by a factor, q_d, which is taken as equal to q unless otherwise stated. In the non-linear analysis methods, ductility is instead accounted for by direct modelling of the post-elastic behaviour of the yielding elements.

All methods require an estimate of the seismic mass of the structure, which is taken as the mass associated with the gravity loading from the combination:

$$\sum_{j\geq 1} G_{k,j} \text{ " + " } \sum_{i\geq 1} \psi_{E,i} Q_{k,i} \qquad 2\text{-}7$$

where $\psi_{E,i} = \varphi\psi_{2,i}$ and the coefficient $\varphi \leq 1$ accounts for the likelihood that not all masses due to imposed loads will be present simultaneous as well as imperfect coupling between these masses and the structure. For modelling purposes, it is common to assume that the mass is lumped at floor levels.

2.1.6.1. Modal Response Spectrum Analysis

To perform a modal response spectrum analysis, first the natural periods, $T_i = 2\pi/\omega_i$, and corresponding mode shape vectors, $\boldsymbol{\phi}_i$, are obtained. If the structure is described by stiffness matrix, K, and mass matrix, M, then the eigenvectors of $M^{-1}K$ give the mode shapes and the corresponding

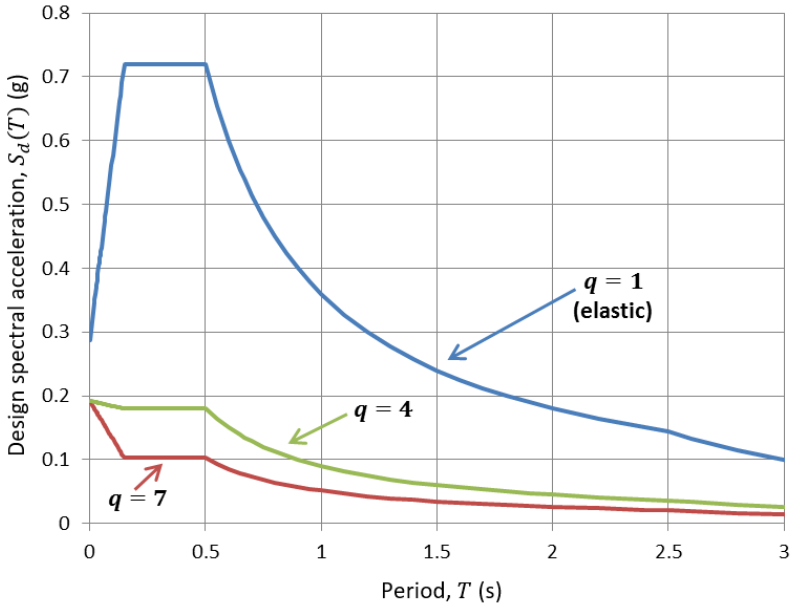

Figure 2.4 – Eurocode 8 design response spectra for Greece (seismic zone II)

eigenvalues give ω_i^2. Higher modes can be neglected provided the effective modal masses of those considered sum to at least 90% of the total modal mass or provided any mode with an effective modal mass exceeding 5% of the total mass is considered. The design spectral acceleration $S_d(T_i)$ is read from the ductility-reduced design spectrum (Figure 2.4) for each mode, from which the lateral force at each floor, j, in each mode, i, can be computed as:

$$F_{i,j,max} = m_j \phi_{i,j} \Gamma_i S_d(T_i) \quad \text{2-8}$$

where m_j is the mass at the j^{th} floor, $\phi_{i,j}$ is the element of $\boldsymbol{\phi}_i$ corresponding to the j^{th} floor, $\Gamma_i = \boldsymbol{\phi}_i^T M\{\mathbf{1}\}/\boldsymbol{\phi}_i^T M \boldsymbol{\phi}_i$ is the modal participation factor and $\{\mathbf{1}\}$ is a column vector of ones. Provided the modes can be assumed independent then the combined response can be taken as the square root of the sum of the squares (SRSS) of the action effects due to each mode. These static loads can then be applied to a linear-elastic structural model to determine the load effects in the members and connections (which must not exceed the resistances), while the design displacements will be q times those given by the linear-elastic model (which must satisfy the drift limitations for the damage limitation performance level).

2.1.6.2. Lateral Force Method of Analysis

The lateral force method of analysis is a simpler method which can be used if the response is dominated by the fundamental mode in each principal direction. This can be assumed to be the case if the fundamental period, T_1, does not exceed the smaller of $4T_C$ (see Figure 2.2) and 2.0s, and the structure satisfies the requirements to be considered regular in elevation. The base shear force F_b is taken as:

$$F_b = S_d(T_1) m \lambda \quad \text{2-9}$$

where m is the total mass of the structure and $\lambda = 0.85$ provided $T_1 < 2T_C$ and the structure has more than two stories (to account for the fact not all of the mass will be participating in the fundamental mode), otherwise $\lambda = 1.0$. The code allows the fundamental period to be approximated as:

$$T_1 \approx C_t H^{3/4} \quad \text{2-10}$$

where H is the height of the building, and C_t is 0.085 for MRFs, 0.075 for EBFs or 0.050 for CBFs. The horizontal seismic forces are distributed through the height of the structure in proportion to the fundamental mode shape and the storey mass:

$$F_j = F_b \frac{s_j m_j}{\sum_i s_i m_i} \quad \text{2-11}$$

where $s_j = \phi_{1,j}$ is the displacement of storey j in the fundamental mode shape. Further simplification is allowed by assuming the fundamental mode shape to be linear so that $s_j = z_j$ where z_j is the height of mass, m_j, above the ground. As for the response spectrum analysis, these static loads will be applied to a linear-elastic structural model to obtain the load effects.

2.1.6.3. Limitations of Linear-Elastic Methods

The linear-elastic methods using equivalent forces are desirable due to simplicity of modelling which they allow, but there are situations where they are not sufficient and nonlinear analysis must be performed. This is the case for structural types not specifically dealt with by Eurocode 8, such as buckling-restrained braced frames (BRBFs) for which the current version of Eurocode 8 does not provide a behaviour factor or simplified design rules. Nonlinear methods require the model to be extended to include the strength of structural members requiring, at the very least, a bilinear force-deformation relationship to be used for any element which undergoes yielding.

2.1.6.4. Nonlinear Static (Pushover) Analysis

To perform a pushover analysis, a constant gravity load is applied to a model, which includes post-elastic behaviour, in combination with a monotonically increasing horizontal load. At least two distributions of lateral loads must be applied, including a "uniform" distribution ($F_j \propto m_j$) and a "modal" distribution ($F_j \propto s_j m_j$). This can be used to find the overstrength ratio α_u/α_1 of the structure, to find the expected plastic mechanism and distribution of damage, to assess structural performance, and as an alternative to the linear-elastic methods based on q (by comparing the ductility supply to the ductility demand). Plotting the total base shear F_b against the displacement d_n of the control node

(usually taken as being at the roof level) produces a pushover curve, although it is normal to first convert the structure to an equivalent SDOF structure by dividing F_b and d_n by a transformation factor, Γ, to give the equivalent SDOF force, F^*, and displacement, d^*. An elastic-perfectly plastic approximation to the pushover curve can be obtained by matching the energy dissipated up to the formation of the global plastic mechanism occurring at equivalent force F_y^* and equivalent displacement d_m^*. From this, the effective natural period, T^*, of the equivalent SDOF structure can be obtained and used to determine the target displacement, d_t, of the control node. It can then be verified from the pushover curves that the structure has sufficient ductility to achieve this displacement without failing.

2.1.6.5. Nonlinear Time History Analysis

The three analysis methods described so far all involve applying equivalent *static* lateral loads to represent the earthquake loading. This allows simpler models to be used but is unable to capture rate-dependent effects (e.g. in a structure fitted with viscous or viscoelastic devices) and does not give information on the cyclic demands on elements (which may undergo multiple yielding cycles during an earthquake). Instead rules are applied to ensure that the cyclic yielding will not compromise the integrity of the structure (such as prescribing the materials and classes of section which can be used and setting limits on slenderness and relative strengths of adjacent elements). Nonlinear time history (NLTH) analysis involves applying an earthquake ground acceleration record (accelerogram) to a dynamic nonlinear model of the structure and performing direct numerical integration of the equations of motion to calculate the complete motion of the structure rather than just peak values. This can give the most complete picture of a structure's dynamic response [17], giving information on the hysteretic demands on yielding elements, and can incorporate rate-dependency (provided suitable numerical models are available). The real-time hybrid simulation (RTHS) testing carried out in this project is essentially an extension of NLTH analysis where part of the simulated structure is taken out of the numerical model and is instead physically tested in real-time.

2.1.6.6. Selection of Ground Motions for Nonlinear Time History Analysis

NLTH analysis requires that specific accelerograms be selected to apply to the model, unlike the static methods which allow peak accelerations to be taken directly from the design response spectrum. Eurocode 8 therefore specifies rules designed to ensure that the accelerograms used are representative of the design seismic action, including:

- A suite of at least three accelerograms must be used, with the most unfavourable response being taken as the action effect, unless seven or more are used, in which case the average response is taken;
- The mean peak ground acceleration of the suite must not be smaller than $a_g S$;
- In the period range $0.2T_1$ to $2T_1$ no value of the mean of the spectra in the suite should be less than 90% of the elastic response spectrum given by the code.

These spectra can be artificially generated, recorded or simulated. The seismic action depends on the location of the structure, which in this project is assumed to be Greece (seismic zone II) on soil type B. This location has a peak ground acceleration, a_{gR}, of $0.24g$ and a soil factor, S, of 1.2, while the periods, T_B, T_C and T_D, are 0.15s, 0.5s and 2.5s, respectively. The structure is assumed to be of ordinary importance so γ_I is taken as 1.0. This produces the elastic response spectrum shown in Figure 2.4 ($q = 1$) and also in Figure 2.5. A suite of three recorded accelerograms were selected from the PEER NGA West database [18] which is a searchable database containing recorded accelerograms and meta data for a great number of earthquakes. The building designs in Chapter 6 have fundamental periods, T_1, of 0.855s and 1.075s, so it was ensured that the suite mean spectrum exceeded 90% of the elastic spectrum over the period range 0.17s to 2.15s so that the same suite could be used for both buildings.

In addition to satisfying the Eurocode 8 requirements, it is desirable to minimise the peak overshoot of the mean spectrum relative to the target to minimise the exaggeration of the response in certain modes. The PEER NGA database has a search tool which determines the scale factor that minimises the weighted mean square error (MSE) between the spectrum of the recorded accelerogram and the user-

specified target spectrum. A uniform weighting over the range 0.17s to 2.15s was therefore used and the resulting MSE was then used to rank the records based on closeness of fit to the target spectrum. Preference was given to records with scale factors close to 1.0 to minimise the effects of scaling and to limit the number of candidate records. The spectra of candidate records were combined in various suites, with appropriate scale factors, until a code compliant suite was found having an acceptably small overshoot relative to the target. This suite consisted of the 1940 El Centro earthquake (North-South), the 1994 Northridge earthquake (East-West), and the 1986 Kalamata earthquake (North-South). The details of these ground motions, along with the scale factors required to satisfy the Eurocode 8 requirements for the ULS action, are given in Table 2.1 which also includes the record sequence numbers (RSN) that can be used to find the ground motion record on the PEER NGA database. The scaled elastic response spectra are shown in Figure A.1 in Appendix A while the combined suite is plotted in Figure 2.5 along with the target spectrum and suite mean, showing that the above requirements are satisfied. The ground acceleration time histories of these ground motions are shown in Appendix A, along with the ground velocity and displacement time histories obtained by integrating the acceleration record. If purely numerical analysis were used, it might be preferable to use a larger suite of ground motions to reduce uncertainty. However, here a small number is preferred as they are to be applied to physical testing of a BRB which will be fatigued by multiple large displacement tests.

The Kalamata ground motion was a natural choice as it was recorded at a location matching that assumed in the design – Greece seismic zone II on ground type B. It gives a good match to the target and only a relatively small amount of scaling was required. It can be seen from Figure A.2 in Appendix A that the Kalamata ground motion is characterised by one significant pulse in the ground displacement. The El Centro and Northridge ground motions complement this as they represent more continuous motion, as seen in Figure A.3 and Figure A.4, with the three ground motions being caused by different fault type mechanisms, as listed in Table 2.1. Another reason for preferring the El Centro and Northridge records over other candidates is that these are well known earthquakes which are widely used in the literature. Figure 2.5 shows that these records complement each other well with

peaks in the spectrum of one motion tending to correspond to troughs in another so that the variability of the mean spectrum is minimised.

The records in the PEER NGA database have undergone processing to correct for the response of the instrument that recorded the motion and to reduce random noise, while maximising the range of usable frequencies [19]. The lowest useable frequencies of the chosen records are shown in Table 2.1, the largest corresponding to a period of 4s, around four times the fundamental period of the modelled buildings so well outside the frequency range of interest. In addition, the records in the database have had baseline correction applied [20]. This ensures that the ground velocity record obtained by integrating the accelerogram returns to zero velocity at the end of the record, as can be seen in Figures A.2 – A.4.

	El Centro	Kalamata	Northridge
Event name:	Imperial Valley-02	Kalamata, Greece-01	Northridge-01
Station:	El Centro Array #9	Kalamata (bsmt)	Sylmar-Converter Sta
Year:	1940	1986	1994
Component:	North-South	North-South	West-East
PEER NGA RSN:	6	564	1048
Scale factor:	**1.02**	**1.18**	**0.87**
Moment magnitude:	6.95	6.2	6.69
Fault type:	Strike slip	Normal	Reverse
Average shear wave velocity, $v_{s,30}$ (m/s):	213.44	382.21	251.24
Lowest useable frequency (Hz):	0.25	0.1625	0.1625

Table 2.1 – Eurocode 8 compliant suite of scaled earthquake accelerograms

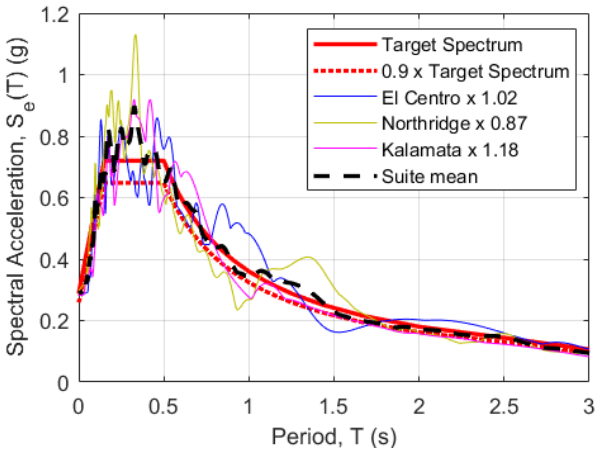

Figure 2.5 – Elastic response spectra for a Eurocode 8 compliant suite of scaled accelerogram records

2.2. Structural Analysis

2.2.1. Finite Element Analysis

For the design of the MDOF structures in Chapter 6, structural analysis has been performed using the Open System for Earthquake Engineering Simulation (OpenSees) software framework [21] [22]. This is an object-oriented framework for creating finite element applications for simulating structural and geotechnical response to earthquakes. The OpenSees source code is written in the C++ programming language [23] and finite element applications are written using Tcl code [24]. An advantage of OpenSees is that it is open-source, allowing users to access the source code and implement their own objects.

The equation of motion of a MDOF structure subjected to a ground acceleration, $\ddot{x}_g$, is given by:

$$M\ddot{\boldsymbol{x}} + C\dot{\boldsymbol{x}} + \boldsymbol{F} = -M\{\mathbf{1}\}\ddot{x}_g \qquad 2\text{-}12$$

where M is the mass matrix, C is the inherent damping matrix, $\boldsymbol{F}$ is the vector of restoring forces, $\{\mathbf{1}\}$ is a vector of ones, $\boldsymbol{x}$ is the vector of displacements relative to the ground and the dot operator ($\dot{}$) indicated differentiation with respect to time. For the NLTH analysis used in the structural design in Chapter 6, this was simulated using direct numerical integration in OpenSees.

2.2.2. Modal Analysis

The model in Eq. 2-12 could not be implemented directly in the MDOF RTHS tests as the large number of degrees-of-freedom (DOFs) prevented the computation from being carried out in real-time with the desired timestep. Various options are available, such as using a sub-stepping procedure to allow a larger timestep to be used in the numerical integration than in the actuator control system [25]. However, the approach in Chapter 6 is to used modal decomposition to reduce the number of DOFs in the numerical substructure. The background to modal decomposition is therefore given here.

A modal decomposition is used to decouple the equations of motion of a linear elastic N-DOF structure into N independent modes of oscillation. The response of each mode can then be obtained by integrating its equation of motion as a SDOF system, and the modal responses can then be combined

to give the overall response. The key advantage of this approach is that it removes the need to model all DOFs of the system directly since modes not contributing significantly to the overall response can simply be ignored. This can be used to remove high frequency components which determine the stability limits of conditionally-stable integration algorithms despite contributing little to the overall response. This will allow a larger integration timestep to be used, increasing the feasibility of performing the integration in real-time. At the same time, the reduction in the number of DOFs of the system will reduce the amount of computation required at each timestep allowing the computation to be completed in less time. A limitation of this approach is that it is derived from linear elastic structural properties. Nonlinear behaviour in the structure, such as yielding of BRBs, will cause the stiffness properties of the structure to change from those assumed in deriving the mode shapes. Yielding due to displacements from one mode will change the stiffness of the BRBs experienced by the other modes so that the modes are no longer truly independent, so care must be taken when using modal analysis in the presence of nonlinear behaviour. Here, the modal decomposition procedure will be described for a linear elastic structure, while the adaption of the method to nonlinear structures will be implemented in Chapter 6.

For a linear elastic structure, the equation of motion can be written as:

$$M\ddot{\boldsymbol{x}} + C\dot{\boldsymbol{x}} + K\boldsymbol{x} = \boldsymbol{f} \tag{2-13}$$

where K is the constant stiffness matrix and $\boldsymbol{f}$ is the vector of external forces, which in the seismic load case will be equal to $-M\{\mathbf{1}\}\ddot{x}_g$. The structural displacements, $\boldsymbol{x}$, are now written as the product of the mode shape matrix, Φ, and the modal displacement vector, $\boldsymbol{q}$:

$$\boldsymbol{x} = \Phi\boldsymbol{q} \tag{2-14}$$

where the columns of Φ contain the eigenvectors, $\boldsymbol{\phi}_i$, of the undamped system. These are obtained by considering free oscillations of the undamped system:

$$M\ddot{\boldsymbol{x}} + K\boldsymbol{x} = \mathbf{0} \tag{2-15}$$

where $\mathbf{0}$ is a column vector of zeroes. The equation of simple harmonic motion can be expressed as:

$$\boldsymbol{x} = \boldsymbol{\phi}\cos(\omega t - \alpha) \tag{2-16}$$

where the vector, $\boldsymbol{\phi}$, contains the peak amplitude of each degree of freedom, ω is the circular natural frequency of oscillation and α is the phase shift angle. Substituting Eq. 2-16 into Eq. 2-15 yields:

$$(M^{-1}K - \omega^2 I)\boldsymbol{\phi} = \mathbf{0} \qquad 2\text{-}17$$

where I is the identity matrix. Eq. 2-17 has non-trivial solutions ($\boldsymbol{\phi} \neq \mathbf{0}$) provided the determinant of the term in brackets is zero, which yields the *characteristic equation*:

$$|M^{-1}K - \omega^2 I| = 0 \qquad 2\text{-}18$$

Solving this equation yields the N eigenvalues, ω_i^2, which are the squares of the circular natural frequencies. Each of these can be substituted into Eq. 2-17 in turn to obtain the N corresponding mode shape vectors, $\boldsymbol{\phi}_i$, which are concatenated to give the modal matrix $\Phi = [\boldsymbol{\phi}_1 \quad \boldsymbol{\phi}_2 \quad \cdots \quad \boldsymbol{\phi}_N]$ in Eq. 2-14. Using Eq. 2-14 to substitute for $\boldsymbol{x}$ in Eq. 2-13 and pre-multiplying by Φ^T (where superscript T indicates the transpose of the matrix) gives:

$$\Phi^T M \Phi \ddot{\boldsymbol{q}} + \Phi^T C \Phi \dot{\boldsymbol{q}} + \Phi^T K \Phi \boldsymbol{q} = \Phi^T \boldsymbol{f} \qquad 2\text{-}19$$

The orthogonality properties of eigenvectors mean that $\Phi^T M \Phi$ and $\Phi^T K \Phi$ are diagonal. It is then assumed that the same is true of C so that $\mathrm{B} = \Phi^T C \Phi$ is also diagonal. This widely made assumption is referred to as *classical damping* and allows the equations of motion to become decoupled into N independent equations so each element of $\boldsymbol{q}$ can be solved for separately. It is not generally true that the C will be diagonalised by the undamped mode shapes, but it is an acceptable assumption given the low levels of inherent damping usually found in structures. This damping comes from a wide variety of mechanisms spread throughout the structure making it infeasible to determine C directly. Instead, assuming classical damping allows the damping to be specified in terms of modal damping ratios which can be estimated from experience of similar structures or from measured structural response. The scaling of the eigenvectors $\boldsymbol{\phi}_i$ is arbitrary, so for convenience the columns of Φ are scaled so that:

$$\Phi^T M \Phi = \mathrm{I} \qquad 2\text{-}20$$

With this condition satisfied, Eq. 2-19 simplifies to:

$$\ddot{\boldsymbol{q}} + \mathrm{B}\dot{\boldsymbol{q}} + \Lambda \boldsymbol{q} = \Phi^T \boldsymbol{f} \qquad 2\text{-}21$$

where $\mathrm{B} = \Phi^T C \Phi = \begin{bmatrix} 2\zeta_1\omega_1 & 0 & \cdots & 0 \\ 0 & 2\zeta_2\omega_2 & \cdots & 0 \\ \vdots & \vdots & \ddots & \vdots \\ 0 & 0 & \cdots & 2\zeta_N\omega_N \end{bmatrix}$ and $\Lambda = \Phi^T K \Phi = \begin{bmatrix} \omega_1^2 & 0 & \cdots & 0 \\ 0 & \omega_2^2 & \cdots & 0 \\ \vdots & \vdots & \ddots & \vdots \\ 0 & 0 & \cdots & \omega_N^2 \end{bmatrix}$,

while ζ_i and ω_i are the modal damping coefficient and circular natural frequency, respectively, in the i^{th} mode. Hence the modes are decoupled into N independent equations of the form:

$$\ddot{q}_i + 2\zeta_i\omega_i\dot{q}_i + \omega_i^2 q_i = p_i \qquad 2\text{-}22$$

where q_i is the i^{th} element of $\boldsymbol{q}$ and $p_i = \boldsymbol{\phi_i}^T \boldsymbol{f}$ is the modal force. Each of these equations can be integrated separately and the combined response of the structure, $\boldsymbol{x}$, recovered using Eq. 2-14. Any modes considered not to contribute significantly to the overall response can simply be ignored and the column corresponding to their mode shapes removed from Φ. The frequencies, ω_i, and mode shapes, Φ, can be extracted from the OpenSees model developed during the design of the building by using the *eigen* function, which uses the initial stiffness for any nonlinear elements. The low levels of inherent damping in building structures has a negligible effect on the mode shapes and natural frequencies, justifying the use of the undamped mode shapes and natural frequencies with the damped system.

2.2.3. Modelling Inherent Damping

It was seen above that the inherent damping state is defined by a damping coefficient, ζ_i, for each of the N modes of oscillation, based on the classical damping assumption used in Eq. 2-21 that the mode shapes, Φ, of the undamped system diagonalise the damping matrix, C. Since M and K are both diagonalised by Φ, so will a linear combination of the two. Hence a damping matrix, C_r, satisfying this classical damping assumption can be produced from:

$$C_r = \alpha M + \beta K \qquad 2\text{-}23$$

where α and β are scalar constants to be chosen. This gives *Rayleigh damping* [26] which is used extensively in NLTH analysis. By selecting appropriate values of α and β, the damping can be set to desired levels at two particular frequencies. For example, the coefficients required to set the damping to a target value, ζ, at two circular frequencies, $\omega_A = 2\pi f_A$ and $\omega_B = 2\pi f_B$, are:

$$\alpha = 2\zeta\omega_A\omega_B/(\omega_A + \omega_B) \text{ and } \beta = 2\zeta/(\omega_A + \omega_B) \qquad 2\text{-}24$$

The damping, ζ_i, at other frequencies, ω_i, is then given by:

$$\zeta_i = \frac{1}{2\omega_i}\alpha + \frac{\omega_i}{2}\beta \qquad 2\text{-}25$$

Hence ζ_i will be less than ζ at frequencies between ω_A and ω_B, and greater than ζ outside of this range. As an example, Figure 2.6(a) shows the damping produced when Rayleigh damping is applied to the MRF building in Chapter 6 with the damping set to a target value of 2% specified at the frequencies of the first and third modes. A clear limitation of this method is that the damping can only be specified at two specific frequencies, requiring a compromise where some modes have more damping and some less than desired. In the example in Figure 2.6(a), it was assumed that the response was dominated by the first three modes, and so damping values greater than the target of 2% is accepted in the higher modes. However, to avoid exceeding the target damping in the first or third modes, it was necessary to accept lower damping than desired in the second mode. In addition, Hall [26] has demonstrated a number of scenarios in which the use of Rayleigh damping can result in unrealistically high damping forces in the simulation, leading to unconservative results. Problems can occur due to the change in stiffness caused by cracking or sliding, and care must be taken to avoid problems when using penalty elements to impose constraints, or when simulating base isolated structures or earthquake response. For example, the equations of motion for earthquake response must be set up in terms of displacements *relative to the ground*, since the use of absolute displacements would include an extraneous damping contribution due to rigid body motion. However, the important issue in these simulations is the occurrence of yielding. Yielding reduces the effective stiffness and limits the structural restoring force, so having the damping remain linear can result in unrealistically high damping forces in relation to the strength of the building. In Figure 2.6(a) it is seen that a reduction in the effective frequency due to yielding leads to a rapid increase in the damping experienced in the fundamental mode, which is not a physical behaviour. It is common to use a frequency lower than the fundamental natural frequency, ω_1, as the lower frequency, ω_A, at which ζ is specified in an attempt to mitigate this – say, $\omega_A = 2\omega_1/3$. In addition, the initial stiffness matrix, K, in Eq. 2-23 is often replaced with the current tangent stiffness, K_t, so that C_r varies when yielding occurs. This reduces the

size of the damping forces produced by the stiffness proportional component of C_r when yielding occurs, and it has been shown that this can significantly reduce the size of the spurious damping forces. However, a number of authors caution that this is an *ad hoc* approach which lacks a physical basis, and it can lead to rapidly changing and even discontinuous damping forces [24] [25]. As an alternative, Hall [26] suggests the use of *capped viscous damping* where upper limits are imposed on the magnitudes of the damping forces to restrict them to realistic values. This is only compatible with stiffness proportional damping, without the mass proportional component, giving a linear increase in damping coefficient with frequency, although this would be offset by the use of appropriate capping values.

Damping can be set to specific values in more than two modes using Caughey damping given by:

$$C_c = M \sum_{j=0}^{N-1} \alpha_j (M^{-1}K)^j \qquad 2\text{-}26$$

where α_j are constants and N is the number of modes for which the damping is being set and can take any positive integer value up to the number of DOFs in the model. Rayleigh damping is a special case of Caughey damping for which $N = 2$. The damping, ζ_i, resulting from C_c at at a frequency, ω_i, is:

$$\zeta_i = \frac{1}{2} \sum_{j=0}^{N-1} a_j \omega_i^{2j-1} \qquad 2\text{-}27$$

and the coefficients, a_j, needed to set the damping to target values, ζ_j, at circular frequencies, ω_j, are obtained by solving:

$$\begin{bmatrix} 1 & \omega_1^2 & \omega_1^4 & \cdots & \omega_1^{2N-2} \\ 1 & \omega_2^2 & \omega_2^4 & \cdots & \omega_2^{2N-2} \\ \vdots & \vdots & \vdots & \ddots & \vdots \\ 1 & \omega_N^2 & \omega_N^4 & \cdots & \omega_N^{2N-2} \end{bmatrix} \begin{bmatrix} a_0 \\ a_1 \\ \vdots \\ a_{N-1} \end{bmatrix} = \begin{bmatrix} 2\omega_1\zeta_1 \\ 2\omega_2\zeta_2 \\ \vdots \\ 2\omega_N\zeta_N \end{bmatrix} \qquad 2\text{-}28$$

This offers better control of damping ratios over a range of frequencies, as shown in Figure 2.6(b) where the damping has been set to 2% in the first four modes ($N = 4$). However, there are practical issues with its implementation. One is the potential for ill-conditioning in the matrix in Eq. 2-25, while another is the potential for the damping in unprescribed modes to become negative [28], as occurs in Figure

2.6(b) when the damping is specified in only the first three modes ($N = 3$). This may explain why Caughey damping has not been popular in practice.

The spurious damping forces associated with the above methods can be avoided by using a damping matrix, C, constructed by superposition of modal damping matrices [29]. The modal analysis, from which modal damping ratios are defined, is based on the assumption that the mode shapes of the undamped system diagonalise C, so that $\Phi^T C \Phi = \mathrm{B}$ where $\mathrm{B}_{i,i} = 2\zeta_i \omega_i$ and $\mathrm{B}_{i,j} = 0$ for $i \neq j$. Hence it is straightforward to determine the coefficients of B based on the desired damping ratio, ζ_i, of each mode and the calculated natural circular frequencies, ω_i. This method inverts the process for obtaining B from C to determine the damping matrix, C, which would result in B. Wilson and Penzien [28] showed that this matrix can be calculated from:

$$C = M\Phi \mathrm{B} \Phi^T M \qquad 2\text{-}29$$

This provides direct control over the damping ratios in all modes but it results in a fully populated matrix, rather than a banded matrix as given by Raleigh damping. However, Chopra and McKenna [29] have shown that, when used with nonlinear analysis solved using iterative strategies, it is not necessary to create a full, dense tangent matrix, making it possible to implement this damping with only minimal increases in computational demand. This has been implemented in OpenSees as the *modalDamping* object (called using the command "*modalDamping $zeta*" where *$zeta* is the desired damping ratio which must be the same for all modes).

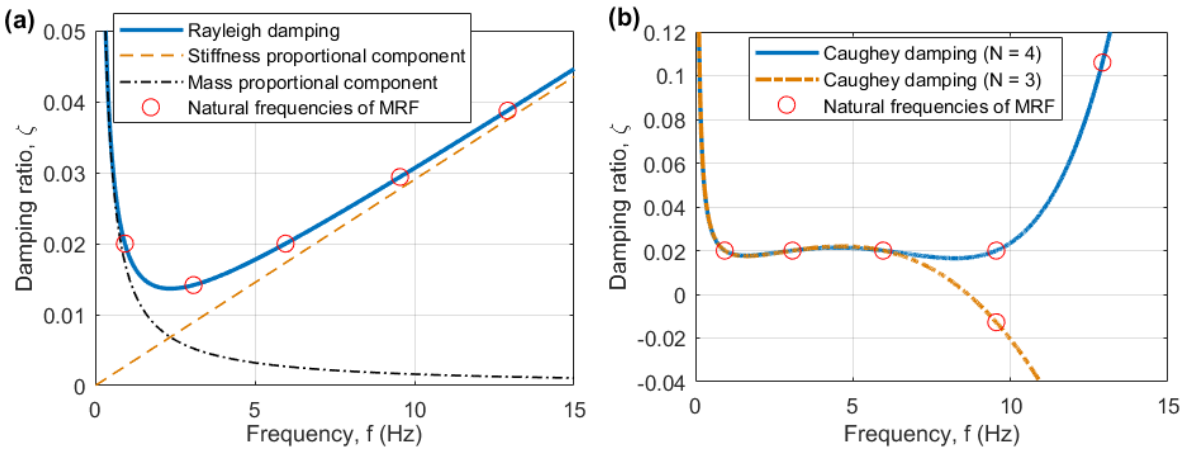

Figure 2.6 – Application of damping models to MRF structure: (a) Rayleigh, and (b) Caughey

2.3. Supplemental Energy Dissipation Devices

A supplemental energy dissipation device, or *damper*, is "an element which can be added to a system to provide forces which are resistive to motion, thus providing a means of energy dissipation" [30]. All structures have some inherent damping which dissipates energy during motion whilst within the elastic limits of the structural components. However, the low level of inherent damping exhibited by most buildings is usually insufficient to prevent the elastic limits from being exceeded during a strong ground motion. The excess energy must then be absorbed through ductile yielding and localised damage of the structural components. Dampers provide an alternative means of energy dissipation which, if correctly implemented, can reduce the structural response so that damage to the main structure is reduced or prevented. By reducing the interstorey drifts and floor accelerations experienced by the structure they can also reduce damage to non-structural components. Dampers are generally designed either to remain undamaged by an earthquake, or to be easily and cheaply replaceable after an earthquake. In buildings they will often be installed between adjacent floors to dissipate energy during relative motion between floors (interstorey drifts). They can also be installed across multiple storeys or can form part of a tuned mass damper or base isolation setup.

The use of dampers has increased rapidly since the mid-1990s [5]. The main types of dampers currently in use can be broadly divided into the categories listed in Table 2.2 [17]. The force produced by *rate-independent* dampers depends only on the displacement applied to the device (both the current displacement and the history of past displacements) and not on the rate at which the displacements are applied. By contrast, the force produced by *rate-dependent* devices depends on the velocity applied across the device, in addition to its displacement.

Type	*Device*	*Principle of Operation*
Rate-independent (Hysteretic)	Metallic yielding	Yielding of metals
	Friction	Frictional sliding
Rate-dependent (Viscoelastic (VE))	VE Solids	Deformation of VE polymers
	Viscous and VE fluids	Deformation of viscous fluids or fluid orificing

Table 2.2 – Classification of supplemental energy dissipation devices

2.3.1. Rate-dependent devices

Rate-dependent devices generally work either by deforming viscoelastic (VE) solids or viscous fluids, or by fluid orificing. A fluid viscous damper (FVD) takes the form on a piston filled with a fluid, typically silicone-based, which can move from one side of the piston head to the other via orifices as the piston head moves back and forth. Friction is generated as the fluid is forced through the orifices at high velocities resulting in the dissipation of energy as heat. The stiffness provided by these dampers at the frequencies of interest is negligible so that their response can be modelled as purely viscous, hence the force F is related to the velocity $\dot{x}$ by the relationship:

$$F(t) = C|\dot{x}(t)|^{\alpha}\mathrm{sgn}\big(\dot{x}(t)\big) \qquad 2\text{-}30$$

where C is the damping coefficient, α is the damping exponent which usually takes values in the range of 0.3 to 1.0, and $\mathrm{sgn}(.)$ is the signum function. If α is set to unity then this produces linear viscous damping of the type extensively used to model the inherent damping in structures due to its analytical amenability, and commonly used as a reference for comparing the energy dissipation due to other types of damping. This gives an elliptical force-displacement response (the size of the ellipse depending of the frequency of oscillation) as shown in Figure 2.7(a). Values of α less than unity can be desirable as they result in higher forces at lower velocities while limiting the forces at high velocities, increasing the energy dissipation for a given peak force. This gives a more rectangular force-displacement response, with a purely rectangular response being obtained for the theoretical case of α equalling zero which is equivalent to the response of a friction damper.

Viscoelastic (VE) solid dampers generally consist of solid pads of elastomeric material (usually polymers) sandwiched between steel plates to which they are bonded. Energy is dissipated through the shearing of the elastomeric polymer caused by relative motion between the steel plates. These devices exhibit both elasticity and viscosity, and can therefore be modelled by a Kelvin model which consists of a stiffness acting in parallel with a viscosity:

$$F(t) = Kx(t) + C\dot{x}(t) \qquad 2\text{-}31$$

where K is the storage stiffness and C is the damping coefficient – although it is common for the relation to be written in terms of stress, strain and strain rate, in which case K and C will be replaced by the storage and loss moduli, respectively. The force displacement response therefore forms a skewed ellipse, as shown in Figure 2.7(b). The values of K and C are dependent on a number of factors, notably: the frequency of oscillation, the strain amplitude and the temperature. Since the dissipated energy is converted to heat, the damper can undergo significant temperature variations during a seismic event. The requirement of EN15129 [31], that upper and lower limits of mechanical properties be accounted for in design is therefore particularly important for VE dampers.

2.3.2. Rate-independent devices

Rate-independent (or displacement-dependent) devices can generally be categorised as either metallic yielding dampers or friction dampers. Friction dampers dissipate energy through sliding friction between surfaces. The Coulomb model of friction is often appropriate for modelling their behaviour which, once sliding has occurred, is given by:

$$F(t) = \mu N sgn\big(\dot{x}(t)\big) \qquad 2\text{-}32$$

where μ is the coefficient of friction and N is the reaction force between the surfaces. It is hard to achieve a constant value of N throughout a seismic motion, and so the effects of variations in N should be taken into account. Eq. 2-32 produces a rectangular hysteretic force-displacement response which is highly non-linear, as shown in Figure 2.7(c). In a slotted-blotted damper [32] a series of steel plates are bolted together to provide the clamping force N which controls the force at which sliding occurs, while cylindrical friction dampers dissipate energy as a steel tube slides against copper pads [33]. The Pall cross-bracing friction damper [34] consists of a set of steel bars bolted together to form a rectangle which sits at the centre of a cross-bracing arrangement. As one pair of diagonals is put in tension and the other pair in compression the rectangle is deformed into a parallelogram resulting in rotation of the bolted connections which is resisted by the friction due to the clamping force provided by the bolts.

Friction dampers provide no restoring force so can be left with permanent deformations after an earthquake, which has led to research into the development of self-centring friction damper [35].

Metallic yielding dampers dissipate energy through cyclic ductile yielding of metal (usually mild steel) as shown in Figure 2.7(d). Buckling-restrained braces dissipate energy through axial yielding of a steel core which is restrained against buckling, usually installed in a diagonal or chevron bracing configuration. As this is the damper type tested in this project, a detailed description is given in the next section. Another metallic yielding damper is the added damping and stiffness (ADAS) damper [36]. This consists of a series of steel plates which are attached at their top to the upper floor and at their base to the chevron bracing joining them to the lower floor. Relative motion between the floors applies a shear to the plates causing them to bend around their weak axis resulting in energy dissipation due to flexural yielding. The plates are shaped to produce uniform flexural stress distributions over their height to distribute the yielding and maximise the ductility, resulting in triangular plates (for fixed-pinned connections) or hourglass shaped plates (for fixed-fixed connections). Various numerical models are available for modelling metallic yielding. The simplest would be a bilinear model; however, for dynamic analysis a more sophisticated model such as the Bouc-Wen model is likely to be required [7].

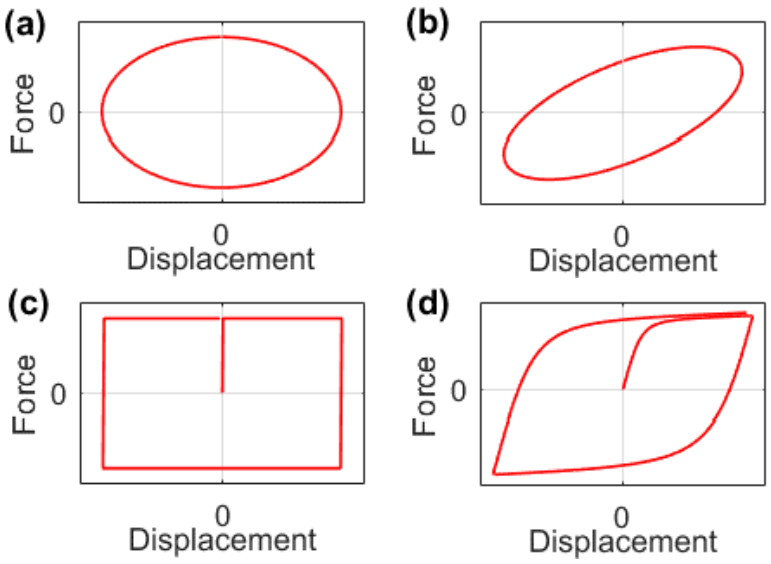

Figure 2.7 – Idealised force-displacement response for various damping mechanisms: (a) viscous, (b) viscoelastic, (c) friction, and (d) metallic yielding

2.3.3. Equivalent Viscous Damping

A useful measure of the energy dissipation potential of a damper is its e*quivalent viscous damping*. This is the damping coefficient, C_{eff}, (or damping ratio, ζ_{eff}) of a linear viscous damper which would dissipate the same amount of energy per cycle as the device in question for the given frequency and amplitude of oscillation. The energy, W, dissipated by a linear viscous damper per cycle is given by the integral of the force, F, (given by Eq. 2-30 with $\alpha = 1$) with respect to displacement, x:

$$W = \oint F dx = \oint C\dot{x} dx = \oint_0^T C\dot{x}^2 dt \qquad 2\text{-}33$$

where $T = 2\pi/\omega$ is the period of oscillation. Assuming sinusoidal oscillations of amplitude, A, at circular frequency, ω, gives:

$$W = \pi\omega C A^2 \qquad 2\text{-}34$$

Hence the equivalent viscous damping coefficient, C_{eff}, of a damper is given by:

$$C_{eff} = \frac{W}{\pi\omega A^2} \qquad 2\text{-}35$$

where W is now the energy dissipated by the actual device during a cycle of amplitude, A, at frequency, ω. This can also be specified in terms of the equivalent damping ratio, ζ_{eff}:

$$\zeta_{eff} = \frac{C_{eff}}{C_{crit}} = \frac{C_{eff}}{2\omega m} = \frac{W}{2\pi\omega^2 A^2 m} = \frac{W}{2\pi K_{eff} A^2} \qquad 2\text{-}36$$

where C_{crit} is the critical damping coefficient, K_{eff} is the effective stiffness of the system and m is the mass of the system which is assumed to be oscillating at its natural frequency, ω. In the case of a displacement-dependent device like a BRB the effective stiffness will be the secant stiffness, K_{sec}, at the design displacement, $A = d_{bd}$ (as illustrated in Figure 2.8).

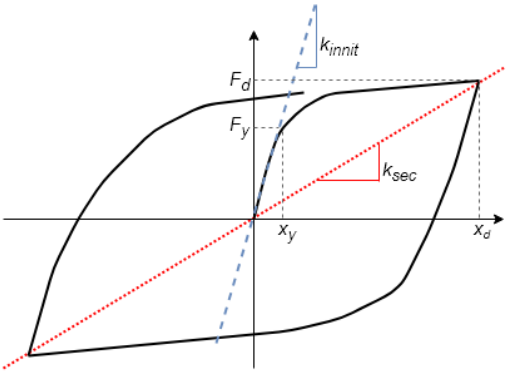

Figure 2.8 – Illustration of secant stiffness, k_{sec}, at peak displacement, x_d

By definition, $K_{sec} = V_{E,bd}/d_{bd}$ where $V_{E,bd}$ is the force at displacement d_{bd}. Substituting into Eq. 2-36 gives the definition of effective viscous damping specified by EN 15129 (3.1.10):

$$\zeta_{eff} = W(d_{bd})/2\pi V_{E,bd} d_{bd} \quad 2\text{-}37$$

which specifies that $W(d_{bd})$ be the measured energy dissipation occurring during the third cycle of the test at the total design displacement d_{bd} [31].

2.3.4. Estimating damping from structural response

It can be useful to be able to estimate the damping from the structural response. This can give an idea of the effectiveness of the damper being tested or can be used to verify that the properties experienced in the simulation match the values specified in the model. This can be done in the time domain by looking at the free vibration displacement response of the system after an initial excitation, such as being released from an initial displacement. The damped natural period is simply given by the time between adjacent peaks. The damping ratio can be estimated from the logarithmic decrement, δ_l, defined as the natural logarithm of the amplitude, x, of adjacent peaks:

$$\delta_l = \frac{1}{n} \ln \left| \frac{x_1}{x_{n+1}} \right| \quad 2\text{-}38$$

where n is an integer number of peaks (allowing the estimate to be averaged over multiple oscillations). From this the damping can be found from the relationship:

$$\zeta = \frac{\delta_l}{\sqrt{4\pi^2 + \delta_l^2}} \quad 2\text{-}39$$

Alternatively, the estimates can be obtained in the frequency domain from the frequency response function (FRF) obtained by dividing the Fourier transform of the system output by the Fourier transform of the input. The damped natural frequency is simply the frequency corresponding to the peak in the FRF. The damping can be estimated from the half power bandwidth using the relation:

$$\zeta = \frac{\omega_2 - \omega_1}{2\omega_n} \quad 2\text{-}40$$

where ω_1 and ω_2 are the frequencies before and after the peak at ω_n, respectively, at which the power has dropped to half its peak value (that is, the amplitude has fallen by 3dB).

2.4. Buckling-Restrained Braces

2.4.1. BRB Principle of Operation

A buckling-restrained brace (BRB) is a structural bracing element in which the axial load carrying system is decoupled from the buckling-resisting system. All BRBs consist of three main components: a steel core, a casing and an unbonding layer, as illustrated in Figure 2.9. The steel core is generally made from low yield mild steel and carries the entirety of the axial load applied to the BRB. It has a uniform cross-section (usually rectangular or cruciform) over most of its length (called the *yielding zone*) to distribute the plasticity as the core yields and maximise the ductility available. The cross-section increases at the ends so that the lengths of core protruding from the casing remain elastic (called the *elastic zones*). The casing surrounds the core to provide lateral restraint and prevent buckling of the core when it is in compression. This usually consists of a rectangular or circular steel tube filled with concrete/mortar. The steel tube provides flexural stiffness to resist global buckling of the BRB, as well as providing confinement to the concrete filling, while the concrete resists lateral movement of the core to prevent local buckling. An alternative casing system which has been the subject of recent research is the *all-steel BRB* [37] in which the core is sandwiched between flanged steel channel sections that are bolted together. Provided sufficient lateral restraint to the core can be achieved, these have the potential to offer a lighter weight solution and could allow access to the core for inspection which is not feasible with a conventional casing system. Key to the functioning of a BRB is the thin debonding layer which separates the core from the casing. This minimises shear transfer between the core and the concrete to prevent composite action and ensure virtually all of the axial load is carried by the core alone.

The effectiveness of conventional steel bracing systems is limited by buckling of the braces in compression. While the braces can reach their full yield strength and undergo significant ductile yielding in tension, they will buckle at a much lower load in compression and therefore cease to provide an effective path for lateral loads. This results in the highly asymmetrical hysteresis curve illustrated in Figure 2.10 (dashed line). This limits the ductility of the system and means braces must be provided in

pairs so that one is in tension when the other is in compression. In BRBs the prevention of buckling allows the steel core to reach its full yield strength and undergo significant ductile yielding in compression as well as in tension. This results in an almost symmetrical hysteresis curve, as illustrated in Figure 2.10 (solid line). This provides stable, ductile hysteretic behaviour with much greater energy dissipated, as indicated by the area enclosed by the hysteretic loop.

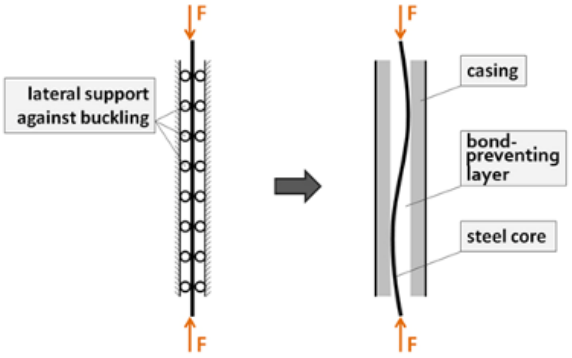

Figure 2.9 – BRB concept [38]

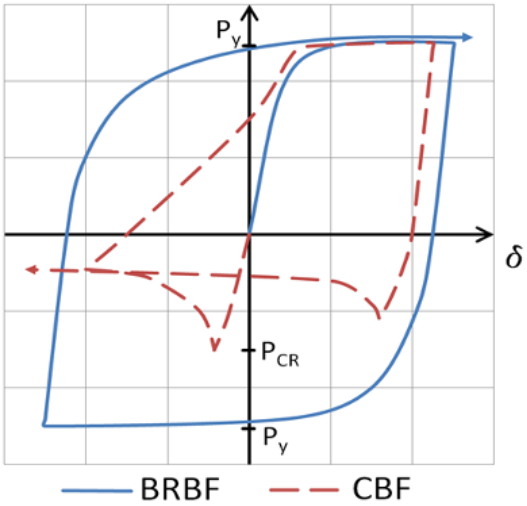

Figure 2.10 – Hysteresis curves for BRBs and conventional braces (CBF) [38]

2.4.2. History of BRBs and Current Applications

The concept behind BRBs began being investigated in the '70s when Wakabayashi et al. [39]–[41] tested flat plate steel braces sandwiched between reinforced concrete panels under cyclic loading. BRB research continued in Japan throughout the '80s and BRBs have been implemented in hundreds of buildings in Japan since the '90s. Interest in BRBs began to develop in the USA towards the end of the '90s leading to their first implementation in a steel construction at the University of California, Davis in 1999 [42]. They have since been used in many new and retrofitted structures in the USA and Canada, most commonly in new steel structures and in the retrofit of existing reinforced concrete structures, with their uptake being greatly facilitated by their incorporation into design codes in 2005 [43]. The majority of applications appear to be in buildings of low to mid-rise height – for reference, ASCE 7 [16] currently sets a maximum height limit for BRBFs of 50m for Seismic Design Categories D and E (high

and very high seismicity) and 30m for Seismic Design Category F (the highest seismic category), which can be increased to 75m and 50m, respectively, provided certain requirements are met.

Established manufacturers of BRBs in the USA include Nippon Steel (Unbonded Brace™) [44] and CoreBrace [45], while in Europe they are produced by Star Seismic Europe [46] who provided the BRB tested in this project. Interest in BRBs has been growing in Europe over recent years, although to date they have still only been used in a handful of structures. It seems likely this will grow as the technology becomes more established, as occurred in Japan and the USA. This is especially likely if they are incorporated into the next version of Eurocode 8, since the use of structural systems not covered by the design code imposes additional burden on the designer which acts as a barrier to their use. Star Seismic Europe BRBs have been used in two recent construction projects in Turkey. One is the new Technopark building at the Istanbul Technical University where they are used in a chevron bracing configuration in a three-storey steel frame building as part of a dual system with moment-resisting connections (BRB lengths of 4m with capacities in the range 105kN to 880kN). The other is in the Renaissance Tower, a 36-40 storey reinforced concrete building also in Istanbul (BRB lengths of 9.5m with capacities of up to 6500kN) [47]. They have also been installed in a technological structure of a power plant in Bulgaria (lengths of 2.8m and 3.1m with capacities of 141kN and 194kN). This is of interest as it used BRBs of the same type used in this project and samples of these BRBs have previously undergone extensive testing [48] in accordance with the European Standard *EN 15129 Anti-seismic Devices* [31] and the *ECCS Recommended Testing Procedure for Assessing the Behaviour of Structural Steel Elements under Cyclic Loads* [49].

2.4.3. Incorporation of BRBs in Design Codes

BRBs have been described above as being a type of damper. However, much literature treats them as braces without direct reference to their damping properties. These designations are not mutually exclusive: BRBs are dampers because they dissipate energy from the structure to reduce motion, and they are braces because they add lateral stiffness to the structure and can form the main lateral load

resisting system. The choice of whether to class the BRBs as part of the damping system or bracing system depends primarily on the design approach being used. Since design approaches for conventional CBFs are well established in design codes, the uptake of BRBs in practice is facilitated by treating them as braces so they can be incorporated into the existing code framework, allowing engineers to use design approaches and analysis methods with which they are already familiar. This is the case in American ASCE 7 code [16] where buckling-restrained braced frames (BRBFs) are treated as braced frame structures and assigned a response modification coefficient, R, of 8. In the *equivalent lateral force procedure* [16] (similar to the *lateral force method* in Eurocode 8) the seismic actions obtained from the response spectrum are divided by R to obtain equivalent static loads for use in linear-elastic analysis which account for the effects of ductility. This is the largest value of R applied to any type of lateral force resisting system, indicating the high ductility expected of BRBFs (for comparison, steel ordinary CBFs and steel special CBFs are assigned values of 3.25 and 6, respectively). The Building Seismic Safety Council (FEMA 450) provisions [50] recommends that R should take a value of 8 when moment resisting connections are used between the beams and columns of the lateral force resisting frame, or 7 when the connections are not moment resisting. Under ASCE 7, BRBFs cannot be classed as a damping system due to the code defining damping devices only as those that remain elastic under the loads associated with the maximum considered earthquake. The R-coefficient does the same job as the behaviour factor, q, in Eurocode 8 [3]; however, specific design provisions or values of q for BRBs are not incorporated into the current version of Eurocode 8. While both q-factors and R-coefficients represent a measure of ductility, one cannot be directly inferred from the other due to the different contexts in which they are used.

The 2009 European Standard *EN15129 Anti-seismic devices* [31] applies to BRBs, where they fall under the classification of displacement dependent anti-seismic devices. This provides a standardised procedure for testing of devices under a prescribed displacement. It also specifies how key parameters such as the first-branch (pre-yield) and second branch (post-yield) stiffness (which would define a bilinear model of the brace) should be calculated. Other significant parameters defined in the standard

are the equivalent damping coefficient and the compression overstrength. Design rules and behaviour factors for BRBFs have been included in the new Romanian Seismic Design Code P100-1/2013 [51] (which is harmonised with Eurocode 8 EN1998-1) where a q-factor of 4 is assigned for structures of ductility class medium (DCM) (the same value as assigned to MRFs, CBFs and EBFs), and $5\alpha_u/\alpha_1$ for structures of ductility class high (DCH) (the same value assigned to MRFs and EBFs, but higher than the value assigned to CBFs which is limited to 4). The default value of α_u/α_1 given for BRBFs is 1.2, giving $q = 6$ for DCH unless analysis is performed to justify a higher value of α_u/α_1. Rules which apply to CBFs are also applied to BRBFs, such as ensuring the overstrength experienced in all braces/BRBs falls within 25% of the minimum value to give uniform ductility. There are BRB-specific rules accounting for post-yield strain hardening and compression overstrength, and both moment-resisting and non-moment-resisting beam-to-column connections are permitted.

It is worth noting that the prevailing design philosophy employed in Japan, where BRBs had been extensively used for a number of years before their first implementation in the USA, takes the alternative view of BRBs, treating them as supplemental energy dissipation devices used in conjunction with MRFs [35] [36]. In this approach, the MRF forms the primary seismic force-resisting system with the BRBs modifying the structural response through hysteretic energy dissipation. The use of a MRF-BRBF dual system gives the structure significant stiffness, even after yield of the BRBs, which helps to limit residual deflections after a seismic event as well as providing extra redundancy in the structure.

2.4.4. Extending Eurocode Rules to BRBFs

A BRBF is essentially a special kind of CBF, so a useful starting point for designing a BRBF is to consider how the Eurocode 8 rules for CBFs would apply to BRBFs and where they might need modifying to account for the unique behaviour of BRBs. A useful reference is the set of modifications and extensions to Eurocode 8 design rules recently proposed by Vigh et al. [54].

Models used to analyse CBFs must account for the buckling of braces in compression. When elastic analysis is performed this is achieved by neglecting the compression braces in diagonally braced frames

and by applying a reduced buckling strength to compression braces in chevron braced frames. Braces in compression can be taken into account when pushover or NLTH analysis is used providing the degradation of the buckled member is appropriately simulated. Since buckling is prevented in BRBs, it is clear that both BRBs in tension and in compression should be modelled. If a pushover analysis is performed a bilinear or, preferably, multilinear material model should be used. If a NLTH analysis is performed then a nonlinear model capable of capturing the cyclic behaviour of BRBs should be used (possible models are investigated in Chapter 6).

CBFs must be designed for the significant asymmetry that results from brace buckling; BRBFs experience much less asymmetry but there is still some due to the stiffer behaviour of BRBs in compression than in tension which must be taken into account. An upper limit is applied to the allowable non-dimensional slenderness of braces in CBFs ($\bar{\lambda} \leq 2$) to avoid premature buckling, with a lower limit ($\bar{\lambda} > 1.3$) also applied when X-bracing is used to avoid overloading the columns in the pre-buckling stage. Since the slenderness concept does not apply to BRBs, this rule can be disregarded for BRBFs. To ensure symmetry in behaviour after load reversals, the difference in the projected cross-sectional areas of tension bracing in each direction in CBFs must not exceed 5%. It seems reasonable to apply a similar restriction when using BRBs in most cases, but an argument could be made for relaxing the restriction due to their ability to resist compression to the same extent as tension. In theory a structure could be built with only a single diagonal BRB in each storey but the structural redundancy would be reduced. This could potentially be acceptable if there were another source of redundancy such as when using the BRBF as part of a dual system with a MRF.

To ensure a ductile global mechanism, Eurocode 8 specifies that the ratio Ω of resistance to demand (computed form linear-elastic analysis) should not vary by more than 25% between all braces in the system. BRBs are generally manufactured to order, allowing much more freedom in specifying the member capacity since it is not limited to standard section dimensions or restricted by slenderness limits. With this in mind, Vigh et al. [54] propose further tightening this restriction to a maximum

variation of 10%. They also recommend requiring sections of class 1 or 2 be used for the columns, while Eurocode 8 does not prescribe section classes for the columns in a CBF since they are classed as non-dissipative members.

Finally, Eurocode 8 requires non-dissipative elements of CBFs (columns, connections, foundations) to be designed to resist $1.1\gamma_{ov}\Omega_{min}$ times the calculated seismic action effects. The same approach will apply to BRBFs but must take account of the significant post yield strain hardening exhibited by BRBs. When an equivalent linear-elastic method is used, this can be done by multiplying the seismic action effects on non-dissipative elements by $1.1\gamma_{ov}\Omega_{min}\omega_b\beta_b$ where ω_b is the strain hardening adjustment factor (the ratio of the BRB force at the design displacement to the BRB yield force in tension) and β_b is the compression strength factor (the ratio of the BRB force at the design displacement in compression to that in tension). If non-linear methods are used then this should be captured in the model.

2.4.5. Sample BRB Tested in this Project

The BRB tested in this project was provided by Star Seismic Europe Ltd [46]. The core of the BRB consists of a flat steel plate with a constant thickness of 15mm and with a width that varies along the length to vary the cross-sectional area, as shown in Figure 2.11. The centre portion of the core, where the area is minimum, is referred to as the *yielding zone*. This has a constant cross-sectional area of 525mm^2 over a length of 1800mm to distribute the plasticity over as great a length as possible and maximise the ductility that can be achieved. The cross-sectional area of the core increases at each end before leaving the casing to ensure these sections remain elastic – hence the end portions of the core are referred to as the *elastic zones*. A smooth, radiused transition is provided between the yielding zone and the elastic zones to minimise the potential for crack propagation. The overall core length is 2500mm, with end-plate connections giving the whole assembly a total length of 2570mm.

The casing providing lateral confinement to the core consists of a steel hollow structural section (HSS) filled with concrete, as shown in Figure 2.12. The dimensions of the overall BRB assembly are shown in Figure 2.13. An air gap acts as the debonding layer between the steel core and the encasing concrete

to avoid significant coupling of the two in the axial direction (although it is not possible to remove friction completely). An additional proprietary feature of Star Seismic BRBs is a centring HSS collar which is attached to the core a short distance (75.9mm) after it leaves the casing and slides over the main HSS casing to resist rotations at the ends of the BRB. This has been shown to prevent out-of-plane buckling

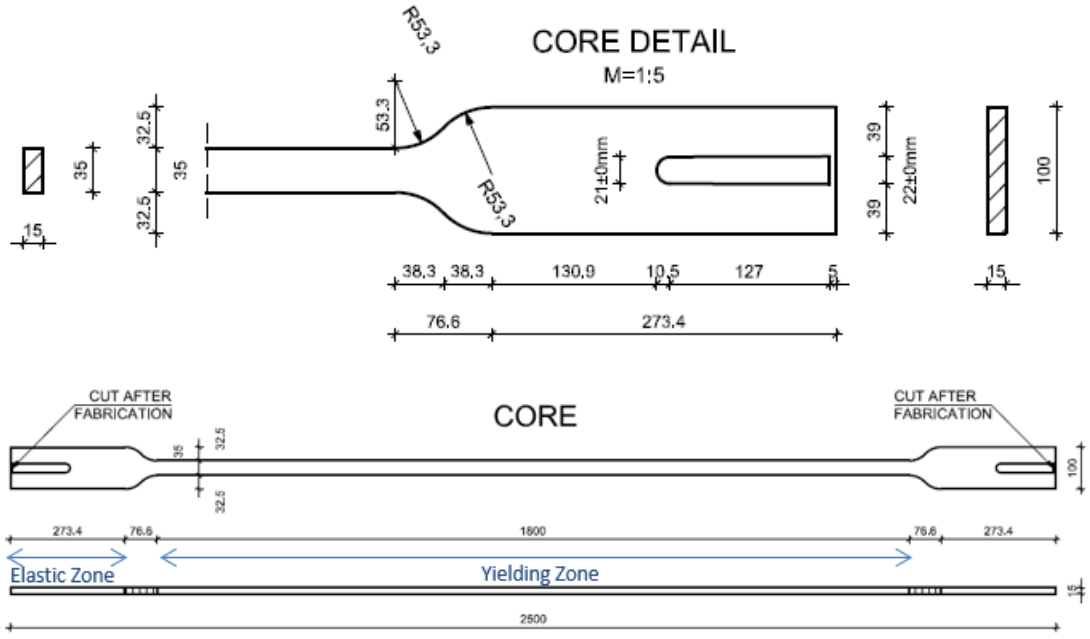

Figure 2.11 – Core of Star Seismic Europe BRB [46]

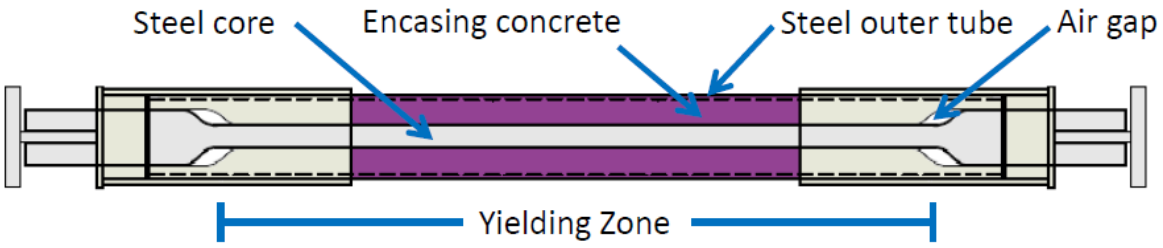

Figure 2.12 – Cut-away view of a Star Seismic Europe BRB

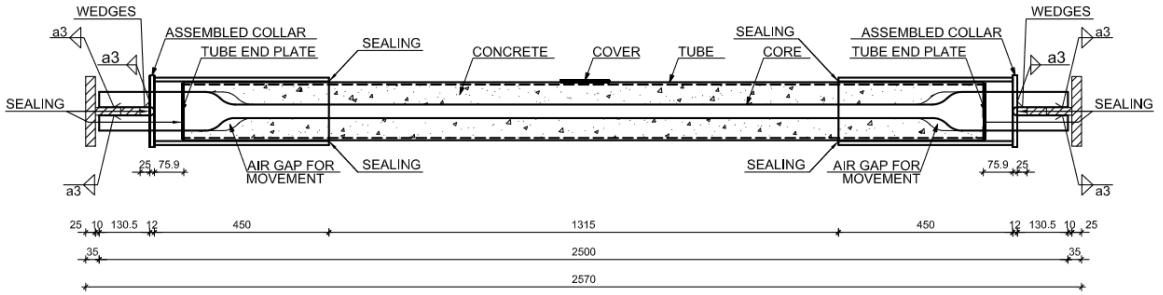

Figure 2.13 – Dimensions of BRB assembly [46]

of the BRB which has been the observed failure mode in some previous tests which did not incorporate end collar attachments [55]. It is necessary for the core to extend a sufficient distance beyond the casing to accommodate its axial deformation. This results in a sudden reduction in flexural stiffness between the encased and exposed sections which could allow this global buckling mode to occur due to excessive rotation concentrated in the core just beyond the end of the encasement. The HSS collar protects against this by providing resistance against rotation to the exposed length of the core. The collar fits snugly around the casing to provide stiffness in flexure but is free to slide to prevent axial loads from being transferred from the core to the casing. BRBs which do not have this feature generally employ a cruciform section for the exposed ends of the core which extends some distance inside the casing to provide resistance against rotation at the exposed ends of the core.

The core is made from steel with a nominal yield strength, $f_{y,nom}$ of 235N/mm^2, giving a nominal yield force, $F_{y,nom}$ of 123.3kN, while the actual yield strength, $F_{y,act}$, was determined from coupon tests to be 135.3kN (an overstrength of 10%).

2.4.6. BRB Design Displacement

To obtain an estimate of an appropriate value for the BRB design displacement, d_{bd}, consider Figure 2.14 which shows a bay of a steel frame of width, b, and height, h, which is diagonally braced by a BRB inclined at an angle, θ. The workpoint-to-workpoint length is the distance between the midpoints of the joints to which the BRB connects – i.e. the length of the BRB plus the dimension of the connection plus the distance from the edge of the joint to its centre of rotation. Shear deformation of the bay resulting in an interstorey drift, d_r, would cause this length to increase from its original value, L_0, to:

$$L = L_0 + d_{bd} = \sqrt{h^2 + (b + d_r)^2} \qquad 2\text{-}41$$

Consider the case where $\theta = 45^o$, which would make $h = b = L_0/\sqrt{2}$. The maximum design interstorey drift allowed by Eurocode 8 (see Section 2.1.2) is 2%, corresponding to $d_r = 0.02h$. Substituting these values into Eq. 2-41 gives $L = 1.01L_0$, hence $d_{bd} = 0.01L_0$. The BRB has a length of 2570mm, so a reasonable workpoint-to-workpoint length is taken as 3200mm, giving a maximum

design displacement, d_{bd}, of 32mm. In testing carried out at Budapest University of Technology and Economics, a slightly larger BRB of the same type (yielding length of 2000mm and yielding area of 800mm^2) was subjected to 30 cycles at a strain level approximately equal to that calculated above. The BRB showed very stable behaviour with no degradation [48].

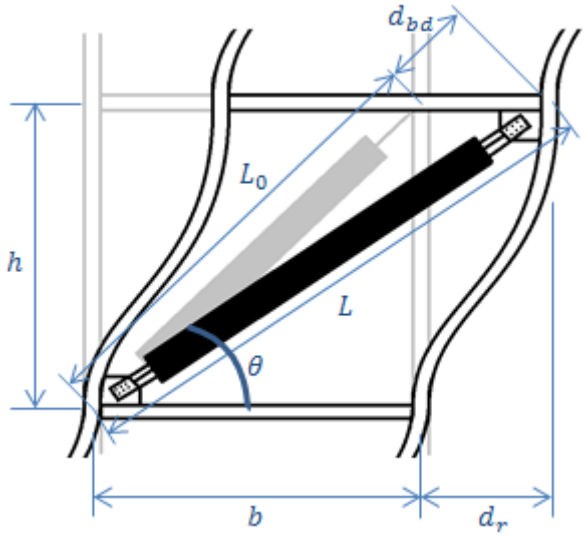

Figure 2.14 – Deflected shape of BRBF bay for determining BRB design displacement

3. Real-Time Hybrid Simulation and Laboratory Setup

3.1. Overview of Hybrid Simulation

Hybrid simulation combines computational modelling with physical testing of a key component or components of interest to provide an efficient means of testing the specimen under realistic loading conditions [56]. The structure to be simulated is split into a physically tested part (the *physical substructure*) and a computationally modelled part (the *numerical substructure*). These are connected in a feedback loop where the displacements at the interfaces between the substructures calculated in the numerical substructure are applied to the physical substructure by servo-hydraulic actuators. The resulting force(s) are then measured by load cells and fed back to the numerical substructure where they will be treated as an external force in the integration of the equations of motion. The process is repeated at each timestep until the simulation is complete. This is illustrated in Figure 3.1. The success of a hybrid simulation is therefore contingent on compatibility and equilibrium being maintained at the interfaces between the two substructures.

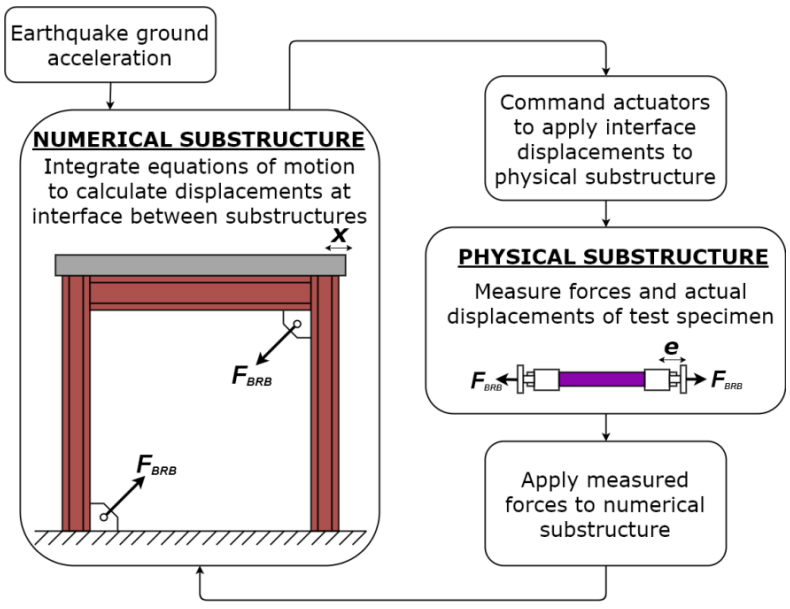

Figure 3.1 – Substructuring for hybrid simulation

As described in Chapter 2, the benefits of energy dissipation from a structure during earthquake-induced motion are well established and have led to the development of many devices with the specific purpose of dissipating energy from the structure (dampers). Testing to demonstrate the performance and effectiveness of these devices is vital for them to be taken-up by the industry and incorporated into design codes. However, the force response from many of these devices, such as viscous and visco-elastic dampers, is highly rate-dependent and this rate-dependence, far from being a secondary characteristic, is fundamental to their principal of operation. The only way to capture the true response of these devices is to test them continuously in *real-time* so that the velocity applied to the physical substructure matches that computed in the numerical substructure. This has led to the development of systems for real-time hybrid simulation (RTHS). Operating in real-time gives rise to additional complications. One significant issue is an inevitable delay in the actuators applying the displacement to the physical substructure [57] which can destabilise the simulation [9]. This has led to several methods of delay compensation being developed which aim to cancel the delay so that compatibility between the substructures is maintained. Another issue is the need to perform all computations in real-time. This can require longer timesteps to allow the integration algorithm to complete the calculations in time for the next timestep, but this can be in conflict with the need to use small enough timesteps to ensure the stability of the integration algorithm and the need to generate a smooth, continuous command signal to the actuator controllers.

3.2. Alternatives to Real-Time Hybrid Simulation

The advantages of hybrid simulation become apparent when the alternative simulation methods are considered. The method requiring the fewest resources would be a purely numerical simulation on a computer. However, this relies on the ability to model the behaviour of the components of the model being simulated. If the structure contains components with a highly nonlinear behaviour, or for which validated numerical models do not exist because of their novelty, then numerical simulation alone may be insufficient to give confidence in the results of the simulation.

At the other end of the spectrum is full-scale *shake table testing* where the structure in question is constructed on a shaking table which applies the ground motion, the response to which is measured directly [58]. A similar method is *effective force testing* [59] where rather than applying a ground motion to the base of the structure, actuators apply the inertial forces that would be produced by the earthquake at the location of each lumped mass and the displacement response is recorded. These forces can be determined in advance based on the earthquake ground motion, so no online computation is required. Testing at full-scale requires a very large facility fitted with a very high power, dynamically rated actuation system. This, along with the fact that the whole structure must be constructed, including its full mass, makes this approach prohibitively expensive with only a handful of facilities around the world being able to test realistic sized building structures at full-scale. It is therefore much more common to perform tests on a reduced scale structure. However, this reduces accuracy because of the impracticality of scaling all parameters of the model commensurately (e.g. scaling material properties or the gravity constant) so that some distortion of the model must generally be accepted [60]. Scaling could be a particular issue when there is a particular device within the structure which is of interest, since scaling will increase uncertainty or may not be possible

A compromise between fully computational and fully physical testing is *pseudo-dynamic testing* – a form of hybrid simulation where the dynamic forces (the inertial and damping forces) are calculated computationally while the static restoring forces from the structure or substructure are measured experimentally. This can be more practical than shake table testing but cannot capture any rate-dependent device properties because the loading is quasi-static. RTHS is essentially an advancement of pseudo-dynamic testing where the test is carried out continuously in real-time so that any rate-dependent properties of the device will be captured. The efficiency of RTHS stems from the fact that only the key components need to be physically tested making this system ideally suited to structures where unpredictability is confined to discrete regions [61].

3.3. History of Hybrid Testing

The origins of hybrid simulation, also referred to as *on-line testing*, can be traced back to 1969 when Hakuno et al. [62] demonstrated the concept by simulating the SDOF response of a cantilever beam to an earthquake. They used an analogue computer to integrate the equation of motion while an electromagnetic actuator loaded the experimental specimen, although the quality of the response obtained was understandably limited by the performance of the hardware available at the time [8]. The concept was extended into its current form in 1974 when Takanashi et al. [63] employed a hybrid system with digital computers implementing a discretised form of the equation of motion. This discretisation with respect to time means that there is no reason why the rate of loading of the test structure need match the velocity computed by the integration algorithm. Once the algorithm has computed the displacement of the structure over one timestep, it pauses while the displacement is applied to the structure by the actuator. Once the actuator has reached the target position, it stops and holds this position while the restoring force is measured by a load cell. The integration algorithm then uses this measured force in calculating the displacement at the next timestep of the simulation and the process is repeated. This process is commonly termed *pseudo-dynamic testing*, since it simulates the dynamic response of a structure by modelling the inertial and damping terms numerically while the restoring forces are obtained from an experimental structure that is loaded quasi-statically. A key limitation of this approach is therefore that it is unable to capture any rate-dependent effects in the experimental structure, restricting it to cases where the restoring forces can be assumed independent of the rate of loading. Since this assumption is generally considered valid for conventional structural materials like reinforced-concrete and steel at the rates of loading expected in an earthquake, the pseudo-dynamic testing method was the subject of multiple research efforts in Japan and the USA from the late 1970s to the early 1990s [64]. Key issues for this research were the problem of experimental error propagation and the choice of integration algorithm to ensure stability of the hybrid simulation.

The potential applications for pseudo-dynamic testing were greatly increased with the introduction of the concept of *substructuring* [61]. Rather than constructing the whole structure to be tested experimentally (limiting the size of the structure that can be modelled at full-scale), only part of the structure is tested experimentally – this is called the *physical substructure*. The remainder of the structure to be simulated is modelled computationally – this is called the *numerical substructure*. This greatly reduces the laboratory resources necessary to simulate the structure, but places increased demand on the computational part of the system which must now simulate the rest of the structure, rather than just the inertia and inherent damping. Extra degrees-of-freedom (DOFs) in the numerical integration would require smaller timesteps to ensure stability (when performing integration using the central difference method) which required the actuators to apply smaller displacement increments at each time interval; since smaller displacement increments are more difficult to control, this could lead to an increase in the propagation of systematic errors [65]. In addition, the boundaries between the substructures must be selected and implemented in a way that ensures the boundary conditions can be accurately enforced by the actuation system. Research into overcoming these difficulties through the second half of the 1980s led to successful pseudo-dynamic substructure testing being carried out by the early 1990s [66].

The desire to capture the rate-dependent response of the physical substructure, along with improvements in technology (such as better dynamic actuators and more powerful computer systems) making it feasible, have led to efforts to develop hybrid testing systems capable of operating in real-time. Early steps in the direction of real-time hybrid simulation were taken in 1983 when Takanashi and Ohi [67] developed a 'fast online test algorithm'. A key step was to provide continuous loading, rather than stopping at the target displacement while the reaction force is measured as was done in previous systems. They then investigated the effect of different expanded time scales on the computed response but could not increase the physical testing rate beyond 23% of the simulation rate due to processing speed limitations. The first real-time hybrid test was carried out in 1992 by Nakashima et al. [66] who simulated a SDOF frame fitted with a viscous damper. The viscous damper, consisting of a viscous

polymer material sandwiched between steel plates, formed the physical substructure and was loaded by a single dynamic actuator, while the mass and stiffness of the frame were modelled on the computer. Limitations on computing power required a timestep of 20ms to be used for integrating the numerical substructure (which was done using the central difference method), so to ensure a smooth loading rate a 'digital servo mechanism' was incorporated between the computer and the analogue actuator controller. This interpolated the signal and compensated for errors in the achieved displacement with a sample time of 2ms, ensuring smooth continuous movement of the actuator within the timestep and accuracy of the displacement reached by the end of the timestep. Variations of this approach (e.g. using more advanced interpolation techniques) are widely used to allow longer timesteps to be used in the integration than in the controller – this is referred to as *sub-stepping* [68]. This produced the 'dual loop' control system consisting of an inner loop controller which works to minimise the error between the target and measured displacements, and the outer loop controller which computes the target displacement by integrating the equation of motion including the force measured from the physical substructure. Hybrid simulation does not need to be limited to a single physical substructure, multiple ones could be used in a single system. This has even led to geographically distributed hybrid testing being carried out, where different physical substructures are tested at different facilities and connected via the internet, allowing the resources of multiple laboratories to be pooled to increase the complexity that can be simulated [69].

A significant issue that occurs at the interface is due to actuation delay – the time taken for the actuators to reach the displacement requested of them. In the context of a closed feedback loop, a time delay (like a phase lag in the frequency domain) has a destabilising effect on the system, and so delay compensation is vital to successfully running RTHS tests. The delay compensator forms part of an additional control loop around the existing PID actuator controller (the *inner control loop*), and therefore forms part of the *outer control loop*. Other issues that had to be dealt with at the interfaces are accounting for the compliance of the test rig (*rig flexibility compensation*) and providing stable force feedback from the physical substructure (*force simulator*).

3.4. Obstacles to Real-Time Hybrid Simulation

In the past, limitations on the processing speed of available computers meant that integrating the equations of motion in real-time was not possible, requiring the hybrid simulation to be run at reduced rates, with the loads being applied to the physical substructure at a lower velocity than assumed in the numerical substructure, even for very simple (e.g. SDOF) structures. This obstacle has been overcome by improvements in computer technology, but it is still not a trivial problem. The computation time increases with the number of DOFs, since this increases the number of equations to be solved at each timestep, so for a given processor with a given integration timestep there will be an upper limit on the number of DOFs which can be modelled in the numerical substructure. The efficiency of the integration algorithm, and the other control loop operations carried out by the processor, is therefore of great importance. The stability properties of the integration algorithm are also of great importance, since these limit the size of the timestep which can be used. If the integration can remain stable with a larger timestep then this will allow more computation time and increase the complexity of the model which can be simulated. This could lead to issues if the size of the actuation timestep required to achieve smooth continuous motion of the actuators is smaller than this, which in most cases requires a sub-stepping approach to be implemented.

In the past, even if computation speeds had been sufficient to allow integration of the equations of motion, it is likely that the system would still be limited by the ability of the available actuators to accurately apply the loads dynamically. Improvements in actuator technology mean that this issue has also been largely overcome since high quality dynamic actuation systems are available which can accurately apply large forces at high velocities.

While the dynamic actuators can give a displacement output which closely matches the shape of the input command displacement, the achieved displacement will be delayed relative to the command. A small part of this delay is due to the digital-to-analogue (D/A) conversion which produces the analogue control signal required by the actuator controller from the digital output produced by the numerical

substructure. However, by far the majority of the delay results from the dynamic properties of the actuators which mean it takes time for the actuators to reach their command position. This can be minimised by optimising the parameters of the actuator controller but can never be removed completely. In an *open loop* test, where a predetermined displacement is applied to the device being tested, this delay is of little importance. Provided the measured displacement and measured force are used in analysing the results (so that they are synchronised) there shouldn't be a problem. However, in a hybrid simulation the measured force is fed back into the numerical substructure in order to determine the displacement of the system at the next timestep. This therefore allows errors to propagate and accumulate through the simulation.

3.5. Test Rig and Laboratory Setup

Here, the equipment in the laboratory used to perform RTHS is described. This consists of the physical test rig used to apply displacements to the physical substructure (BRB), the actuator controller which determines the control signal to send to the servo-hydraulic actuators, the transducers which measure the response of the physical substructure, the data acquisition system, and the computer system on which the numerical substructure and outer loop controller are implemented. The physical substructure used throughout this project is the BRB described in Section 2.4.5.

3.5.1. Actuators and Power

Two Instron® servo-hydraulic actuators work in parallel to apply displacements to the sample BRB, as shown in Figure 3.2. Each has a dynamic load rating of $\pm$250kN (maximum stall rating of $\pm$311kN) and a piston stroke of $\pm$125mm. This configuration was necessary to achieve the required forces with the actuators available in the lab. The BRB and actuators are connected at one end (left in Figure 3.2) to a fixed reaction plate which is bolted to the lab's 166 tonne concrete strong floor. At the other end they all connect to a stiff cross-beam via pinned bearings to prevent unintentional moments being transferred to the BRB. Horizontal plates welded to each end of the cross-beam rest on low-friction rollers proving vertical support to the cross-beam while leaving it free to move back and forth

horizontally. Steel circular hollow sections, each prestressed by four steel threaded bars, accommodate for the extra length of the BRB relative to the actuators.

A DARTec® power pack containing three pumps provides oil at 210bar with a peak flow rate of 180L/min (although fewer pumps can be run when demand is lower). The pumps feed accumulators which store high pressure oil to be used at times of peak consumption, enabling the oil flow to be approximately doubled for short periods of time. The accumulators feed two substations, each of which runs one actuator (although each substation can supply up to two actuators). The actuators are also connected to a return line which transports oil back to the oil reservoir. Each actuator is fitted with two Moog® servo-valves (each having a capacity of 40L/min) acting in parallel to give up to 80L/min of flow.

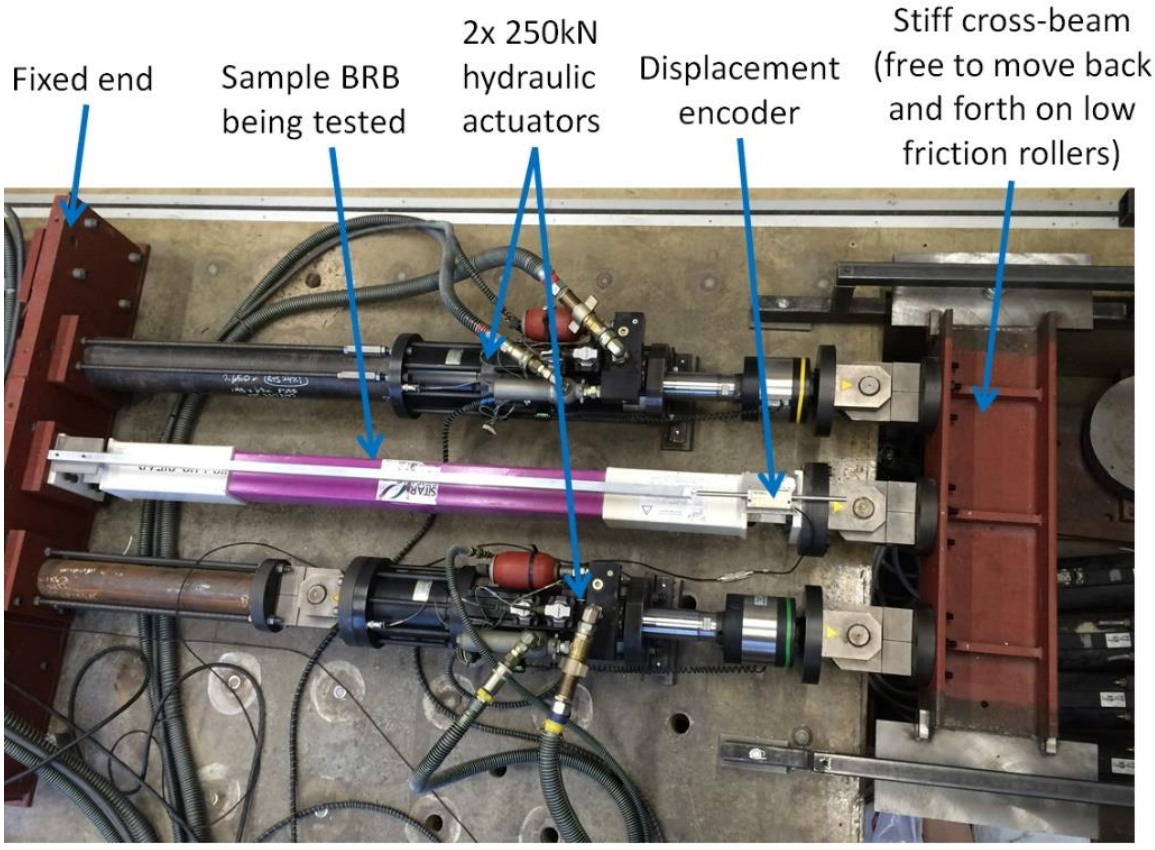

Figure 3.2 – Physical test rig (viewed from above)

3.5.2. Transducers

A linear variable differential transducer (LVDT), located within the body of each actuator, measures the piston displacement relative to the actuator body. These provide feedback to the displacement control system. A load cell attached to the external end of each piston rod measures the applied forces. Two Newall SHG-TT Mark III displacement encoders (having 203mm scale measuring length and a resolution of 1 micron) are attached across the BRB to allow direct measurement of the BRB deformation (which will differ from the actuator displacement measured by the LVDTs due to compliance of the test rig). One encoder is positioned above the BRB and the other symmetrically below. The encoders consist of a reader head, which is the main body of the encoder containing the coil assembly and supporting electronics, and a scale, consisting of a stainless-steel tube filled containing a row of spherical nickel chrome elements. A 10kHz sinusoidal drive current is passed through a drive coil in the reader head to generate an electromagnetic field which interacts with the nickel chrome elements in the scale which passes through the reader head. A relative displacement between the scale and the reader causes a variation in the induced field which is detected by a set of four pickup coils within the reader head, from which the displacement is calculated.

The upper displacement encoder can be seen above the BRB in Figure 3.2 with the reader connected to the far right end of the BRB (at the point where the BRB attaches to the pinned bearing which connects it to the cross-beam), while the scale which slides through the reader head is connected to the far left end of the BRB (at the point where it connects to the fixed reaction plate) via a rod running parallel to the BRB core. The lower encoder is attached in the same configuration symmetrically below the BRB. The BRB deformation is taken as the average of these two encoder readings. The reason for using two encoders rather than just one is explained below.

The test rig is designed to apply purely axial loads to the BRB, with the motion confined to the horizontal plane. However, it is possible for a very small amount of unintended vertical displacement to occur at the right-hand end of the BRB, where it meets the cross-beam. This could occur due to an accidental

eccentricity between the force applied to the cross-beam by the actuators and the BRB axis due to construction tolerances. This would tend to twist the cross-beam about its longitudinal axis (i.e. about the horizontal axis perpendicular to the BRB). Confinement is provided by the low friction rollers, but some deformation could occur due to flexibility of the rig components. Twisting of the cross-beam would cause a small vertical displacement to occur at the right-hand end of the BRB. Since the other end of the BRB is restrained, this will cause rotation of the BRB that will introduce some secondary moments. The vertical offset of the encoder with respect to the BRB core means that the inclination created by a vertical displacement of the right-hand end of the BRB will cause a displacement to be measured by the encoder even if the length of the BRB remained unchanged. Such an effect was found to be present, albeit small, so two encoders were used, installed symmetrically above and below the BRB. By taking the average of the two encoder readings, the effects of rotation are cancelled out, maximising the accuracy of the measured BRB displacement.

Based on the measured disparity between the readings of the two encoders and the dimensions of the rig, the upper bound on the inclination of the BRB caused by this effect at maximum displacements is calculated to be around 0.12°. Based on the analysis performed in Section 2.4.6 to determine the maximum design displacement of the BRB, the relative rotation of the BRB caused by deformation of the frame at the design displacement can be calculated to be 0.567°, so the unintended inclination introduced in the test rig is much less than the rotation the BRB would be expected to accommodate in service. In the testing of a similar BRB undertaken at the Budapest University of Technology and Economics [48] (see Section 2.4.6) an inclination of 0.912° was intentionally introduced in order to take account of the effect of second order moments induced in the BRB due to bolted connection to the frame, and no noticeable detrimental effects were observed due to second order moments. It is therefore not considered necessary to include the effects of second order moments directly in this project as the focus is on hybrid testing under controlled conditions. In modelling the structure, the BRB will therefore be assumed to be connected to the frame by pinned connections.

3.5.3. Controller

The actuators are controlled by the Instron Labtronic® 8800 controller which can provide either displacement control using feedback from the LVDTs or force control using feedback from the load cells – in this project displacement control is used throughout. This implements a proportional-integral-derivative (PID) controller for each actuator. The PID coefficients (as well as other parameters such as displacement limits, output gains and signal filtering) are set via the Instron® RS+ software which is run on a PC (the 'control PC') connected to the controller unit by a GPIB interface. These can either be input manually or determined using an auto-tuning procedure included in the RS+ software [70] – Section 4.2 describes the selection of these coefficients. It is possible to specify simple command signals (such as sinusoidal, triangular or square waves, as well as ramps) from the control PC, or alternatively the command signal can be taken from an external source via a BNC input on the controller unit. Implementing a hybrid simulation requires additional functionality which is provided by a second PC (the 'data acquisition PC') which runs the dSpace ControlDesk® software.

3.5.4. dSpace® Board

To perform a hybrid test in real time it is vital that all of the necessary computations can be completed within the simulation timestep – this includes solving the equation(s) of motion forming the numerical substructure as well as other calculations such as delay compensation. To ensure rapid computation without interruption from other PC tasks, the computational part of the RTHS loop (the numerical substructure and control interfaces) is compiled to a dSpace® DS1104 R&D controller board (dSpace® board) connected to the PCI slot of the data acquisition PC. The dSpace® board is specifically designed for real-time simulations, as well as the development of high-speed multivariable digital controllers, and is based on a 603 PowerPC floating-point processor running at 250MHz.

The numerical substructure is first created in Simulink®, a graphical programming environment integrated with Matlab® and designed for modelling, simulating and analysing dynamical systems [71]. The model is then compiled and downloaded to the dSpace® board using the ControlDesk® software

provided by dSpace®. Once the compiled model is running on the dSpace® board, the data acquisition PC interfaces with it via the PCI connection using ControlDesk® [72], which also records the data of interest (such as measured forces and displacements). The 16-bit digital command signals from the dSpace® board are converted to analogue signals and sent to the auxiliary input of the Instron® controller via BNC coaxial connections. The outputs from the Instron® controller are sent back to the dSpace® board via a 16-bit analogue-to-digital converter.

An overview of the system is shown in Figure 3.3. The key to the success of this implementation is fast communication directly between the dSpace® board and the Instron® controller, with the PCs being used only to set up, monitor and start/stop the simulations, and not taking a direct role in the hybrid simulation feedback loop. The numerical substructures which will be implemented on the dSpace® board for hybrid simulations will be looked at in Chapters 5 and 6 but, for the open loop tests described in the next chapter, the dSpace® board will simply output the prescribed cyclic command displacement and record the measured signals that result.

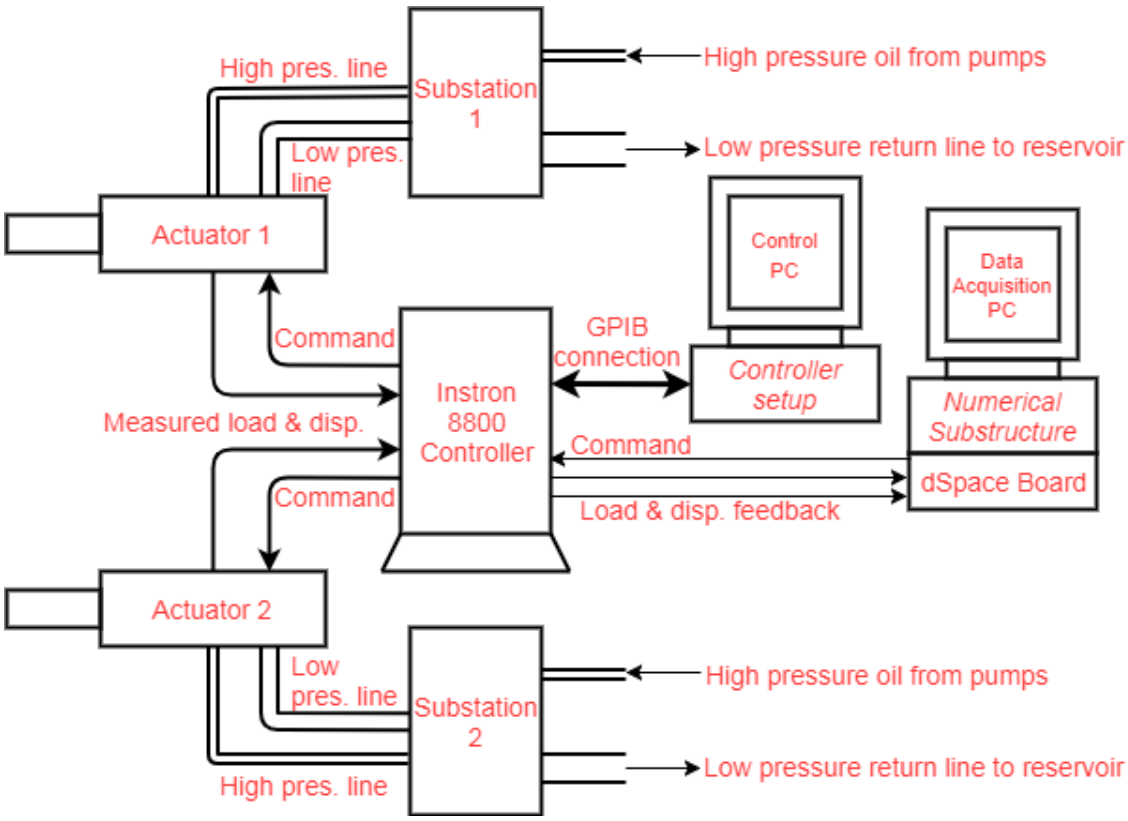

Figure 3.3 – Overview of laboratory setup (based on [73])

3.5.5. Data Acquisition

The LVDTs within the actuators were calibrated by comparing the command displacement to that measured manually with a vernier calliper. Both gave a linear relationship, so calibration was achieved through the application of a simple scale factor for each actuator. Calibration of the Instron load cells was carried out prior to each batch of tests using the Instron auto-calibration feature [70] to ensure consistency between tests. The encoders were pre-calibrated by the supplier, Newall, to an accuracy of $\pm 10\mu m$. The encoders are digital with a resolution of $1\mu m$ while the LVDTs and load cells generate analogue signals so that the resolution of these signals is determined by the quantisation error introduced by the analogue-to-digital converter (ADC).

A key feature of the hybrid testing system developed in this project is that it implements adaptive displacement control based on the displacement measured directly across the BRB by the encoders rather than the displacement of the actuators measured by the LVDTs. This means that the accuracy of control that is achieved is not restricted by the accuracy of calibration of the LVDTs since the control system automatically compensates for errors based on the displacement measured by the encoders which have a high resolution with minimal noise and are finely calibrated.

The dSpace® board has four 16-bit ADC channels and four 12-bit ADC channels which it samples once per timestep, which is 1ms throughout this project. The 16-bit channels were used to convert the $\pm 10V$ analogue voltage signals from the LVDTs and load cells into digital signals. The 12-bit channels allowed additional data to be captured, such as recording command signals to ensure they behaved as expected, but they were not used as part of the main testing system. The 16-bit ADC channels are multiplexed so that each channel is sampled one after the other. This results in a slight time offset between each sampled signal, but this is small enough to be considered negligible, with the ADC being rated with a conversion time of $2\mu s$. The four 12-bit channels are parallel channels, so they can be sampled simultaneously (along with one 16-bit channel) but in this system this would provide negligible benefit to make up for the loss of accuracy due to the lower resolution. Maximising the resolution is important not only for maximising the accuracy of the results but also for giving finer control over the

actuator displacements. The dSpace® board also has two independent TTL RS422 input channels which connected to the two digital encoders. It has eight digital-to-analogue output channels with 16-bit resolution, two of which were used to output the command displacements (via BNC connections) to the Instron 8800 controller which implemented PID control of the actuator displacements.

The gains applied to the analogue signals from the LVDTs and load cells were adjusted prior to each test according to the expected peak displacement and force so as to maximise the resolution while avoiding saturation of the signals. The smallest gain applied to the LVDT signals was 0.2V/mm, giving a measurement range of $\pm$50mm with a resolution of 4μm for the largest displacement tests. The measurement range must exceed the range of displacements applied to the BRB by enough to accommodate deformation occurring in the rig as well as allowing a margin of safety since the peak displacements in a hybrid test are not known precisely in advance. The smallest gain applied to the load cell signals was 0.05V/kN, giving a measurement range of $\pm$200kN for each load cell ($\pm$400kN combined) with a resolution of 6N. For tests were a smaller range was required, the gains were increased to improve the resolution.

No filtering was applied to the transducer signals prior to analogue-to-digital conversion due to the phase lag it would introduce in the signals. Phase lags and delays within the hybrid testing feedback loop have a destabilising effect which is discussed in detail in Chapter 4. Testing using timesteps much smaller than the 1ms timestep used in the hybrid testing system showed no significant noise in the signals for sampling frequencies above 1kHz, so aliasing was not an issue. Some filtering of displacement signals was required for the implementation of the adaptive delay compensator (see Section 4.3.4.3) but this was performed digitally on the dSpace® board where required.

Noise was removed from the encoder signal, x_{enc}, using the procedure illustrated in Figure 3.4 which was developed by Ojaghi [74] and was implemented on the dSpace® board. The output is held constant until the magnitude of the difference between the output and the input exceeds the user-specified noise band. This provides a hysteretic response so that changes in the direction of the signal caused by noise are not passed to the output, providing the noise band value has been set high enough. Ojaghi

determined that for this system a noise band value of 2.5μm was sufficient to remove direction reversals due to noise, so this value was used in this project. This procedure has been shown to be effective at removing noise and it gives a fast response when the displacement is changing rapidly. This produces a dead-gap which effectively reduces the resolution to 2.5μm but this is still sufficiently small and less than the calibration range.

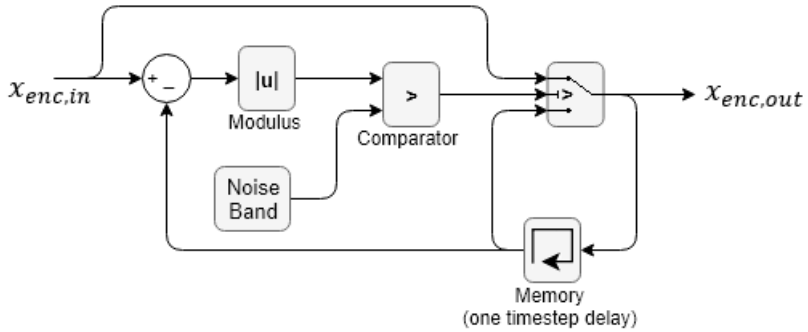

Figure 3.4 – Signal processing applied to digital encoder signal

3.6. Conclusion

This chapter has given a very brief background to the RTHS procedure and described the equipment which is used in the experiments performed in the remaining chapters. The RTHS feedback loop is made up of multiple components:

1. The physical substructure and test rig;
2. The PID controller, delay compensator and rig flexibility corrector;
3. The stiffness simulator used to ensure stable force feedback;
4. The numerical substructure and integration algorithm.

The first has been introduced above and the second is the subject of Chapter 4. The third and fourth are introduced in Chapter 5 with SDOF hybrid simulations, which are extended to MDOF hybrid simulations in Chapter 6. For clarity, background to each component is given in the chapter in which it is introduced.

4. Stability and Accuracy of Actuation

4.1. Stability of the RTHS Feedback Loop

4.1.1. Sources of Instability

To perform a hybrid simulation in real time, the stability of the closed feedback loop making up the RTHS system must be ensured. Figure 4.1 shows a simplified overview of the key components of the feedback loop. There are multiple potential sources of instability. For example, the equations of motion in the numerical substructure must be integrated using a numerical algorithm which may only be conditionally stable. This can result in instability if the properties of the simulated structure move outside of the stable range for the given integration timestep – this could occur due to nonlinear behaviour of the physical substructure. These issues will be dealt with in the next chapter when the numerical substructure is introduced. In this chapter, the effect of actuation quality on the stability of the system is investigated and a system for achieving stable control of applied displacements is developed. Instability is introduced because the actuators take time to respond to a change in command resulting in a delay in the response. Control theory dictates that a delay in a closed feedback loop has a destabilising effect on the system – analogous to a lag in the frequency domain. This is not a significant issue in non-continuous PsD testing since the system can wait for the target displacement to be achieved in the physical substructure before measuring the force to feed back. However, it becomes a significant problem in a continuous hybrid testing system where the displacements in the numerical and physical substructure must be synchronised for the correct response to be obtained.

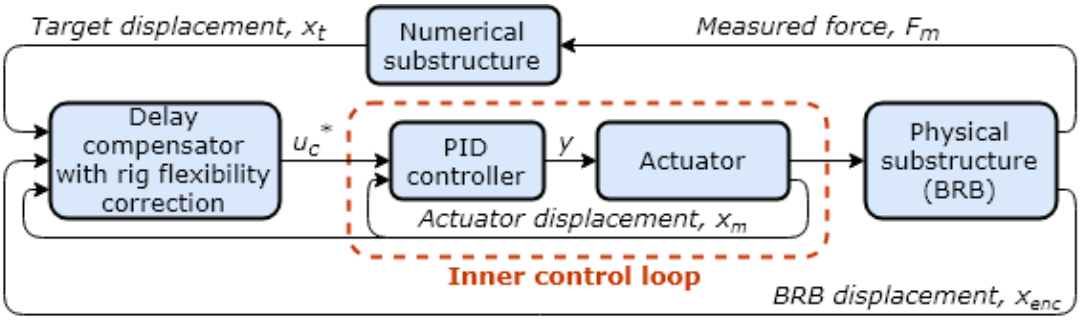

Figure 4.1 - Simplified overview of RTHS feedback loop

4.1.2. Actuation Delay and Amplitude Error

Actuation delay is the time it takes the actuators to reach the displacement requested of them, visible in Figure 4.2 as the horizontal offset between the command displacement, u_c, sent to the actuator controller and the measured displacement, x_m, achieved by the actuator. This is an unavoidable characteristic of any actuator since the dynamics of the system prevents an instantaneous response to a change in command signal [57]. Signal processing (A/D and D/A conversion) also contributes to the delay, although this only accounts for around 10% of the overall delay. This project uses servo-hydraulic actuators, common for RTHS due to the large forces required. Factors affecting the size of the delay include the tuning of the parameters of the PID controller, the frequency/rate of motion, the flow rate of oil through the control valves and the resisting force from the physical substructure being tested.

Delays are of less concern in open-loop testing, where a predetermined displacement is applied to the specimen. However, in hybrid testing, the displacement to be applied to the physical substructure at each timestep depends on the force feedback from the previous timestep. Inaccuracy in the applied displacement will lead to inaccuracy in the measured force, since it will correspond to a different amount of deformation to that assumed in the numerical substructure. The feedback nature of RTHS therefore allows errors due to poor actuation quality to propagate and accumulate over the duration of the test. In cases of practical interest, the destabilising effect of the delay will generally prevent simulations being performed in real-time without some form of delay compensation being applied.

Another potential source of inaccuracy is what is called an *amplitude error*, where the actuator either fails to achieve the desired displacement or overshoots it (also illustrated in Figure 4.2). This will depend on factors such as the quality of the actuation system, the tuning of the controller parameters and the frequency of oscillation. Amplitude error is less detrimental to the stability of the test than a delay [73] but it is a related problem since, from the data at a single point in time, there is no way of knowing how much of the error is due to a time delay and how much to the amplitude error. To separate the two requires assumptions to be made about the signal.

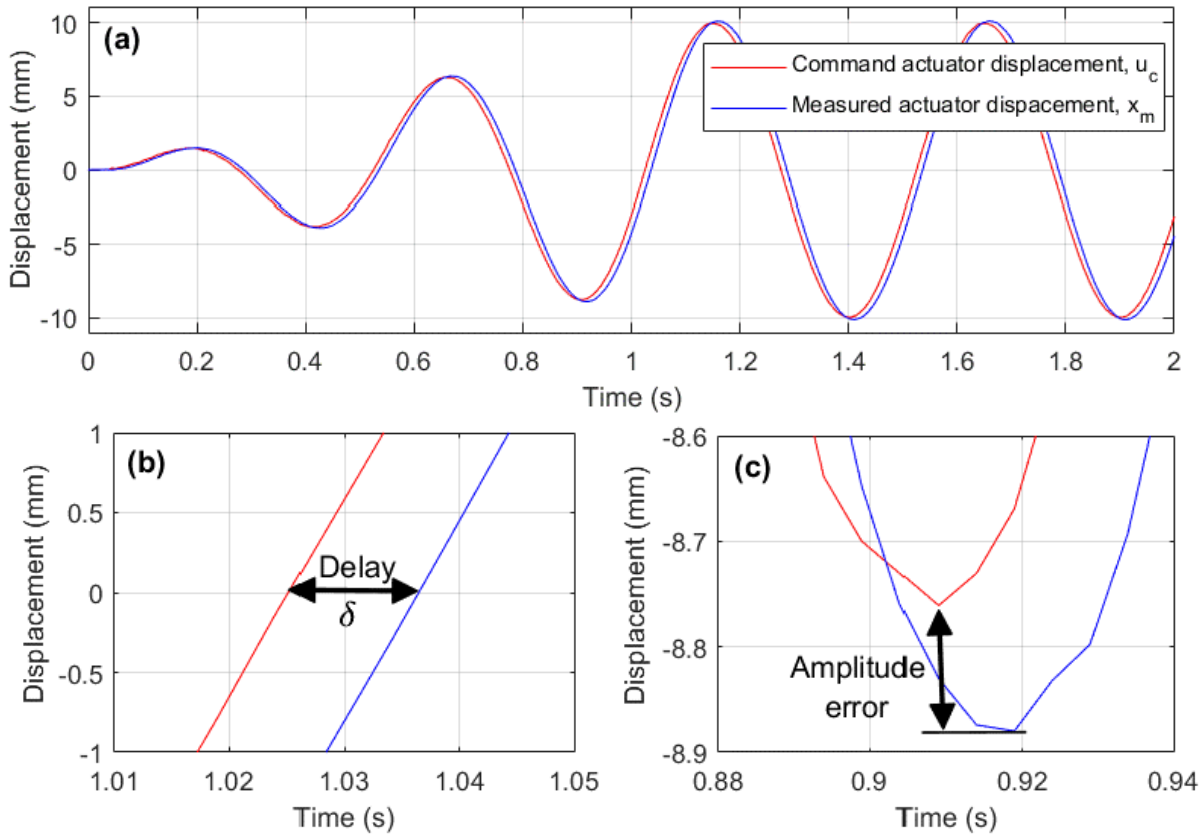

Figure 4.2 – (a) Displacement response of bare actuators with close-ups of (b) delay at zero-crossing and (c) amplitude error at peak

4.1.3. The Destabilising Effect of Actuation Delay

The equation of motion of a SDOF structure subjected to a ground acceleration, $\ddot{x}_g$, is:

$$m\ddot{x}(t) + c\dot{x}(t) + F(t) = -m\ddot{x}_g(t) \quad 4\text{-}1$$

where m is the mass, c is the damping coefficient accounting for inherent damping, x is the displacement of the mass relative to the ground, F is the restoring force and the dot operator $(\dot{})$ indicates differentiation with respect to time, t. In a hybrid simulation, F will be the sum of the force computed in the numerical substructure, R, and that measured from the physical substructure, r, so ideally:

$$F(t) = R(t) + r(t) \quad 4\text{-}2$$

However, a delay, δ, in the feedback from the physical substructure will mean that the actual restoring force experienced by the simulation will be:

$$F(t) = R(t) + r(t - \delta) \quad 4\text{-}3$$

Horiuchi et al. [75] demonstrated the destabilising effect of the delay by showing that it introduces negative damping, i.e. a spurious source of energy exciting the system. Consider a physical substructure with elastic stiffness, K, so $r(t) = Kx_m(t)$. With constant delay, δ, a command of $x_t = A\sin(\omega_o t)$ would result in an achieved displacement of $x_m = A\sin(\omega_o t - \omega_o \delta)$ giving a force feedback of $r = KA\sin(\omega_o t - \omega_o \delta)$, where A is the amplitude and ω_o the frequency of oscillation. The change in total energy, ΔE_k, per period of oscillation, $T = 2\pi/\omega_o$, in the simulation would therefore be:

$$\Delta E_k = \oint r\, dx_t = \int_0^T r \frac{dx_t}{dt} dt = \frac{KA^2}{2} 2\pi \sin(\omega_o \delta) \qquad 4\text{-}4$$

The change in total energy, ΔE_c, for an equivalent linear viscous damper ($F_D = -C_{eq}\dot{x}_t$) per cycle of displacement, x_t, with no delay is:

$$\Delta E_c = \oint F_D dx_t = \int_0^T F_D \frac{dx_t}{dt} dt = -\int_0^T C_{eq} \left(\frac{dx_t}{dt}\right)^2 dt = -\frac{C_{eq} A^2}{2} 2\pi\omega_o \qquad 4\text{-}5$$

Equating these energies shows the delay to be equivalent to a negative viscous damping of:

$$C_{eq} = -\frac{K \sin(\omega_o \delta)}{\omega_o} \approx -K\delta \qquad 4\text{-}6$$

since $\omega_o \delta$ will be small.

If all the structural stiffness is provided by the physical substructure, i.e. the delay affects the entirety of the restoring force, and the oscillations occur at the structure's natural frequency ($\omega_o = \omega$), then this is equivalent to a damping ratio, ζ_{eq}, of:

$$\zeta_{eq} = \frac{C_{eq}}{2\omega m} = -\frac{\omega\delta}{2} \qquad 4\text{-}7$$

If δ were large enough that ζ_{eq} exceeded the inherent damping of the simulated structure, then the system would become unstable and the output would diverge. Even at values of δ not sufficient to cause overall instability, the accuracy of the simulation will be compromised by the introduction of this spurious energy. This is illustrated in Figure 4.3 which shows the displacement response produced by integrating Eq. 4-1 for a linear 2Hz structure with 5% damping undergoing free vibration ($\ddot{x}_g = 0$) with various levels of delay, δ, in the restoring force. Eq. 4-7 predicts that the limit of stability (when the

negative damping introduced by the delay equals the inherent damping in the model) will occur for a delay of 7.96ms. Figure 4.3 confirms this, with the oscillations just decaying for a 7ms delay but growing without bound for an 8ms delay. For a mode of oscillation at 10Hz the onset of instability would occur for a delay of just 1.6ms. Hence, in a simulation of a MDOF structure, even though the system is stable for the lower modes with the given delay, it may be destabilised by the presence of higher modes, even if they do not contribute significantly to the actual structural response. The levels of actuation delay experienced in actual tests is found to be of the order of 11ms, so it is not possible to perform successful tests in real-time for realistic natural frequencies without employing a method of delay compensation.

In the case of the BRB tested in this project, the effective stiffness reduces as yielding occurs which will reduce the negative damping caused by the delay – hence using the initial elastic stiffness as K in Eq. 4-6 will give the upper limit on the level of negative damping to expect. To determine the delay stability limit for other types of physical substructure, a process similar to that used in Eqs. 4-4 to 4-6 can be applied, replacing r in Eq. 4-4 with the constitutive equation of the device being tested. For example, if the test specimen consisted of a linear viscous damper with a damping coefficient, C_v, then a delay, δ, would result in an effective negative damping coefficient of:

$$C_{eq} = -C_v(1 - \cos(\omega_o \delta)) \qquad 4\text{-}8$$

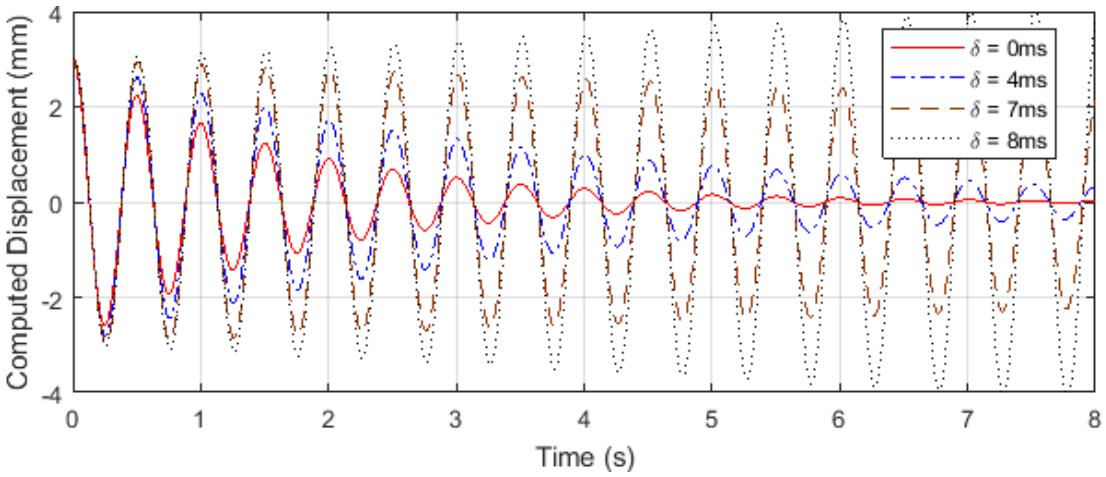

Figure 4.3 – Effect of various sizes of delay, δ, on the computed free response of a 2Hz structure with 5% damping

4.1.4. Conditions Affecting Stability in the Presence of Actuation Delay

Eqs. 4-6 and 4-7 show that the destabilising effect of an actuation delay depends not only on the magnitude of the delay but also on the properties of the structure being simulated. In particular, the natural frequency, level of inherent damping and proportion of the overall stiffness that originates in the physical substructure. The stiffness, k_{num}, modelled within the numerical substructure will not be subject to a delay so, the greater the proportion of the overall stiffness which is numerical, the better in terms of stability. For a hybrid simulation with a physical substructure stiffness, K_{phys}, the equivalent negative damping calculated by Eq. 4-7 would be reduced by a factor of $K_{phys} \,/\, (K_{phys} + k_{num})$. Of course, hybrid simulation is of most interest when the physical substructure has a significant effect on the structural response, so it is desirable to be able to perform tests with a significant proportion of the stiffness being physical in origin. Similarly, stability could be achieved by increasing the inherent damping modelled in the numerical substructure to artificially high levels to cancel out the negative damping introduced, or by reducing the natural frequency of the simulated structure.

Stability can also be improved by running the hybrid simulation at a dilated timescale so that the velocity applied to the physical substructure is lower than that assumed in the numerical substructure. Applying a time-dilation factor, $\eta > 1$, to the hybrid simulation would mean that the test would take η seconds to complete 1s of the simulation. This is done with a simple modification to the integration algorithm applied to the numerical substructure, which is described in Section 5.2.3. This improves stability (in accordance with Eq. 4-6) since the effective delay is reduced from δ to δ/η as far as the integration is concerned. Repeating the same hybrid simulation with different levels of time dilation can therefore be useful for assessing the stability and accuracy of the system during initial testing. It can also give information on any rate-dependent characteristics.

In a realistic hybrid simulation, the properties of the structure will be predetermined based on the structural design to be tested and are not free to be varied. Similarly, the aim of this project is to achieve testing in real-time without the need for time dilation. However, the above information is useful in the

planning of initial tests of the RTHS system where the focus is on determining the stability and accuracy of the system before applying it to realistic structural models. After performing open-loop tests of the delay compensator, initial hybrid simulations were carried out with low natural frequencies (0.5Hz), relatively high damping (5%) and with a high proportion of the overall stiffness being modelled numerically (90%). After each successful test these constraints were relaxed until eventually structures were being modelled with high natural frequencies (up to 15Hz), relatively low damping (around 2%) and all of the stiffness coming from the physical substructure.

4.2. Inner Control Loop and Actuation Delay

The displacement of each actuator is controlled by a PID controller (within the Instron 8800 controller shown in Figure 3.3) which determines the voltage signal sent to the actuator based on the difference between the input command and the actuator displacement measured by the LVDT. This control loop, comprising the actuator and PID controller, sits within the larger RTHS feedback loop, as shown in Figure 4.1 and is therefore referred to as the 'inner control loop'. Using PID control alone gives an error between the target and achieved displacement across the BRB (measured by the encoders) due to the inherent delay in the inner control loop and due to flexibility in the test rig. Additional control components are therefore introduced which modify the input command to the PID controllers to compensate for actuation delay and correct for rig flexibility using feedback of the actual BRB displacement measured by the encoders. These additional control components are referred to as the 'outer control loop'. This section investigates the performance of the inner control loop. Sections 4.3 - 4.5 deal with the outer control loop and then the results of testing the combined control system are given in Sections 4.6 and 4.7.

4.2.1. The PID Controller

The hydraulic actuators are powered by high pressure oil which enters the actuator's piston chamber via Moog® servo-valves. The servo-valves control the movement of the piston by directing the

pressurised oil to one side of the piston while simultaneously connecting the other side to the return line. The operation of the servo-valves is governed by the controller output received from the proportional-integral-derivative (PID) controller implemented on the Instron® 8800 controller machine. The controller output, $y(t)$, is determined based on the error, $e(t)$, between the command displacement, $u_c(t)$, and the measured actuator displacement, $x_m(t)$, using the relationship:

$$y(t) = K_p\left(e(t) + T_d\frac{de(t)}{dt} + \frac{1}{T_i}\int e(t)dt\right) \qquad 4\text{-}9$$

where $e(t) = u_c(t) - x_m(t)$. K_p is the proportional gain, T_d is the derivative time, and T_i is the integral time. The transfer function of the PID controller is therefore:

$$\frac{Y(s)}{E(s)} = K_p\left(1 + T_d s + \frac{1}{T_i s}\right) \qquad 4\text{-}10$$

where $E(s)$ and $Y(s)$ are the Laplace transforms of $e(t)$ and $y(t)$, respectively, and s is the Laplace variable. The Instron® 8800 controller also incorporates a lag term to help prevent the amplification of high frequency noise, which effectively multiplies the right-hand side of Eq. 4-10 by $1/(1 + T_l s)$ where T_l is the lag time. The block-diagram implementation of this system is shown in Figure 4.4 and includes a limiter to prevent integral windup. This stops the integral term rising to excessively high values when the servo-valves are fully open and cannot provide any further increase in oil flow. The performance of the inner control loop is therefore dependent on the four parameters: K_p, T_d, T_i and T_l.

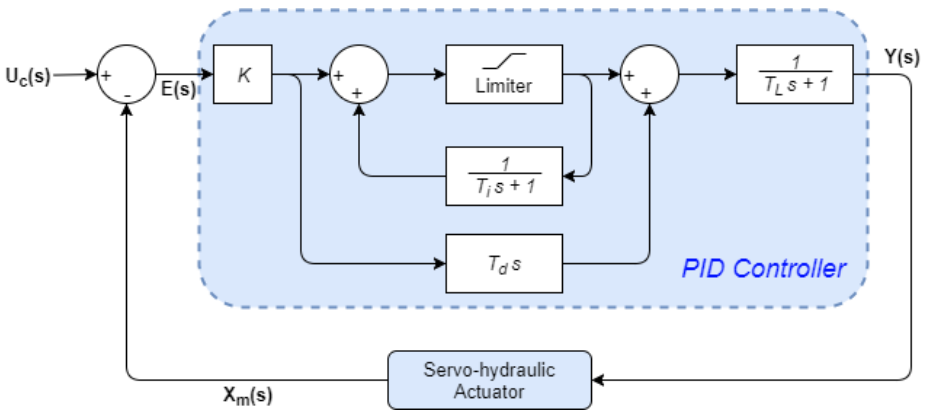

Figure 4.4 – The inner control loop for the hydraulic actuator

4.2.2. Effect of PID Parameters on Stability and Delay

The Instron® 8800 controller incorporates an 'autotuner' that optimises the PID parameters to achieve a target level of overshoot in response to a square wave input. The user must specify the target damping level along with the amplitude and frequency of the square wave. The autotuner then applies this input and varies the PID parameters until the response overshoot matches the target. The choice of target damping is a compromise between speed of response and size of overshoot: the lower the damping the faster the response but the greater the overshoot. This was therefore set to 0.707 to aim for a fast response with minimal overshoot. Since the autotuner works on each actuator separately, the test rig layout, with two actuators operating in parallel, prevents it from being used once the BRB is installed. It was therefore run for each actuator separately prior to installing the BRB and cross-beam.

The autotuner was run for each actuator with square wave frequencies of 1Hz and 5Hz at amplitudes of 0.1mm, 0.2mm and 1.0mm. It sets T_d, T_i and T_l to the same values each time while varying K_p to achieve the desired response. The derivative time, T_d, is always set to zero, as is common due to noise being amplified when the derivative of the error signal is taken. The integral time, T_i, is always set to 1s. The integral term accumulates as long as an error exists to remove steady state error, but it tends to slow down the response and increase the overshoot. The lag time, T_l, is always set to 0.8ms, acting as a low pass filter with a cut off of 199Hz. Similar values of proportional gain, K_p, (here given in decibels) were given for the various inputs, all in the range 35.5dB – 37.9dB with a mean of 36.5dB. Figure 4.5 shows the mean delay at zero-crossings for sinusoidal displacements of the bare actuator ($\pm$80mm) for various maximum actuator velocities before and after PID tuning. It is clear that tuning of the PID parameters can significantly affect the performance of the system.

Bonnet [73] points out that the PID proportional gain determined by the autotuning process is conservative since the optimisation process uses the square wave response whereas the signals produced during hybrid testing will be smoother and therefore have a less onerous effect on control. This implies that it may be possible to improve the response by increasing K_p above the levels given by

the autotuner. In general, increasing K_p will speed up the response while, for an underdamped system, increasing the overshoot, and there will be some limit above which the control system becomes unstable. For this system with the bare actuators, this occurs at a K_p of approximately 48.5dB.

To investigate the effects of the proportional gain, open loop cyclic tests were performed for a range of K_p values and repeated with the integral term removed (effectively $1/T_i = 0$). The error (defined in the next subsection) between the target and measured actuator displacements are plotted in Figure 4.6, showing that increasing K_p does reduce the displacement error, but that the marginal benefit decreases as K_p increases. It is also seen that removing the integral term has a minimal effect on the error, so T_i is kept at its default value of 1s. Figure 4.6 also shows the results when these tests were repeated with one of the delay compensation techniques (the ATS compensator that will be introduced in the next section) applied to the outer control loop. Once delay compensation is incorporated, the sensitivity of the system to the exact value of the PID gains becomes very small, and so there is little benefit in pushing the proportional gain too high and risking instability. Even so, the larger the delay that the compensator must correct for, the greater will be the uncertainty in the extrapolation. This may become more significant for the less uniform displacements experienced in a hybrid test. Hence values of K_p in the range 37.5dB – 40dB were used, while keeping the other coefficients at their default values ($T_i = 1s$, $T_d = 0s$, $T_l = 0.8ms$).

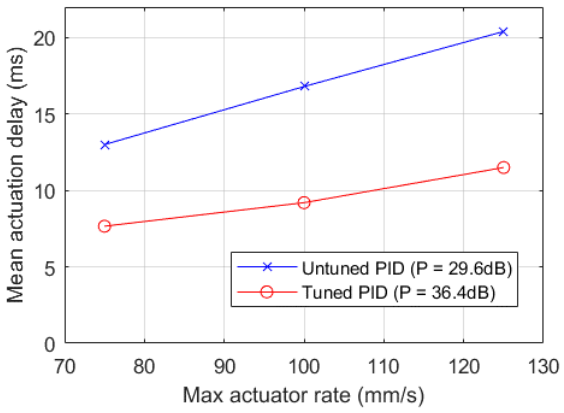

Figure 4.5 – Effect of PID tuning on delay for the bare actuator

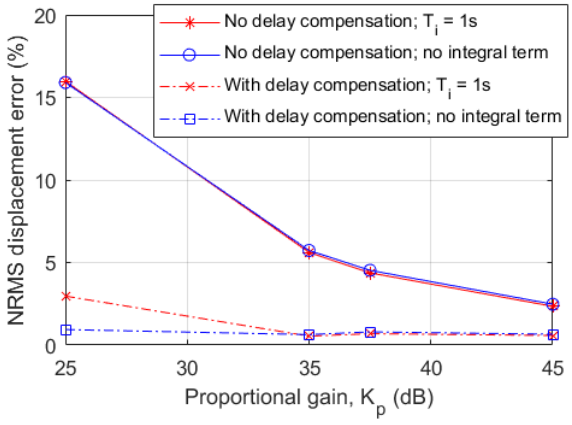

Figure 4.6 – Effect of PID proportional gain on accuracy with and without integral term

Once the BRB had been installed, open-loop cyclic tests were performed at 5Hz for various levels of proportional gain, with the displacements limited to the elastic range of the BRB, giving the responses shown in Figure 4.7. The mean delay at zero-crossings and ratio of achieved displacement to target displacement at peaks are shown in Figure 4.8. These results confirm that a K_p of 40dB is appropriate once the BRB stiffness is included and indicate that even with optimised PID coefficients the minimum delay which can be achieved is around 11ms.

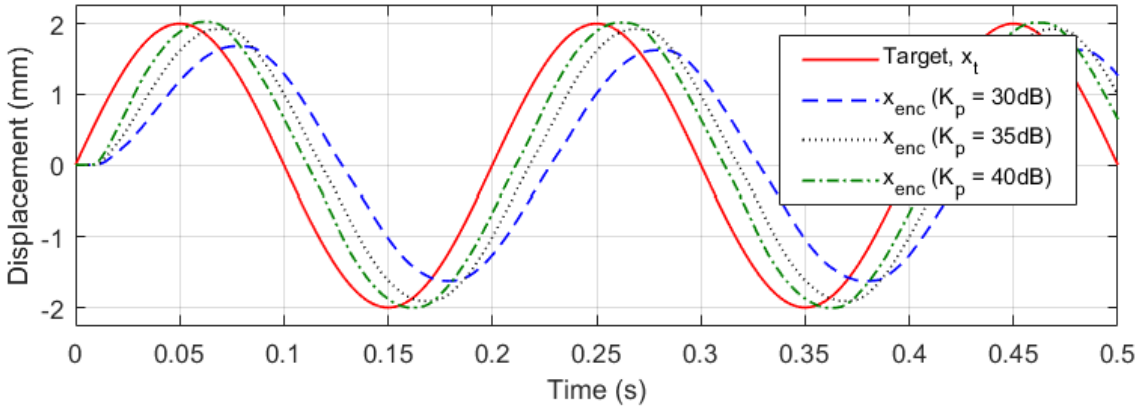

Figure 4.7 – Effect of PID proportional gain, K_p, on open-loop response at 5Hz

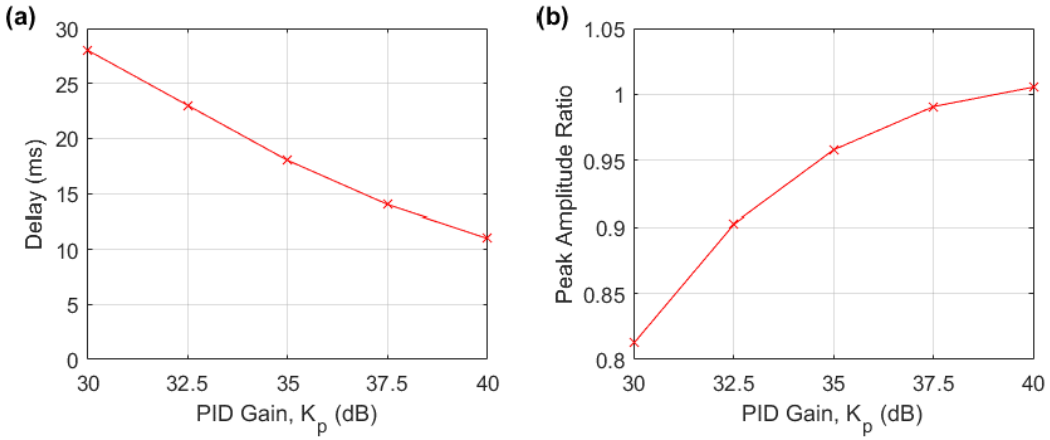

Figure 4.8 – Effect of PID proportional gain, K_p, on (a) mean delay at zero crossing and (b) ratio of achieved displacement, x_{enc}, to target displacement, x_t, at peaks

4.2.3. Measuring Actuation Delay

An actuation delay gives a horizontal shift between the command and achieved displacements on the displacement-time plot. In the absence of an amplitude error, the delay can therefore be measured as

the horizontal offset between the two lines – see the line for $K_p = 40dB$ in Figure 4.7. However, an amplitude error causes the achieved displacement to be scaled in the vertical direction making this approach inaccurate, particularly near peaks – see the line for $K_p = 30dB$ in Figure 4.7. A reasonable assumption in most cases is that the amplitude error will be negligible at zero displacement, and therefore the time between the zero-crossings of the command and achieved displacements can give a good measure of the delay. This may not hold if yielding of the physical substructure causes a significant offset in the equilibrium position. Alternatively, the time between peaks could be measured. Similarly, a measure of the amplitude error can be obtained from the ratios of the peak displacements of the two signals. However, these methods only give estimates at specific points. Bonnet [73] estimated the delay at intermediate points by assuming that the amplitude error varied linearly between adjacent local peaks. The measured displacement would then be scaled to approximately correct for the amplitude error, allowing the delay to be estimated at any point as the time between equivalent points. Adaptive delay compensation methods require "online" estimates of the current delay as a test progresses and must therefore take the presence of an amplitude error into consideration, as will be seen in the next subsection.

To investigate the delay within the inner control loop (i.e. between the command, u_c, to the actuators and the measured displacement, x_m, of the actuators), sinusoidal displacements of 10s duration were applied at frequencies of 0.5Hz, 2Hz and 5Hz. The amplitude was set to 2.6mm to give a displacement across the BRB of 2mm (to keep it in the elastic range). The difference between the actuator displacement and the BRB deformation is due to deformation of the components of the test rig, an issue which is dealt with in Section 4.5. The delays measured at the zero-crossings and at the peaks are given in Table 4.1. The zero-crossing locations are found by detecting a change in sign of the signal, while the peaks can be located by detecting a change in the sign of the increment between timesteps. The signals were first filtered using a zero-phase filter (the Matlab® *filtfilt* function) to smooth the signal without adding a phase shift and were then interpolated to allow greater precision. There is seen to be some variation in mean delay between tests and during a test, but it is not overly significant.

	Frequency of Oscillation (Hz)		
	0.5 Hz	2 Hz	5 Hz
Mean Delay at zero-crossings (ms)	8.1	9.0	8.9
Range of delays at zero-crossings (ms)	7.3 – 9.2	8.2 – 10.1	8.5 – 9.7
Mean Delay at peaks (ms)	8.8	8.5	8.6

Table 4.1 – Delays measured for cyclic tests at various frequencies

Large displacement tests were later run with actuator displacements of approximately 5mm, 10mm and 19mm (giving BRB deformations of 4.375, 8.75, 17.5mm). At these large displacements the BRB yields so that its effective stiffness changes, with the secant stiffness decreasing with increased levels of deformation. The mean delays at zero-crossings (over three cycles at each amplitude) were 8.2ms, 7.7ms and 6.9ms, respectively, indicating that the stiffness of the physical specimen affects the delay.

While it is the delay and amplitude error which is of key interest, it can be impractical to use these as measures for comparing different tests since they can vary during the test, and taking mean values, for example, can be hard to compute and will not give the full picture. An alternative measure of accuracy used by Chae et al. [12] is the normalised root mean square (NRMS) error, which gives a single value in the form of a percentage error for each test. They defined the NRMS error as:

$$E^*_{NRMS} = \sqrt{\frac{\sum_{i=0}^{N-1} \left(x_{t,i} - x_{m,i}\right)^2}{\sum_{i=0}^{N-1} \left(x_{t,i}\right)^2}} \qquad 4\text{-}11$$

where integer i is the timestep of the simulation, N is the total number of timesteps, and $x_{t,i}$ and $x_{m,i}$ are the values of $x_t(t)$ and $x_m(t)$, respectively, sampled at timestep i. Note that this measure does not distinguish between errors due to delay and those due to amplitude error; however, it provides a practical method for making comparisons of actuation quality between tests simulating the same structure but with different control conditions.

Chae et al. used a viscoelastic (VE) damper as the physical substructure, which remains in its elastic range. The BRB, however, undergoes yielding which causes a permanent offset in the equilibrium position, x_0, about which oscillation occurs. Consider a hybrid simulation consisting of a large initial displacement resulting in yielding, followed by smaller displacements about the new equilibrium

position. The error in Eq. 4-11 is normalised with respect to the displacement relative to the initial position so the offset will cause the denominator to be much larger than if the small displacements had not been preceded by yielding, giving an artificially small error measurement. In this case, a more meaningful measure of the error would be obtained by normalising with respect to the target displacement *relative* to the equilibrium position. As an approximation to this, the error is normalised with respect to the displacement relative to the mean displacement, $x_{t,mean}$, rather than the initial displacement, giving:

$$E_{NRMS} = \sqrt{\frac{\sum_{i=0}^{N-1} \left(x_{t,i} - x_{m,i}\right)^2}{\sum_{i=0}^{N-1} \left(x_{t,i} - x_{t,mean}\right)^2}} \qquad 4\text{-}12$$

where $x_{t,mean} = \frac{1}{N}\sum_{i=0}^{N-1} x_{t,i}$.

4.3. Delay Compensation

4.3.1. Aims of Delay Compensation

Above it was shown how an unavoidable delay exists in the inner control loop which can cause instability when introduced into the closed loop feedback system of a RTHS test. The success of a hybrid simulation relies on how closely the applied displacement, x_m, matches the target displacement, x_t, prescribed by the numerical substructure. The aim of delay compensation is therefore to determine the command signal, u_c, to send to the inner control loop so that $x_m = x_t$. Numerous authors have demonstrated the improvement in accuracy and stability of a RTHS that can be achieved by introducing delay compensation into the outer control loop, using a variety of compensation methods (e.g. [10], [11], [73], [76], [77]). While the implementation varies between the methods proposed by different authors, all delay compensation methods comprise the following key steps:

i. Obtain an estimate of the actuation delay, δ, in the system;

ii. Use an extrapolation technique to predict what the target displacement will be at a time in the future equal to the actuation delay;

iii. Send this extrapolated signal as the command, u_c, to the actuator PID controller in place of the current target displacement, x_t.

This is illustrated in Figure 4.9 which shows the displacement response from a hybrid test with delay compensation. The target displacement, x_t, is the displacement calculated by the numerical substructure which is to be applied to the physical substructure. The command displacement, u_c, is the signal sent to the PID controller to try and get the measured displacement, x_m, of the device to match x_t. Without delay compensation, u_c would simply be set equal to x_t but, with delay compensation, u_c is modified by an extrapolation procedure which, if correctly implemented, will greatly reduce the error between x_t and x_m. The effectiveness of a delay compensation procedure is therefore dependent on the ability to: (i) predict the future values of the target displacement, and (ii) estimate the value of the actuation delay.

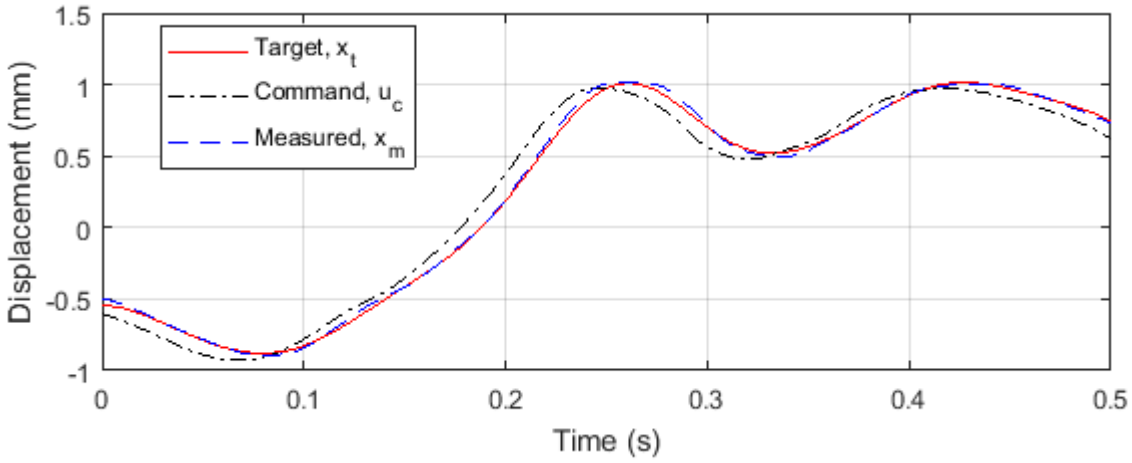

Figure 4.9 – Example of a system with delay compensation producing an extrapolated command to cancel out the delay between the target and achieved displacements

4.3.2. Constant Delay Methods

Delay compensation procedures can be broadly divided into those which extrapolate by a fixed amount throughout the test, and those which update the delay estimate as the test progresses and vary the amount of extrapolation accordingly. Earlier efforts relied on the constant delay assumption with the mean delay being estimated from past tests. This allowed a significant improvement in stability, but the

assumption is limiting since the actuation delay is likely to vary during the test and may not be known in advance. More recent efforts have attempted to build on these methods by allowing the delay estimate to be continually updated in real time. First the constant delay compensators are reviewed.

4.3.2.1. Exact Polynomial Fitting

Horiuchi et al. [9] proposed fitting an exact polynomial to recent values of the target displacement signal, x_t, and using this to extrapolate ahead by the delay time, δ, to generate the command signal, u_c, which is the predicted value of $x_t(t+\delta)$:

$$u_c(t) = \sum_{i=0}^{n} a_i x_t(t - i\delta) \qquad 4\text{-}13$$

Horiuchi et al. chose a third order polynomial, so the curve would be fitted through four data-points, with compensator coefficients, a_0, a_1, a_2 and a_3, of 4, -6, 4 and -1, respectively. An issue is that, when the delay is not an integer number of timesteps, the values of $x_t(t - i\delta)$ will not be known as they lie in between datapoints of the discretised system. However, the delay is expected to be much larger than the controller timestep so rounding δ to the nearest integer timestep gives a close approximation.

4.3.2.2. Least Squares Polynomial Fitting

An alternative to fitting a polynomial of order n through the most recent $n+1$ data points, producing an exact fit, is to fit through more than $n+1$ points using a least squares polynomial fit. This was done by Wallace et al. [78] who fitted a fourth order polynomial to the last sixteen points. The polynomial will no longer necessarily pass through all of the points, but the advantage of this smoothing out is the potential for resilience against noise. This may, however, cause a small discontinuity as the prediction steps from one polynomial to the next since no point actually lies on the polynomial [73].

4.3.2.3. Linear Acceleration Extrapolation

Horiuchi and Konno [76] noted that extrapolation using a third-order polynomial is equivalent to assuming that the acceleration at the interface between substructures varies linearly with respect to

time. They therefore sought to improve on the exact polynomial method by making explicit use of this assumption. First the predicted acceleration, $\ddot{x}_p(t)$, at the delay time, δ, in the future is estimated from:

$$\ddot{x}_p(t) = 2\ddot{x}_t(t) - \ddot{x}_t(t-\delta) \quad 4\text{-}14$$

where $\ddot{x}_p(t)$ is the prediction at time t of the future target acceleration, $\ddot{x}_t(t+\delta)$. This extrapolates from the current acceleration, $\ddot{x}_t(t)$, assuming the acceleration increment over the extrapolation time (t to $t+\delta$) is equal to the increment, $\ddot{x}_t(t) - \ddot{x}_t(t-\delta)$, over the delay time ($t-\delta$ to t). Assuming that the acceleration varies linearly from $\ddot{x}_t(t)$ at time t to $\ddot{x}_p(t)$ at time $t+\delta$, the predicted value of the future target displacement, $x_t(t+\delta)$, which forms the command signal, $u_c(t)$, is given by:

$$u_c(t) = x_t(t) + \delta\dot{x}_t(t) + \left(\frac{1}{3}\delta^2\right)\ddot{x}_t(t) + \left(\frac{1}{6}\delta^2\right)\ddot{x}_p(t) \quad 4\text{-}15$$

This is a variation on the displacement equation of the Newmark integration method [79] with linear acceleration ($\beta = 1/6$) which will be described in Section 5.3.3. Since values of $\ddot{x}_t(t-\delta)$ only exist when δ is an integer number of timesteps, Eq. 4-15 can only be implemented directly if δ is rounded to an integer number of timesteps. Alternatively, an interpolation procedure can be used to obtain an estimate for other values of δ. The system is reliant on the current values of velocity, $\dot{x}_t$, and acceleration, $\ddot{x}_t$, being available in addition to the displacement, x_t. Horiuchi and Konno used the Central Difference Method (described in Section 5.3.4) which cannot provide the current values of $\dot{x}_t$ and $\ddot{x}_t$, but allows them to be computed for the previous timestep. The extrapolation was therefore performed from the previous timestep, with δ being increased by the integration timestep, Δ, to $\delta + \Delta$. The method is shown to exhibit superior performance to the fitted polynomial extrapolation, increasing the stability of the RTHS system [76] allowing higher frequency structures to be simulated.

4.3.2.4. Taylor Expansion

For a system with a constant delay, δ, the relationship between u_c and x_m can be expressed as:

$$u_c(t) = x_m(t+\delta) \quad 4\text{-}16$$

The aim of making $x_m = x_t$ would be achieved by sending the command signal:

$$u_c(t) = x_t(t+\delta) \quad 4\text{-}17$$

Of course, at time t, the future target displacement, $x_t(t+\delta)$, will not yet be known. Taking the Taylor series expansion of $x_t(t+\delta)$ about $x_t(t)$ gives:

$$u_c(t) = x_t(t) + \delta\dot{x}_t(t) + \frac{\delta^2}{2}\ddot{x}_t(t) + \cdots + \frac{\delta^n}{n!}\frac{d^n x}{dt^n} + \cdots \quad 4\text{-}18$$

Truncating this infinite series to a second-order system, the command signal can be calculated as:

$$u_c(t) = x_t(t) + \delta\dot{x}_t(t) + \frac{\delta^2}{2}\ddot{x}_t(t) \quad 4\text{-}19$$

which is extrapolation on the assumption that the acceleration remains constant at $\ddot{x}_t(t)$ over the time δ. As for the linear acceleration extrapolation, this requires the current target velocity, $\dot{x}_t$, and target acceleration, $\ddot{x}_t$, in addition to x_t. If not available from the integration algorithm, these can be approximated by numerical differentiation of x_t since it will be a clean signal coming from the numerical substructure. If the system were truncated to a third-order system, a linear acceleration extrapolation would result. This is the same as the method by Horiuchi and Konno [76] except the rate of change of acceleration between t and $t + \delta$ is taken as the current value, $\dddot{x}_t(t)$, rather than the mean value over the time $t - \delta$ to t. However, since $\dddot{x}_t(t)$ is not generally available from the integration algorithm, the method could only be implemented by using an approximation to estimate $\dddot{x}_t(t)$. Using the approximation $\dddot{x}_t(\mathrm{t}) \approx (\ddot{x}_t(t) - \ddot{x}_t(t-\delta))/\delta$, gives the linear acceleration method presented above.

4.3.2.5. Inverse Compensation Method

The Inverse Compensation Method proposed by Chen [10] uses a delay model relating the actuator displacement, x_m, to the command, u_c. The inverse of this model is then used to generate the command from the target, x_t, that aims to cancel out the delay. Consider the interval between the times t_{i-1} and $t_i = t_{i-1} + \Delta$ during which the command changes from $u_{c,i-1}$ to $u_{c,i}$ and assume that at t_{i-1} the actuator displacement, $x_{m,i-1}$, equals $u_{c,i-1}$. The delay means that at t_i the actuator will not yet have reached $u_{c,i}$, so $x_{m,i}$ will lie between $x_{m,i-1}$ and $u_{c,i}$. Assume that the actuator displacement reaches $u_{c,i}$ at time $t_d = t_{i-1} + \alpha\Delta$ and varies linearly during this time, i.e. the velocity

is constant. Note that α is related to the delay, δ, by $\delta = (\alpha - 1)\Delta$, so α would be 1.0 if there were no delay and is greater than 1.0 when a delay is present. The relationship between x_m and u_c is then:

$$x_{m,i} = x_{m,i-1} + \frac{1}{\alpha}(u_{c,i} - x_{m,i-1}) \quad 4\text{-}20$$

Applying the discrete z-transform to Eq. 4-20 gives the transfer function in the z-domain:

$$G_d(z) = \frac{X_m(z)}{U_c(z)} = \frac{z}{\alpha z - (\alpha - 1)} \quad 4\text{-}21$$

where z is the complex variable in the z-domain, and $X_m(z)$ and $U_c(z)$ are the z-transforms of $x_{m,i}$ and $u_{c,i}$, respectively. Chen applied the inverse of this transfer function to x_t to generate the command:

$$G_c = \frac{U_c(z)}{X_t(z)} = \frac{\alpha z - (\alpha - 1)}{z} \quad 4\text{-}22$$

where $X_t(z)$ is the z-transform of $x_{t,i}$. The inverse z-transform of Eq. 4-22 gives the compensator equation in the time domain, which is seen to be equivalent to extrapolating ahead using the discrete approximation to the velocity taken over the last timestep:

$$u_{c,i} = \alpha x_{t,i} - (\alpha - 1)x_{t,i-1} \quad 4\text{-}23$$

4.3.2.6. Phase Lead Compensator

Zhao et al. [77] proposed the use of a first order phase-lead compensator (PLC) of the type widely used in the control of mechanical and electrical systems [80], which has the Laplace transfer function:

$$G_{PLC}(s) = \frac{T_d s + 1}{\beta T_d s + 1} \quad 4\text{-}24$$

where T_d is the time constant of the delay compensator and the constant β takes a value less than 1.0 to produce a phase lead (Zhao et al. used $\beta = 0.1$). This transfer function modifies the amplitude of the signal in addition to its phase, which Zhao et al. used to compensate for the reduction in amplitude which occurred in their system as the frequency increased.

4.3.3. Pre-Recorded Delay Estimates

Bonnet [73] implemented a scheme which varied the delay estimate during the test based on a record of the delay from a previous test. This generally requires an iterative procedure because the delay

depends on the applied displacement, which in turn depends on the effectiveness of the delay compensation. For example, a hybrid test could first be performed with constant delay compensation from which the variation of the actual delay could be measured. The test would then be repeated using the recorded delay to determine how far to extrapolate at each timestep. This would then be repeated, each time compensating based on the delay recorded from the previous test, until the delays were reduced to sufficiently small levels. This might require starting with reduced scale tests and gradually building up to full scale. Apart from being time consuming, this method becomes impractical for devices which are damaged or permanently altered by the test because of the need to replace the device each time. BRBs are such devices since their properties are permanently altered each time yielding occurs.

4.3.4. Adaptive Compensation Methods

Since the delay can vary during a hybrid simulation, some researchers have investigated schemes for *adaptive delay compensation* – that is, a delay compensator which varies the amount of time by which the command signal is extrapolated based on a continually updated estimate of the current delay. Prominent systems proposed in the literature include: the Darby Estimator [11] (as modified by Bonnet [73]) and the Adaptive Time Series (ATS) Compensator [12]. The first of these estimates the delay at each timestep by updating the estimate from the previous timestep according to the measured difference between the target and measured displacements. An extrapolation procedure such as one of those mentioned above would then be used, but now with the extrapolation time varied according to the delay estimate. The ATS combines delay estimation and extrapolation using a Taylor series expansion of the target displacement but with the coefficients varying based on a least square fit over a given time window of previous measurements. Advantages of the ATS method include that it also accounts for amplitude error and that it does not require the use of empirically-tuned gains.

4.3.4.1. The (Modified) Darby Estimator

Darby et al. [11] proposed and demonstrated a method for continually updating the delay estimate based on the error between the target displacement, x_t, and the measured displacement, x_m:

$$\delta_{i+1} = \delta_i + C_p\left(x_{t,i} - x_{m,i}\right)\tanh\left(C_v\frac{x_{t,i+1} - x_{t,i}}{\Delta}\right) \quad 4\text{-}25$$

where Δ is the timestep and i is the integer number of the most recently completed timestep. The constants, C_p and C_v, must be set empirically, as must the initial value, δ_0. The hyperbolic tangent function approaches unity when the target velocity is high (i.e. far from a peak) and approaches zero when the velocity is small (i.e. close to a peak). This pragmatic approach is designed to prevent amplitude errors, which will be most significant near the peaks, from being treated as a delay and leading to inaccurate delay estimates. The choice of C_v determines the abruptness of the cut-off between these regions, while C_p should be set large enough to allow the delay estimate to update rapidly without being so large as to cause instability. Bonnet [42] [50] proposed a modification to Darby's estimator which removes the need to set a fixed value of C_p empirically and instead scales the error based on the current estimate of the velocity. This is based on the observation that the velocity is approximately equal to the displacement error divided by the delay remaining after compensation:

$$\dot{x}_{t,i} \approx \frac{x_{t,i+1} - x_{t,i}}{\Delta} \approx \frac{x_{t,i} - x_{m,i}}{\delta} \quad 4\text{-}26$$

Hence Eq. 4-25 is modified to:

$$\delta_{i+1} = \delta_i + \left(\frac{\Delta}{x_{t,i+1} - x_{t,i}}\right)\left(x_{t,i} - x_{m,i}\right)\tanh\left(C_v\frac{\left|x_{t,i+1} - x_{t,i}\right|}{\Delta}\right) \quad 4\text{-}27$$

One of the extrapolation procedures above is then used to calculate the corrected command [81].

4.3.4.2. Adaptive Inverse Compensation

Chen and Ricles [82] implemented an adaptive version of the inverse compensation method described above. This replaced the fixed delay coefficient, α, in Eq. 4-22 with the term $\alpha_{es} + \Delta\alpha$ where α_{es} is a fixed estimate of the actuator delay coefficient and $\Delta\alpha$ is a correction term calculated using:

$$\Delta\alpha = k_p TI(t) + k_i\int_0^t TI(\tau)d\tau \quad 4\text{-}28$$

where k_p and k_i are fixed gains, and TI is a tracking indicator. The tracking indicator used was based on the difference between the enclosed and complimentary areas of the synchronisation plot of target

displacement against achieved displacement. Mercan [83] showed that this tracking indicator will grow when the achieved displacement lags behind the target and decrease when it leads ahead of the target. The gains, k_p and k_i, must be chosen empirically and require a compromise between speed at which $\Delta\alpha$ adapts to changes in delay and the amount of oscillation of $\Delta\alpha$.

4.3.4.3. The Adaptive Time Series (ATS) Compensator

More recently, Chae et al. [12] proposed and demonstrated an adaptive compensation procedure which they called Adaptive Time Series (ATS) compensation. This method calculates the command, u_c, as a linear combination of the target displacement, x_t, and its derivatives ($\dot{x}_t$ and $\ddot{x}_t$). The coefficients of the model are continually updated by computing the values which minimise the error between x_m and x_t over a set of previous values. The processes of delay estimation and extrapolation are therefore combined, but an estimate of the delay can easily be calculated. This method also provides adaptive correction for amplitude error. A modified version of the ATS compensator has been developed for this project, so the method is described in detail below, followed in the next section by the proposed modification which reduces the computational and storage demands of the procedure.

The ATS compensator is based on the following assumed relationship between the input command displacement, u_c, and the resulting measured displacement, x_m:

$$u_c(t) = \frac{1}{A} x_m(t + \delta) \tag{4-29}$$

where A is the amplitude ratio (the ratio of output to input displacement amplitudes) and δ is the delay. Eq. 4-29 can be approximated by a Taylor series expansion at time t, giving:

$$u_c(t) \approx \frac{1}{A}\left[x_m(t) + \delta\dot{x}_m(t) + \frac{\delta^2}{2!}\ddot{x}_m(t) + \cdots + \frac{\delta^n}{n!}\frac{d^n x_m}{dt^n}\right] \tag{4-30}$$

To determine the command signal required to make $x_m \approx x_t$, the measured displacement, x_m, and its derivatives are replaced in Eq. 4-30 with the target displacement, x_t. Writing in the discrete time domain, the command signal at timestep k is calculated from:

$$u_{c,k} \approx a_0 x_{t,k} + a_1 \dot{x}_{t,k} + \cdots + a_n \frac{d^n x_{t,k}}{dt^n} \tag{4-31(a)}$$

where

$$a_j = \frac{\delta^j}{Aj!}, \quad j = 0,1,\dots,n \tag{4-31(b)}$$

Fixed values of the a_j coefficients could be determined by substituting an estimate of the mean delay and amplitude error into Eq. 4-31, as in Eq. 4-19. However, the performance can be improved by continually updating the coefficients to give the best fit. Consider the command signal, $u_{est,k}$, which would have been given if x_m had been used in place of x_t in Eq. 4-31:

$$u_{est,k} \approx a_0 x_{m,k} + a_1 \dot{x}_{m,k} + \cdots + a_n \frac{d^n x_{m,k}}{dt^n} \tag{4-32}$$

To make x_m as close to x_t as possible, the coefficients (a_0, a_1, ..., a_n) must be selected so as to minimise the error between u_c and u_{est}. This is done by minimising the cost function:

$$J_k = \sum_{i=1}^{q} \left(u_{c,k-i} - u_{est,k-i}\right)^2 \tag{4-33}$$

where q is the number of timesteps over which the error is computed, and therefore represents the size of the time window over which the coefficients are optimised. The coefficients which minimise J_k can be found from the set of simultaneous equations given by:

$$\frac{\partial J_k}{\partial a_j} = 0, \quad j = 0,1,\dots,n \tag{4-34}$$

which can be solved in matrix form as:

$$\boldsymbol{A} = (X_m^T X_m)^{-1} X_m^T \boldsymbol{U_c} \tag{4-35}$$

where $\boldsymbol{A} = \left[a_{0,k}, a_{1,k}, \dots a_{n,k}\right]^T$, $X_m = \left[\boldsymbol{x_m}, \dot{\boldsymbol{x}}_{\boldsymbol{m}}, \dots, \frac{d^n \boldsymbol{x_m}}{dt^n}\right]$, $\boldsymbol{x_m} = \left[x_{m,k-1}, x_{m,k-2}, \dots, x_{m,k-q}\right]^T$, and $\boldsymbol{U_c} = \left[u_{c,k-1}, u_{c,k-2}, \dots, u_{c,k-q}\right]^T$. By substituting the coefficients of $\boldsymbol{A}$ from Eq. 4-35 at each timestep into Eq. 4-31(a), the command signal, u_c, is obtained.

The order at which to truncate the Taylor series must be selected. The use of higher order terms may be undesirable due to their amplifying effect on noise; also, for a sufficiently small δ their effect becomes negligible. The authors chose a second-order system ($n = 2$), so that Eq. 4-31(a) becomes:

$$u_{c,k} = a_{0,k} x_{t,k} + a_{1,k} \dot{x}_{t,k} + a_{2,k} \ddot{x}_{t,k} \tag{4-36}$$

While it is not necessary to calculate the amplitude ratio, A_k, or delay, δ_k, in the system, Eq. 4-31(b) shows that these values can be estimated from the coefficients of the ATS compensator:

$$A_k \approx \frac{1}{a_{0,k}}, \quad \delta_k \approx \frac{a_{1,k}}{a_{0,k}} \tag{4-37}$$

This relationship between the ATS coefficients and the system parameters is extremely useful. For example, having an estimate of the delay in the system allows appropriate initial values for the compensator to be chosen easily.

4.3.4.3. Practical Implementation of the Adaptive Time Series (ATS) Compensator

The practical implementation of the ATS compensator requires the size of the time window (the value of q) to be selected. This is a compromise between ensuring stability and ensuring a rapid response to a change in delay. A larger q offers stability of the coefficients by averaging out the fit over a longer time period; however, it means it will take longer for the compensator to react to a change in delay. The value of q also affects the computational memory (RAM) requirements of the processor since it must keep a record of the previous q values of x_m, $\dot{x}_m$, $\ddot{x}_m$ and u_c. The value of q chosen by the authors in their original paper was 1024. With a timestep of 1/1024 s, this gives a time window of 1s. Hence $4 \times 1024 = 4096$ data points must be kept in the memory, which is done using a tapped delay. To implement Eq. 4-35 fully would require multiplying matrices, X_m, of size 1024 by 3, which was found to be too demanding a computation to complete within the real-time timestep. To get around this, the authors down-sampled the data before forming X_m and $\boldsymbol{U_c}$, taking only every 16th value, reducing the matrix size to 64 by 3 and thereby reducing the computational demand of Eq. 4-35 to a level which could be handled within the timestep. However, the memory requirements remain the same. Down-sampling by too large a factor could also reduce the accuracy of the calculation by reducing the number of data points over which the coefficients are fitted.

Additional practicalities include the need to compute the first and second derivatives of x_t and x_m with respect to time. This is done using the simple first-order discrete approximation to the derivative:

$$\dot{x}_k = \frac{x_k - x_{k-1}}{\Delta} \qquad 4\text{-}38$$

to obtain the velocity, which is applied again to obtain the acceleration. This can be applied directly to x_t, for use in Eq. 4-36, since it comes directly from the numerical substructure and is therefore free of measurement noise. However, the measured displacement signal, x_m, will contain noise which would be amplified in taking the derivatives, destabilising the calculation of the ATS coefficients, hence the x_m signal is filtered before being fed back into the system. While there should be no noise on the command signal, u_c, this must also be filtered with the same filter before being used in Eq. 4-35 so as to maintain phase with the filtered x_m signal. A 6th order low-pass Butterworth filter with a 15Hz cut-off is used for this purpose. The phase lag introduced is acceptable since the coefficients are being fitted over a large time window anyway – clearly, filtering of x_t would be unacceptable as it would introduce a delay in the target signal.

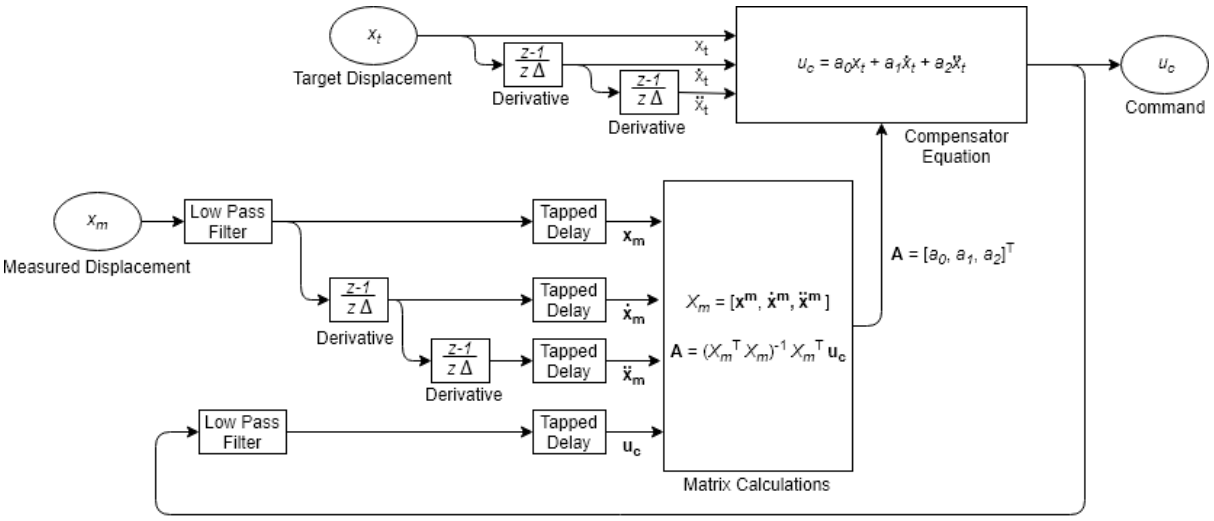

Figure 4.10 – Implementation of ATS compensator

An initialisation procedure is required since there will initially be no displacement data to fit to (X_m will be a matrix of zeros). The authors held the ATS coefficients constant at initial values until enough motion has occurred for the output of Eq. 4-35 to be meaningful, which they take as being when the

actuator displacement first exceeds 0.2mm. Finally, there is a risk that the matrix to be inverted, $X_m^T X_m$, could become ill-conditioned when the displacement is small. The system therefore stopped updating the compensator coefficients when the displacements occurring over the time-window became small. This was originally triggered when the peak value over the time-window fell below a threshold value. However, in later testing [84], this was deemed not practical and the root-mean square (RMS) value of displacement over the time-window was used instead, stopping the updating of the coefficients when this fell below 1.0mm. In addition, the maximum and minimum values of the ATS coefficients were limited to a reasonable range, as was the rate at which they were allowed to change.

In the original paper introducing ATS compensation [12], the authors applied the system to the testing with a single viscous damper. This was first done with a predefined earthquake displacement response at a variety of displacement amplitudes. It was then applied to a RTHS of a three-storey steel MRF combined with a damper braced frame (DBF), where the physical substructure was the damper in the top storey of the DBF. The mean delay before compensation was approximately 21ms. The addition of the ATS compensator gave a significant reduction in NRMS error compared to the uncompensated tests during the predefined displacement testing, and also gave an improvement over the fixed delay methods of inverse compensation and second-order compensation which used coefficients optimised before the test based on the results of testing with randomised displacements. For example, in the largest predefined displacement test (peak of 40mm) the NRMS error was reduced from 16.3% (in the uncompensated case) to 1.4% with the ATS compensator, while inverse compensation and second-order compensator methods gave larger NRMS errors of 2.9% and 2.6%, respectively.

The ATS compensator was then used in successful RTHS of the structure in response to the ground motions of the 1979 Imperial Valley earthquake and the 1994 Northridge earthquake scaled to three different levels: the low-level design basis (LDBE) earthquake, the design basis earthquake (DBE) and the maximum considered earthquake (MCE). The system using the ATS compensator outperformed both constant delay methods in all cases, giving a mean NRMS error of 1.9%, compared to 3.1% for the

inverse compensation method and 2.3% for the second-order compensator. Since the actuation quality affects the computed structural response, the peak displacements differed depending on the compensation method used, with a maximum disparity between the ATS system and the constant delay systems being 12%. The a_1 coefficient of the ATS compensator (which approximates the delay, since the a_0 coefficient remained close to unity) varied quite significantly, ranging from around 17ms to around 26ms, justifying the need for adaptive compensation. It was also noted that, with the viscous damper as the physical substructure, the delay was largest during large displacement oscillations (when the damper force was greatest) and reduced for smaller amplitude oscillations. As a final demonstration of the versatility of the system, the authors repeated some of the RTHS tests but with the proportional gain of the actuator's PID controller reduced from 20dB to 15dB which, as shown in the previous section, increases the delay. This led to a doubling or tripling of the NRMS errors when using the fixed delay methods (using the same coefficients as before the PID gain was changed) but a negligible increase in the error (just 0.1 percentage points) when using the ATS compensator.

Since then, the ATS compensator has been successfully implemented in more complex situations, such as the RTHS of a MDOF (three storey) combined steel MRF with DBF structure with a large scale MDOF physical substructure [85]. Here, the MRF and mass of the structure formed the numerical substructure while the DBF, fitted with a nonlinear viscous damper in each storey, formed the physical substructure with a scale factor of 0.6. This used three actuators, one for each floor level, each with its own ATS compensator. Similar testing has also been performed with the MRF forming part of either the numerical substructure or the physical substructure, allowing comparison of the different modelling approaches [84]. There was very close agreement between the two cases, and with numerical simulations, indicating good accuracy of the RTHS method and the substructuring procedure.

4.4. Proposed Modification to ATS Compensator

4.4.1. Advantages of Modified System

The computational efficiency of the numerical components of a RTHS setup is of vital importance since, for a given processor and integration timestep, there will be a fixed limit on the number of calculations and processor operations that can be performed within that timestep. If the computational demand exceeds the available processing power, then it will not be possible to perform the hybrid simulation in real-time. The ATS compensator has been demonstrated to be very effective at compensating for delay but its computational demand is high due to the size of the matrices which must be multiplied (which are large even after down-sampling) and the substantial amount of data which must be stored. Improved compensator efficiency will free up processing power and RAM which can be put to use in the modelling and/or integration of the numerical substructure. This can allow the complexity of the model to be increased and/or the size of the timestep to be reduced to improve stability and accuracy.

A modified version of the ATS compensator has therefore been developed which replicates the performance of the original ATS compensator but with a greatly reduced computational demand. Extensive testing (which will be presented shortly) shows the more computationally efficient Modified ATS (mATS) matches, or even slightly improves on, the delay compensation provided by the original ATS. This is achieved by making a modification to the cost function (Eq. 4-33) used to optimise the ATS coefficients which changes the fitting time-window from a rectangle (giving equal weighting to all of the previous q data points) to an exponentially decaying time-window (where the weighting of a data point decreases the further back in time it occurred). This allows the compensator equations to be formulated into a recurrence relationship where the fitting matrices and vectors are formed by updating the previous matrix/vector based on the most recent measurements, rather than performing the whole calculation from scratch at each timestep. With this new system, the matrices and vectors to be multiplied are reduced to size 3×3 and 3×1, respectively. The memory requirement is also reduced to a 3×3 matrix and 3×1 vector (i.e. 12 elements) from the previous timestep (rather than,

say, 4096 elements from the previous 1024 timesteps). Significantly, in the mATS, the computational demand becomes independent of the size of the effective time window, and no down-sampling is necessary as all previous values are carried forward but with a reduced weighting after each step.

4.4.2. Derivation of Modified ATS Equations

To derive the Modified ATS compensator, replace the cost function to be minimised (Eq. 4-33) by:

$$R_k = \sum_{i=1}^{q} \rho^{i-1} \left(u_{c,k-i} - u_{est,k-i} \right)^2 \qquad 4\text{-}39$$

which is the same as Eq. 4-33 except for the inclusion of a decay factor, ρ, where $0 < \rho \leq 1.0$. If ρ is set to 1.0 then the error function is the same as before but if $\rho < 1$ then the weighting applied to data points reduces over time. This is equivalent to altering the shape of the time-window over which data is fitted from a constant rectangular window to an exponentially decaying window, as shown in Figure 4.11 for a timestep, Δ, of 1ms. The smaller the value of ρ, the more the weighting is skewed in favour of more recent values, roughly equivalent to fitting over a shorter time-window.

As before, the values of the compensator coefficients which minimise R_k are obtained by solving the set of simultaneous equations given by $\frac{\partial R_k}{\partial a_{0,k}} = 0$, $\frac{\partial R_k}{\partial a_{1,k}} = 0$ and $\frac{\partial R_k}{\partial a_{2,k}} = 0$. Writing these out in matrix form gives:

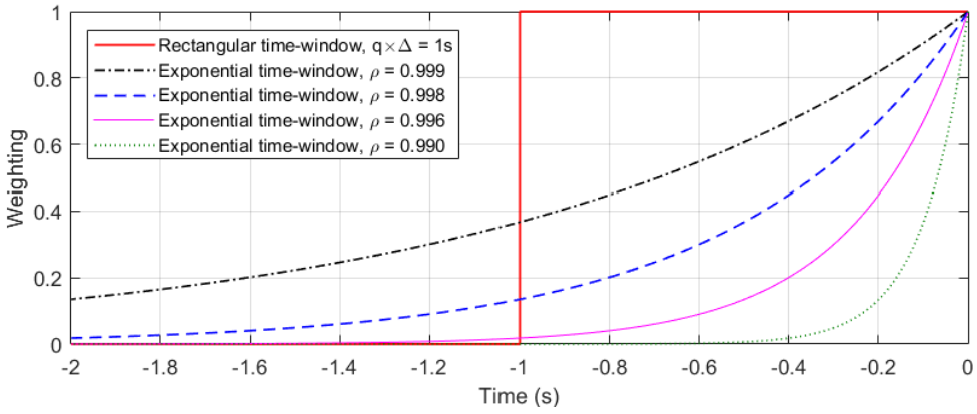

Figure 4.11 – Weighting given by rectangular time-window used in ATS compensator and exponential time-window used in mATS compensator for various decay factors, ρ, with a timestep of 1ms

$$\begin{bmatrix} x_{m,k-1} & \rho x_{m,k-2} & \rho^2 x_{m,k-3} & \cdots \\ \dot{x}_{m,k-1} & \rho \dot{x}_{m,k-2} & \rho^2 \dot{x}_{m,k-3} & \cdots \\ \ddot{x}_{m,k-1} & \rho \ddot{x}_{m,k-2} & \rho^2 \ddot{x}_{m,k-3} & \cdots \end{bmatrix} \begin{bmatrix} u_{c,k-1} \\ u_{c,k-2} \\ u_{c,k-3} \\ \vdots \end{bmatrix}$$

$$= \begin{bmatrix} x_{m,k-1} & \rho x_{m,k-2} & \rho^2 x_{m,k-3} & \cdots \\ \dot{x}_{m,k-1} & \rho \dot{x}_{m,k-2} & \rho^2 \dot{x}_{m,k-3} & \cdots \\ \ddot{x}_{m,k-1} & \rho \ddot{x}_{m,k-2} & \rho^2 \ddot{x}_{m,k-3} & \cdots \end{bmatrix} \begin{bmatrix} x_{m,k-1} & \dot{x}_{m,k-1} & \ddot{x}_{m,k-1} \\ x_{m,k-2} & \dot{x}_{m,k-2} & \ddot{x}_{m,k-2} \\ x_{m,k-3} & \dot{x}_{m,k-3} & \ddot{x}_{m,k-3} \\ \vdots & \vdots & \vdots \end{bmatrix} \begin{bmatrix} a_{0,k} \\ a_{1,k} \\ a_{2,k} \end{bmatrix} \quad \text{4-40(a)}$$

or
$$X_\rho^T \boldsymbol{U}_c = X_\rho^T X_m \boldsymbol{A}_k \quad \text{4-40(b)}$$

which is similar to Eq. 4-35 except for the inclusion of powers of ρ in the coefficients. Hence the compensator coefficients, $\boldsymbol{A}_k = \left[a_{0,k}, a_{1,k}, a_{2,k}\right]^T$, are given by:

$$\boldsymbol{A}_k = \left(X_\rho^T X_m\right)^{-1} X_\rho^T \boldsymbol{U}_c \quad \text{4-41}$$

The matrices X_ρ and X_m have dimension $q \times 3$, the vector $\boldsymbol{U}_c$ has dimension $q \times 1$, and the vector A_k has dimension 3×1. Now define the matrix, M_k, and vector, $\boldsymbol{W}_k$, to be:

$$M_k = (X_\rho^T X_m) \quad \text{4-42}$$

$$\boldsymbol{W}_k = X_\rho^T \boldsymbol{U}_c \quad \text{4-43}$$

so that Eq. 4-41 can be rewritten in the form:

$$\boldsymbol{A}_k = M_k^{-1} \boldsymbol{W}_k \quad \text{4-44}$$

Notice that M_k is always a 3×3 matrix and $\boldsymbol{W}_k$ is always a 3×1 vector, no matter what the value of q. Now, if q is not limited to a fixed value then the matrix M_k can be updated from the recurrence relation:

$$M_k = \rho M_{k-1} + \boldsymbol{x}_k \boldsymbol{x}_k^T \quad \text{4-45}$$

where $\boldsymbol{x}_k = [x_{m,k} \quad \dot{x}_{m,k} \quad \ddot{x}_{m,k}]^T$. While the vector, $\boldsymbol{W}_k$, can also be updated using:

$$\boldsymbol{W}_k = \rho \boldsymbol{W}_{k-1} + u_{c,k} \boldsymbol{x}_k \quad \text{4-46}$$

Note, M_k and $\boldsymbol{W}_k$ depend only on their values at the previous timestep $(k-1)$, the current measurement of the displacement and computed derivatives, and the current command signal. The computed mATS coefficients would be used in Eq. 4-36 to determine the command signal to send to the actuator controllers.

4.4.3. Implementation of the mATS Compensator

Figure 4.12(a) shows a block diagram of the mATS compensator while Figure 4.12(b) shows the implementation of the mATS matrix calculations described by Eqs. 4-44 - 4-46. Notice that the tapped delay blocks used in the original ATS compensator are no longer needed. The 'matrix calculations' subsystem takes only the values of x_m, $\dot{x}_m$, $\ddot{x}_m$ and u_c at the current timestep as its inputs, while the 'memory' blocks implement a delay of one timestep to store the values of M_k and $\boldsymbol{W}_k$ from the previous timestep only. This system was programmed in Simulink® and compiled to the dSpace® board along with the numerical substructure.

Figure 4.12(a) shows how the target displacement, x_t, coming from the numerical substructure is differentiated once to obtain the target velocity, $\dot{x}_t$, and then again to obtain the target acceleration, $\ddot{x}_t$. This is done using the first-order finite difference approximation given by Eq. 4-38. These are used in the compensator equation (Eq. 4-36), along with the fitting coefficients calculated by the matrix calculations, to produce the command output, u_c. The target displacement, x_t, comes directly from the numerical substructure which is implemented on the same processor and is therefore not affected by signal noise. Even though there will be measurement noise on the measured force signal forming the input to the numerical substructure, the dynamics of the structure being simulated act as a filter, so the output x_t is smooth. Differentiating this signal, therefore, causes no problems.

Unfortunately, the same is not true of the measured displacement, x_m, which will inevitably contain signal noise because it comes from the analogue voltage generated by the LVDT which has then been converted to a digital signal by the ADC. As for x_t, x_m must be differentiated to obtain $\dot{x}_m$ and $\ddot{x}_m$ for use in the coefficient fitting in Eqs. 4-44 - 4-46. However, errors due to high frequency measurement noise are amplified when the signal is differentiated using the finite difference method, leading to very large errors in $\dot{x}_m$ and $\ddot{x}_m$ which would prevent the mATS coefficients from being fitted effectively. A low-pass filter is therefore applied to x_m to remove high frequency noise prior to differentiation. This

introduces a phase lag, but the effect is acceptably small given the mATS coefficient fitting is already being performed over a time-window of previous values.

As mentioned in Section 3.5.5, no filtering is applied to the measured signals during data acquisition due to the phase lag it would introduce, and it will be seen in Section 4.5 that the unfiltered x_m signal is also required in the final system. Digital low-pass filtering is therefore applied to x_m within the mATS compensator. A digital sixth order Butterworth filter is used with a cut-off frequency of 20Hz – low enough to remove the effects of random noise but without affecting the frequency components of interest. The calculated command, u_c, is also fed back into the 'matrix calculations' subsystem for use in Eq. 4-46. To account for the phase lag introduced by filtering of x_m, this u_c signal is passed through an identical low-pass digital filter so that the two inputs are synchronised in time.

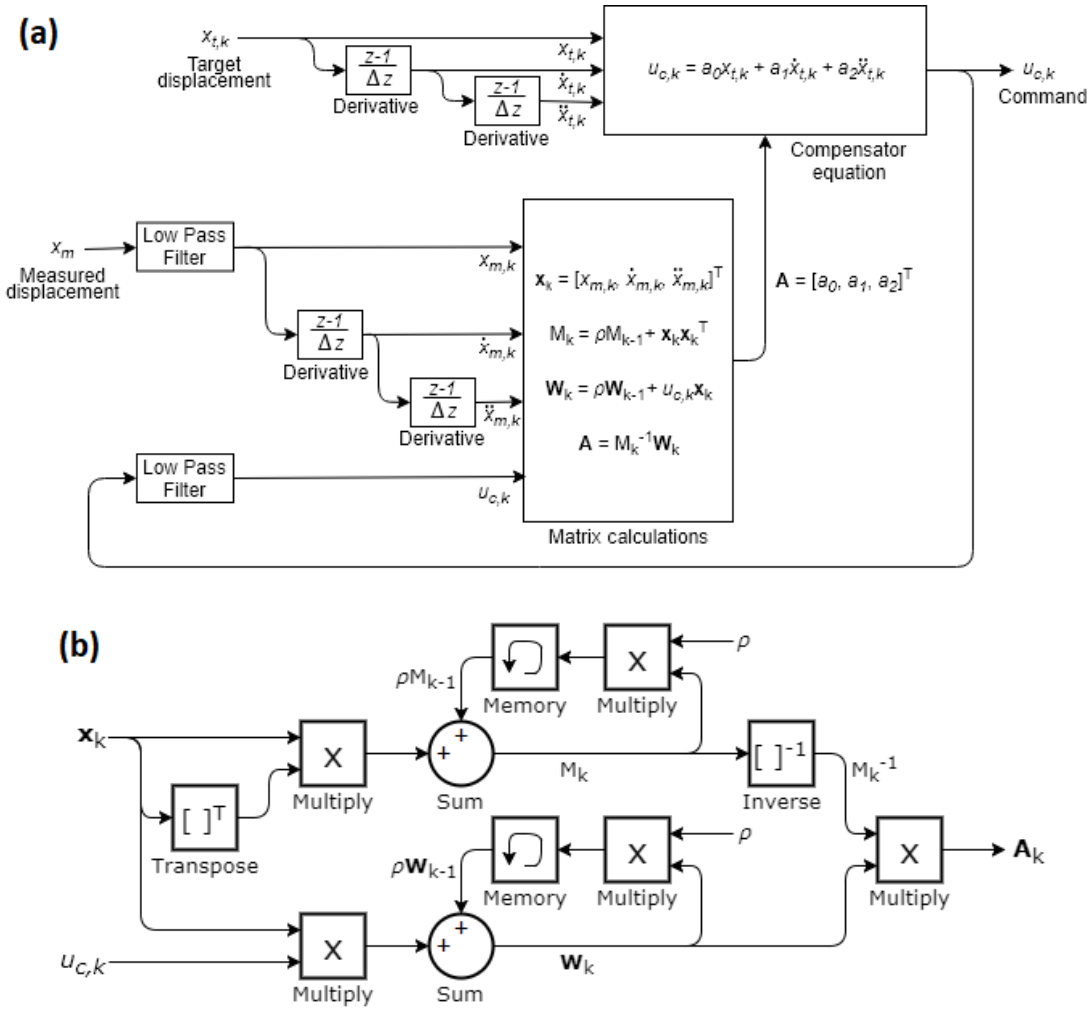

Figure 4.12 – Block diagram of mATS compensator: (a) overall system; (b) implementation of matrix calculations (Eqs. 4-44 - 4-46)

4.4.4. Effective Time Window

In the modified ATS compensator, the user must specify the decay factor, ρ, rather than the time window size, q. There is no longer a sharp cut off to the fitting window, instead all past values are included but their effect on the fitting process decreases with each timestep that passes, eventually becoming vanishingly small, as shown in Figure 4.11. The smaller the value of ρ, the more rapidly the effect of previous data points diminishes, i.e. the more heavily the fit will be weighted towards more recent values. If ρ were set to one, then all past values would be weighted equally, and the compensator would calculate coefficients corresponding to the mean delay and amplitude error over the whole test so far. Decreasing ρ in the modified compensator is equivalent to decreasing q in the original. However, the choice of a suitable value of ρ is less obvious than for q which represents a clear physical quantity: time. To facilitate the selection of values of ρ in the modified ATS system, an *effective time window*, q_{eff}, is introduced. This is defined by the centroid (geometric centre) of the area under the exponential time-window, given by:

$$q_{eff} = -\frac{1}{\ln \rho} \qquad 4\text{-}47$$

where $\ln()$ is the natural logarithm and q_{eff} has units of timesteps. This is also the number of timesteps taken for the weighting on the past data to have reduced to $1/e \approx 0.37$ (or the 'e-folding time'). Table 4.2 gives examples of the ρ factors corresponding to some likely values of q_{eff}. If the timestep is changed, for example, q_{eff} simply needs to be divided by the ratio of the new timestep to the old one to give the same time-widow shape with the new timestep, making q_{eff} more practical to work with than ρ.

Effective time-window, q_{eff} (timesteps)	2000	1000	500	200	100	50	25
Decay factor, ρ	0.9995	0.9990	0.9980	0.9950	0.9900	0.9802	0.9608

Table 4.2 – Decay factors corresponding to various effective time-windows

4.4.5. Initialisation of mATS compensator

As for the ATS compensator, it is necessary to hold the compensator coefficients at their initial values until sufficient displacement has occurred. Activating the updating of the coefficients too early was observed to cause an initial spike in the mATS coefficients due to ill-conditioning of the fitting matrix. The longer the effective time-window, q_{eff}, the longer it takes the values of the coefficients to settle to their true values. To avoid this behaviour, the compensator was started q_{eff} timesteps after the start of the motion, taken as when x_t first exceeds $\pm$0.1mm. This ensured there was sufficient data for a good fit to be achieved before the compensator takes over. This meant that the shorter q_{eff}, the sooner the adaptive compensation could start, which is one reason for preferring a value of q_{eff} at the lower end of the acceptable range. It was not found to be necessary to deactivate updating of the coefficients during the test as the displacements did not reach small enough values for sufficient lengths of time for problems to occur due to the fitting matrix becoming ill-conditioned. Only after the ground motion had ceased, if the simulation was left for the displacements to decay to very small values, was this seen, by which point the response is no longer of interest.

4.5. Compensating for Compliance of the Test Rig

4.5.1. The Issue of Rig Flexibility

While the test rig is designed to be significantly stiffer than the physical substructure, there will always be some deformation of the components of the rig when loaded by the actuators (e.g. in the piston shafts, the pinned joints, the cross-beam and the struts connecting the actuators to the reaction wall). This leads to a disparity between the measured displacement of the actuators, x_m, and the deformation of the physical substructure, x_{enc}, measured by the encoder. The rig deflection, d_{rig}, is given by:

$$d_{rig} = x_m - x_{enc} \tag{4-48}$$

where x_m is taken as the mean of the displacements measured in each of the two actuators:

$$x_m = (x_{m1} + x_{m2})/2 \tag{4-49}$$

since the two actuators operate in parallel either side of the physical device. The aim will be to control the actuator displacements so that $x_{m1} = x_{m2}$. Figure 4.13 shows the disparity between x_{enc} and x_m for a cyclic test where, to achieve a displacement of 2.5mm across the BRB, the actuators have had to move by 3.3mm indicating that the rig is a little over three times the pre-yield stiffness of the BRB. In many cases in the literature, rig flexure is not specifically addressed [84], the implicit assumption being that the relative stiffness of the rig is sufficient for d_{rig} to be negligible. However, for the rig in this project, the amplitude error due to rig flexure is not negligible. This is perhaps exacerbated by the configuration of the rig, shown in Figure 3.2, which uses two actuators in parallel requiring the use of a cross-beam. This was necessary to achieve the required forces with the available actuators but introduces more flexibility. A system was therefore developed to compensate for this issue by increasing the displacement of the actuators by d_{rig}. Figure 4.14 plots the total actuator force, F_m, against d_{rig} during cyclic testing, showing that the rig remains in its elastic range with approximately linear stiffness. An alternative method of estimating d_{rig} is therefore to divide F_m by an estimate of the rig stiffness. However, since the measurement noise on the F_m signal is comparable to that on the x_m signal, this approximation gives no benefit over the direct measurement used in Eq. 4-48.

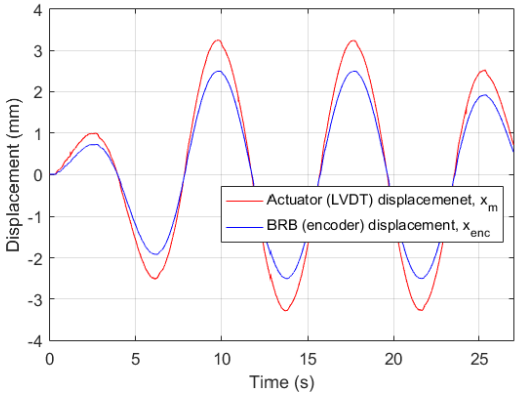

Figure 4.13 – Disparity between actuator and BRB displacements due to rig flexure

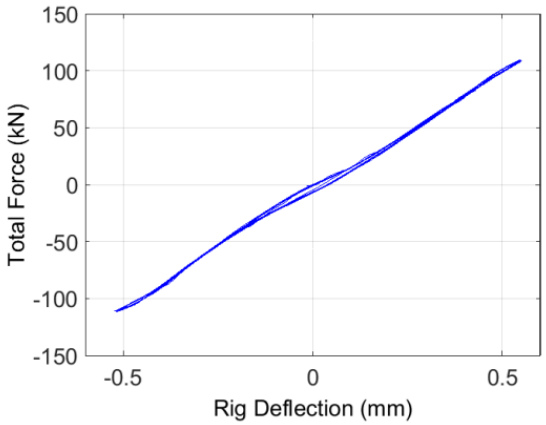

Figure 4.14 – Force-deflection response of test rig

4.5.2. Method of Correcting for Rig Flexibility

Dong et al. [84] compensated for rig flexure by replacing the feedback to the PID controller with the displacement of the physical substructure, x_{enc}, measured directly by a displacement encoder, rather than the actuator displacement, x_m, measured by the LVDT within the actuator. In turn, the encoder displacement was used as the measured feedback to the ATS compensator, thus removing d_{rig} from the control loop. This is difficult to implement directly with the laboratory's Instron® controller as the encoder feedback is in the form of a digital differential TTL signal which would have to be converted to an analogue signal before it could be fed into the Instron® controller. However, since the PID operates on the control error, e, between the command, u_c, and the measured displacement, x_m, it can be seen that subtracting d_{rig} from the feedback signal (equivalent to replacing x_m with x_{enc}) is exactly equivalent to adding d_{rig} to the command signal:

$$e = u_c - x_{enc} = u_c - (x_m - d_{rig}) = (u_c + d_{rig}) - x_m \qquad 4\text{-}50$$

Hence, this more practical implementation was used with d_{rig} being added to the command, u_c, from the mATS compensator before it is sent to the PID via the DAC. While this modification is implemented outside of the inner control loop, Eq. 4-50 shows that the effect is mathematically identical to removing d_{rig} from the inner control loop so that the PID works to control x_{enc} rather than x_m.

4.5.3. Accounting for Two Actuator System

There is an additional complication in the case of the test rig used here due to the use of two actuators in parallel. While Dong et al. [84] used multiple actuators, this was with a MDOF physical substructure, so that each actuator operated on an individual DOF and therefore had its own encoder measurement to use as feedback. The test rig in this project uses two actuators working in parallel, giving the actuation system two DOFs, x_{m1} and x_{m2}, while the physical substructure has just one, x_{enc}. This means that simply replacing the feedback to the PIDs with x_{enc} instead of x_{m1} or x_{m2} would leave an uncontrolled DOF (rotation of the cross-beam) since a multitude of combinations of x_{m1} and x_{m2} can result in the same x_{enc}. It is therefore necessary to constrain out this additional DOF. Note that this only becomes an issue once rig flexibility compensation is included – without this, it would simply be necessary to send the same target, x_t, as the input to the delay compensator for each actuator.

This is achieved by adding the calculated rig deflection, d_{rig}, to the command to both PID controllers (u_{c1} and u_{c2}), while the PID feedback remains the LVDT-measured displacement of the corresponding actuator (x_{m1} or x_{m2}). The effect of this can be seen by considering the control error signals (e_1 and e_2) generated in each PID controller:

$$e_1 = \left(u_{c1} + d_{rig}\right) - x_{m1} \text{ and } e_2 = \left(u_{c2} + d_{rig}\right) - x_{m2} \tag{4-51}$$

substituting for d_{rig} from Eqs. 4-48 and 4-49 shows that this is equivalent to:

$$e_1 = \left(u_{c1} + \left(\frac{x_{m1} + x_{m2}}{2} - x_{enc}\right)\right) - x_{m1} = u_{c1} - \left(x_{enc} + \frac{x_{m1} - x_{m2}}{2}\right) \tag{4-52(a)}$$

$$e_2 = \left(u_{c2} + \left(\frac{x_{m1} + x_{m2}}{2} - x_{enc}\right)\right) - x_{m2} = u_{c2} - \left(x_{enc} + \frac{x_{m2} - x_{m1}}{2}\right) \tag{4-52(b)}$$

This shows that when $x_{m1} = x_{m2}$, the measured feedback is simply x_{enc}, giving control of the physical substructure displacement, as desired. However, if a discrepancy arises between the displacements in the two actuators, the error signals to both actuators are modified in such a way as to correct for the discrepancy. For example, if x_{m1} were greater than x_{m2} then e_1 would decrease, reducing the

displacement in the first actuator, while e_2 would rise, increasing the displacement in the second actuator, bringing the two back into sync.

This method is effective at removing the amplitude errors due to rig flexure. Stability is maintained since a change of x_m in a given direction will cause a change in x_{enc} in the same direction. The scale factor between the two will depend on the stiffness of the physical substructure relative to that of the rig, which will vary due to nonlinearity in the device while the rig remains linear. Instability would only be likely if the physical substructure were much stiffer than the rig, since this would mean that large rig deflections (which are excluded from the feedback loop) could occur with only small displacements being measured in the physical substructure which are used as feedback. This could lead to there being insufficient PID feedback to maintain control, leading to oscillations in the actuation system. In general, all rigs will be designed to be stiffer than the physical substructure. However, a property of the BRB tested in this project was a momentarily extremely high tangent stiffness when first extended or after a change in direction of motion. This is attributed to friction transferring axial force from the steel to the concrete. The stiffness quickly drops off to smaller levels once sliding begins but could cause oscillations to develop at very small displacements due to the rig being able to flex with minimal displacement occurring across the device. This only occurs for extremely small displacements (less than around 0.04mm), so is only an issue at the start of the test (when x_t is zero) and at the end of the test when the motion has decayed away to almost zero. Oscillations will develop under these conditions, but will not exceed around 0.04mm since, once they do, sufficient movement would occur in the physical substructure for control to be regained. At the end of the test, this is not a problem because such small displacements are not of interest – the structural motion can be assumed to have ceased by this point. Oscillations can be prevented before the start of the test by only starting the flexibility compensation once the test begins by holding d_{rig} at zero until the earthquake motion starts (although even if this wasn't done, such small oscillations would be unlikely to affect the outcome of the test). The tests in this project all start at zero initial conditions, with zero initial force, so d_{rig} will initially be zero producing no discontinuity when the rig flexibility compensation is switched on.

4.5.4. Combining Rig Flexibility Correction with the Delay Compensation

The effect of adding the rig deflection, d_{rig}, to the command input of the PID controllers is to give the inner control loop direct control over the displacement of the physical specimen, rather than just the displacements of the actuators. It then becomes necessary to modify the feedback to the delay compensator commensurately to maintain consistency between the inner and outer control loops. The target displacement, x_t, which forms the input to the delay compensator is the displacement which the numerical substructure has calculated should be applied across the physical specimen, so the measured feedback signal should be the displacement across the physical substructure (i.e. excluding the rig deflection). With a single actuator setup this would be achieved by simply using x_{enc} as the displacement feedback to the mATS compensator (in place of x_m in Figure 4.12). With two actuators, each with their own delay compensator, feeding back the same displacement, x_{enc}, to both compensators would result in them both performing the same calculations and producing the same command signal output which would effectively be attempting to compensate for the mean delay and amplitude error between the two actuators, equivalent to using a single delay compensator. This may be acceptable if both actuators have identical specifications and produce a sufficiently similar response, and provided the system has sufficient tolerance for the discrepancy between actuator displacements which may occur. The connections of the actuators and the BRB to the cross-beam are pin-jointed to allow some difference between x_{m1} and x_{m2} to be tolerated through rotation of the cross-beam. However, a preferable system is to provide separate delay compensation for each actuator to allow for possible differences in the characteristics of each. This is achieved by subtracting d_{rig} from the measured actuator displacement feedback to each mATS compensator. This modifies the feedback to each delay compensator to be x^*_{m1} and x^*_{m2}, in place of x_{m1} and x_{m2}, given by:

$$x^*_{m1} = x_{m1} - d_{rig} \text{ and } x^*_{m2} = x_{m2} - d_{rig} \quad \text{4-53}$$

Substituting for d_{rig} from Eqs. 4-48 and 4-49 shows that these feedback signals are equivalent to:

$$x^*_{m1} = x_{enc} + \frac{x_{m1}-x_{m2}}{2} \text{ and } x^*_{m2} = x_{enc} + \frac{x_{m2}-x_{m1}}{2} \quad \text{4-54}$$

As was the case for the inner loop controller, if $x_{m1} = x_{m2}$ then the feedback to both compensators is simply x_{enc} whereas, if they differ, the feedback signal to one compensator will increase while that to the other decreases in such a way as to stabilise the system. The implementation of the combined control system, compensating for delay as well as correcting for rig flexibility, is shown in Figure 4.15. Essentially, for each actuator, the calculated rig deflection is subtracted from the measured actuator displacement to form the measured displacement feedback to the mATS compensator for that actuator. The calculated rig deflection is then added to the command generated by each mATS compensator to produce the input command to the PID controller for each actuator.

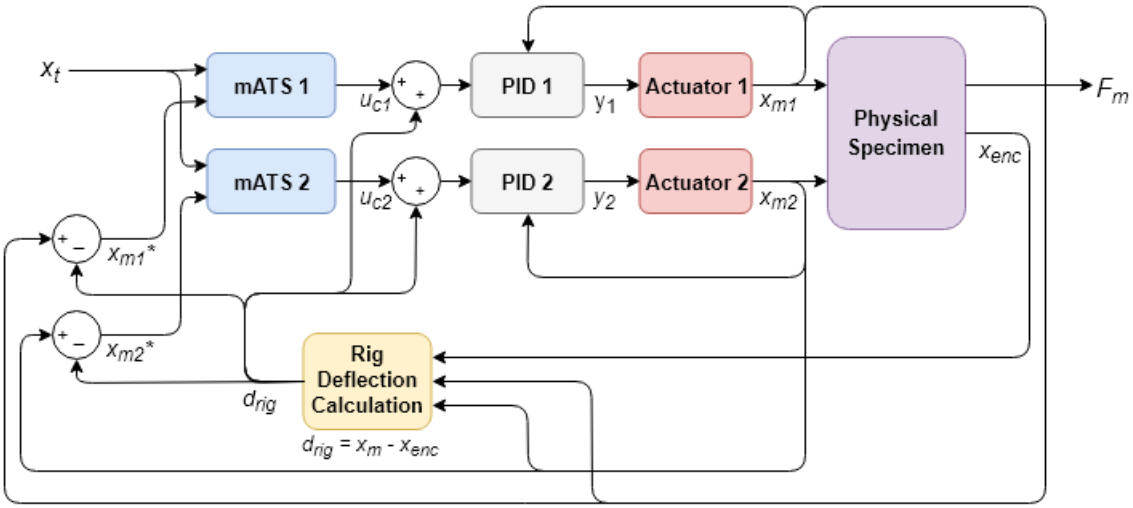

Figure 4.15 – Actuator control system combining delay compensation and correction for rig flexibility

4.5.5. Rig Flexibility Correction Considerations

The control system above is formulated so that both the inner and outer control loops are effectively working on the displacement of the physical specimen rather than the displacement of the actuators, but with the necessary modifications to constrain the actuator displacements to be equal. Other potential arrangements that were considered are briefly presented below to show why they are not feasible.

To achieve x_t across the physical substructure, the actuators must displace by $x_t + d_{rig}$. A simple idea would therefore be to set the target displacement input to each delay compensator to $x_t + d_{rig}$ whilst leaving the measured displacement feedback as the actuator displacements, x_{m1} and x_{m2} – hence the

whole control system would operate on the actuator displacement rather than the deformation of the physical specimen. The mATS outputs, $u_{c,1}$ and $u_{c,2}$, would then be fed straight into the PID controllers. Each PID controller and each delay compensator would be acting on the feedback, x_{m1} or x_{m2}, of its own actuator so there would be no issue with constraining the actuator displacements to be the same as the two controllers would act independently. However, the problem with this system is that d_{rig} is calculated from measured signals from the LVDTs and encoders, as per Eq. 4-48, and therefore contains measurement noise. The mATS compensator, like most delay compensators, requires that the target displacement input is a clean signal since it must be differentiated to obtain the target velocity and target acceleration, as shown in Figure 4.12(a). This is true of x_t as it comes straight from the numerical substructure, as described in Section 4.4.3. However, the error due to any noise introduced by adding d_{rig} would be amplified when it is differentiated using the finite difference method, degrading the accuracy of the computed velocity and acceleration. The mATS output command, u_c, computed from these signals would therefore have significant errors and rapid variation causing the compensator to become unstable. Filtering of the target displacement input to the delay compensator to remove the noise is unacceptable since it would introduce a lag, defeating the purpose of the compensator. Therefore, this is not a viable approach.

Another method could be proposed based on the observation that the rig deflection manifests itself as an amplitude error, and the mATS compensator is designed to compensate for amplitude errors, as quantified by A in Eq. 4-29. The feedback to the mATS compensator could therefore be set as the measured displacement, x_{m1}^* or x_{m2}^*, across the physical specimen, as calculated in Eq. 4-53, to ensure the actuator displacements are constrained to be the same, while the target input to the compensator is kept as x_t and the PID controller in the inner loop uses the measured actuator displacement, x_{m1} or x_{m2}, as its feedback without modification. Unlike the target displacement input of the delay compensator, the measured displacement feedback contains measurement noise and is therefore filtered, as shown in Figure 4.12(a). There is therefore no problem caused by noise in d_{rig} when it is subtracted from the displacement feedback. The discrepancy between x_m and x_{enc} caused by rig

deflection would therefore be treated as an amplitude error which is compensated for by the mATS coefficients. For example, the coefficient a_0 would be expected to take a value of approximately x_m/x_{enc} to increase the actuator displacement by the required amount. If both the test rig and physical specimen behaved linearly (had constant stiffness) then the amplitude ratio, A, caused by d_{rig} would be constant – providing the test began with zero force so that $d_{rig} = 0$ when $x_{enc} = 0$. The rig behaves almost linearly (Figure 4.14), as does the BRB when in its elastic range ($\pm$2.5mm) except for a small amount of hysteresis due to friction. This approach therefore works reasonably well while the BRB is in its elastic range, although it cannot respond rapidly to the stiff behaviour immediately after direction reversal. However, yielding causes the secant stiffness of the BRB to vary so that A changes with displacement. A shifted equilibrium position, so that d_{rig} was not zero when x_{enc} equalled zero, would also cause A to vary with displacement, even within the elastic range. The correction provided by the mATS compensator cannot adapt to this change quickly enough because the mATS coefficients are based on a fit over a weighted average of previous timesteps so, when d_{rig} varies continuously, the correction will always be outdated leading to a delay which, again, defeats the purpose of the system.

A final possibility considered was a system like the chosen system shown in Figure 4.15 but with the mATS output, u_c, scaled by a factor rather than having d_{rig} added to it. An appropriate factor to provide compatibility between the outer control loop (operating on the displacement of the physical specimen) and the inner control loop (operating on the displacement of the actuators) might be:

$$\frac{x_m}{x_{enc}} \left(= 1 + \frac{d_{rig}}{x_{enc}}\right) \qquad 4\text{-}55$$

Clearly there is an issue with this factor becoming undefined when x_{enc} approaches zero. With a modification to prevent numerical issues when x_{enc} became very small (setting a minimum magnitude for the denominator in Eq. 4-55), this system was feasible for tests in the elastic range of the BRB and allowed stable RTHS testing to be performed. It was able to give a good fit between x_t and x_{enc} over much of the test, but the two will always diverge at zero crossings due to the factor becoming ill-defined. However, this ad hoc approach breaks down once yielding occurs so that d_{rig} and x_{enc} no

longer pass through zero at the same time. Even for hybrid tests within the elastic range of the BRB, this system was significantly outperformed by the chosen system described earlier. The chosen system not only provides superior actuation quality but also has the advantages of requiring no tuning of empirical coefficients making it resilient to changes in testing conditions, and of being simple to implement on the digital processor with minimal computational requirements.

4.5.6. Measuring Actuation Quality

When introducing delay compensation above, no distinction was made between the actuator displacement, x_m, and the deformation of the physical substructure, x_{enc}, as the issue of rig flexibility had not yet been introduced. With the BRB installed and rig flexibility compensation included, the measure of performance of the control system is how closely x_{enc} (rather than x_m) matches the target, x_t. The delay and amplitude error are therefore measured between x_t and x_{enc}, since these are the errors directly affecting the hybrid simulation, and the definition of NRMS error from Eq. 4-12 becomes:

$$E_{NRMS} = \sqrt{\frac{\sum_{i=0}^{N-1} \left(x_{t,i} - x_{enc,i}\right)^2}{\sum_{i=0}^{N-1} \left(x_{t,i} - x_{t,mean}\right)^2}} \qquad 4\text{-}56$$

4.6. Small Displacement Open-Loop Testing

4.6.1. Predefined Displacement Testing

At this stage, the BRB displacements were kept small – below the yield displacement of 2.5mm. This was to maximise the repeatability of the tests since yielding permanently alters the BRB, affecting future tests, and to allow a large number of tests to be performed without fatiguing the BRB. The

system was tested by applying a 10s predefined cyclic displacement of 2mm amplitude across the BRB at frequencies of 0.5Hz, 2Hz and 5Hz. This was repeated for various values of effective time-window, q_{eff}, with the mATS compensator and for various values of time-window, q, with the ATS compensator. The mean value of the compensator coefficients and the resulting NRMS errors between the target and achieved displacements of the BRB are listed in Table 4.3 for the mATS system and in Table 4.4 for the original ATS system. For consistency, the NRMS error was taken between 2s and 10s to exclude the effects of initialisation of the delay compensator, giving a comparison of the 'steady-state' performance of the compensators. The maximum time window which could be achieved with the ATS was 450ms, down-sampled by a factor of 9, due to the computational demands of managing the large amount of stored data. The NRMS errors from Table 4.3 and Table 4.4 are also plotted in Figure 4.16. Full results will be given for the 0.5Hz and 5Hz tests with $q_{eff} = 200\text{ms}$ in Sections 4.6.5 and 4.6.6, respectively, including the displacement responses (Figure 4.21 and Figure 4.25) showing the closely matched target and achieved displacements of the BRB along with the actuator displacement and command signal.

Comparable performance is achieved by the mATS compensator over a wide range of effective time windows, with minimal difference in performance between 100ms and 1000ms, while the errors grow for time windows below around 100ms. It gives similar performance to the ATS compensator, and may give a slight improvement, which could be attributed to there being no down-sampling in the mATS due to new time window shape and/or due to the increased weighting given to the most recent measured data. Note that the difference in NRMS errors between the tests at different frequencies isn't necessarily significant, one would expect higher NRMS error at higher frequencies since the NRMS error measures the difference between the target and achieved displacements, so a given delay, for example, would result in a larger difference between these displacements at any given point in time. For comparison, the NRMS errors without delay compensation were 3.19%, 13.48% and 36.63% at 0.5Hz, 2Hz and 5Hz, respectively. Hence the values with delay compensation of 0.29%, 1.00% and 2.27% (for $q_{eff} = 200\text{ms}$) represent a very significant improvement in accuracy.

f (Hz)	q_{eff} (ms)	ρ_{ATS}	$NRMS$ (%)	$a_{0,mean}$	$a_{1,mean}$ (ms)	$a_{2,mean}$ (ms^2)
0.5	1000	0.9990	0.2973	1.0025	11.076	112.24
	200	0.9950	0.2970	1.0029	10.846	112.78
	100	0.9900	0.2958	1.0030	10.798	107.40
	50	0.9802	0.3174	1.0027	10.542	82.196
	25	0.9608	0.3871	1.0028	10.529	68.617
2	1000	0.9990	0.9637	1.0043	11.335	93.212
	200	0.9950	0.9989	1.0051	11.336	98.826
	100	0.9900	1.0748	1.0047	11.433	96.742
	50	0.9802	1.1981	1.0023	11.461	80.393
	25	0.9608	1.4225	0.9990	11.424	60.928
5	1000	0.9990	2.1924	1.0243	11.559	94.118
	200	0.9950	2.2702	1.0186	11.581	88.465
	100	0.9900	2.3324	1.0104	11.524	80.645
	50	0.9802	2.5717	0.9917	11.609	62.232
	25	0.9608	3.4260	0.9814	11.551	54.394

Table 4.3 – Results of 2mm cyclic tests using mATS compensator

f (Hz)	q_{eff} (ms)	$NRMS$ (%)	$a_{0,mean}$	$a_{1,mean}$ (ms)	$a_{2,mean}$ (ms^2)
0.5	450	0.3405	1.0026	11.202	120.93
	200	0.3289	1.0026	11.061	97.556
	100	0.3921	1.0024	10.626	67.982
	50	0.6503	1.0051	8.739	56.043
	25	1.4359	0.9919	5.801	39.581
2	450	1.0566	1.0022	11.621	91.749
	200	1.1497	1.0026	11.846	92.465
	100	1.7640	0.9991	11.599	55.362
	50	2.9318	0.9986	10.656	52.223
	25	4.5871	0.9950	9.4547	45.544
5	450	2.4697	1.0096	11.877	87.064
	200	2.4333	1.0135	11.984	91.762
	100	2.4393	1.0170	11.720	92.284
	50	3.8175	0.9439	11.645	27.497
	25	5.4590	0.9455	11.357	36.442

Table 4.4 – Results of 2mm cyclic tests using ATS compensator

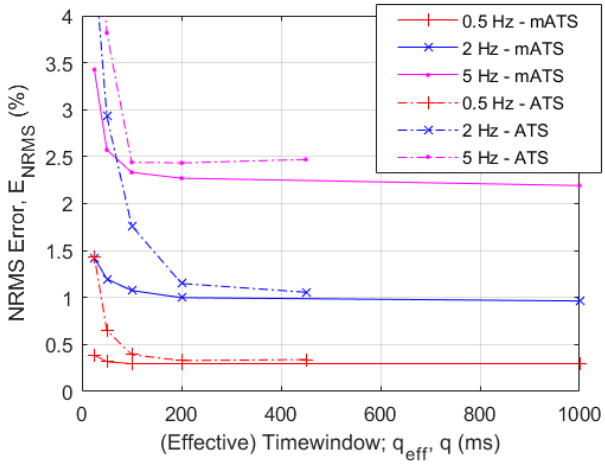

Figure 4.16 – NRMS errors in 2mm cyclic tests (between 2s and 10s)

4.6.2. Effect of Time Window on Compensator Coefficients

Figure 4.17 to Figure 4.19 show the coefficients of the mATS compensator (a_0, a_1 and a_2, respectively) for tests at 2Hz with effective mATS time windows, q_{eff}, of 1000ms and 25ms, demonstrating how the size of the effective time window affects the variability of the coefficients. The longer the effective time window, the lower the variability of the coefficients, since the averages are taken over a longer period. Attempting to fit to too small a time-window can lead to excessive fluctuations in the coefficients due to over-fitting to the most recent measurements, causing a reduction in performance. Fitting over too large a time window limits the rate at which the compensator coefficients can be updated in response to changes in the delay and amplitude error. The choice of a suitable value of q_{eff} is therefore a compromise and the optimal value is likely to be linked to the rate at which the system properties vary, which in turn depends on the dominant frequencies of oscillation in the response of the simulated system.

4.6.3. Control of Actuator Displacements

A key requirement of the control system is that it constrains the displacements, x_{m1} and x_{m2}, of the two actuators to be the same. As an example, Figure 4.20 shows the displacement of both actuators during a 0.5Hz cyclic test. Except for signal noise, they are identical, and the same behaviour is found in all tests. Hence the effectiveness of the system described in Section 4.5.3 at constraining the actuator displacements to be the same is verified. For clarity, therefore, only the mean values of the measured displacements, $x_m = (x_{m1} + x_{m2})/2$, and command signals, $u_c = (u_{c1} + u_{c2})/2$, of the two actuators will be plotted in the figures.

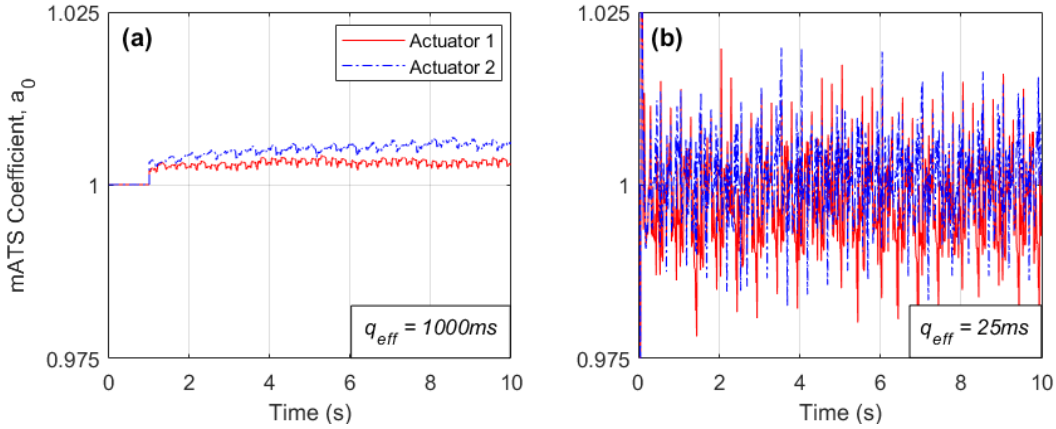

Figure 4.17 – Coefficient a_0 of mATS compensators during 2Hz cyclic tests for (a) $q_{eff} = 1000ms$, and (b) $q_{eff} = 25$ms

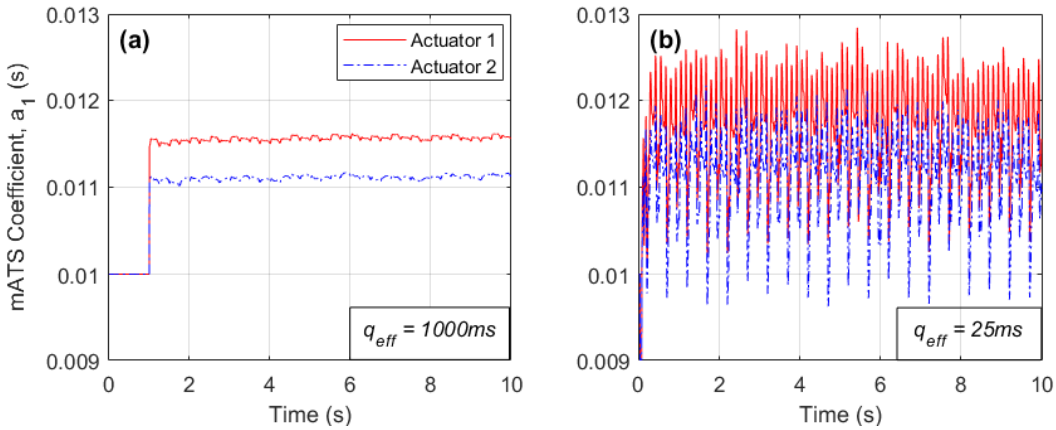

Figure 4.18 – Coefficient a_1 of mATS compensators during 2Hz cyclic tests for (a) $q_{eff} = 1000$ms, and (b) $q_{eff} = 25$ms

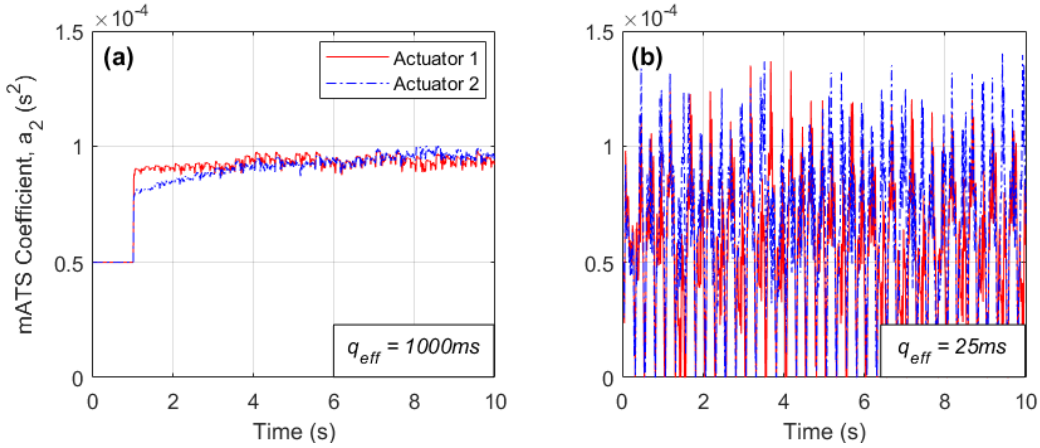

Figure 4.19 – Coefficient a_2 of mATS compensators during 2Hz cyclic tests for (a) $q_{eff} = 1000$ms, and (b) $q_{eff} = 25$ms

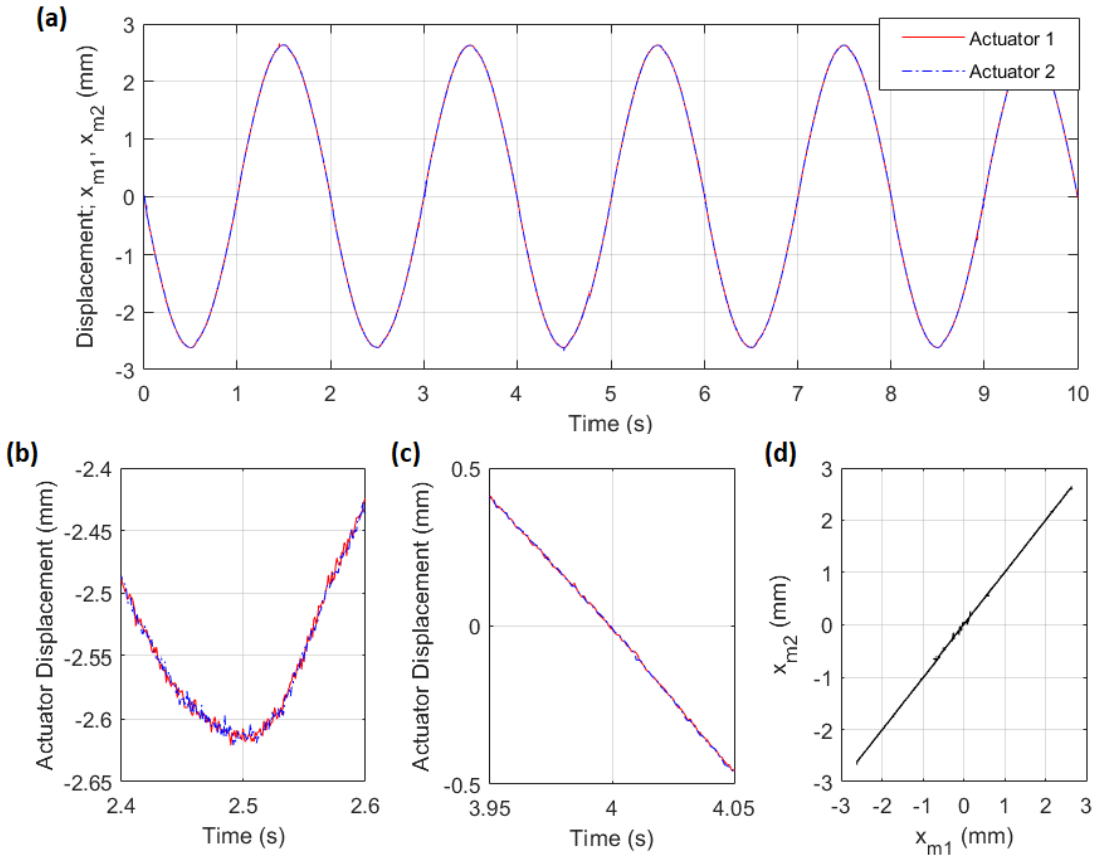

Figure 4.20 – Actuator Displacement during 0.5Hz cyclic test: (a) full test, (b) close-up of peak displacement, (c) close-up of displacement at zero-crossing, and (d) relationship between actuator displacements

4.6.4. Sample Open-Loop Test Results

The displacement responses and mATS coefficients for tests at 0.5Hz and 5Hz are presented in the following sections as representative examples from the set of cyclic tests from Table 4.3. This is followed by the results from a test with a predefined displacement representing a more realistic displacement pattern for a BRB installed in a multi-storey structure subjected to a ground motion, which therefore contains components at multiple frequencies. All three cases used the mATS compensator with an effective time window, q_{eff}, of 200ms – that is, a decay factor, ρ, of 0.995. The initial values and limits applied to the mATS coefficients are listed in Table 4.5. These were kept the same throughout the testing, except for the initial values of a_1 and a_2 being improved to 11ms and 60.5ms^2, respectively, in some later tests. Having selected initial values and limits for the coefficients a_0 and a_1 based on the amplitude error and delay observed in previous tests, appropriate values for

the initial value and limits of a_2 can be obtained using 4-31(b). The maximum and minimum limits were set to allow a large range and weren't actually reached in the tests. This is desirable as it shows that the compensator does not rely on limits to ensure the stability of the compensator coefficients. Similarly, the rate limits were set very high (at least 3 times the values used by Chae et al. [12]) so that they were rarely activated during the hybrid simulations. If excessive variability of the mATS coefficients were a problem, it would probably be preferable to address this by increasing q_{eff} rather than through rate limits. The cut-off frequency of the filter applied to the mATS feedback signals was 20Hz, significantly higher than the frequencies dominating the response in the tests, but low enough to prevent noise from causing instability of the mATS coefficients.

	a_0	a_1	a_2
Initial value	1.0	0.01s	0.00005s^2
Minimum value	0.75	0.04s	0.0008s^2
Maximum value	1.15	0.0s	0.0s^2
Maximum rate of change	$\pm$6/s	$\pm$0.24s/s	$\pm$0.0048s^2/s

Table 4.5 – Limits on coefficients of mATS compensator

4.6.5. Open-Loop Cyclic Test at 0.5Hz

Figure 4.21 shows the displacement across the BRB, x_{enc}, produced in response to a prescribed target displacement, x_t, consisting of a sine wave with a frequency of 0.5Hz and an amplitude of 2mm. It also shows the mean of the command signals, u_c, produced by the mATS compensators, the mean of the command signals corrected for rig deflection, $u_c + d_{rig}$, sent to the PID controller, and the mean of the measured actuator displacements, x_m, which result. There is almost perfect agreement between x_{enc} and x_t over almost the whole test so that the two lines are almost indistinguishable, despite significant rig deflection requiring the actuators to displace around 30% more than the BRB. Figure 4.22 plots the error between these two values which remains small throughout the test, giving an NRMS error of 0.297% between time 2s and 10s. The only location where a noticeable disparity develops is for a very short time immediately after a peak, when the direction of motion has just changed. After the reversal in direction of x_t, x_{enc} remains stationary for a moment before starting to move in the

new direction and catches up with x_t within about 0.05s. This generates a momentary spike in the error shown in Figure 4.22. The cause of this effect can be seen from the plot of measured force, F_m, against displacement, x_{enc}, for the BRB, shown in Figure 4.23. It shows that, while the behaviour is close to linear since the BRB remains within its elastic range, there is a small amount of hysteresis due to a very high tangent stiffness experienced after a change in direction. The stiffness remains very high until the magnitude of the force has reduced by a few kilonewtons, and then gradually reduces as the next few kilonewtons of force are removed, returning to the linear stiffness by the time the magnitude of the force has reduced by around 10kN. The effect is greater after peaks in compression than in tension, giving the BRB a larger stiffness when the force is reducing than when it is increasing, with tension being taken as positive. This behaviour is attributed to friction between the encasement and the steel core and shoulder components causing a small proportion of the axial force to be transferred to the encasement. Since the encasement has an axial stiffness vastly greater than the core, the BRB shows extremely stiff behaviour until sufficient force has built up to overcome the frictional force and allow sliding to occur. The effect being greater when the BRB is in compression could be because, when in compression, the core will attempt to buckle but be restrained by the encasement leading to a reaction force between the two which will increase the greater the compression applied. This generates a frictional resistance in accordance with Eq. 2-32.

This very stiff behaviour at each load reversal means that initially the rig will deflect under the change in force while the deflection in the BRB is minimal. This leads to the delay in starting the motion in the new direction because the actuator motion is initially taken up by the rig deflection until enough of a change in force has developed. It is seen from x_m in Figure 4.21 that the velocity of the actuators is increased by the controller immediately after a peak as the system catches up. As well as showing the true physical behaviour of the BRB (F_m vs. x_{enc}), Figure 4.23 also shows the behaviour as it would appear to the numerical substructure in a hybrid test (F_m vs. x_t). This shows that the effect of the momentary delay is to reduce the apparent stiffness immediately after a direction reversal. However, the resulting disparity is very small, only occurs momentarily and has a negligible effect on the enclosed

area of the hysteresis loop. The reduction in the apparent maximum stiffness may, in fact, be beneficial to the integration algorithm due to the detrimental effect very stiff behaviour can have on stability.

Figure 4.24 shows the values of the ATS coefficients (a_0, a_1 and a_2) during the test, which remain stable and close to their expected values. Their variation during the test is small, indicating that the delay and amplitude error are relatively constant. Figure 4.24(a) shows that a_0 remains close to one, implying the amplitude error is minimal. Figure 4.24(b) shows that a_1 (which, since $a_0 \approx 1$, can be taken as an estimate of the delay, δ) varies slightly around the mean value of 10.8ms, remaining almost constantly in the range 10 – 12ms. A spike is observed in the value of a_1 immediately following each reversal of direction of motion indicating that the compensator is responding to the increase in delay after each peak caused by the effect described above.

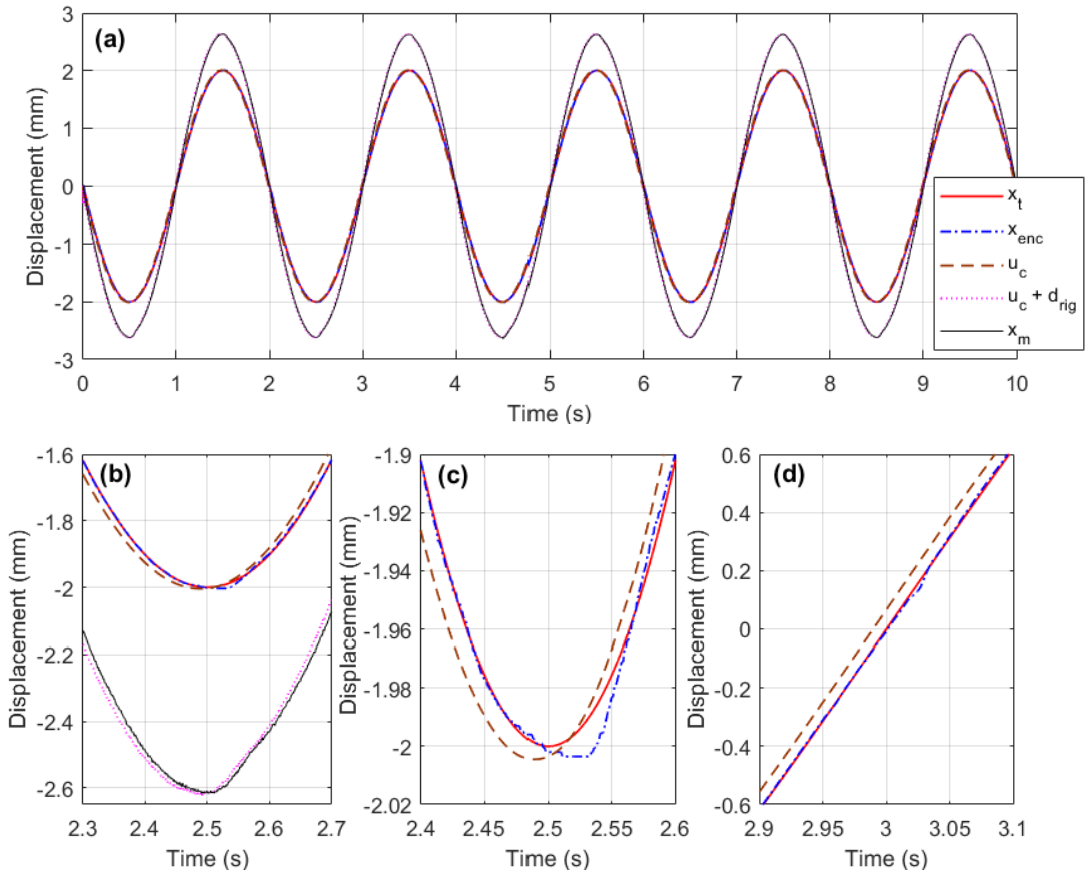

Figure 4.21 – Displacement response for 0.5Hz open-loop test: (a) full test, (b) close-up of peak including actuator displacements, (c) close-up of BRB displacement at peak, (d) close-up of BRB displacement at zero-crossing (x_m and $u_c + d_{rig}$ omitted for clarity)

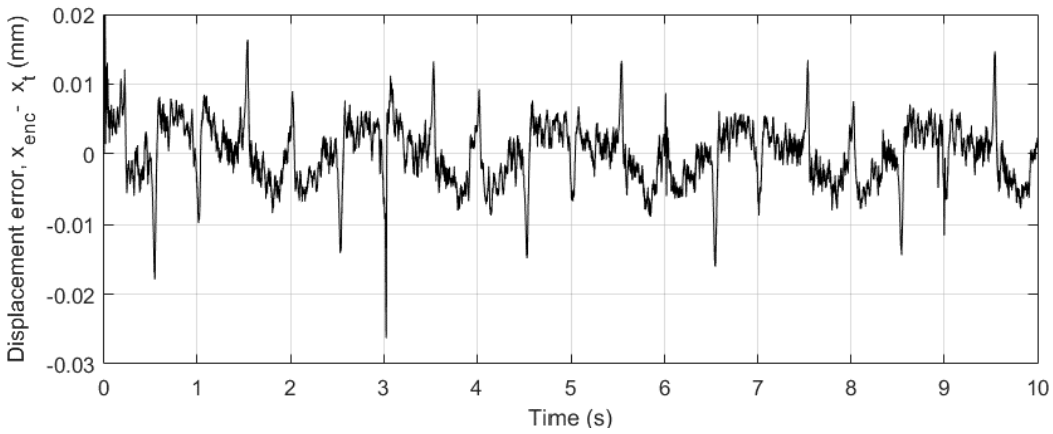

Figure 4.22 – Displacement error during 0.5Hz open-loop test

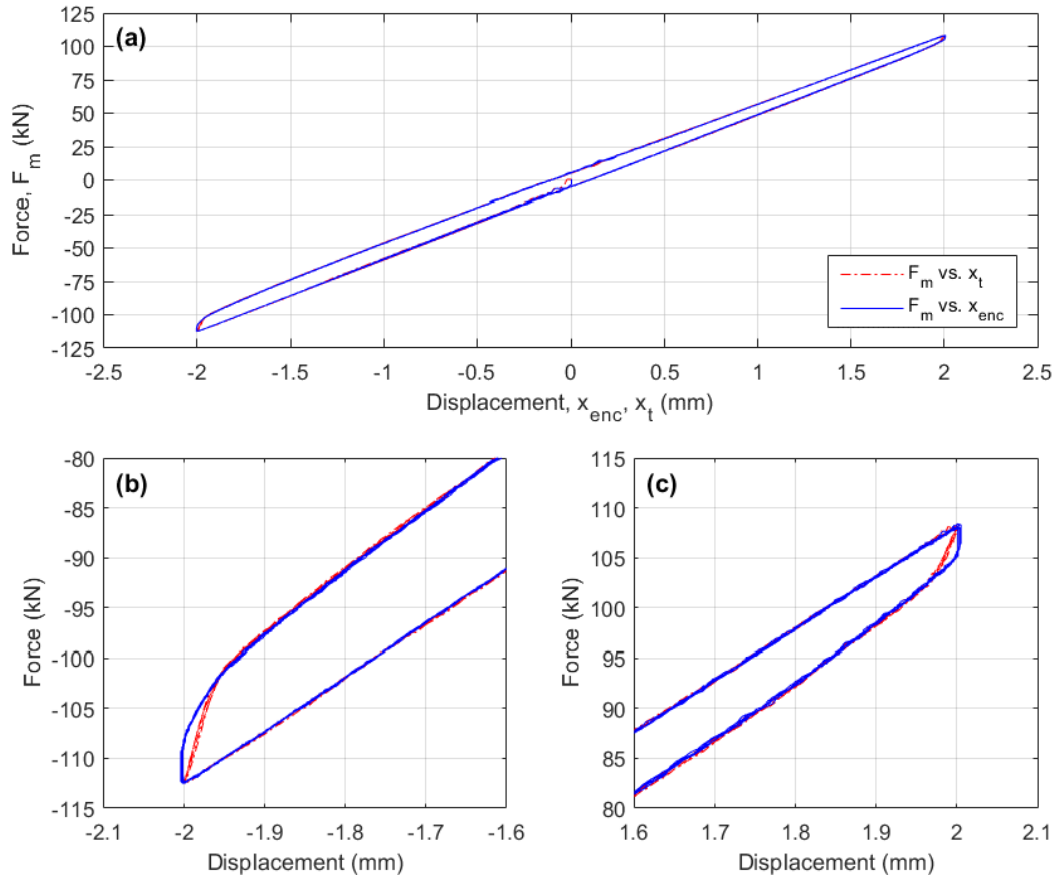

Figure 4.23 – Hysteresis curve for 0.5Hz open-loop test: (a) full-curve, (b) close-up at compression peak, (c) close-up at tension peak

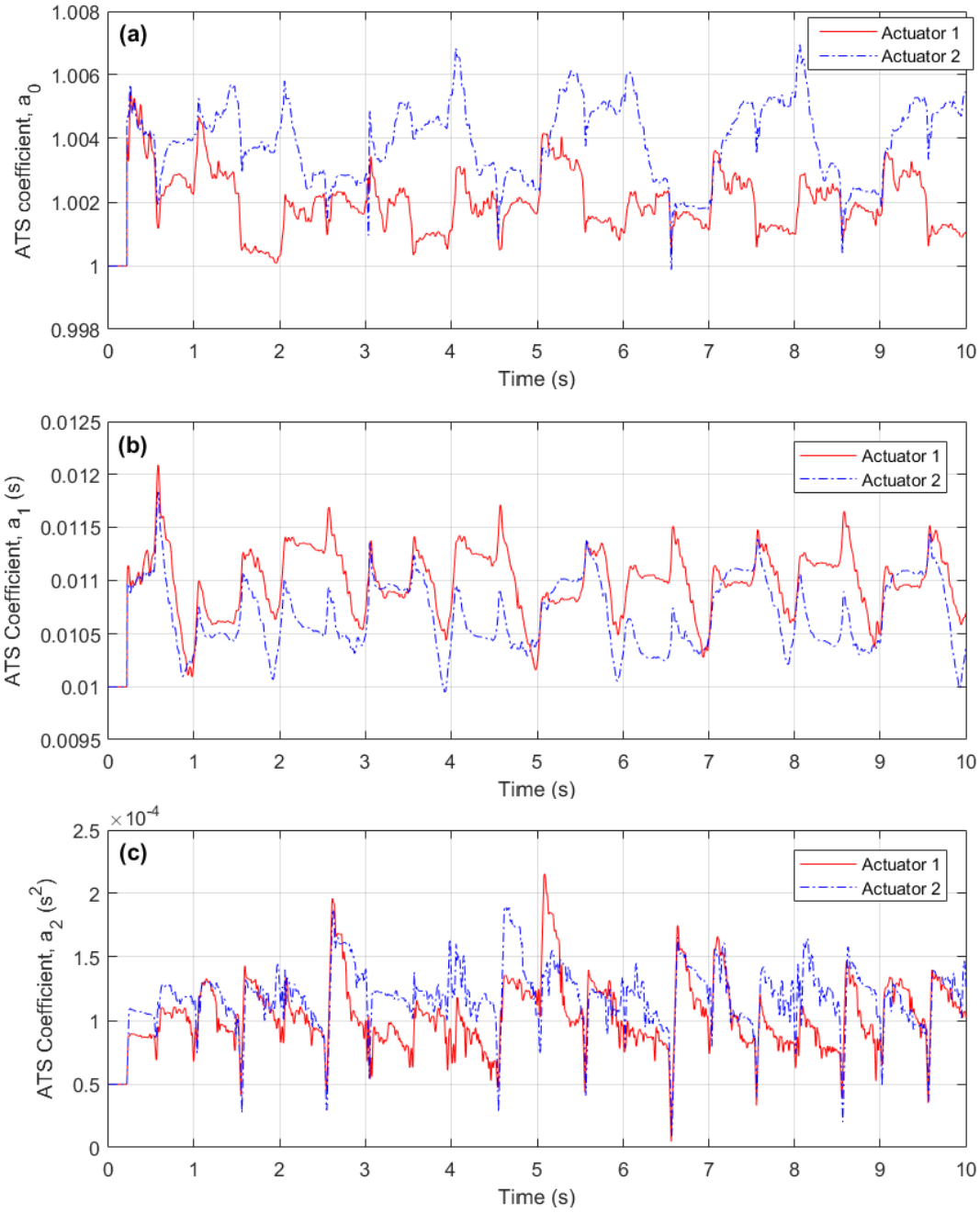

Figure 4.24 – mATS coefficients during 0.5Hz open-loop test: (a) a_0, (b) a_1, and (c) a_2

4.6.6. Open-Loop Cyclic Test at 5Hz

The above test was repeated for a target displacement, x_t, with a frequency of 5Hz, and the displacement response is shown in Figure 4.25. There is a slight increase in the mean delay from approximately 10.8ms in the 0.5Hz test above to approximately 11.6ms in this test. As might be expected, the displacement error is greater at this higher frequency, as shown in Figure 4.26, but it remains sufficiently small. Despite the ten-fold increase in the rate of motion, a very good match is still

achieved between x_{enc} and x_t, with an NRMS error of 2.270% between time 2s and 10s. Figure 4.27 shows the values of the mATS coefficients, a_0, a_1 and a_2, which have mean values of 1.019, 11.58ms and 88.47ms^2, respectively. The a_0 coefficient is slightly higher in this test, indicating a slight undershoot in the inner control loop, but remains very close to 1.0. The variation of the a_1 and a_2 coefficients is relatively small in the test, indicating the delay does not vary significantly, although there is a notable difference between the mean values of the a_1 coefficients for each actuator, which justifies the use of a separate delay compensator for each. Figure 4.28 shows the hysteresis curve for the BRB (F_m vs. x_{enc}) along with the behaviour as would be seen by the numerical substructure in a hybrid simulation (F_m vs. x_t) and there is still a good match between the two.

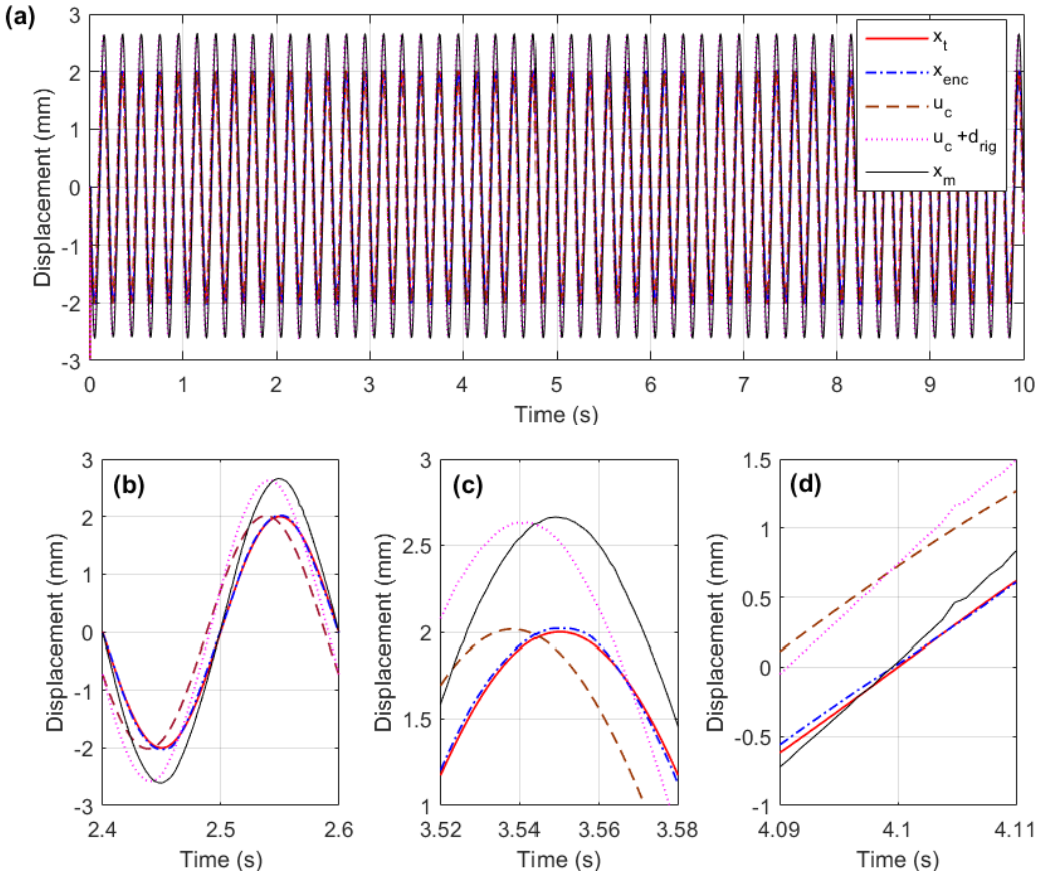

Figure 4.25 – Displacement response for 5Hz open-loop test: (a) full test, (b) close-up of single cycle, (c) close-up at peak, (d) close-up at zero-crossing

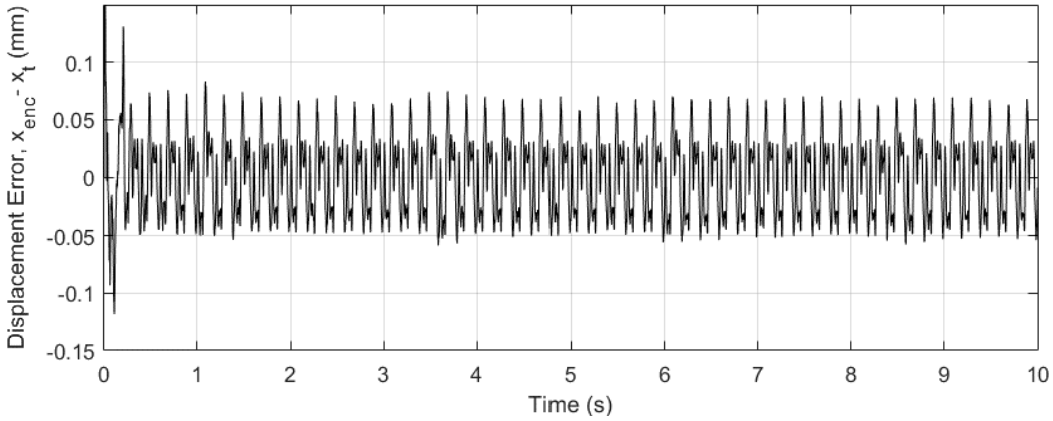

Figure 4.26 – Displacement error during 5Hz open-loop test

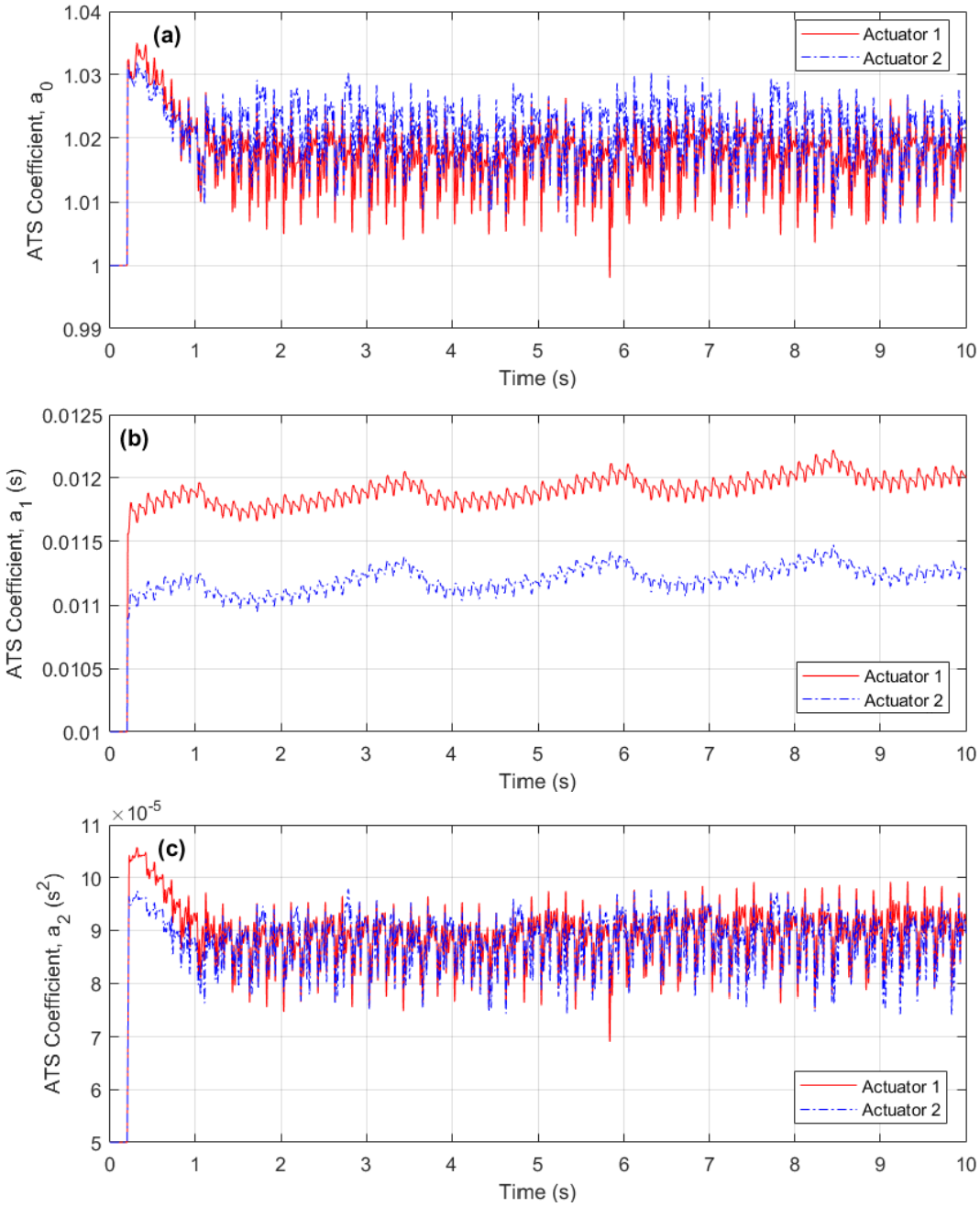

Figure 4.27 – mATS coefficients during 5Hz open-loop test: (a) a_0, (b) a_1, and (c) a_2

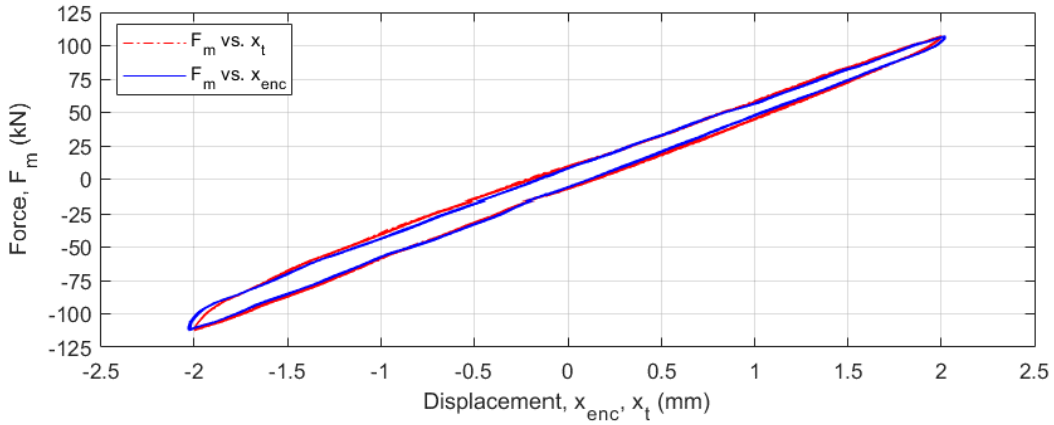

Figure 4.28 – Hysteresis curve for 5Hz open-loop test

4.6.7. Open-Loop Cyclic Test with Realistic Predefined Displacement

Having tested the control system for simple sine waves, a more realistic predefined displacement was generated by numerically modelling the response of a BRB in a 5-storey structure subjected to the Northridge ground motion to give a displacement time history with components at multiple frequencies. The displacement of a BRB in the first storey was scaled to give a peak displacement of 2.6mm to produce the target displacement, x_t, taking the BRB just up to its yield point. The discrete Fourier transform of this predefined displacement is plotted in Figure 4.29 showing the main contribution around the fundamental frequency of 1.17Hz, as well as a notable contribution at around 4Hz with some minor contribution from higher modes. This target displacement is shown in Figure 4.30 along with the achieved displacement, x_{enc}, during the open-loop test, and the contribution of the higher mode to the response is clearly visible. As before, there is very good agreement between x_{enc} and x_t with no visible delay and only a very small discrepancy at the peaks due to the frictional effect mentioned above. This is confirmed by the displacement error plotted in Figure 4.31 which remains small throughout the test and results in an NRMS error of 1.027%. The variation of the coefficients of the mATS compensator, shown in Figure 4.32, remains reasonably small suggesting little variation in delay or amplitude ratio during the test, with the mean values of a_0, a_1 and a_2 being 1.0004, 11.315ms and 100.28ms^2, respectively. The hysteresis curve in Figure 4.33 confirms that the BRB response that would be experienced by the integrator in a hybrid simulation (F_m vs. x_t) matches very closely with the actual BRB response (F_m vs. x_{enc}).

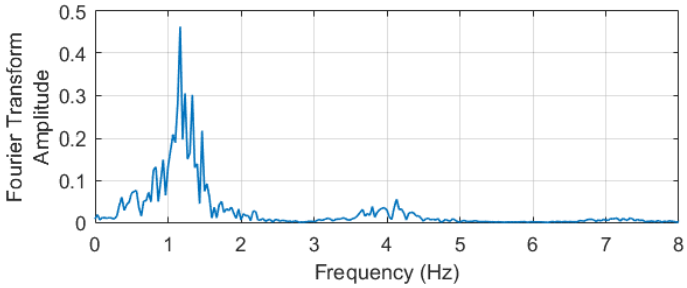

Figure 4.29 – Discrete Fourier transform of prescribed displacement used in open-loop test

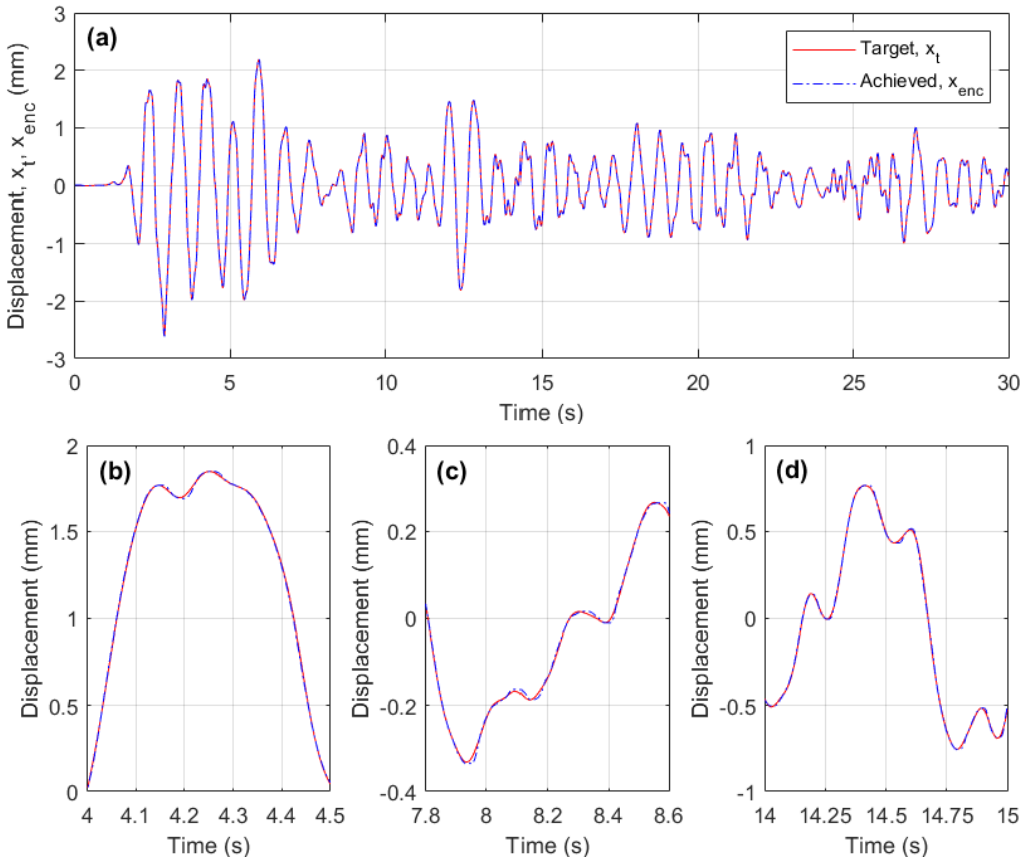

Figure 4.30 – Displacement response for open-loop test with pre-recorded earthquake displacement: (a) full test, (b)-(d) close-ups of representative locations

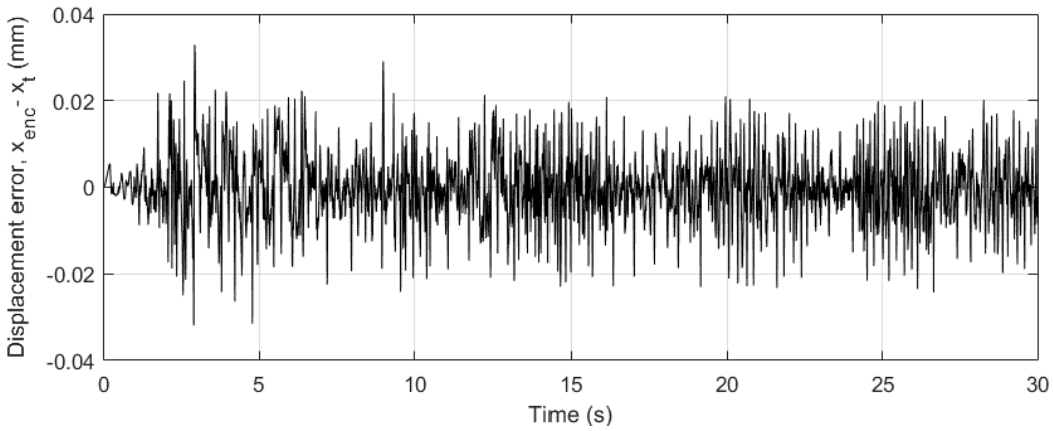

Figure 4.31 – Displacement error during open-loop test with pre-recorded earthquake displacement

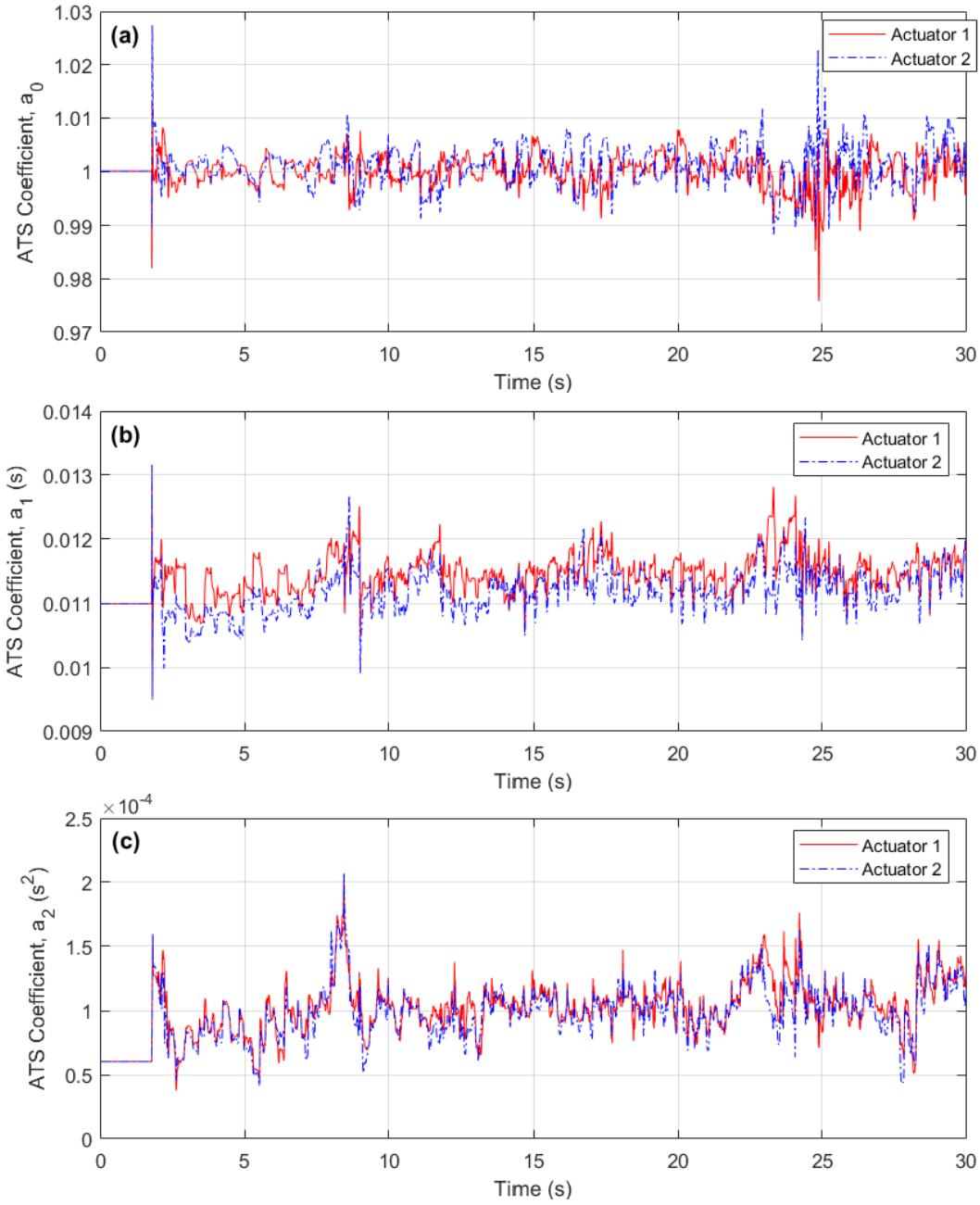

Figure 4.32 – mATS coefficients during open-loop test with pre-recorded earthquake displacement: (a) $\mathbf{a_0}$, (b) $\mathbf{a_1}$, and (c) $\mathbf{a_2}$

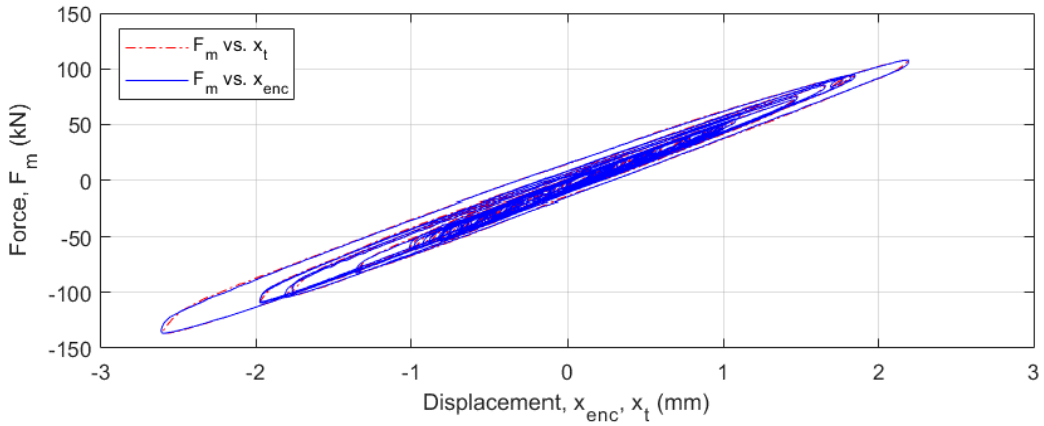

Figure 4.33 – Hysteresis curve for open-loop test with pre-recorded earthquake displacement

4.6.8. Open-Loop Tests with Different Delays

In Section 4.2, it was shown that reducing the proportional gain of the PID controller, K_p, would increase the delay between the command and achieved displacement, as well as increasing the amplitude error. The largest feasible value of K_p was therefore used to minimise the delay, which was 40dB. For tests within the elastic range of the BRB, the variation of the delay during a test and between tests at different frequencies was found to be quite small so, to test the performance of the mATS compensator for larger delays, cyclic tests were performed with K_p reduced to increase the delay. The tests consisted of a $\pm$2mm sinusoidal displacement at frequencies of 0.5Hz and 5Hz. The mATS effective time-window, q_{eff}, was kept at 200ms and the initial conditions of the compensator were kept at their previous values to check the ability to adapt to the new delay conditions, which assumed an amplitude ratio of 1.0 and a delay of 10ms. The mean results for each test are shown in Table 4.6, where the measured delay values are those between the mATS command, u_c, (prior to adjustment for rig flexure) and the measured BRB deformation, x_{enc}. The time, δ_0, between zero-crossings of the two signals gives a better measure of the mean delay in the system that the time, δ_p, between peak values. This is because the frictional behaviour at reversals in direction of motion causes a skewing of x_{enc} at its peaks, as was seen in Figure 4.21(b), resulting in a momentary increase in delay which is not representative of the behaviour during most of the displacement. This effect is significant for the low frequency tests, resulting in a doubling of the measured delay, while it is minimal for the high frequency tests. For a given value of K_p, the difference in mean delay between the tests at different frequencies was minimal, confirming that the delay is not significantly affected by the frequency of oscillation. The vast improvement in accuracy of the applied displacements is demonstrated by the significant reduction in NRMS error between the target and achieved displacements, x_t and x_{enc}. The variation in NRMS error with mean delay is plotted in Figure 4.34(a). It shows that, in the low frequency tests, the error increases as the actuation delay increases which might be expected since the delay compensator is having to predict further into the future. However, in the high frequency tests the opposite is found, with the error reducing as the delay increases. This suggests that, depending on the frequencies present in the

hybrid simulation, there are cases when the best PID coefficients for use in the combined system differ from those giving the best control without delay compensation, with the error being minimised by easing off the control in the inner loop and allowing the delay compensator in the outer loop to take up the slack. Note that this is only the case because the mATS compensator also corrects for the amplitude error, which grows as K_p is reduced. Many delay compensation methods correct for delay only, so in these cases the value of K_p would be determined by the need to minimise amplitude error. The variation of the mean values of the mATS compensator coefficients, a_0, a_1 and a_2, is shown in Figure 4.34(b)-(d). The most important conclusion from these tests is that the mATS compensator can adapt to a wide range of delays and amplitude errors without the need to retune the compensator coefficients or modify the compensator in any way, reducing errors to acceptably small values despite significant variations in system characteristics.

Frequency (Hz)	Proportional Gain, K_p (dB)	Mean Delay, δ (ms)		Mean mATS Coefficients			NRMS Error (%)	
		at zero-crossings	at peaks	a_0	a_1 (ms)	a_2 (ms^2)	With mATS	Without mATS
0.5	40	11.0	25.5	1.003	10.8	112.8	0.297	3.19
	35	18.0	39.9	0.995	17.0	159.9	0.382	5.28
	30	30.2	58.1	0.980	28.5	241.7	0.549	9.27
5	40	11.5	11.6	1.019	11.6	88.5	2.279	36.63
	37.5	14.6	14.8	0.989	14.7	85.5	2.249	44.70
	35	18.2	18.0	0.949	18.5	80.5	2.199	55.49
	32.5	22.8	23.1	0.893	23.8	70.3	2.087	67.83
	30	28.3	30.9	0.818	31.8	45.9	1.818	79.68

Table 4.6 – Performance during cyclic tests with various delays

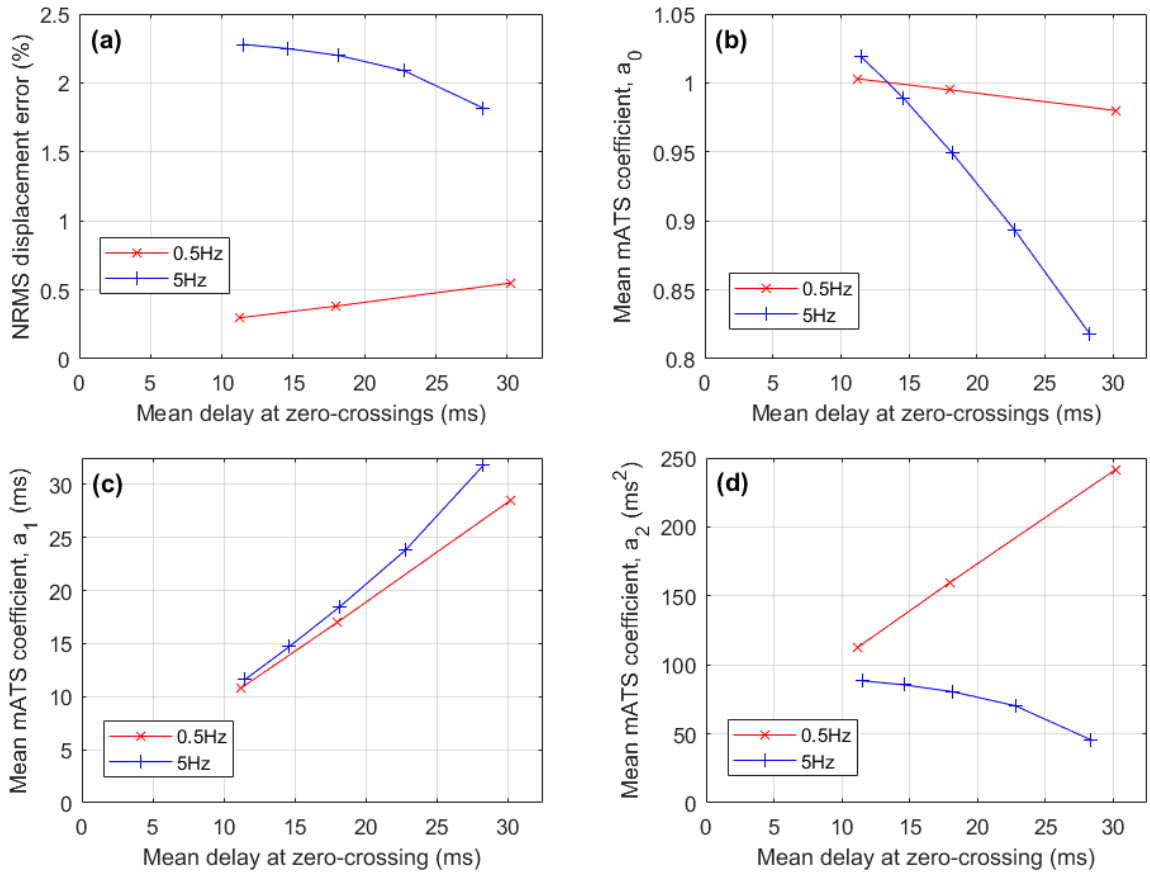

Figure 4.34 – Effect of varying mean actuation delay on: (a) NRMS error, (b) a_0 coefficient, (c) a_1 coefficient, and (d) a_2 coefficient

4.6.9. Discussion

The open-loop tests presented in this section have shown that the mATS compensator with rig flexure correction is effective at compensating for actuation delay and accurately applying the target displacement to the physical substructure. The mean, pre-compensation delay experienced in a test was found to increase with frequency, but only very slightly – a ten-fold increase in frequency increasing the actuation delay by just 7%. The lack of dependence of the delay on frequency explains why it is better quantified as a delay in the time domain rather than a phase lag in the frequency domain.

The control system performed well for a wide range of values of q_{eff} in the mATS compensator, so it is not necessary to perform precise tuning of the compensator coefficients to achieve good results. Additionally, mATS compensators with the same coefficients perform well over a wide range of frequencies, so it is not necessary to calibrate them for the specific frequencies of the test – this is

important because a MDOF hybrid simulation will include components at multiple frequencies. The delay compensation was shown to be effective for a wide range of delays, created by varying the PID gain in the inner control loop, demonstrating the adaptiveness of the mATS compensator but also showing that the use of the mATS compensator makes the performance significantly less dependent on the tuning of the PID controller. While the mATS compensator was robust to different delays, even if they were very different to the initial values specified in the system, the variation of the mATS coefficients during the tests was small, and a similar level of performance could be achieved using fixed coefficients – provided appropriate values were calculated from previous tests. However, these small displacement tests remained within the elastic limit of the BRB, with only a small amount of nonlinearity due to the frictional effect. Testing conducted by Darby [11] showed that the delay could be significantly dependent on the properties of the physical substructure, which will change once yielding occurs. The next section therefore looks at the application of larger displacements which cause the BRB to yield and provide a nonlinear response.

BRBs are considered displacement-dependent devices meaning the response should be independent of the rate at which the displacement is applied. This is shown to be a reasonable assumption by Figure 4.35 which plots the hysteresis curves for the measured response at 0.5Hz and 5Hz, showing a close match between the two.

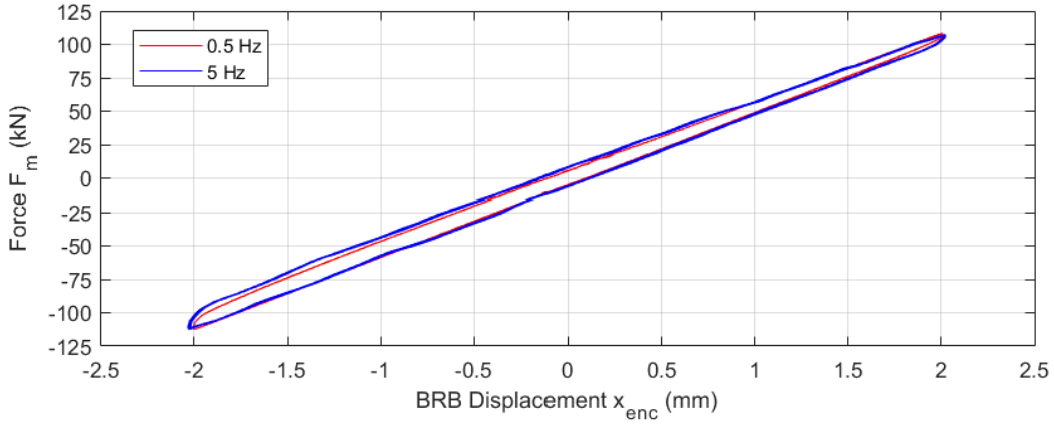

Figure 4.35 – Hysteresis curves for the BRB displaced at different frequencies

4.7. Large Displacement Open-Loop Testing

4.7.1. Large Displacement Pre-Defined Displacement

During the tests in the previous section, the variability of the mATS coefficients was small, indicating that similar performance could be achieved using constant coefficients, provided appropriate values were known in advance. The adaptive system still has the advantage of removing the need to determine the coefficients in advance, as shown in 4-25(b) where a_1 was set to an initial value of 10ms and immediately jumped to a mean of around 11.5ms when the compensator kicked in. However, those tests were restricted to the elastic range of the BRB, giving almost linear behaviour, with a small nonlinearity due to the frictional effect. Tests of interest will involve yielding of the BRB and hence a high degree of nonlinearity in the response. A large displacement cyclic test was therefore performed to investigate the performance of the system in the presence of significant nonlinear behaviour. The maximum displacement, d_{max}, was set to 17.5mm, which was estimated to be the BRB displacement that would correspond to just over a 1% insterstorey drift for a BRB inclined at 45° and is around half the expected strain capacity of the BRB. The test consisted of three cycles at $0.25d_{max}$, three cycles at $0.5d_{max}$ and three cycles at the full d_{max}, followed by three more at each of $0.5d_{max}$ and $0.25d_{max}$. The frequency of oscillation was varied between each set of cycles to avoid discontinuity, so that the maximum velocity of all cycles was the same at 55mm/s which is approximately 50% of the maximum actuator velocity. The effective time-window of the mATS compensator was kept at 200ms.

4.7.2. Results of Large Displacement Open-Loop Test

Figure 4.36 shows how the BRB displacement, x_{enc}, compared to the target, x_t. It shows a very good match with minimal discrepancy between the two, which is confirmed by Figure 4.37. The measured force resulting from this imposed displacement is shown in Figure 4.38 in which the significant amount of yielding is apparent. Figure 4.39 shows synchronisation plots illustrating the performance of the system. Figure 4.39(a) plots x_{enc} against the input to the inner-loop controller, $u_c + d_{rig}$, giving an indication of the actuation quality that would be obtained without compensation for delay or rig

flexure. Figure 4.39(b) plots x_{enc} against the output of the mATS compensator, u_c, giving an indication of the actuation quality that would be obtained with compensation for rig flexure but not for delay. Figure 4.39(c) plots x_{enc} against the target displacement, x_t, showing the actual performance achieved by the system with compensation for both delay and rig flexure. This forms a straight line indicating very good accuracy, a significant improvement over Figure 4.39(a) and (b). Figure 4.40 shows the values of the ATS coefficients, a_0, a_1 and a_2, during the test. There is a clear change in the variability of a_0 between the sets of cycles, with the coefficient remaining more consistent for the larger displacement, lower frequency cycles than for the smaller displacement, higher frequency ones. However, the values remain very close to 1.00 throughout the test, indicating that the amplitude error remains small. More interesting is a_1, which shows a distinct change in behaviour between sets of cycles, both in terms of mean value and variability, indicating a change in the delay properties of the system. This can be linked to the change in stiffness properties due to yielding seen in the hysteresis curve in Figure 4.41 which shows three distinct, approximately symmetrical sets of loops for the three displacement amplitudes. The mean value of a_1 over each set of cycles decreases as the displacement increases. It was around 11ms for the elastic tests in the previous section and, in this test, the approximate mean value goes from 10.5ms at $0.25d_{max}$ to 9.5ms at $0.5d_{max}$ to 8.5ms at d_{max}. This implies that the delay decreases as more yielding occurs. In addition, there is variability in a_1 over each cycle, with the amount it varies by also being affected by the displacement amplitude – the larger the displacement amplitude, the larger the variation in a_1. It is at its largest during the elastic part of the cycle, when the tangent stiffness of the BRB is at its greatest, and decreases with yielding, as the tangent stiffness decreases. The larger the displacement, the more yielding and the larger the variability in the tangent stiffness, hence the greater variability in a_1 over the cycle. Hence the delay in the system appears to depend on both the secant stiffness over the cycle and the tangent stiffness within the cycle. This confirms the findings of Darby et al. [11] that the actuation delay varies due to nonlinearity of the physical substructure, with stiffer behaviour giving a larger delay.

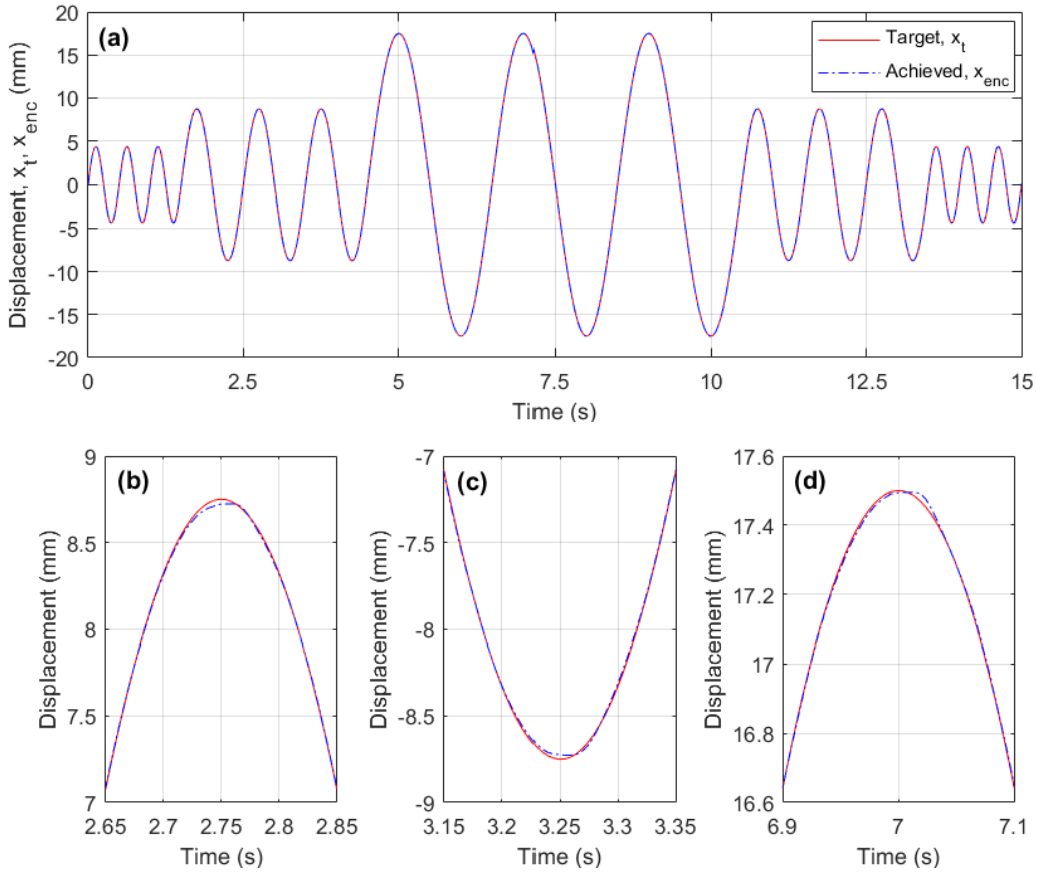

Figure 4.36 – Displacement response during large displacement open-loop test: (a) full test, (b)-(d) close-ups of peaks

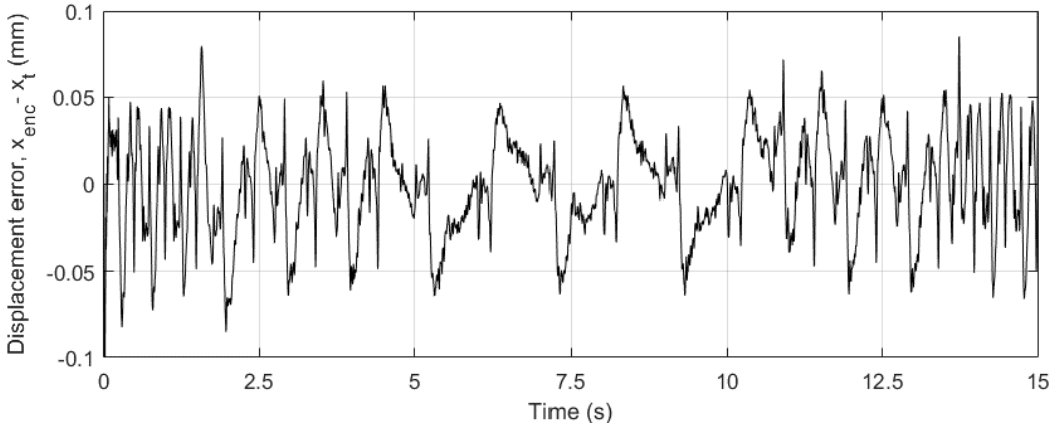

Figure 4.37 – Displacement error during large displacement open-loop test

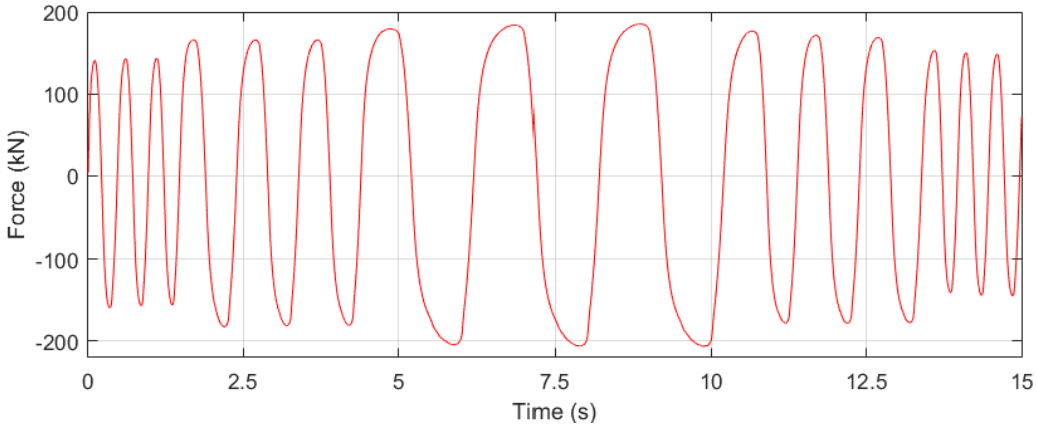

Figure 4.38 – Measured force during large displacement open-loop test

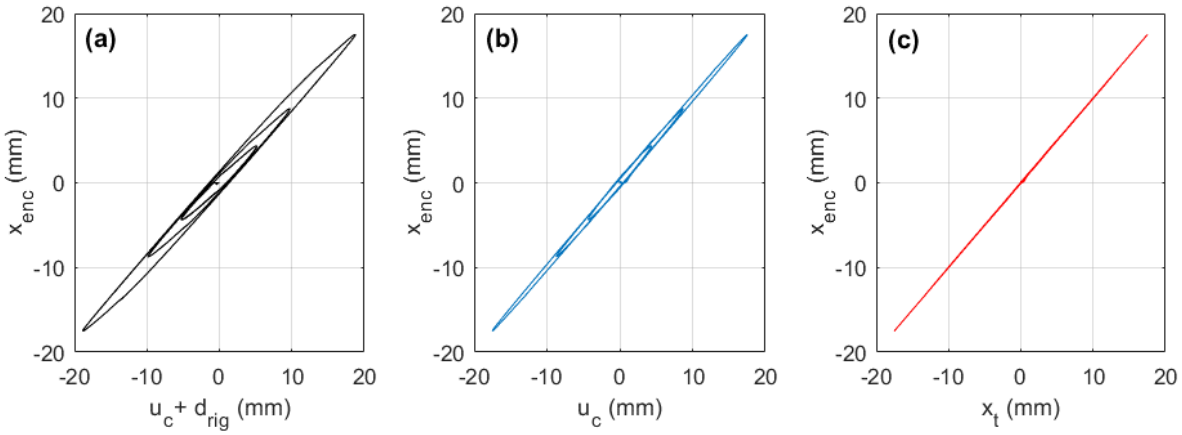

Figure 4.39 – Synchronisation plots for large displacement open-loop test: (a) performance with no compensation for delay or rig flexure, (b) performance with compensation for rig flexure but not delay, and (c) performance with compensation for both delay and rig flexure

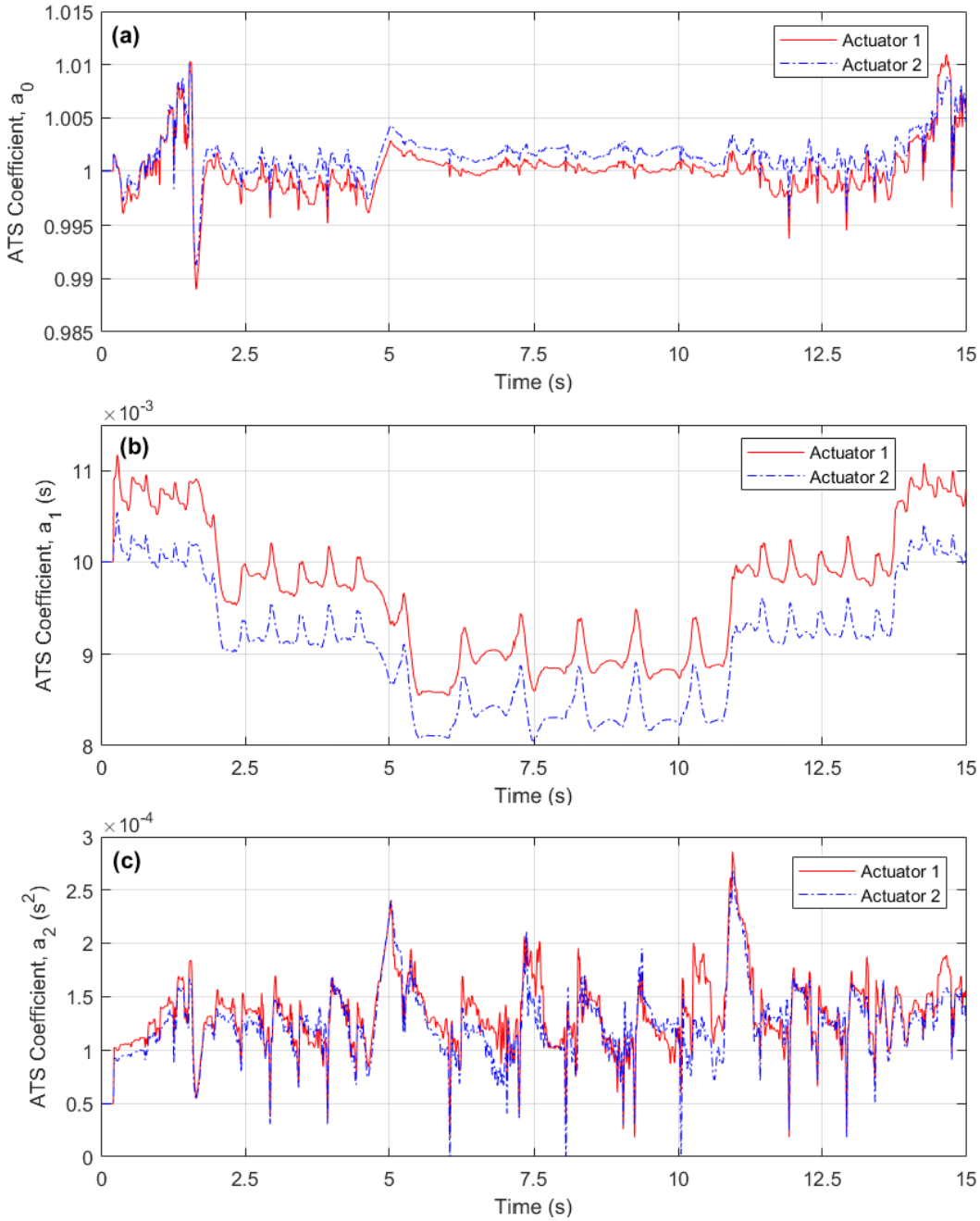

Figure 4.40 - mATS coefficients during large displacement open-loop test: (a) $\mathbf{a_0}$, (b) $\mathbf{a_1}$, and (c) $\mathbf{a_2}$

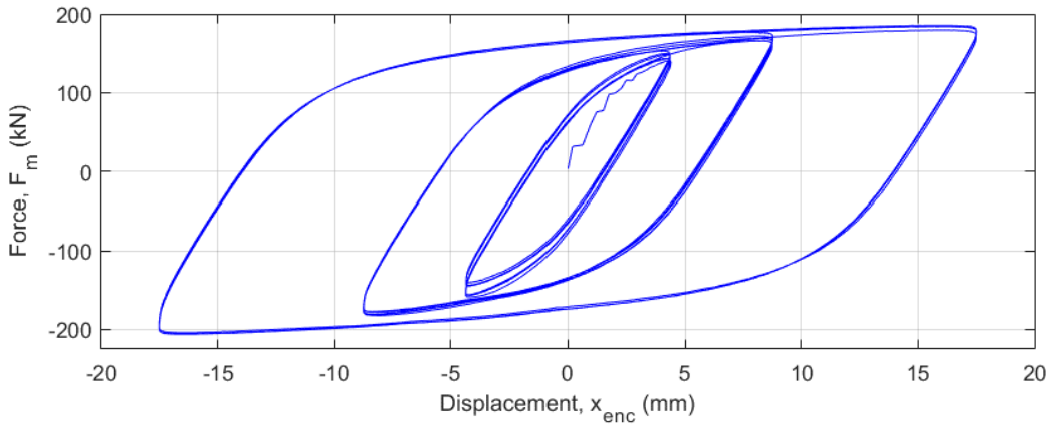

Figure 4.41 – Hysteresis curve for large displacement open-loop test

4.7.3. Discussion

This large displacement test has shown that there can be a notable variation in the actuation delay during a test. It has also shown that the main cause of variability in the actuation delay is the nonlinearity of the physical substructure – specifically, the change in stiffness caused by yielding of the BRB. This is an assertion that is confirmed by the results of the closed loop tests presented in the following chapters. Hence the value of adaptive delay compensation has been established, and the effectiveness of the ATS compensation procedure, as modified in this project, is demonstrated. In the open-loop testing presented so far, very little variation has been seen in the a_0 coefficient, indicating little variability in the amplitude ratio. However, it will be seen to vary in the hybrid testing presented in the following chapters. This is attributed to the fact that the displacements applied in the open-loop tests have been symmetrical. It appears that asymmetrical yielding, causing a change in the equilibrium position about which the BRB oscillates, can cause a notable change in a_0 during the test.

A smoothing function should have been applied to the first quarter-cycle of the test to avoid a discontinuity at the start, where the target velocity jumps instantly to its maximum value. However, this was accidentally omitted resulting in the oscillation seen in the first loading branch of the Figure 4.41. The frictional effect meant that the initial displacement of the actuators was taken up by the rig deflection until the slipping force was reached. During this time, the displacement error grew causing the PID output to grow, increasing the actuator velocity to catch up. This meant that, when slipping did occur, a very large acceleration was applied to the cross-beam, followed by a significant deceleration as x_{enc} caught up with x_t. While the inertia of the cross-beam and connections is small enough to be neglected for the expected levels of acceleration, these very high values generated enough force to be visible in the hysteresis curve. This oscillation had died away by the time the first peak was reached, and did not cause a direction reversal, so the effect on the overall test is minimal. In other cyclic tests, a smoothing function was applied to the initial motion to avoid an initial discontinuity, while for hybrid simulations this is not of concern as such a discontinuity will not occur in the structural response.

4.8. Summary

This chapter has focused on the control system used to ensure that the target displacements from the numerical substructure are accurately applied to the physical specimen. Of concern has been the unavoidable delay within the inner control loop due to its destabilising effect on the hybrid simulation. It has been shown that the tuning of the parameters of the PID controller can significantly affect the accuracy of the applied displacements. However, it was also shown that even with optimised PID parameters, the delays could not be reduced to small enough values to ensure the stability of the real-time hybrid simulations in this project. Delay compensation methods were therefore reviewed with specific attention on adaptive methods since the delay varies during the simulation due to nonlinearity of the physical substructure, higher stiffness leading to larger delays. The adaptive time series (ATS) compensator was shown to be effective at compensating for variable delays and has several advantages over other adaptive methods including that it does not require empirically tuned gains and that its coefficients represent physical quantities related to the delay and amplitude error. By compensating for amplitude error as well as delay, the ATS compensator greatly reduces reliance on the tuning of the PID gains, giving comparable performance for a wide range of values of PID proportional gain. The main downside found with the ATS compensator was the significant computational demand due to the number of calculations at each timestep and the amount of data to be stored, which made it impractical with the available hardware. A modification to the ATS compensator was presented which retains the advantages of the original but greatly reduces the computational demand by using a recursive relationship to update the fitting matrix and vector at each timestep, requiring storage of values from only the previous timestep. The system was modified to compensate for the disparity between the displacement of the actuators and the physical specimen due to rig flexure, while ensuring the displacements of the two actuators were constrained to be the same. This system was shown to provide accurate actuation and adaptability to varying delay, while the coefficients remain stable throughout the test and the performance is not overly reliant on the specific parameters used in the compensator.

5. Single-Degree-of-Freedom Hybrid Testing

5.1. Substructuring Overview

Figure 5.1 shows a simplified overview of the RTHS system. For simplicity, it is drawn as a single actuator system, omitting the additional complexity described in Section 4.5 (Figure 4.15) for controlling the two actuators in parallel. The previous chapter dealt with the design of the control system for accurately applying the target displacement, x_t, to the physical substructure, and therefore covered the components in the shaded box in Figure 5.1. This chapter covers the implementation of the remaining components required to complete the RTHS feedback loop, and then presents the results of RTHS testing with the complete system. The most significant part will be the numerical substructure. First the target properties of the numerical substructure must be specified, based on the structure to be simulated, and the equations of motion which model the behaviour must be determined. A numerical integration algorithm must then be implemented to integrate these equations of motion in real-time, while including the effect of the numerical substructure as an external force based on the measured response. Many integration algorithms have been developed for numerical simulation of the dynamic response of structures, but RTHS testing imposes additional constraints on the choice of methods. The need to apply continuous motion, as well as the correct hysteretic path, rules out the use of methods requiring iteration on the physical substructure, and prevents the use of implicit algorithms which are

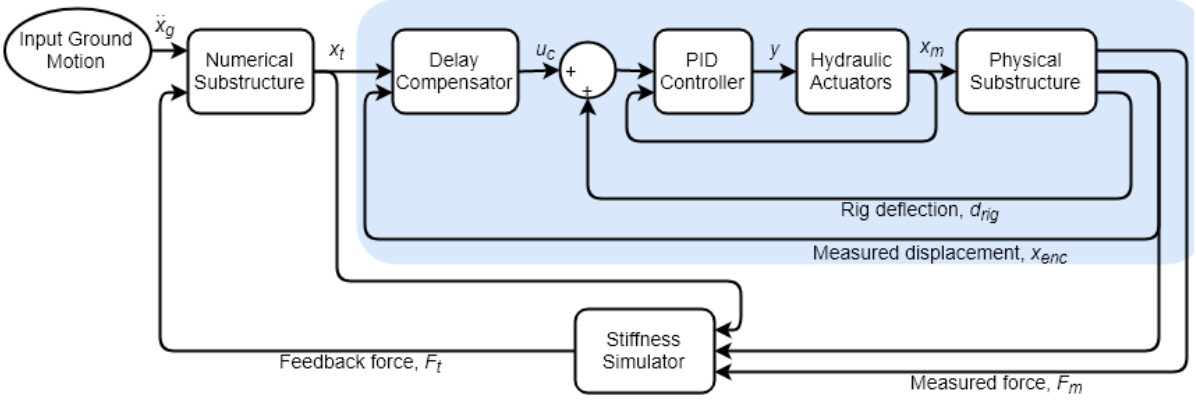

Figure 5.1 – Simplified overview of RTHS system

preferred in purely numerical simulations due to their unconditional stability and efficiency the larger timestep permits. The efficiency of the algorithm becomes especially important for RTHS because all calculations for each timestep must be completed within the duration of the timestep. This can be at odds with the requirements of stability and accuracy which require that the timestep be sufficiently small relative to the frequencies present in the simulated response.

The final component completing the RTHS feedback loop in Figure 5.1 is the *stiffness simulator*, which works on the force interface going from the physical substructure back to the numerical substructure. This contains a numerical model of the BRB's force-displacement response, the coefficients of which are continually updated based on the measured data, F_m and x_{enc}. It uses this model to generate the feedback force, F_t, from the target displacement, x_t. This improves the stability of the system by ensuring continuous, stable force feedback, while the accuracy is kept high by fitting the model closely to the most recent measurements. The derivation and performance of the stiffness simulator will be detailed in Section 5.4 after the implementation of the numerical substructure has been introduced.

The aim in this chapter is to investigate the effectiveness of the actuation control system developed in the previous chapter, along with the stiffness simulator introduced in this chapter, at providing a stable, accurate RTHS feedback loop. The numerical substructure is kept simple, modelling a linear elastic single-degree-of-freedom (SDOF) structure, so that the performance can be tested at particular frequencies prior to simulating multi-degree-of-freedom (MDOF) structures which will have multiple modes of oscillation present. For the same reason, the scaling of the input ground motions will be based on the target peak displacements, rather than by reference to a specific performance level.

5.2. Numerical Substructure

5.2.1. Single-Degree-of-Freedom Model

The structure simulated in this chapter consists of an elastic SDOF portal frame diagonally braced with a BRB, as shown in Figure 5.2. The numerical substructure consists of a mass, m, which is assumed to

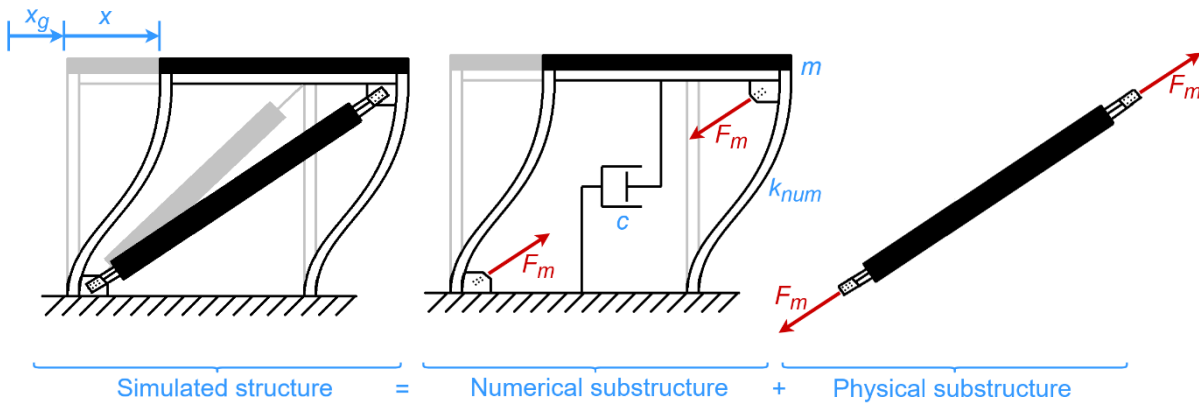

Figure 5.2 – Simulated SDOF structure with constituent numerical substructure (portal frame) and physical substructure (BRB)

be constrained to horizontal motion, supported on a frame with lateral stiffness, k_{num}, and with inherent damping modelled as linear viscous damping with damping coefficient, c. The BRB forms the physical substructure and is assumed to be inclined at 45°. This provides an axial force, F_m, with a horizontal restoring force component, $r = F_m \cos(45^o)$. When the structure is excited by a ground acceleration, $\ddot{x}_g$, the stiffness and damping forces will be proportional to the relative displacement, x, and velocity, $\dot{x}$, between the mass and the ground, respectively; while the inertia force will be proportional to the absolute acceleration, $\ddot{x} + \ddot{x}_g$. Newton's Second Law yields the equation of motion:

$$m(\ddot{x} + \ddot{x}_g) = -k_{num}x - r - c\dot{x} \qquad 5\text{-}1(a)$$

or

$$m\ddot{x} + c\dot{x} + k_{num}x = -m\ddot{x}_g - r \qquad 5\text{-}1(b)$$

where the total restoring force is seen to be split between the frame in the numerical substructure ($k_{num}x$) and the BRB in the physical substructure (r).

5.2.2. Selection of Numerical Substructure Properties

The linear SDOF numerical substructure is defined by the parameters m, c and k_{num} on the left-hand side of eq. 5-1(b). For investigating the properties of the RTHS system, it is useful to define the simulated structure in terms of its elastic natural frequency, f, its damping ratio, ζ, and its stiffness factor, C_k, defined as:

$$C_k = K_{phys}/K \qquad 5\text{-}2$$

where the total stiffness, K, is the sum of the stiffness from the physical substructure, K_{phys}, and the stiffness from the numerical substructure, k_{num}. Hence C_k would be zero for a purely numerical

simulation and would be 1.0 for a hybrid simulation where all of the stiffness came from the physical substructure. The elastic stiffness of the BRB, K_{BRB}, is taken as 53.8kN/mm, calculated as the mean of the secant stiffnesses up to the yield point in tension and in compression. The BRB is assumed to be inclined at an angle, θ, to the horizontal, so K_{phys} is taken as:

$$K_{phys} = K_{BRB} \cos^2 \theta = 26.9kN/mm \quad 5\text{-}3$$

since θ is taken as 45° for all SDOF tests. This can then be used to obtain the total stiffness, K, using eq. 5-2, from which the stiffness of the numerical substructure can be obtained from:

$$k_{num} = K_{phys}\left(\frac{1}{C_k} - 1\right) \quad 5\text{-}4$$

provided $C_k \neq 0$, which would indicate no contribution from the physical BRB and would therefore not be a hybrid simulation. The mass is then selected to give the desired natural frequency:

$$m = K/(2\pi f)^2 = K/\omega^2 \quad 5\text{-}5$$

Finally, the damping coefficient, c, is determined from:

$$c = 2\zeta\omega m \quad 5\text{-}6$$

It is important that the circular natural frequency of the *combined* structure, $\omega = 2\pi f$, is used to determine c. Using the natural frequency of the numerical substructure, ω_{num}, without including the stiffness of the BRB will result in the damping ratio experienced in the hybrid simulation being lower than intended since $\omega_{num} < \omega$.

5.2.3. Time Dilation

This project is aimed at performing hybrid tests in real time, but it is useful to have the ability to perform tests at a dilated time scale (i.e. slower than real-time) to allow the rate-dependency of the system to be investigated. To do this, a time dilation factor, η, is employed which relates the simulation time, t, in the integration to real-time, τ, by:

$$\tau = \eta t \quad 5\text{-}7$$

This means it would take η seconds to complete one second of the simulation. The system here uses Simulink® integrator blocks which integrate with respect to real-time, so a conversion factor must be

applied to the output of the integrator to give the correct value with respect to the simulation time. For example, given the relationship $d\tau/dt = \eta$ from eq. 5-7, integrating the simulation velocity, dx/dt, with respect to real time, τ, gives:

$$\int \frac{dx}{dt} d\tau = \int \frac{dx}{dt}\left(\frac{d\tau}{dt}\right) dt = \eta x \qquad 5\text{-}8$$

Hence the displacement, x, is obtained by dividing the output of the integrator by η, and similarly when integrating acceleration to obtain velocity. By the same token, if differentiation is performed, the output must be multiplied by η.

Operating at a dilated timescale will improve the stability of the numerical integration since the effective frequencies of the system are divided by η, and will reduce the rate demands on the actuators. In addition, for a given actuation delay, δ, the effective delay in the integration will be δ/η, improving the stability of the system. This comes at the cost of losing the rate-dependent properties of the physical substructure, which is why the aim is for η to be 1.0 but, when testing with a rate-independent physical substructure, repeating tests with different values of η can provide information about the accuracy of the hybrid simulation.

5.2.4. Earthquake Ground Motions

The recorded accelerograms of the El Centro, Northridge and Kalamata earthquakes described in Table 2.1 were used as the ground motion inputs for the hybrid simulations in this chapter. At this stage, the focus is on investigating the performance of the RTHS system, rather than simulating realistic structures, so the scaling of the ground motions was performed based on the target peak displacement rather than based on specific performance levels. The peak displacement for a given earthquake scale factor was estimated from numerical simulation with an approximate BRB model and from the results of previous tests.

5.3. Integration Algorithm

5.3.1. Integration Algorithm Properties

The numerical substructure, defined by eq. 5-1, must be integrated using a numerical algorithm, which first requires it to be expressed in discretised form:

$$m\ddot{x}_i + c\dot{x}_i + k_{num}x_i = -m\ddot{x}_{g,i} - r_i \qquad 5\text{-}9$$

where $x_i = x(i\Delta)$, Δ is the timestep and integer i is the timestep number. At each timestep, i, the algorithm calculates what the displacement, x_{i+1}, will be at the next timestep. There are a variety of methods which have been used, and a great deal of research has taken place into the properties of these methods. Key properties to consider are:

- Stability – will the output remain bounded?
- Accuracy – how close is the numerical solution to the exact solution?
- Computation time – can the calculations be completed in time for the next timestep?
- Numerical dissipation – does the algorithm add damping, and how does this vary with frequency?

Integration algorithms are broadly divided into two types: explicit and implicit. In an explicit algorithm the calculation of the displacement at the next timestep contains only values from previous timesteps, while in an implicit algorithm the calculation will also contain values at the next timestep, which are not yet known. For this reason, implicit algorithms must use an iterative process to obtain the solution at each timestep. This requires multiple function evaluations and hence implicit algorithms tend to take longer to complete each integration timestep than their explicit counterparts. However, implicit algorithms are available which exhibit far superior stability properties than can generally be achieved with explicit algorithms. This allows much larger timesteps to be used so that the overall computation time for a purely numerical simulation will be reduced, while explicit algorithms can require very small timesteps to ensure stability and convergence. In fact, the most popular implicit algorithms are chosen

because they are unconditionally stable – they remain stable regardless of the timestep used. Explicit algorithms tend to be only conditionally stable, meaning they produce a stable output provided the timestep of the integration is sufficiently small with the critical timestep being a function of the highest natural frequency in the model. Models with a large number of degrees-of-freedom (DOFs) often require very small timesteps due to the presence of high frequency modes, even though these modes may make a negligible contribution to the overall response of the structure. This has led to the development of algorithms with favourable energy dissipation at high frequencies – the aim being to improve the stability of the simulation by artificially damping out the response from the higher modes while leaving the lower modes unaffected. An alternative to this is the modal approach used in the next chapter, where higher frequency modes can be omitted from the integration if it is deemed their contribution to the response can be neglected [86].

While implicit algorithms are usually preferred for numerical simulations, they are not feasible for hybrid simulation due to difficulty in accurately determining the tangent stiffness matrix during a test and due to the need to iterate in order to converge on a solution [87]. This iteration would result in a displacement history being applied to the physical substructure which differed from the displacement computed by the simulation, leading to inaccuracy due to the path dependency of the device [88]. This being said, some implicit schemes have been adapted to pseudo-dynamic testing [89], although their implementation becomes much more complex than the explicit methods. Moreover, when extending this approach to real-time testing, the need for continuous motion to be applied to the physical substructure at high speeds makes iteration, and hence implicit algorithms, unviable.

The conventional wisdom that unconditional stability could only be achieved with implicit algorithms has recently been refuted by the proposition of Chang's Algorithm [88] and the CR-Algorithm [90] which have been developed for hybrid simulation and promise unconditional stability from explicit algorithms. Unlike the unconditionally stable implicit methods which are stable for any simulated structure, in order to offer unconditional stability, the coefficients of these explicit algorithms depend on the properties

of the simulated structure ($\boldsymbol{M}$, $\boldsymbol{C}$ and $\boldsymbol{K}$) and so the algorithm must be modified between tests if the properties of the structure being simulated are changed. Since it is the properties of the combined structure which are of importance, it means reasonable estimates of the properties of the physical substructure will be required which, in the case of the BRB, will be its stiffness $\boldsymbol{K}$. It is worth noting that the stability properties of numerical integration algorithms are defined in terms of linear systems, so the effects of nonlinearity in the physical or numerical substructure will complicate the issue.

The equations of the integration algorithms presented in this section are given in their multi-degree-of-freedom (MDOF) forms in anticipation of the next chapter. For a system with $\boldsymbol{N}$ DOFs, the mass, damping and stiffness matrices, $\boldsymbol{M}$, $\boldsymbol{C}$ and $\boldsymbol{K}$, will have dimension $\boldsymbol{N \times N}$, while the displacement, velocity, acceleration and force vectors, $\boldsymbol{x}$, $\dot{\boldsymbol{x}}$, $\ddot{\boldsymbol{x}}$ and $\boldsymbol{F}$, will have dimension $\boldsymbol{N \times 1}$. In the SDOF case, these matrices and vectors simply reduce to their 1×1 equivalents: m, c, k, x, $\dot{x}$, $\ddot{x}$ and f, respectively.

5.3.2. Integration Timestep and Controller Timestep

There are three timesteps used in the RTHS: the inner control loop timestep, the outer control loop timestep and the integration timestep. The inner control loop requires the smallest timestep to maintain tight, continuous control of the actuator displacements. Here the PID controllers are implemented in the Instron® controller which uses a timestep of 0.2ms. The timestep in the outer controller, which implements the delay compensation, is constrained by the need for smooth, continuous displacements – if the timestep is too large the displacement will be applied in steps rather than the smooth motion which is required. A timestep of 1ms is used as it is sufficiently small to give smooth actuator displacements, while allowing enough time for the delay compensator computations to be carried out. This timestep, or something close, is common in modern RTHS testing.

The timestep used in the integration algorithm is constrained by the stability limits of the algorithm and the time taken to complete the computations at each timestep – it must be long enough for all of the calculations to be completed within that amount of time. This will depend on the complexity of the numerical substructure (e.g. number of DOFs), the efficiency and stability of the integration algorithm,

and the available computing power. In the system used here, the compiler checks the computation time of the computational part of the system and will fail to compile it to the controller board if this exceeds the specified integration timestep. Very often, the size of the numerical substructure prevents the calculations from being computed within the timestep of the outer-loop controller. In this case, a longer timestep must be used for the integration algorithm along with a sub-stepping procedure to maintain compatibility between the numerical substructure and the controller. This interpolates the output from the numerical substructure to provide a smoothly varying target displacement to the outer loop controller [91] [68]. This does not apply to the testing in this chapter which uses a simple SDOF substructure which can be integrated with the same 1ms timestep used in the outer loop controller, so the two are synchronised. In the MDOF testing in the next chapter, rather than employ a sub-stepping procedure, a modal approach is used to reduce the DOFs of the numerical substructure to allow the same 1ms timestep to be used.

The question of how much complexity it is appropriate to include in the numerical substructure is open to debate. The opinion taken here is that, given the multiple sources of uncertainty and that the main response of interest is that of the physical substructure, there may be limited benefit in overly complex numerical substructures. Therefore, here they have been made only as complex as necessary to provide a realistic structural response to the physical substructure.

5.3.3. Newmark Family of Methods

In 1959, Newmark [79], [92], proposed a numerical integration method for structural dynamics which has been widely used for numerical simulation and has formed the basis of further methods [88] [90] [93]. The Newmark method computes the system values at timestep $i+1$ using the equations:

$$M\ddot{\boldsymbol{x}}_{i+1} + C\dot{\boldsymbol{x}}_{i+1} + K\boldsymbol{x}_{i+1} = \boldsymbol{F}_{i+1} \quad \text{5-10(a)}$$

$$\boldsymbol{x}_{i+1} = \boldsymbol{x}_i + \Delta\,\dot{\boldsymbol{x}}_i + (0.5-\beta)\Delta^2\ddot{\boldsymbol{x}}_i + \beta\Delta^2\ddot{\boldsymbol{x}}_{i+1} \quad \text{5-10(b)}$$

$$\dot{\boldsymbol{x}}_{i+1} = \dot{\boldsymbol{x}}_i + (1-\gamma)\Delta\ddot{\boldsymbol{x}}_i + \gamma\Delta\ddot{\boldsymbol{x}}_{i+1} \quad \text{5-10(c)}$$

where Δ is the timestep, the external force vector, $\boldsymbol{F}_{i+1}$, will be equal to $-m\ddot{x}_{g,i+1} + r_{i+1}$ for the SDOF hybrid simulation (or $-M\{\mathbf{1}\}\ddot{x}_{g,i+1} - \boldsymbol{r}_{i+1}$ for the MDOF case), and the coefficients β and γ are chosen by the user. Numerical damping can be introduced by setting $\gamma > 0.5$, but this reduces the order of accuracy to one and has a significant impact on the lower modes of oscillation, so it is usual to fix γ at 0.5 to produce a scheme with second order accuracy and no numerical dissipation. With γ set to 0.5, unconditional stability is achieved for $\beta \geq 1/4$. Commonly used values are $\beta = 1/6$ resulting in the conditionally stable linear acceleration method, and $\beta = 1/4$ resulting in the unconditionally stable constant average acceleration method (CAAM) which has the lowest frequency distortion of the unconditionally stable second order schemes.

In general, the Newmark method is implicit but, when $\beta = 0$, the future acceleration is removed from Eq. 5-10(b) resulting in an explicit method. This is fast because no iteration is required but it requires a small timestep to ensure stability. This has the same stability properties as the central difference method (CDM) described below. Note that Eq. 5-10(c) isn't explicit so to implement this scheme Eqs. 5-10(a) and 5-10(c) must be combined so as to eliminate $\dot{\boldsymbol{x}}_{i+1}$ and allow $\ddot{\boldsymbol{x}}_{i+1}$ to be computed once $\boldsymbol{x}_{i+1}$ has been applied to the physical substructure and $\boldsymbol{r}_{i+1}$ has been measured.

Hilber et al. [93] modified the Newmark method to produce more favourable numerical dissipation by incorporating an additional parameter α into the equilibrium equation so that 5-10(a) becomes:

$$M\ddot{\boldsymbol{x}}_{i+1} + (1+\alpha)C\dot{\boldsymbol{x}}_{i+1} - \alpha C\dot{\boldsymbol{x}}_i + (1+\alpha)K\boldsymbol{x}_{i+1} - \alpha K\boldsymbol{x}_i = (1+\alpha)\boldsymbol{F}_{i+1} - \alpha\boldsymbol{F}_i \qquad 5\text{-}11$$

The finite difference relations for $\boldsymbol{x}_{i+1}$ and $\dot{\boldsymbol{x}}_{i+1}$ remain the same but β and γ are constrained to:

$$\gamma = 1/2 - \alpha \text{ and } \beta = (1-\alpha)^2/4 \qquad 5\text{-}12$$

This gives the implicit HHT method (or α-method) which is unconditionally stable for $-1/3 < \alpha \leq 0$. For $\alpha = 0$ the CAAM is recovered, with no numerical dissipation, but as α is reduced below zero numerical dissipation is introduced while retaining second order accuracy. The numerical dissipation increases in proportion to the square of the frequency (rather than linearly, as occurs when setting $\gamma > 0.5$ in the Newmark scheme) to effectively damp out high modes.

5.3.4. Central Difference Method

The central difference method (CDM) is an explicit algorithm that has been extensively used in hybrid testing. It is derived by substituting the central difference approximations to the velocity and acceleration into the equilibrium equation:

$$M\ddot{\boldsymbol{x}}_i + C\dot{\boldsymbol{x}}_i + K\boldsymbol{x}_i = \boldsymbol{F}_i \quad \text{5-13(a)}$$

$$\ddot{\boldsymbol{x}}_i = (\boldsymbol{x}_{i+1} - 2\boldsymbol{x}_i + \boldsymbol{x}_{i-1})/\Delta^2 \quad \text{5-13(b)}$$

$$\dot{\boldsymbol{x}}_i = (\boldsymbol{x}_{i+1} - \boldsymbol{x}_{i-1})/(2\Delta) \quad \text{5-13(c)}$$

Substituting for $\ddot{\boldsymbol{x}}_i$ and $\dot{\boldsymbol{x}}_i$ in eq. 5-13(a) using eq. 5-13(b) and 5-13(c), and rearranging for $\boldsymbol{x}_{i+1}$ gives an expression for the displacement at the next timestep based on the displacements at the current timestep (i) and previous timestep ($i-1$):

$$\boldsymbol{x}_{i+1} = \left(\frac{M}{\Delta^2} + \frac{C}{2\Delta}\right)^{-1}\left[\boldsymbol{F}_i - \left(K - \frac{2M}{\Delta^2}\right)\boldsymbol{x}_i - \left(\frac{M}{\Delta^2} - \frac{C}{2\Delta}\right)\boldsymbol{x}_{i-1}\right] \quad \text{5-14}$$

It can be shown that this method is, in fact, identical in response to the Newmark explicit method, and so the only distinction between the two is the numerical implementation – the CDM only uses measured displacements, but from the last two timesteps, while the Newmark explicit method uses only values from the previous timestep but requires the velocity to be computed after the displacement has been applied. These methods have no numerical dissipation and produce zero amplitude error but result in period shortening which increases with the size of the timestep [94]. To ensure stability for a system with a highest circular natural frequency of $\omega_{max} = 2\pi f_{max}$, the timestep must satisfy:

$$\delta t < 2/\omega_{max} \quad \text{5-15}$$

5.3.5. Runge-Kutta Methods

The numerical substructures defined by Eq. 5-1 can be represented graphically by the block diagrams shown in Figure 5.3, where s is the Laplace variable so the "$1/s$" block indicates integration with respect to time. Alternatively, the second order differential equation of motion can be reduced to a first order differential equation using state space representation. For example, in the case of the SDOF system the state vector, $\boldsymbol{z}$, and input vector, $\boldsymbol{u}$, would be defined as:

$$\boldsymbol{z} = \begin{bmatrix} x \\ \dot{x} \end{bmatrix} \text{ and } \boldsymbol{u} = \begin{bmatrix} \ddot{x}_g \\ r \end{bmatrix} \tag{5-16}$$

Then the state-space equations, corresponding to the block diagram in Figure 5.4, would be:

$$\dot{\boldsymbol{z}} = A\boldsymbol{z} + B\boldsymbol{u} \text{ and } x = C\boldsymbol{z} + D\boldsymbol{u} \tag{5-17}$$

where $A = -\begin{bmatrix} 0 & 1 \\ m^{-1}k & m^{-1}c \end{bmatrix}$, $B = -\begin{bmatrix} 0 & 0 \\ 1 & m^{-1} \end{bmatrix}$, $C = [1 \quad 0]$ and $D = [0 \quad 0]$. Whichever representation is used, the problem is then to find a suitable solver to carry out the numerical integration in the integrator block. The RTHS system requires an explicit solver with a fixed timestep. Simulink® includes a range of solvers belonging to the Runge-Kutta family named *ode1*, *ode2*, etc. on the basis of their order of accuracy, as listed in Table 5.1. The problem to be solved by the integrator can be expressed as:

$$\frac{dz}{dt} = f(t, z) \tag{5-18}$$

The simplest member of the Runge-Kutta family is the Euler method, which calculates the value at the next timestep as:

$$z_{i+1} = z_i + \delta t f(t_i, z_i) \tag{5-19}$$

However, this only has first order accuracy since it assumes the gradient to be constant over the timestep and is insufficient for RTHS with a practical timestep increment. To increase the order of accuracy, additional function evaluations must be made during each timestep. For example, the second order Heun's method uses the mean of the gradient at the start of the interval and a prediction of the gradient at the end of the interval (obtained using the Euler method) and can be expressed as:

$$z_{i+1} = z_i + \frac{\delta t}{2}\Big(f(t_i, z_i) + f\big(t_i + \delta t, z_i + \delta t f(t_i, z_i)\big)\Big) \tag{5-20}$$

which requires two function evaluations per timestep. The method referred to as the Bogacki-Shampine method in Simulink® [95] is:

$$z_{i+1} = z_i + \delta t \left[\frac{2}{9} f(t_i, z_i) + \frac{1}{3} f\left(t_i + \frac{1}{2}\delta t, z_i + \frac{1}{2}\delta t f(t_i, z_i)\right) + \frac{4}{9} f\left(t_i + \frac{3}{4}\delta t, z_i + \frac{3}{4}\delta t f\left(t_i + \frac{1}{2}\delta t, z_i + \frac{1}{2}\delta t f(t_i, z_i)\right)\right)\right] \tag{5-21}$$

which achieves third order accuracy using three function evaluations. This is, in fact, due to Ralston [96] – Bogacki and Shampine [97] extended this method to include an embedded second order method to allow an error estimate to be obtained. This information can then be used to adapt the step size when a variable timestep is used but, since a fixed timestep is required for RTHS, the embedded method is not used. Clearly, the cost of increasing the order of accuracy of the integration method is extra function evaluations, and therefore an increased computation time.

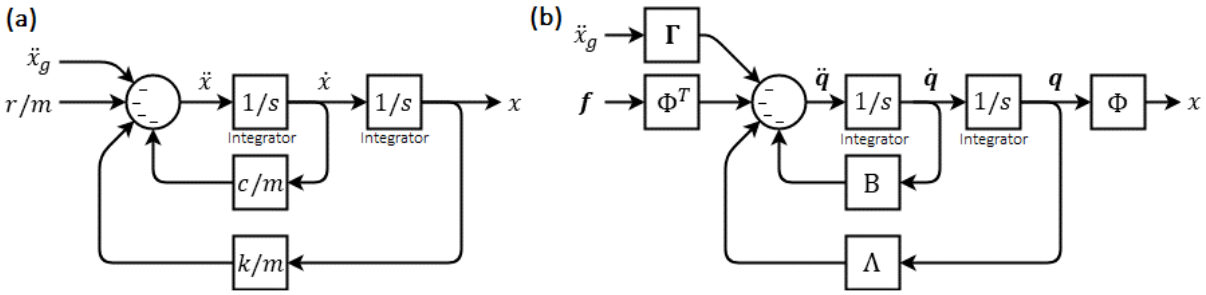

Figure 5.3 – Block diagram representation of numerical substructure: (a) SDOF structure, and (b) MDOF structure using modal superposition

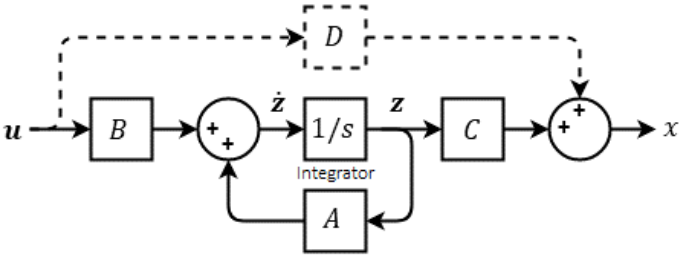

Figure 5.4 – State-space system

Order of Accuracy	Name	Method
1	ode1	Euler
2	ode2	Heun
3	ode3	Bogacki-Shampine
4	ode4	Runge-Kutta
5	ode5	Dormand-Prince
8	ode8	Dormand-Prince

Table 5.1 – Runge-Kutta type methods in Simulink®

5.3.6. Unconditionally Stable Explicit Methods

The requirement that explicit algorithms be used for hybrid testing restricted researchers to using conditionally stable algorithms, such as the CDM, imposing limitations on size of timestep which could be hard to achieve. However, this limitation was challenged when Chang [88] proposed a method for pseudo-dynamic testing which is both explicit and unconditionally stable. Chang's algorithm follows the same steps as the Newmark explicit method but with the scalar coefficients $(0.5-\beta)$ and β in Eq. 5-10(b) replaced by coefficient matrices β_1 and β_2 which are determined prior to the test based on the

mass, damping and initial stiffness matrices, and the timestep. Its computational cost is therefore similar to the Newmark Explicit and CDM methods, with the only added complexity being the need to determine the initial stiffness of the physical substructure prior to the test so that the initial stiffness matrix can be determined for calculating β_1 and β_2. For linear systems, the method has been shown to exhibit the same properties, in terms of period elongation and equivalent damping, as the unconditionally stable, implicit CAAM.

Chen and Ricles [90] later used discrete control theory methods to produce another unconditionally stable, explicit method, referred to as the CR-algorithm. Like Chang's method, this algorithm follows the Newmark Explicit method in terms of implementation, while exhibiting the accuracy properties of the CAAM. The CR-algorithm is defined by:

$$M\ddot{\boldsymbol{x}}_{i+1} + C\dot{\boldsymbol{x}}_{i+1} + K\boldsymbol{x}_{i+1} = \boldsymbol{F}_{i+1} \quad \text{5-22(a)}$$

$$\boldsymbol{x}_{i+1} = \boldsymbol{x}_i + \Delta\, \dot{\boldsymbol{x}}_i + \alpha_2 \Delta^2 \ddot{\boldsymbol{x}}_i \quad \text{5-22(b)}$$

$$\dot{\boldsymbol{x}}_{i+1} = \dot{\boldsymbol{x}}_i + \alpha_1 \Delta \ddot{\boldsymbol{x}}_i \quad \text{5-22(c)}$$

where the coefficient matrices, α_1 and α_2, are calculated before the start of the test using:

$$\alpha_1 = \alpha_2 = 4(4M + 2\delta t C + \delta t^2 K_0)^{-1} M \quad \text{5-23}$$

where K_0 is the initial stiffness of the combined structure. In the case of a SDOF structure, or for an individual mode when using the modal superposition approach, this reduces to:

$$\alpha_1 = \alpha_2 = \frac{4}{4 + 4\zeta\omega_n \delta t + \omega_n^2 \delta t^2} \quad \text{5-24}$$

where, in the case of modal superposition, ω_n should be the circular natural frequency of the mode in question. A potential advantage of the CR-algorithm over Chang's algorithm is that it is explicit in terms of velocity as well as displacement (Eq. 5-22(c)) which can simplify the implementation of the algorithm.

Notice that, unlike the unconditionally stable implicit algorithms (like the CAAM), the coefficients or coefficient matrices of these algorithms depend on the properties of the system (M, C, and K) in addition to Δ. It is therefore important to consider how the properties of the system will be affected by the nonlinearity of the physical substructure and of the numerical substructure, if that includes

nonlinear behaviour, since this will change the effective properties of the system (most significantly K, and hence ω_n). It can be shown that the CR-algorithm remains unconditionally stable as $\omega_n \to 0$, and hence the algorithm is stable for structures with softening behaviour [10] [90]. This applies to BRBs since their effective stiffness decreases as yielding occurs.

Just as Hilber et al. [93] modified the Newmark implicit method [79] to provide favourable numerical dissipation of high modes through the use of a factor α, Kolay and Ricles [98] have incorporated controllable numerical dissipation into an unconditionally stable, explicit algorithm to produce the KR-α method. The numerical dissipation is controlled by a parameter, ρ_∞, and the algorithm reduces to the CR-algorithm for $\rho_\infty = 1$.

5.3.7. Selected Algorithm

The Heun method has been chosen for this project, implemented as in Figure 5.3. Runge-Kutta solvers are built into Simulink® making them convenient to implement and, with the exception of the first order Euler method, they give good stability and accuracy. The Heun method is a predictor-corrector method. In each timestep, it first evaluates the function to obtain the gradient at the start of the timestep. It then uses the Euler method to extrapolate ahead by one timestep and the function is evaluated again to obtain an estimate of the gradient at the end of the timestep. Finally, in the corrector step, the mean of the gradients at the start and end of the timestep is taken and used to calculate a more accurate estimate of the values at the end of the timestep. To implement this precisely in a RTHS test, the predicted displacement would have to be applied to the physical substructure in order to obtain the predicted force to be used in the second function evaluation to obtain the corrected displacement to be applied. This would generate a discontinuity in the motion of the physical substructure and, when the acceleration is negative, it would result in an overshoot during the predictor step and therefore a reversal of direction during the corrector step. It is not possible to apply such a displacement pattern in a real-time test due to the need for continuous motion. Even in a slow PsD test with discretised loading intervals where this would be possible, it would be undesirable because it would result in an

incorrect load path being applied to the physical substructure leading to errors in the resulting hysteretic response. In the RTHS, the measured force is therefore held constant over the timestep, equivalent to applying a zero-order hold. This slightly reduces the accuracy since the force is not updated for the corrector step but, given the small timestep, the performance remains satisfactory. This also means that the additional benefit of using a higher order Runge-Kutta method is reduced due to the force not being updated at intermediate points during the timestep. In addition, the effects are mitigated by the use of the stiffness simulator introduced in the next section as the force output from the simulator is based on a numerical model which can extrapolate ahead during the predictor step. However, this is only a supplemental benefit, its purpose being to improve stability by providing continuous, stable force feedback in spite of any actuation errors remaining after delay compensation.

5.4. Stiffness Simulator

5.4.1. Ensuring Stable Force Feedback

The stability of the structure being simulated, and hence the stability of the overall simulation, is dependent on the structural restoring force. In RTHS testing, a significant proportion of this force can come from the physical substructure, so the properties of the measured force fed back from the physical substructure can affect the stability of the RTHS feedback loop. The previous chapter focused on the control system at the interface from the numerical substructure to the physical substructure for ensuring the target displacements are applied to the physical substructure accurately since the correct feedback force can only be obtained if the correct displacement is applied. To ensure the force feedback does not cause instability, an additional component is proposed at the interface from the physical substructure back to the numerical substructure, which is referred to here as the *stiffness simulator*. The purpose of the stiffness simulator is to generate a numerical model of the BRB's force-displacement response which can be used to provide stable force feedback, F_{sim}. The model is continually updated based on the latest available measurements of F_m and x_{enc}, whilst fitting over a large enough range to ensure a smooth variation in coefficients and avoid susceptibility to noise. The

stiffness simulator can then provide continuous force feedback based on the target displacement, x_t, even if the achieved displacement, x_{enc}, in the device differs from this. Figure 5.5 shows how the secant stiffness and tangent stiffness vary over one half-cycle of sinusoidal motion going from +17.5mm to -17.5mm, taken from the test presented in Section 4.7. Here it is the tangent stiffness that is of interest. This is initially very large due to the frictional effect, it then levels off temporarily at the elastic stiffness before decreasing again as yielding occurs and approaches zero asymptotically. As mentioned above, stiff behaviour can have a detrimental effect on the stability of conditionally stable integration algorithms, like the explicit algorithms commonly used in RTHS, potentially requiring infeasibly short timesteps to ensure stability.

To mitigate the destabilising effect of the delay, Jung and Shing [99] applied an approximate correction to the force fed back from the physical substructure which, if applied to this system, would give:

$$F_{sim,i} = F_{m,i} + K_1\left(x_{t,i} - x_{enc,i}\right) \qquad 5\text{-}25$$

where K_1 is the initial stiffness of the physical substructure. When a difference occurs between x_t and x_{enc} due to a delay, this extrapolates from the measured force to give an estimate of what the force would be if the target displacement had been achieved, if the current stiffness were equal to the initial stiffness. A similar approach was implemented by Bonnet et al. [68]. If eq. 5-25 is substituted into Eq. 4-4 in the derivation of Eq. 4-6, it can be shown that this correction can potentially be used to reduce the negative damping introduced by the delay. If the physical substructure had a constant stiffness

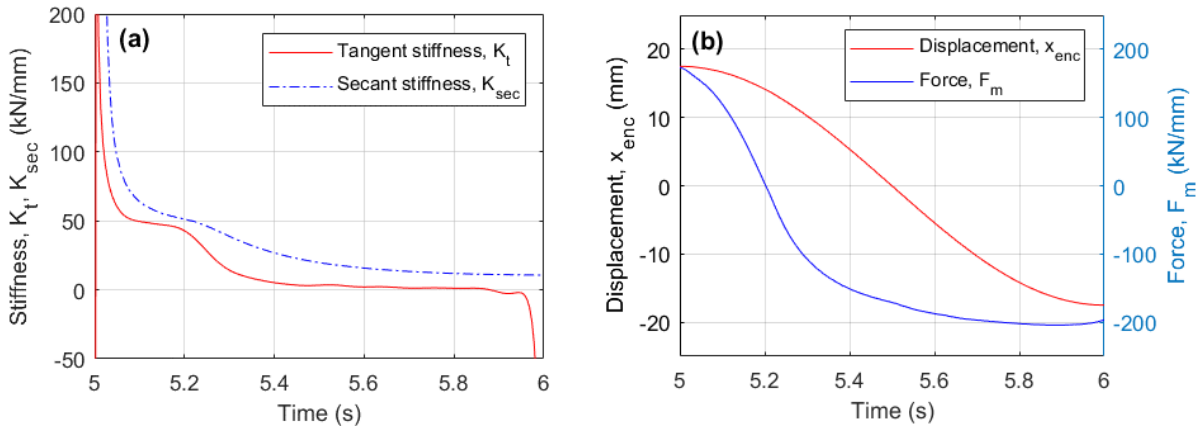

Figure 5.5 – (a) Variation of tangent stiffness and secant stiffness over a half-cycle, (b) displacement and force over half-cycle from which stiffnesses calculated

equal to K_1 then eq. 5-25 would completely cancel out the effect of the delay and therefore prevent the introduction of negative damping. Of course, in cases of practical interest, the actual stiffness of the physical substructure will vary but provided the value of K_1 is greater than the actual stiffness then the correction based on K_1 will introduce additional damping to the system. This means that for a softening system, where the current stiffness is always less than or equal to the initial stiffness, this correction will not destabilise the hybrid simulation. The introduction of additional damping will, however, affect the accuracy of the simulation, and this will depend on the size of the delay and the variability of the stiffness during the test. While this improves the stability properties of the system, it does not remove the need for delay compensation in the applied displacements, since only if the correct displacement history is applied will the true hysteretic response of the device be obtained.

Chen and Tsai [100] adopted a similar approach but replaced the initial stiffness, K_1, in eq. 5-25 with an estimate of the current tangent stiffness of the physical substructure, K_t, to improve the accuracy of the corrected force. In general, it is not possible to measure K_t accurately over an individual interval due to noise in the measured signals so a moving average of the tangent stiffness over a number of previous timesteps was used to provide an estimate to the tangent stiffness:

$$K_{t,i}^{*} = \frac{1}{w} \sum_{j=i-w+1}^{i} \frac{F_{m,j} - F_{m,j-1}}{x_{enc,j} - x_{enc,j-1}} \qquad 5\text{-}26$$

where w is the number of timesteps prior to the current timestep, i, over which the average is taken. A small w is desirable to give a close approximation to the current stiffness, but it must be large enough to prevent the approximation becoming sensitive to measurement noise. It was shown in numerical studies that using force compensation in addition to delay compensation could significantly reduce the accumulated displacement error compared to using delay compensation alone [100]. The stiffness simulator derived below is designed to improve on this approach by not just extrapolating about the current measured force but by fitting a continually updated numerical model to the measured force displacement response of the physical substructure.

5.4.2. Stiffness Simulator Equations

Since BRBs are displacement dependent devices, the following numerical model is proposed:

$$F_{sim}(t) = \alpha_0 + \alpha_1 x_t(t) \tag{5-27}$$

where F_{sim} is the estimate of what the force will be at displacement x_t, and the fitting coefficients, α_0 and α_1, are continually updated using feedback of the actual force, F_m, and actual displacement, x_{enc}, to give the best fit. The coefficient α_1 is an estimate of the tangent stiffness while α_0 is the force offset – where the line of gradient α_1 passing through the point (x_t, F_{sim}) intersects the force axis. For fitting the coefficients, the following error function is proposed which incorporates an exponential term to give more recent terms a heavier weighting so that the model fits to the most recent data:

$$R^2(t) = \frac{1}{\lambda}\int_0^t e^{-\tau/\lambda}\left[F_m(t-\tau) - F_{sim,est}(t-\tau)\right]^2 d\tau \tag{5-28}$$

where λ is the time-constant of the weighting function and $F_{sim,est}$ is the force given by the model when the actual displacement of the BRB, x_{enc}, is used in place of the target displacement, x_t:

$$F_{sim,est}(t) = \alpha_0 + \alpha_1 x_{enc}(t) \tag{5-29}$$

A relationship for determining the coefficients is obtained by setting the partial derivatives of eq. 5-28 with respect to each of the coefficients to zero:

$$\frac{\partial R}{\partial \alpha_0} = 0, \qquad \frac{\partial R}{\partial \alpha_1} = 0 \tag{5-30}$$

Expanding Eqs. 5-30 and writing them in matrix form gives:

$$\begin{bmatrix} \int_0^t \frac{e^{-\frac{\tau}{\lambda}}}{\lambda} d\tau & \int_0^t \frac{e^{-\frac{\tau}{\lambda}}}{\lambda} x_{enc}(t-\tau) d\tau \\ \int_0^t \frac{e^{-\frac{\tau}{\lambda}}}{\lambda} x_{enc}(t-\tau) d\tau & \int_0^t \frac{e^{-\frac{\tau}{\lambda}}}{\lambda} x_{enc}^2(t-\tau) d\tau \end{bmatrix} \begin{bmatrix} \alpha_0 \\ \alpha_1 \end{bmatrix} = \begin{bmatrix} \int_0^t \frac{e^{-\frac{\tau}{\lambda}}}{\lambda} F_m(t-\tau) d\tau \\ \int_0^t \frac{e^{-\frac{\tau}{\lambda}}}{\lambda} x_{enc}(t-\tau) F_m(t-\tau) d\tau \end{bmatrix} \tag{5-31(a)}$$

or:

$$A\boldsymbol{\alpha} = \boldsymbol{b} \tag{5-31(b)}$$

Notice that, due to the use of the exponential weighting function, the coefficients of the fitting matrix, A, and the vector, $\boldsymbol{b}$, can be determined by filtering the relevant signal ($x_t(t)$, etc.) through a filter with the transfer function:

$$\frac{1}{s+1/\lambda} \qquad 5\text{-}32$$

which provides a computationally efficient means of determining the continually updated matrix coefficients. In this system, the filtering is performed digitally. Providing A is invertible, the coefficients of the simulator, $\boldsymbol{\alpha} = [\alpha_0, \alpha_1]^T$, at each timestep can be determined by solving the matrix equation:

$$\boldsymbol{\alpha} = A^{-1}\boldsymbol{b} \qquad 5\text{-}33$$

The behaviour of the filter depends on the value of the time constant λ: the smaller the value of λ, the more heavily the more recent data points are weighted in the error function. Hence the choice of λ is a compromise, a smaller value allows the coefficients α_0 and α_1 to vary more rapidly, giving a closer fit to more recent data, but it also increases the susceptibility of the system to noise and other errors. The implementation of the above system is shown in Figure 5.6.

Note that the coefficient fitting procedure described by equations Eqs. 5-27 to 5-33 is, in fact, the same as the procedure used to fit the coefficients of the mATS compensator described in Section 4.4. Here the process is expressed in continuous form with the values in the fitting equations determined by filtering the signals; while in the mATS compensator the process was expressed in discrete form with the values in the fitting equations determined from a recursive formulation. However, either

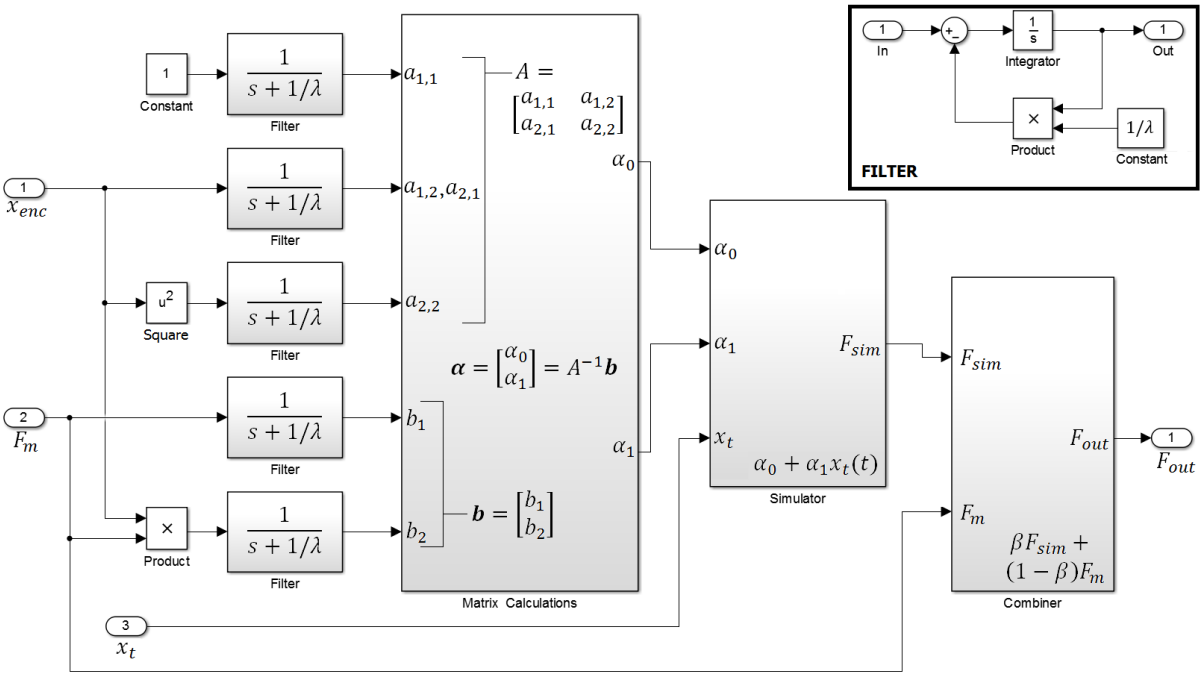

Figure 5.6 – Schematic of stiffness simulator

implementation could be used in either case and produce the same output. For a timestep, Δ, it can be shown that the relationship between the effective time-window, q_{eff}, of the mATS compensator and the time constant, λ, of the stiffness simulator which would produce the same response is:

$$\lambda = q_{eff}\Delta = -\frac{\Delta}{\ln(\rho)} \qquad 5\text{-}34$$

where q_{eff} is expressed in timesteps and λ in units of time.

The force simulator provides continuous, stable force feedback but it will affect accuracy since the coefficients, α_0 and α_1, are fitted to past data and will therefore lag behind the actual values. The resulting delay in the estimated stiffness properties is not destabilising, however, like a delay in the force response would. The closeness of fit of the simulator response increases as λ is decreased, since this means the fit is more heavily weighted to the most recent measurements and can therefore track the changing properties more closely, but only up to a point. If λ is too small the coefficients become over-fitted and become sensitive to noise in F_m and x_{enc}. While the delay compensator aims to make $x_{enc} = x_t$, it will not always achieve this exactly, in which case the stiffness simulator extrapolates to predict what the force will be at x_t. If α_0 and α_1 are varying wildly due to fitting to noise in the signal, this extrapolated force estimate could be far from the true value.

In the final step of the simulator the output force, F_t, is calculated as a weighted average of the simulated force, F_{sim}, and measured force, F_m:

$$F_{out} = \beta F_{sim} + (1 - \beta)F_m \qquad 5\text{-}35$$

where β is a constant between 0, resulting in direct force feedback from the physical substructure, and 1, resulting in all the force feedback coming from the simulator. It was found that, due to the accuracy of displacement provided by the mATS compensator, having only a portion of the force feedback coming from the simulator was enough to ensure stability so this was combined with the measured force to improve the accuracy.

5.4.3. Stiffness Simulator Initial Coefficients

At the start of the test, there will be no past data for the simulator to fit to, so the coefficients, α_0 and α_1, must be set to suitable initial values. This can be achieved by specifying the initial values of the coefficients of the fitting matrix, A, and vector, $\boldsymbol{b}$, from eq. 5-31. This is done by specifying the initial values of the integrator block ($1/s$) in the filters which generate these coefficients in Simulink®. Begin by labelling the coefficients so that eq. 5-31 becomes:

$$\begin{bmatrix} a_{1,1} & a_{1,2} \\ a_{2,1} & a_{2,2} \end{bmatrix} \begin{bmatrix} \alpha_0 \\ \alpha_1 \end{bmatrix} = \begin{bmatrix} b_1 \\ b_2 \end{bmatrix} \quad 5\text{-}36$$

Appropriate initial values of the simulator coefficients are $\alpha_0 = 0$ and $\alpha_1 = K_1$, where K_1 is the initial (pre-yield) stiffness of the BRB, calculated as 53.8kN/mm. The off-diagonal terms, $a_{1,2}$ and $a_{2,1}$, must be equal, so one solution is to start by setting $a_{1,2} = a_{2,1} = 0$ to decouple the equations, leaving:

$$a_{1,1}\alpha_0 = b_1 \quad 5\text{-}37$$

$$a_{2,2}\alpha_1 = b_2 \quad 5\text{-}38$$

The value of α_0 can therefore be set to zero by setting $a_{1,1} > 0$ and $b_1 = 0$ in eq. 5-37, and α_1 can be set to K_1 by setting $a_{2,2} > 0$ and $b_2 = K_1/a_{2,2}$ in eq. 5-38. Since $a_{1,1}$ and $a_{2,2}$ can be scaled freely, it makes sense to set $a_{1,1} = a_{2,2}$ to produce a well-conditioned matrix. Finally, the final value theorem shows that $a_{1,1} \to \lambda$ as $t \to \infty$, giving an indication of suitable magnitudes for the initial values of the coefficients: $a_{1,1} = a_{2,2} = \lambda$. After the start of the hybrid simulation, it may take some time for enough displacement to occur to allow the simulator to accurately fit the coefficients. To prevent problems with initialisation, when insufficient motion has occurred for eq. 5-33 to give a good fit, the simulator coefficients are held constant until a specified amount of displacement has occurred, after which the simulator takes over.

5.4.4. Testing Stiffness Simulator

The time-constant, λ, of the stiffness simulator controls the speed at which the simulator coefficients, α_0 and α_1, are updated in response to changes in the stiffness properties of the BRB. To investigate appropriate values of λ for RTHS testing, the force simulator was tested with various values of λ in response to pre-recorded inputs: x_{enc}, F_m and x_t. These inputs were recorded from a previous RTHS test so that they contain the signal noise, BRB nonlinearity and residual actuation errors actually experienced in the test. The hybrid test these inputs were recorded from simulated a structure with a natural frequency of 1Hz (close to the expected fundamental frequency of a BRBF) subjected to the El Centro ground motion scaled to 20.4%. This had a peak displacement of 11.5mm, giving a significant amount of yielding and hence a significant variation in tangent stiffness. Figure 5.7 shows the force, F_{sim}, produced by simulators having time-constants of 25ms, 12.5ms and 6.25ms for this set of inputs.

The simulated force, F_{sim}, for $\lambda = 25ms$ (Figure 5.7(a)) follows the measured force, F_m, quite closely, with a difference noticeable around the peaks, especially just after the peak where there is a sudden change in stiffness as the direction reverses, and it takes a small amount of time for the simulator coefficients to catch up. For $\lambda = 12.5ms$ (Figure 5.7(b)), F_{sim} follows F_m even more closely. A difference is still noticeable just after the peaks, but this is greatly reduced, and the simulator catches up in much less time. When λ is further reduced to $6.25ms$ (Figure 5.7(c)) it is apparent that the simulator has become over fitted, leading to a discontinuity in the force response after a direction reversal. The high rate at which the coefficients are updated leads to it fitting very closely to the very high tangent stiffness which occurs immediately after a direction reversal. This coincides with a disparity occurring between x_{enc} and x_t due to the high stiffness combined with the flexibility of the rig. While the disparity is small and momentary, when combined with the very high simulator stiffness, a_1, it leads to a significant error in the extrapolated force and causes a discontinuity as the force overshoots before being corrected. Figure 5.8 shows the hysteresis curves for these three cases, comparing the measured BRB behaviour, F_m vs. x_{enc}, to the simulated BRB behaviour, F_{sim} vs. x_t.

These show a disparity developing following changes in stiffness due to direction reversal and due to yielding, which reduces as λ is decreased. Figure 5.8(d) shows a close up of the behaviour at peaks for $\lambda = 6.25ms$ showing the undesirable behaviour caused by overfitting. The effect of λ on the variation of the simulator coefficients is shown in Figure 5.9, which also shows the computed tangent stiffness, $K_t = dF_m/dx_{enc}$, for comparison. The simulator stiffness, a_1, is seen to match the shape of K_t but with a small delay, which increases with λ. Increasing λ also smooths out the peaks, avoiding very large simulated stiffnesses, which is beneficial to the stability of the system. Based on this testing, 12.5ms

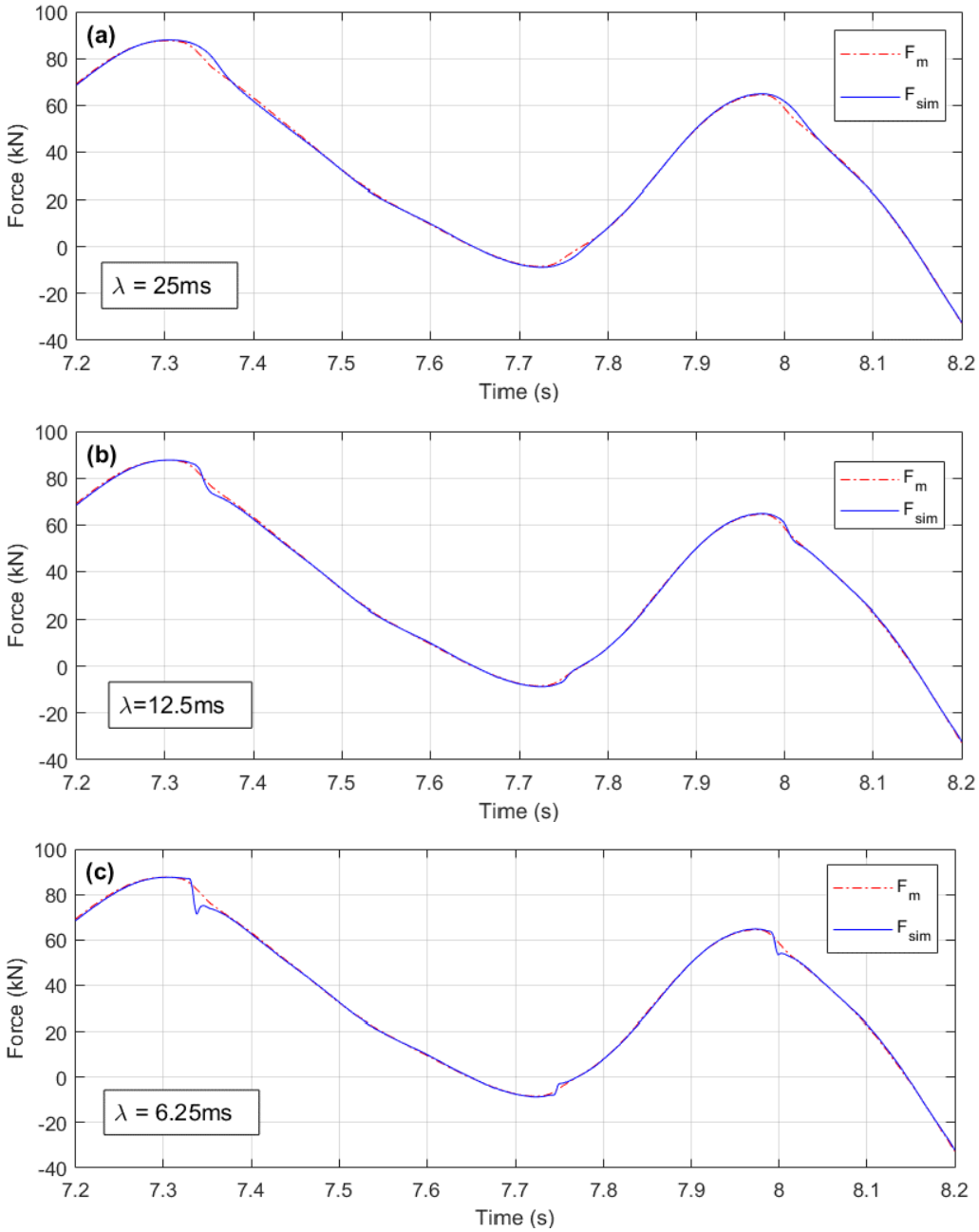

Figure 5.7 – Stiffness simulator force response: (a) $\lambda = 25\text{ms}$, (b) $\lambda = 12.5\text{ms}$, and (c) $\lambda = 6.25\text{ms}$

was selected as a suitable value for λ for use in RTHS testing, giving a balance between matching the BRB stiffness closely while avoiding extrapolation errors by limiting the peak stiffnesses experienced by the system. The use of such a small value is made possible by the performance of the delay compensator which ensures a close match between x_t and x_{enc} so that the amount of extrapolation carried out by the simulator is very small. Note that a *delay* in the simulated stiffness properties will result in an *amplitude error* in the simulated force, F_{sim}, and so does not have the destabilising effect that a straightforward delay in the force feedback would have.

The coefficient β from Eq. 5-35 is used to create a force feedback signal, F_t, which is a weighted average of the measured force, F_m, and the simulator force, F_{sim}. The system remained stable for values of β less than 1.0, so a proportion of F_m was included in the feedback to improve accuracy. In fact, in a number of cases, it was possible to run the tests without the simulator ($\beta = 0$). Figure 5.10 shows the computed displacement, x_t, for one such RTHS test, along with that for the same hybrid simulation

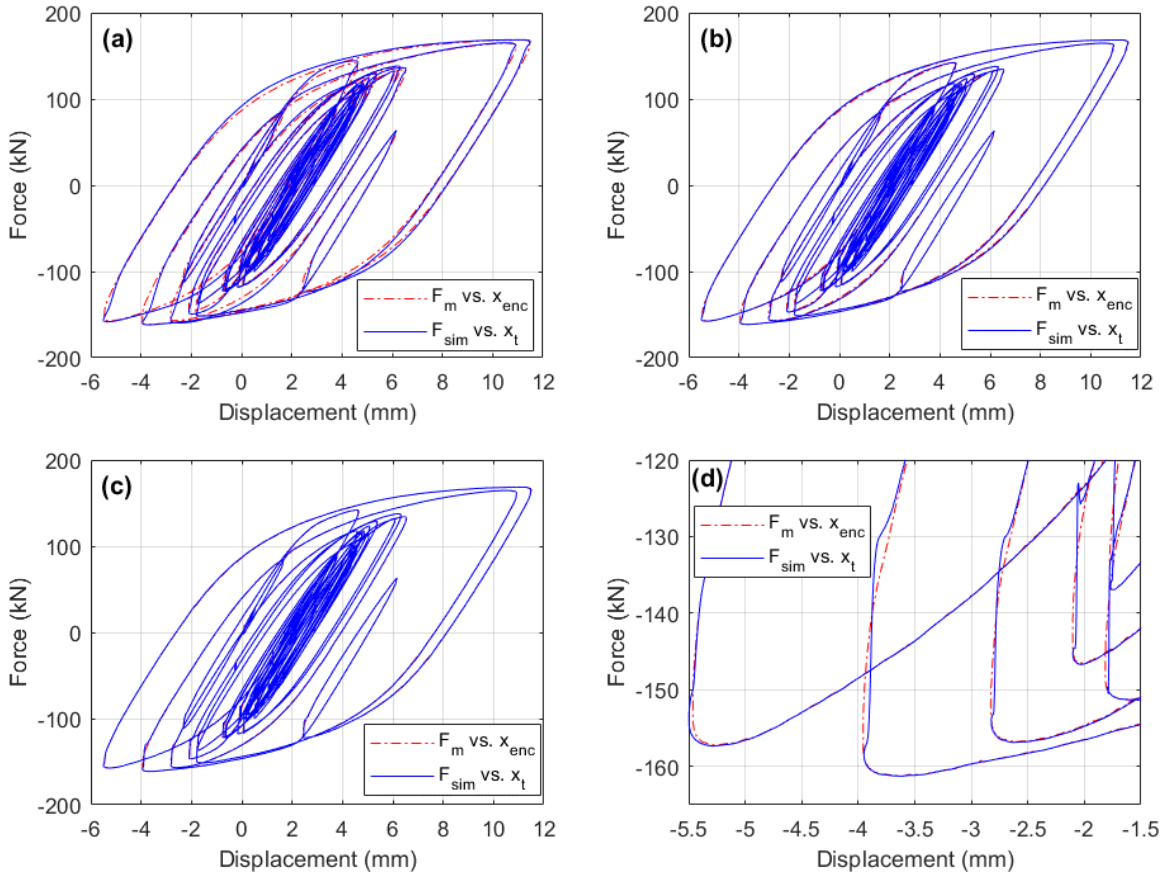

Figure 5.8 – Comparison of hysteresis curves of measured behaviour and simulator response: (a) $\lambda = 25ms$, (b) $\lambda = 12.5ms$, (c) $\lambda = 6.25ms$, and (d) close up of peak for $\lambda = 6.25ms$

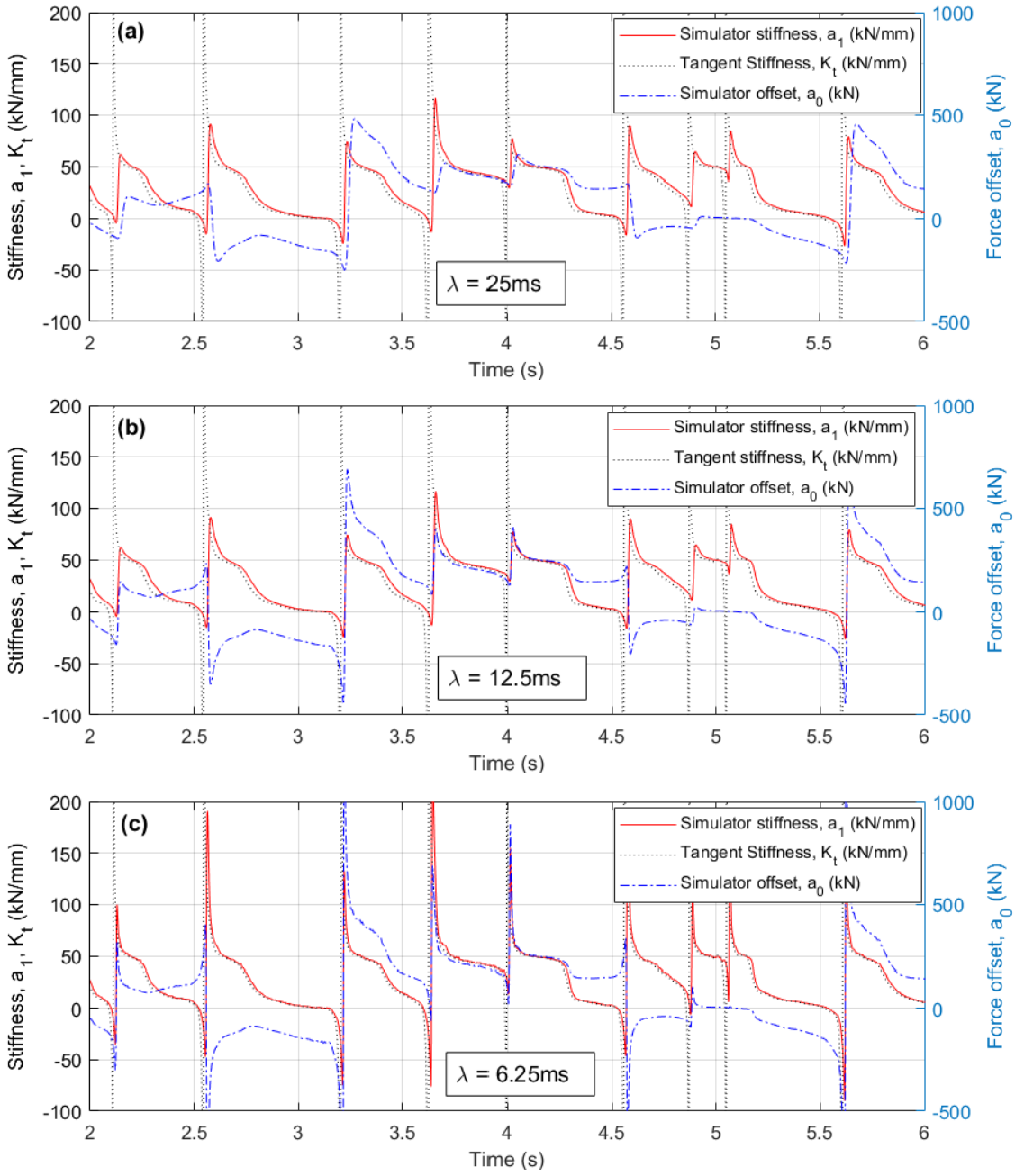

Figure 5.9 – Effect of simulator time-constant, λ, on coefficients of stiffness simulator: (a) $\lambda = 25ms$, (b) $\lambda = 12.5ms$, and (c) $\lambda = 6.25ms$

repeated with $\beta = 0.9$. This simulated a 1Hz structure with 2% inherent damping responding to the El Centro ground motion scaled to 20.4% where all of the stiffness came from the physical substructure to maximise the effect of the force feedback on the response. Yielding resulted in a residual deformation of 2.87mm after the first test, so the test was repeated with the direction of the input ground acceleration reversed to cancel this out as far as possible to improve the comparability of the results, although a small residual deflection of 0.8mm remained. Figure 5.10 shows a difference in the

computed displacement over the first few seconds due to the simulator operating on initial values and only kicking in after approximately 1.3s. After this, however, a very close match is seen between the two for the next ten seconds or so, with virtually identical peak displacement (less than 0.05% difference). After approximately 12s, an offset develops between the two due to slightly different amounts of yielding, although the shapes of the displacement histories continue to match well but with just a small offset between the two. Figure 5.11 shows the corresponding hysteresis curves, showing that the shapes match well with a slight offset between the two sets on the compression side (negative displacement) during the initial cycles. In the lower left corner, a disparity between F_{sim} and F_m is apparent for the $\beta = 0.9$ case, which is due to the simulator still being in its starting up phase. After this time the hysteresis curve of F_{sim} matches that of F_m closely. Finally, Figure 5.12 compares F_{sim} and F_m for the case where $\beta = 0.9$. It shows a very close match with an NRMS force difference of 1.69% between 2s and 30s.

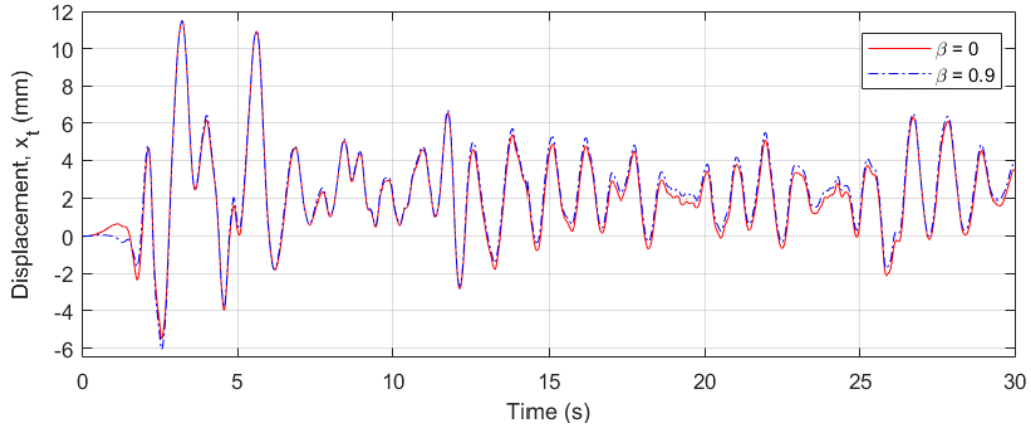

Figure 5.10 – RTHS displacement response for different simulator proportions, β

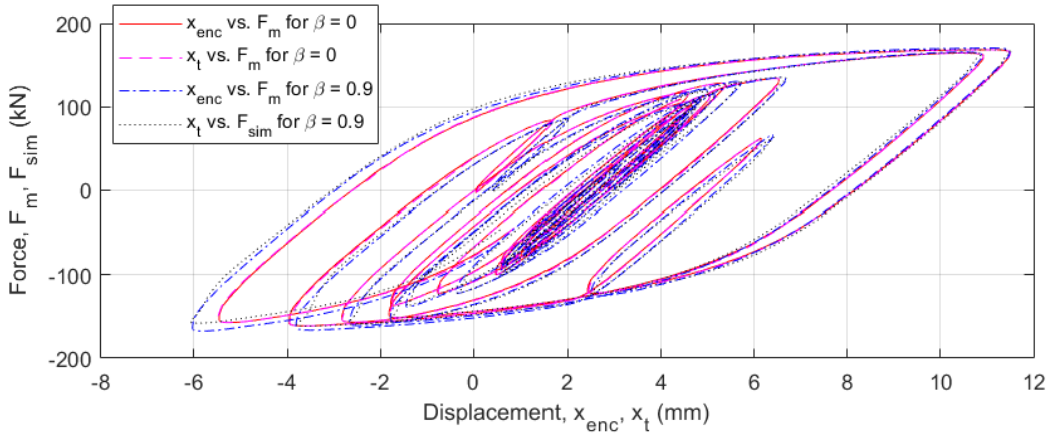

Figure 5.11 – Comparison of hysteresis curves for RTHS tests with different simulator proportions, β

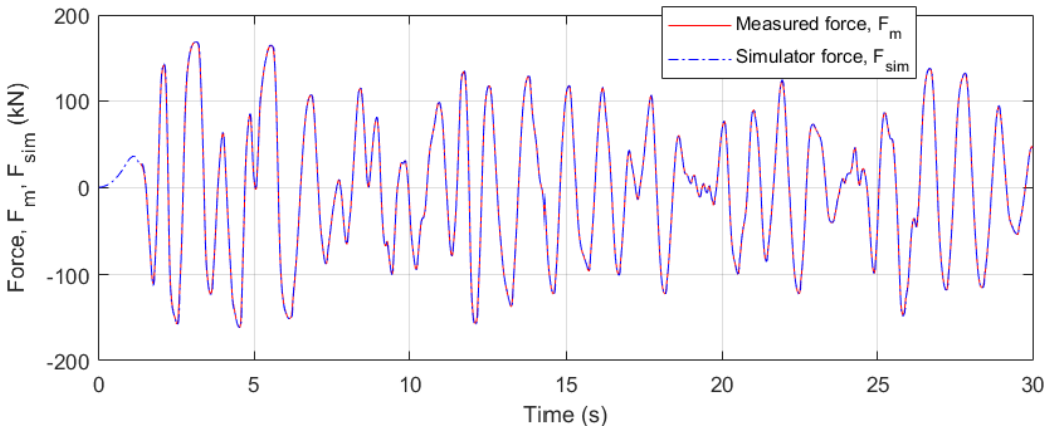

Figure 5.12 – Comparison of measured force and simulator force for RTHS with $\beta = 0.9$

5.5. Free Vibration Hybrid Testing

5.5.1. Initial Excitation

Section 5.2.2 laid out the procedure used to determine the coefficients of the numerical substructure in order to achieve a target natural frequency and inherent damping level of the simulated structure. To assess the effectiveness of this procedure and the accuracy of the combined hybrid system, a series of free vibration RTHS tests were performed. This was done by applying a ground acceleration to excite the structure at its natural frequency, after which all external inputs were held at zero so that the free response of the system could be observed. From this, the natural frequency and effective viscous damping were calculated (Eqs. 2-38 and 2-39).

The ground acceleration input, a_g, chosen for exciting the system was a Gaussian enveloped sinusoid generated by multiplying an approximation to a confined Gaussian window with a width of 2.5 times the natural period of the structure, $T_n = 1/f_n$, by a sine wave with a period of T_n, as illustrated in Figure 5.13(a). The approximate confined Gaussian window, as defined by Starosielec and Hägele [101], is given by:

$$a_g(k, N, s_t) \propto G(k) - G\left(-\frac{1}{2}\right)\left(\frac{G(k + N) + G(k - N)}{G\left(-\frac{1}{2} + N\right) + G\left(-\frac{1}{2} - N\right)}\right) \quad 5\text{-}39$$

in which the discrete Gaussian function is defined by:

$$G(k) = exp\left\{-\Delta^2\left(\frac{\left(k-\frac{N-1}{2}\right)^2}{4s_t^2}\right)\right\} \quad 5\text{-}40$$

where N is the number of timesteps making up the window, Δ is the size of the timestep, k is the integer number of the current timestep, and s_t is an approximation to the temporal width. The approximate Gaussian envelope was used because the Fourier transform of a Gaussian is also a Gaussian, so it can be used to control the bandwidth of the spectrum, as shown by the Fourier transform of the signal plotted in Figure 5.13(b).

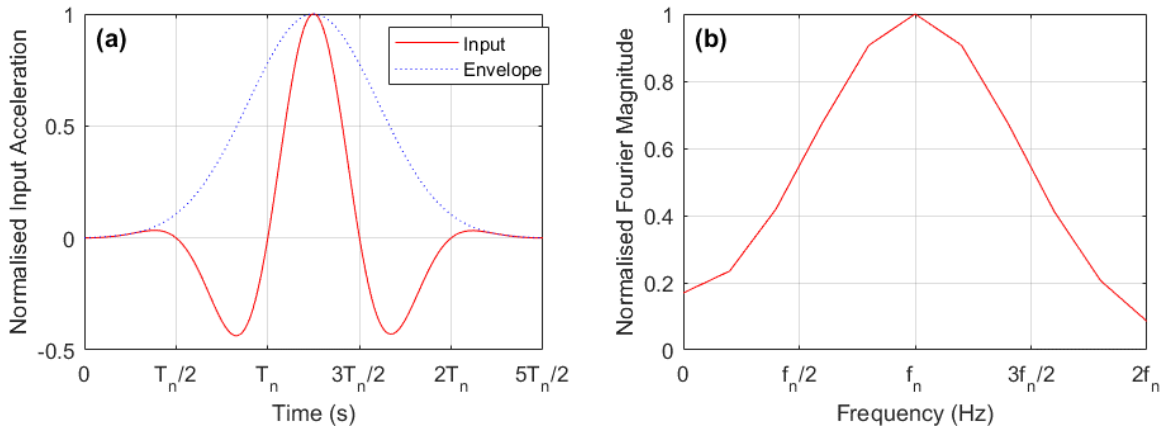

Figure 5.13 – (a) Normalised input ground acceleration; (b) Fourier transform of input ground acceleration

5.5.2. Free Vibration Response

Presented here are the results of free vibration RTHS tests for a structure with the natural frequency, f, set to 5Hz and with a range of inherent damping levels, ζ, considered in the numerical substructure. The stiffness coefficient, C_K, was set to 1.0 so that all of the stiffness came from the BRB, with none in the numerical substructure, since this is the most onerous stability case and maximises the effect of the BRB on the response of the system. The mass in the numerical substructure given by Eq. 5-5 is therefore $m = K_{phys}/\omega^2 = K_{BRB}\cos^2\theta\,/(2\pi f)^2$ where K_{BRB} is estimated to be 53.8kN/mm and θ is set to 45°.

The tests were performed for inherent damping levels of 5%, 3%, 2%, 1%, 0.5%, 0.1% and 0%. The system remained stable and the response decayed away even for the case of no damping being provided by the numerical substructure. The input ground acceleration was scaled to give a peak of 0.909mm/s^2 in order to give a peak displacement of 2mm at the start of the free motion at $t = 0.5s$, occurring for the zero-damping case (ensuring the BRB remained within its elastic range). The BRB displacement for the tests with inherent damping ratios of 5%, 2% and 0% are shown in Figure 5.14.

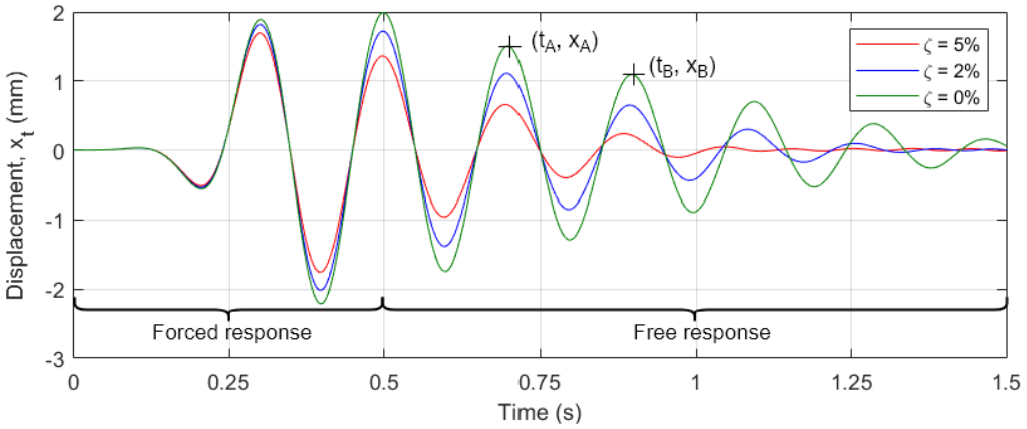

Figure 5.14 – BRB Response in 5Hz SDOF system to initial excitation for various levels of inherent damping from numerical substructure

For each test, f was calculated from the time between adjacent peaks for the first three oscillations of free vibration. For example, the coordinates, $(t_A,\ x_A)$ and $(t_B,\ x_B)$, of two adjacent peaks are indicated in Figure 5.14. The period, T, of the oscillation between these peaks is simply $t_B\ - t_A$, and f is one divided by this value. The frequencies calculated in this way are plotted in Figure 5.15(a) against the amplitude, x_A, of the peak at the start of the oscillation in question. These points form a clear trend with the frequency levelling off to the target value of 5Hz at displacements of around 2mm and above, but with the frequency increasing above the target value as the peak displacements decrease. The natural frequency is relatively constant for larger displacements, ranging from 5.1Hz at 1mm to 5.0Hz at 2mm, and increases rapidly as displacements are reduced below 1mm, reaching 5.4Hz at 0.5mm and exceeding 6Hz at 0.25mm. This behaviour can be explained by the apparent frictional behaviour observed in the BRB which introduces nonlinearity to the response even while the BRB remains elastic. This has the effect of increasing the secant stiffness of each half cycle as the peak displacement of the

cycle decreases. Since m remains constant, this increase in the effective stiffness of the structure with decreased amplitude will result in an increase in natural frequency. Hence, it is concluded that this behaviour is physical and, since the natural frequency tends towards the target value of 5Hz as the oscillation amplitude tends towards 2.5mm (the displacement for which the system coefficients are calibrated), the system is behaving as desired.

For each test, the effective damping, ζ_m, was also calculated from the logarithmic decrement between adjacent peaks for the first three oscillations:

$$\zeta_m = \frac{\delta}{\sqrt{(4\pi^2 + \delta^2)}} \quad \text{where} \quad \delta = \ln\left|\frac{x_A}{x_B}\right| \tag{5-41}$$

It was apparent that the damping experienced by the system, measured as the effective viscous damping ratio, was greater than that specified in the numerical substructure. This is expected since the aforementioned frictional effect acts to dissipate energy, seen as the area enclosed by the hysteresis curve. It is also noted that the effective viscous damping increases as the amplitude of oscillation decreases. To allow comparison between tests, the effective damping, ζ_{BRB}, due to the BRB is calculated by subtracting the damping ratio, ζ_{num}, simulated in the numerical substructure from the damping ratio, ζ_m, measured from the hybrid simulation output:

$$\zeta_{BRB} = \zeta_m - \zeta_{num} \tag{5-42}$$

These values are plotted in Figure 5.15(b) against the peak displacement at the start of the oscillation in question. The increase in ζ_{BRB} with decreased amplitude is consistent with a significant proportion of the energy dissipation being frictional in origin. Consider Eq. 2-36, which gives the equivalent viscous damping for a non-viscous device to be:

$$\zeta_{eff} = \frac{W}{2\pi K_{eff} A^2} \tag{5-43}$$

The energy dissipated per oscillation at amplitude A by a purely frictional device defined by the Coulomb model in Eq. 2-32 is:

$$W = \oint F\, dx = 2\mu NA \tag{5-44}$$

Substituting Eq. 5-44 into Eq. 5-43 and assuming the magnitude of the frictional force, μN, and the effective stiffness, K_{eff}, are constant gives:

$$\zeta_{eff} \propto 1/A \qquad 5\text{-}45$$

This is a simplification since K_{eff} has been shown to vary, but much less than in proportion to $1/A$, and the frictional component of the force varies, being larger in compression than in tension. However, it explains the hyperbolic shape of the trend seen in Figure 5.15(b), showing this to correspond to physical properties of the BRB. Figure 5.15(b) also shows an approximate trend line given by $\zeta_{BRB} = (0.055 / A) + 0.015$, where A is in mm. This indicates a source of approximately viscous damping in addition to the frictional damping component. This suggests some rate-dependency is present in the BRB response, although it is very small. This is consistent with Figure 4.35 which shows a slightly larger area enclosed by the hysteresis loop of the 5Hz cyclic test than by that of the 0.5Hz one.

The variation in natural frequency with displacement will have some effect on the damping provided by the numerical substructure, since for a fixed damping coefficient, c, the effective damping ratio is related to the natural frequency, f, by:

$$\zeta = \frac{c}{2\omega m} = \frac{c}{2(2\pi f)m} \qquad 5\text{-}46$$

Hence the effective damping from the numerical substructure reduces as the natural frequency increases but, since the variability in natural frequency is less than 10% for $A > 0.5mm$, the effect of this will be minimal.

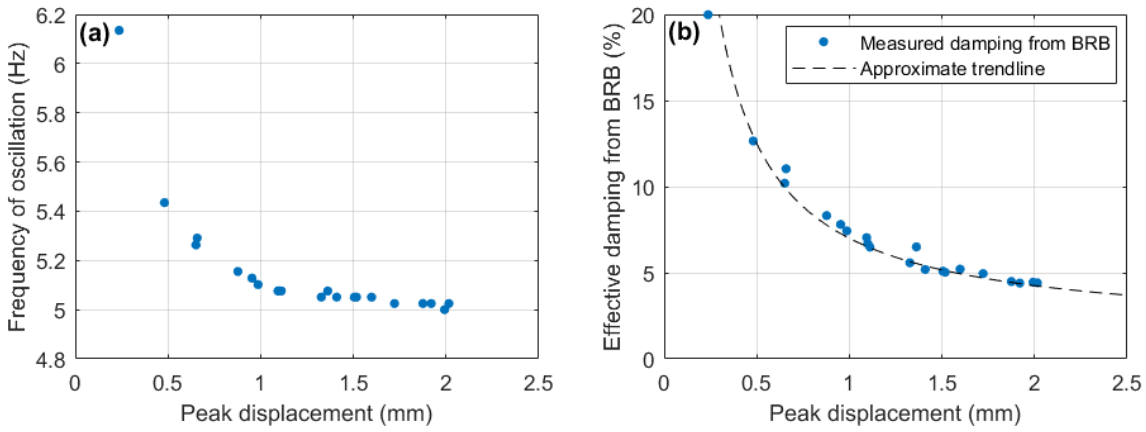

Figure 5.15 – Variation of (a) frequency of individual oscillation and (b) damping over individual oscillation with peak displacement at start of oscillation

5.5.3. Conclusions

The above RTHS tests were used to assess the modelling accuracy of the hybrid system by comparing the measured response parameters to the target values used to specify the properties of the numerical substructure (Section 5.2.2). Nonlinearity within the elastic range of the BRB causes the natural frequency of the simulated structure to vary with displacement amplitude. The BRB stiffness assumed when determining the parameters of the numerical substructure (53.8kN/mm) was the mean secant stiffness up to the yield displacement of 2.5mm. The observed natural frequency is seen to approach the target value of 5Hz as the amplitude approaches the yield displacement, showing that the hybrid simulation is accurate. The BRB is also observed to contribute a notable amount of damping while in the pre-yield range. This varies approximately hyperbolically with displacement amplitude indicating that it is largely frictional in origin. This gives large damping ratios for very small displacements but approaches reasonable values of a little under 5% as the yield displacement is approached.

5.6. High Frequency RTHS Testing

5.6.1. Stability at High Frequencies

During an earthquake, the *global* response of most structures is dominated by the lower frequency modes of oscillation. However, when simulating the structural response, the stability of the system is most dependent on the highest frequency modes. As described in Section 5.3, the stability of the integration algorithm will be compromised if the simulated structure has natural frequencies exceeding its stability limits. It was also shown in Eq. 4-7 that the negative damping introduced to the hybrid simulation by a given actuation delay is approximately proportional to the natural frequency so, even if a delay has negligible effect on the modes of interest, it could destabilise the system due to the effective damping of the highest modes becoming negative. Both sources of instability can potentially be alleviated by using methods to reduce or remove the response due to the higher frequency components. This can be achieved by using an integration with favourable numerical damping at high

frequencies, such as the HHT or KR algorithms; by adapting the numerical substructure to have artificially high damping in the higher frequency modes; or by using a modal decomposition method to remove the higher frequency modes from the simulation, which is reviewed in the next chapter. These stability requirements may clash with accuracy requirements due to the desire to minimise the effect on the modes of interest. In this section, therefore, the performance of the system at high frequencies is investigated, with the results of tests at 10Hz and 15Hz being presented here. This is around 10 times the likely fundamental frequency of a BRBF structure so the contribution of modes at this frequency to the global response is likely to be small. Hence the accuracy of the hybrid simulation for these frequencies is much less important than that for lower frequencies, the main concern being that the simulation remains stable.

5.6.2. RTHS of 10Hz Structure

To test the performance of the RTHS system at high frequencies, a hybrid simulation was run for a 10Hz SDOF structure. All of the stiffness came from the physical substructure ($C_K = 1$) to give the most onerous case for stability of the system, with the inherent damping set to 2%. The magnitude of displacements that can be applied at such a high frequency is significantly limited by the rate limits of the actuators. A conservative estimate of the maximum amplitude of oscillation that can be sustained at 10Hz is 1.8mm – conservative since it is based on a sinusoidal oscillation at the maximum amplitude, whereas the earthquake response is less uniform, so the accumulators would be able to provide a higher flow rate at the peak and to recharge during subsequent smaller magnitude oscillations.

The El Centro earthquake was used as the input ground acceleration, which was scaled to avoid saturation of the actuator velocity. Prior to performing the hybrid simulations, numerical simulations were run with the bilinear model shown in

Figure 5.16 used in place of the physical substructure to estimate an appropriate earthquake scale factor. This bilinear model has a high stiffness of 112.5kN/mm for the first 0.04mm of displacement to model the frictional effect followed by a stiffness of 53.8kN/mm. This predicted a peak displacement

of 1.75mm in tension for an earthquake scale factor of 1.75 (a PGA of 5.98mm/s^2), so this scale factor was used in the RTHS test. In addition to the real-time test, an identical test was run but with a time dilation factor, η, of 5 so that, from a stability stand-point, the effective frequency was 2Hz.

Figure 5.17 shows the displacement response during the real-time hybrid simulation, which had a peak displacement of 1.67mm, just slightly less than was predicted. It shows that the system not only remains stable at this high natural frequency, but also that the accuracy of the applied displacement is very good. This can be seen by the relatively small error in Figure 5.18, resulting in an NRMS error of 5.42%, while the difference in peak values of x_{enc} and x_t was just 0.17%. The coefficients of the mATS compensator are shown in Figure 5.19. They vary rapidly due to the frequent reversals of direction but remain within the range of reasonable values. Also, they remain stable in spite of relatively long periods with very small displacement (e.g. the displacement does not exceed 0.2mm between 6s and 8s). The mean actuator delay before delay compensation is 10.7ms which, by Horiuchi's approximation (Eq. 4-7), would introduce a negative damping, ζ_{eq}, of −34%, which demonstrates the vital role of the mATS compensator. Figure 5.20 shows the force response, with Figure 5.20(a) showing that the force from the stiffness simulator, F_{sim}, closely matches the measured force, F_m. The close-up shown in Figure 5.20(b) corresponds to the displacement in Figure 5.17(c). Comparing the two, it is seen that where a displacement error occurs due to imperfect actuation the stiffness simulator extrapolates the force to compensate. Figure 5.20(c) compares the measured hysteresis curve (F_m vs. x_{enc}) to that given by the force simulator (F_{sim} vs. x_t) which shows a good match given the high frequency of the test.

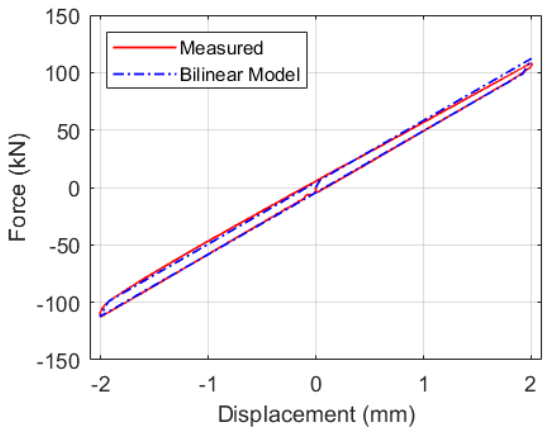

Figure 5.16 – Bilinear numerical model of BRB in elastic range

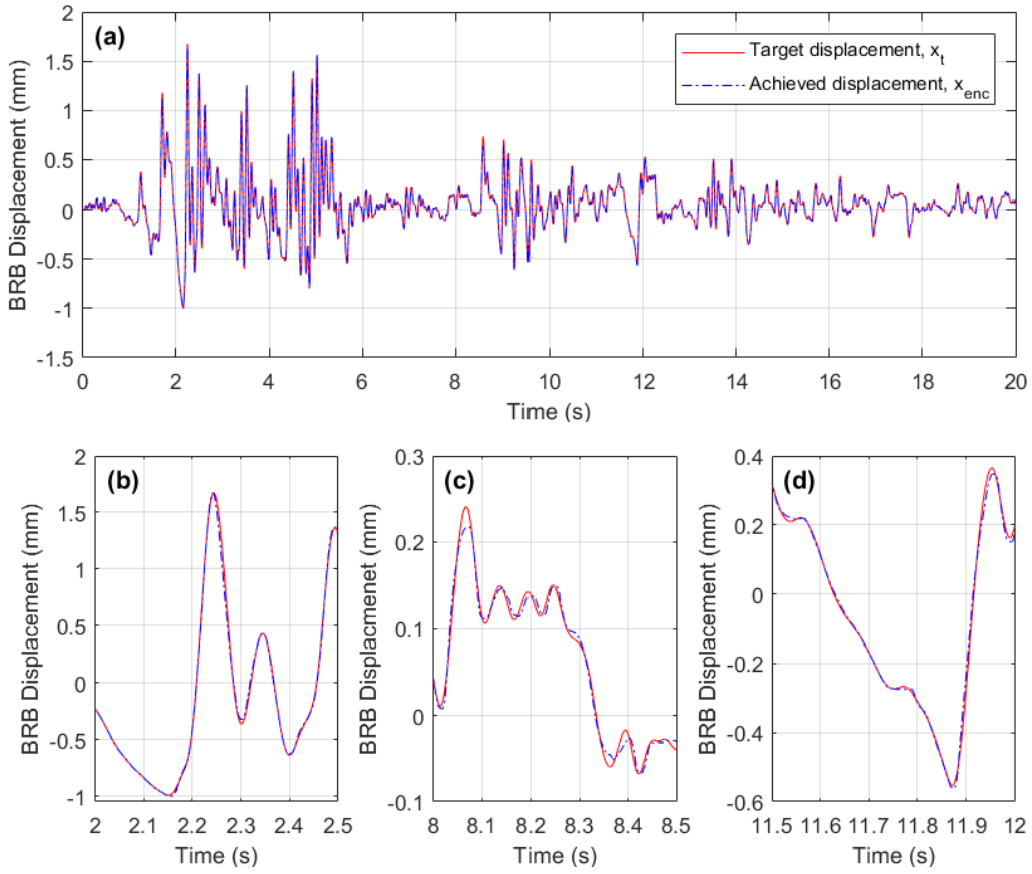

Figure 5.17 – Displacement applied to BRB during 10Hz RTHS test: (a) full test, (b)-(d) close-ups of representative locations

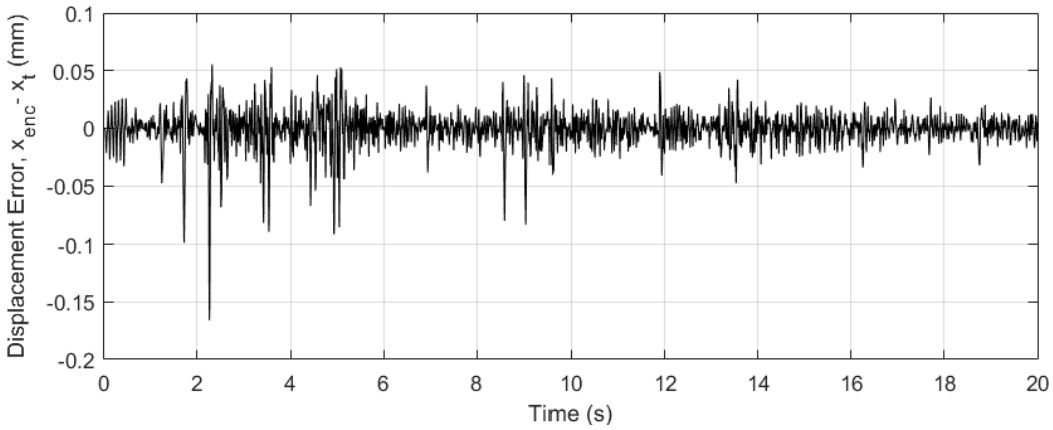

Figure 5.18 – Displacement error during 10Hz RTHS Test

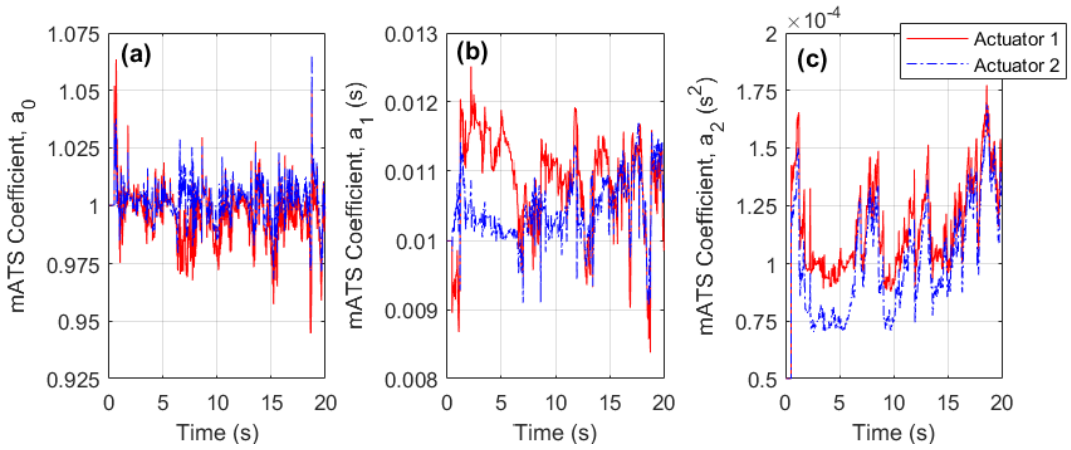

Figure 5.19 – Coefficients of mATS compensator during 10Hz RTHS test: (a) a_0 coefficient, (b) a_1 coefficient, and (c) a_2 coefficient

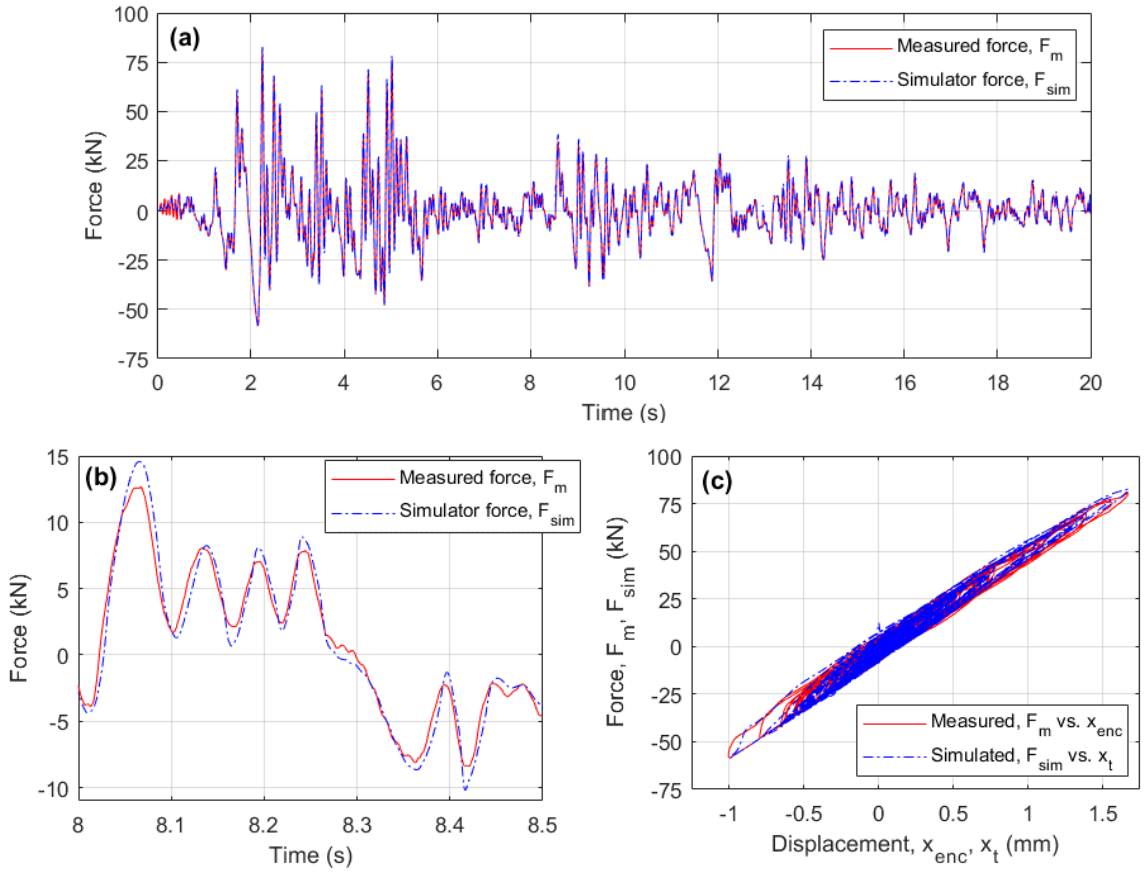

Figure 5.20 – BRB Force response during 10Hz RTHS test: (a) full test, (b) close-up, and (c) hysteresis curves

The test above was repeated at a dilated time scale of $\eta = 5$, meaning the displacements were applied to the BRB at 1/5th the rate assumed in the simulation. This reduces the demands on the actuators and inner loop controller, allowing improved accuracy, and any delay in the feedback will appear to the integrator as being $1/\eta$ its actual value, improving the stability of the hybrid simulation. BRBs are essentially rate-independent devices so, with perfect actuator control, the real-time and time-dilated tests would be expected to give virtually the same response. How closely the two match can therefore give an indication of the performance of the RTHS interface components developed in this project (the mATS compensator and stiffness simulator). Figure 5.21 shows the displacement response for this time-dilated test, which is plotted against the time in the simulation, t, to allow direct comparison with the real-time hybrid simulation. The overall response matches that of the real-time test very closely, having a peak of 1.71mm compared to 1.67mm in the real-time test. The displacement accuracy is seen to be excellent, better than for the real-time hybrid simulation, as would be expected. This is reflected in the small displacement error seen in Figure 5.22, which gave an NRMS error of 1.39%, while the difference in peak values of x_{enc} and x_t was just 0.09%.

Figure 5.23 compares the displacement response of the real-time and time-dilated hybrid simulations which indicates that, not only does the RTHS system remain stable at very high frequencies, it also achieves very good accuracy given the high speed of the RTHS test. Figure 5.23 also shows the displacement computed by the numerical simulation using the simple bilinear model described above. This approximate model would not be expected to give an exact match, but it confirms that the simulated response from the hybrid simulations is reasonable. Figure 5.24 shows the difference in displacement between the real-time and time-dilated tests, which remains quite small, while Figure 5.25 compares the hysteresis curves of the different tests.

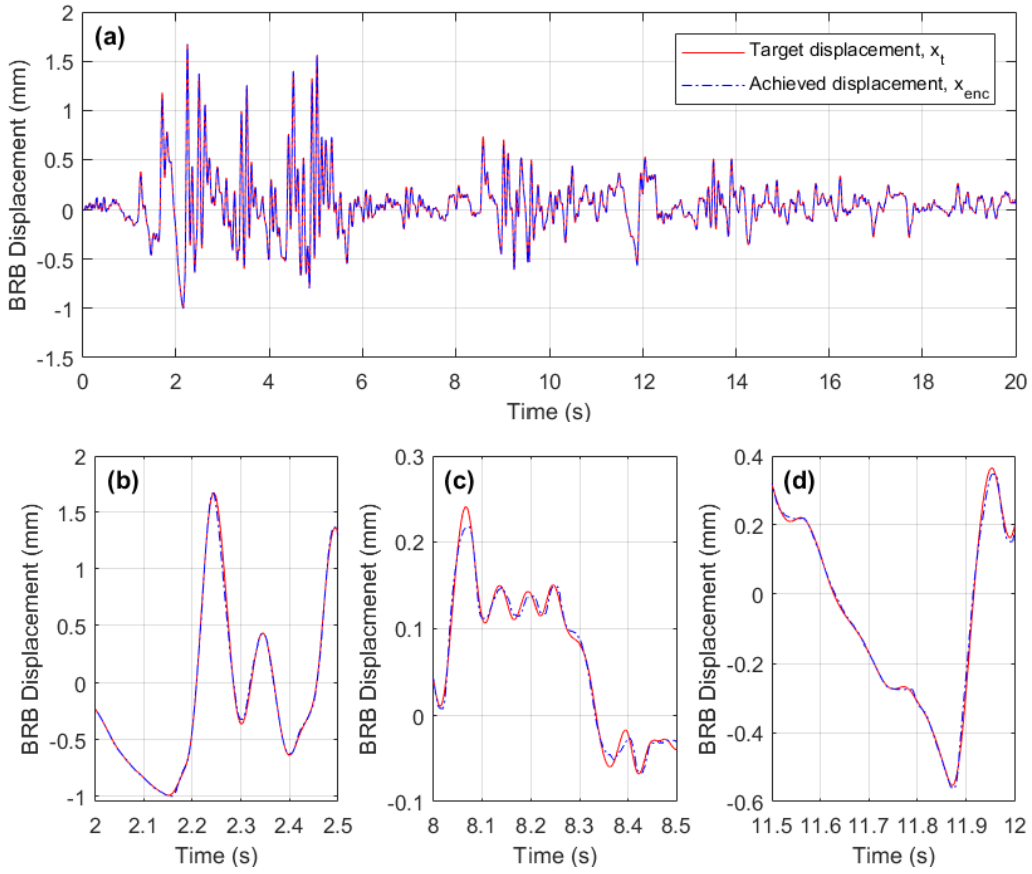

Figure 5.21 – Displacement applied to BRB during 10Hz hybrid simulation with time dilation ($\eta = 5$): (a) full test, (b)-(d) close-ups of representative locations

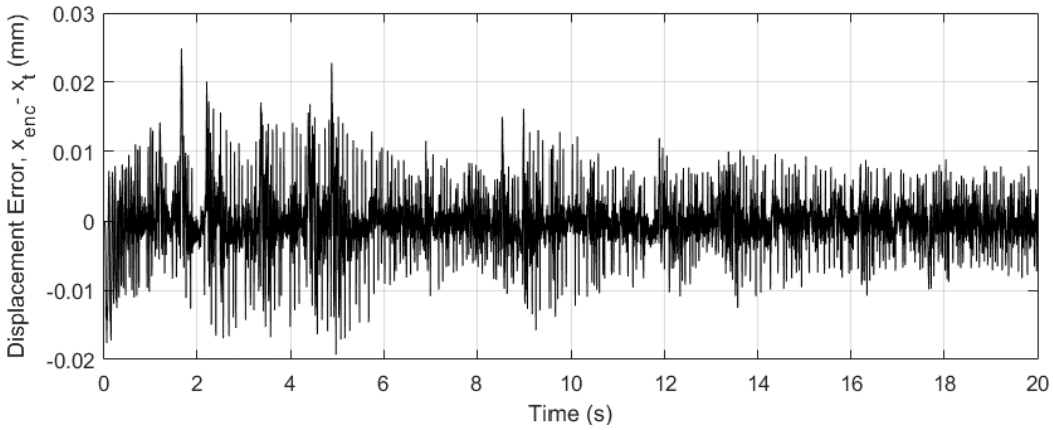

Figure 5.22 – Displacement error during 10Hz hybrid simulation with time dilation ($\rho_t = 5$)

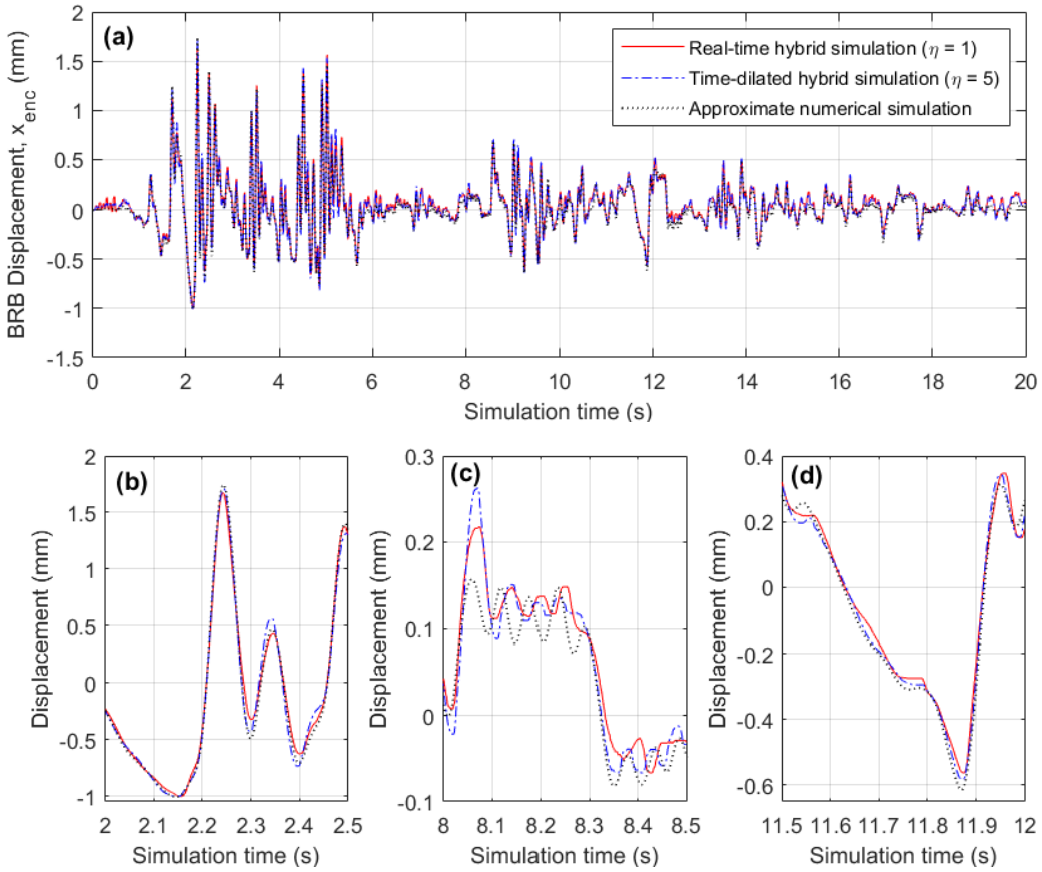

Figure 5.23 – Comparison of BRB displacement during the real-time hybrid simulation, the time-dilated hybrid simulation and the numerical simulation with an approximate BRB model: (a) full test, (b)-(d) close-ups of representative locations

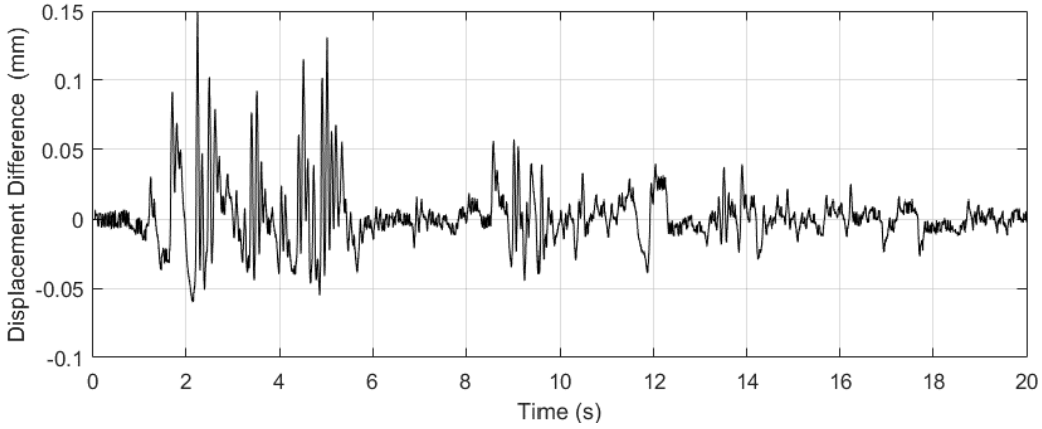

Figure 5.24 – Difference in BRB displacement during real-time and time dilated hybrid simulations

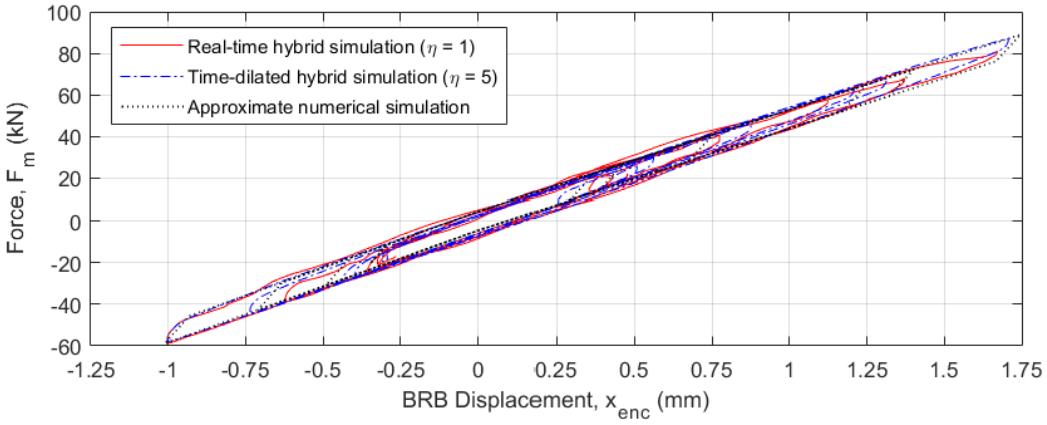

Figure 5.25 – BRB Hysteresis curves of the real-time hybrid simulation, time-dilated hybrid simulation and numerical simulation with an approximate BRB model, only time 1.6s to 2.6s shown for clarity

5.6.3. RTHS of 15Hz Structure

A SDOF structure with a natural frequency of 15Hz was the highest natural frequency structure tested during this RTHS testing. The test parameters were as for the 10Hz test except for the natural frequency and the earthquake scale factor. A conservative estimate of the maximum amplitude which can be achieved at this frequency without risking saturation of the actuator velocity is 1.2mm. Numerical simulation using the approximate numerical model described above predicted a peak displacement magnitude of 1.11mm for an earthquake scale factor of 2.75, and so this scale factor was used.

The BRB displacement produced by the RTHS test is shown in Figure 5.26, which has a peak of 0.98mm. For such a stiff structure, the displacement response takes a shape closely resembling the shape of the input ground acceleration but overlaid with a high frequency oscillation at the structure's natural frequency. The system remains stable even at this high frequency and the accuracy of the applied displacements, while less than for lower frequency tests, is still considered good given the high demands of the test, as shown in Figure 5.27, resulting in an NRMS error of 8.88%. The coefficients of the mATS compensator are shown in Figure 5.28. These generally behave as expected, although spikes are seen during the small displacement part of the response (between 6s and 8s) which might indicate that the compensator fitting matrix is starting to become ill-conditioned. However, this does not cause any problems for the hybrid simulation and this situation is highly unlikely in a realistic RTHS with much larger displacements and lower frequencies present.

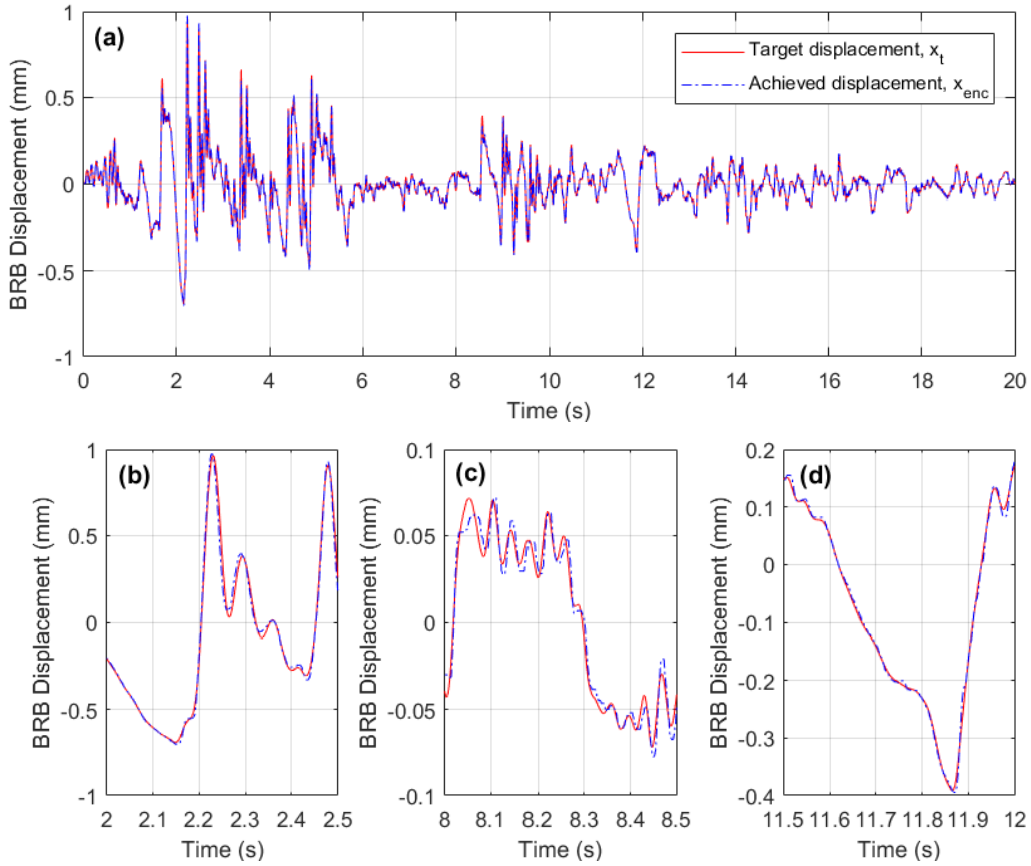

Figure 5.26 – Displacement applied to BRB during 15Hz RTHS test: (a) full test, (b)-(d) close-ups of representative locations

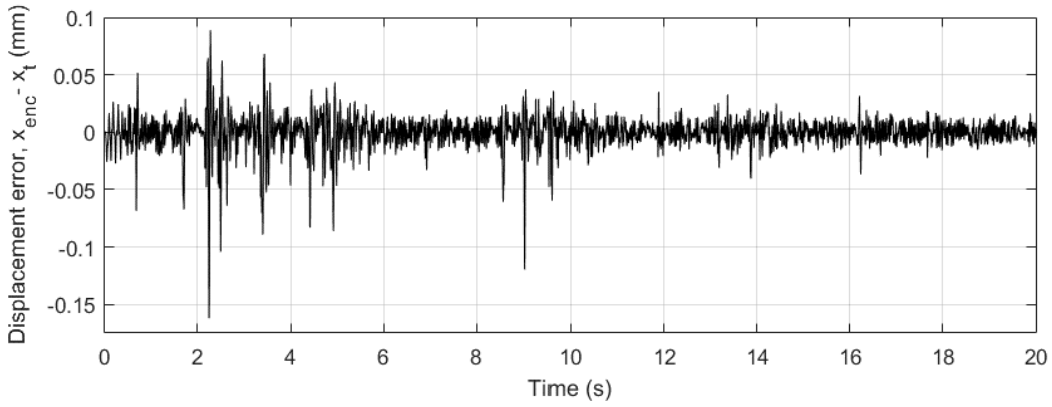

Figure 5.27 – Displacement error during 15Hz RTHS Test

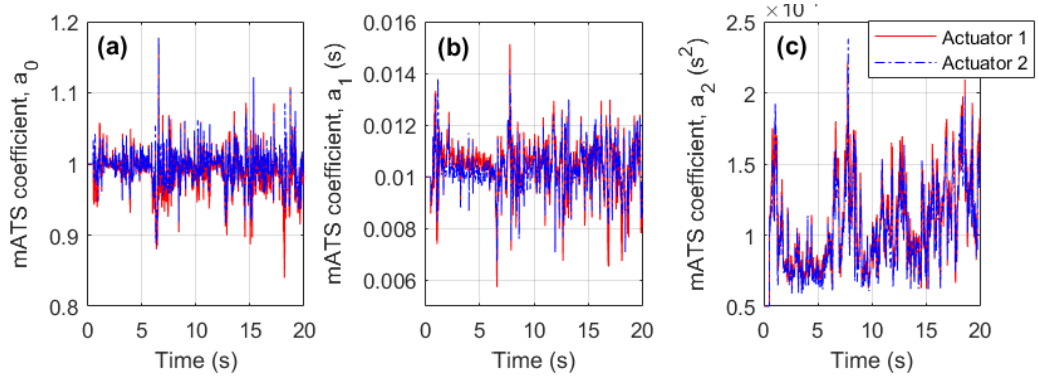

Figure 5.28 - Coefficients of mATS compensator during 10Hz RTHS test: (a) a_0, (b) a_1, and (c) a_2

5.7. Large Displacement SDOF Hybrid Testing

Having verified the stability of the RTHS system at high frequencies, the system is now applied to hybrid simulations with natural frequencies more representative of the fundamental frequencies found in BRBFs, which are likely to be in the region of 0.5 to 1Hz [48]. The displacement levels are also increased to produce yielding in the BRBs and therefore nonlinearity. First a structure is tested in which the numerical substructure contributes stiffness, followed by a structure in which all of the stiffness comes from the physical substructure. The El Centro ground motion is used in both cases and, as before, the scaling is based on the target peak displacement to control the amount of yielding occurring in the BRB.

5.7.1. RTHS of a 1Hz SDOF Structure with Numerical Stiffness

In the RTHS test presented here, the natural frequency was set to 1Hz and the inherent damping to 2%. The stiffness factor, C_K, was set to 0.5 so that the numerical substructure provides an elastic stiffness equal to the initial stiffness provided by the BRB. A target peak displacement of around 8mm was selected to give sufficient yielding while preserving the BRB for later testing. Prior to the hybrid test, an appropriate scale factor to apply to the El Centro input acceleration was estimated using a numerical simulation with an approximate numerical BRB model (the multilinear model given in Section 6.1.4). A scale factor of 0.125 was used, which was predicted to give a peak displacement of 8.35mm. The displacement response produced by the hybrid simulation is given in Figure 5.29, which gave a peak of 8.34mm. A very good match is obtained between the target and achieved BRB displacements, as shown by the displacement error in Figure 5.30, which resulted in an NRMS error of 0.491%. Figure 5.31 shows the coefficients of the mATS compensator, where a reduction in the a_1 coefficient is clearly visible during the large displacement section due to the reduction in actuator delay caused by yielding of the BRB. Figure 5.32 shows the force response produced and Figure 5.33 shows the hysteresis curve. The BRB is seen to undergo a notable amount of yielding, providing significant energy dissipation, and the force response from the stiffness matches the measured force very closely (the minimal displacement error means the size of the extrapolation performed by the stiffness simulator is very small).

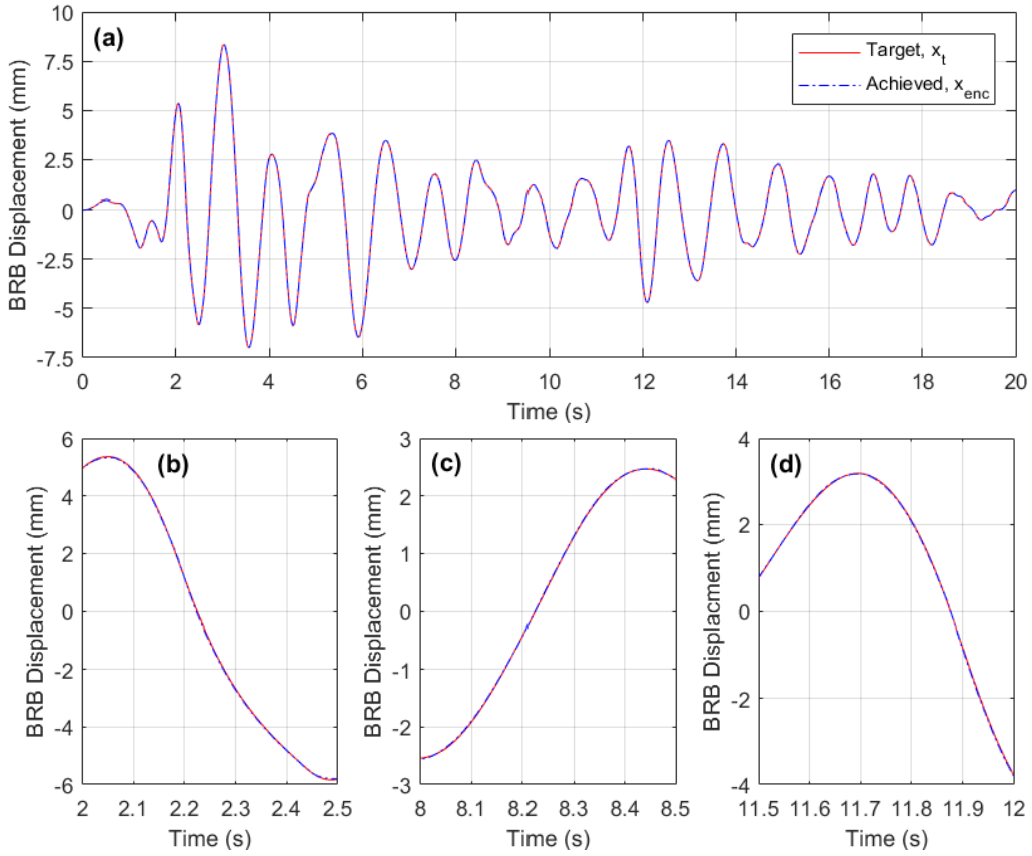

Figure 5.29 – Displacement applied to BRB during RTHS of 1Hz structure with 2% damping and 50% of stiffness from numerical substructure: (a) full test, (b)-(d) close-ups of representative locations

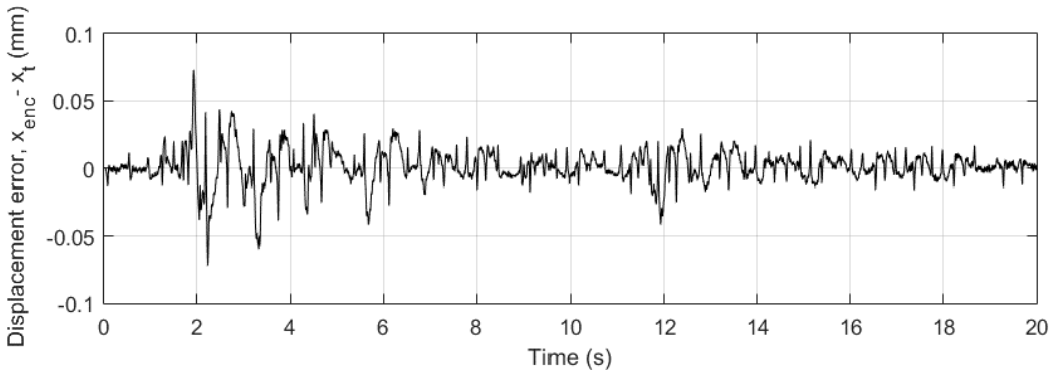

Figure 5.30 – Displacement error for RTHS of 1Hz structure with 2% damping and 50% of stiffness from numerical substructure

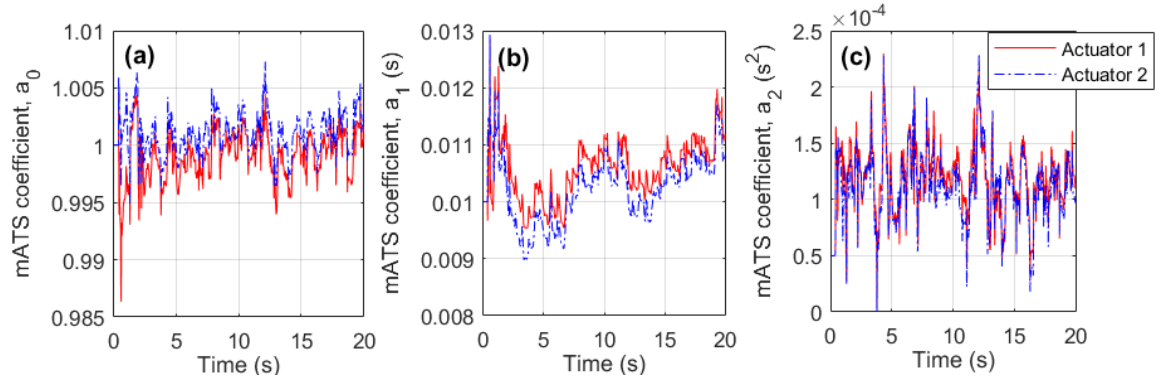

Figure 5.31 – Coefficients of mATS compensator during 1Hz RTHS test: (a) a_0, (b) a_1, and (c) a_2

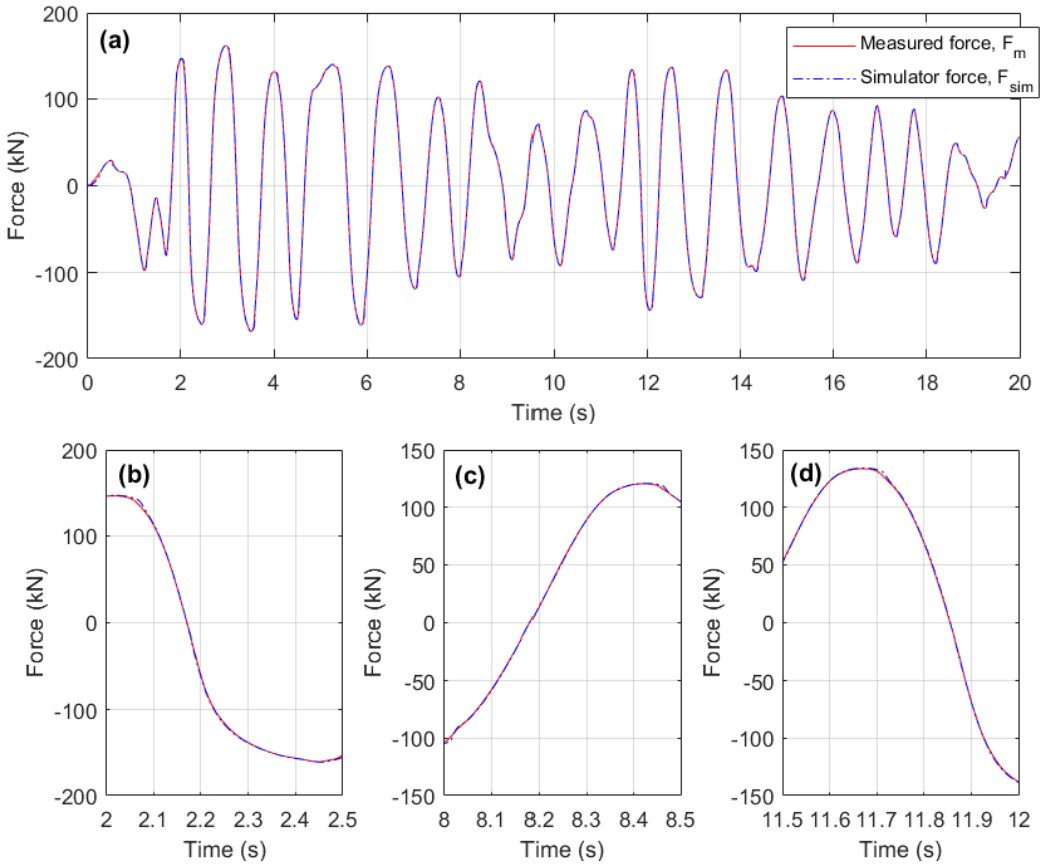

Figure 5.32 – BRB Force response for RTHS of 1Hz structure with 2% damping and 50% of stiffness from numerical substructure: (a) full test, (b)-(d) close-ups of representative locations

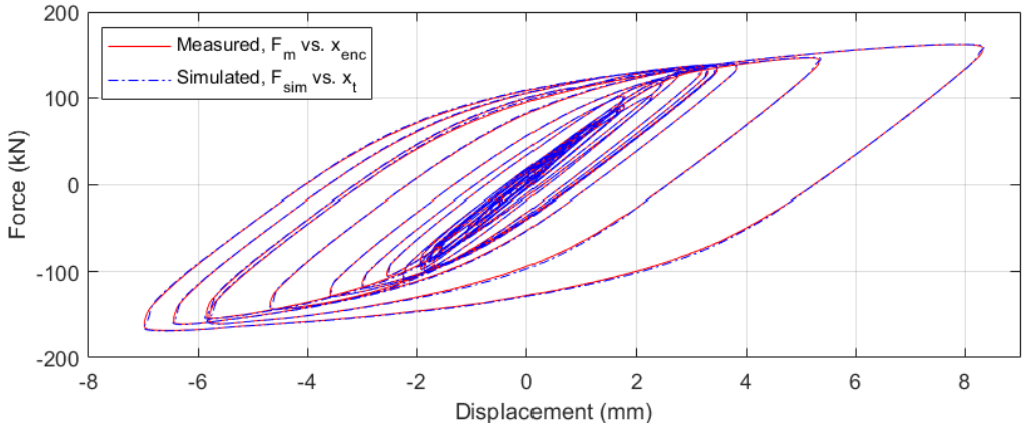

Figure 5.33 – BRB Hysteresis curve for RTHS of 1Hz structure with 2% damping and 50% of stiffness from numerical substructure

For comparison, the above test was repeated with a time dilation factor, η, of 5. This resulted in an NRMS error of 0.164% between x_{enc} and x_t, and a peak displacement of 8.35%. Figure 5.34 shows a comparison of the displacement response given by the real-time and time-dilated hybrid simulations. They give an excellent match with an NRMS error of 0.53% between the displacement responses of the two hybrid simulations, and a difference in peak displacement of just 0.034%.

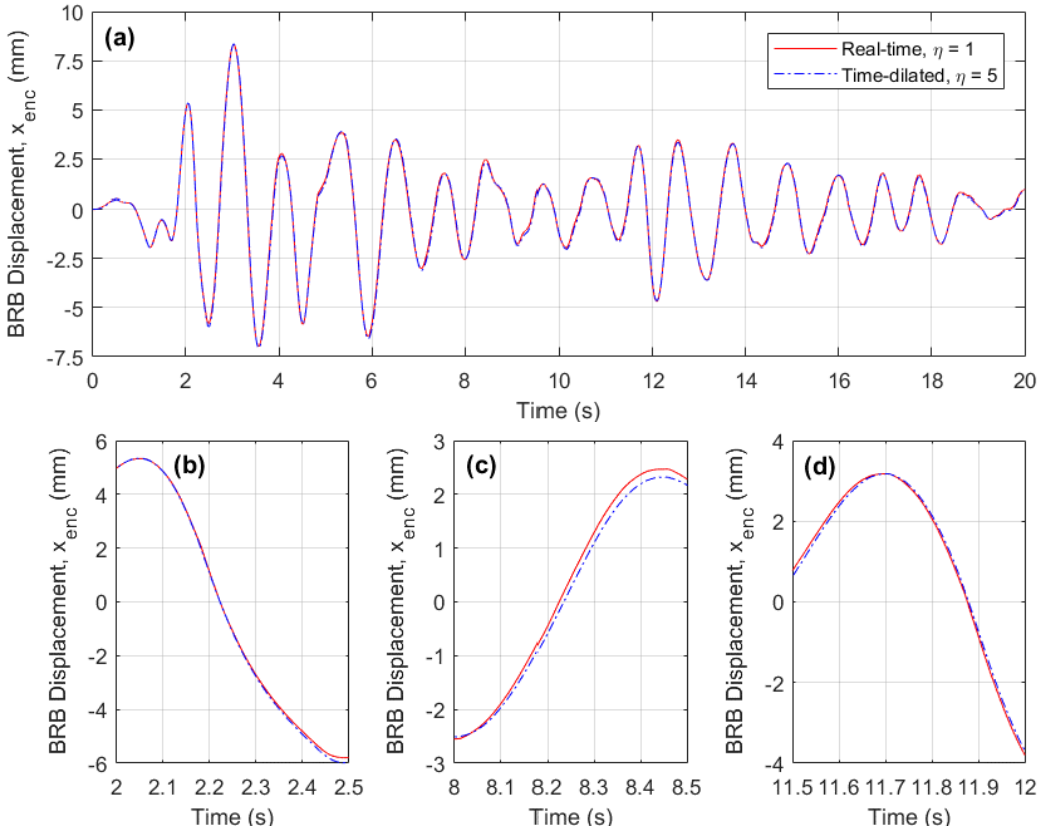

Figure 5.34 – Comparison between real-time and time-dilated hybrid simulations of 1Hz structure: (a) full test, (b)-(d) close-ups of representative locations

5.7.2. RTHS of a 1Hz SDOF Structure with No Numerical Stiffness

The results presented here are for a hybrid simulation similar to the one above but with C_K set to 1.0 so that all of the stiffness comes from the BRB, which represents a more onerous case from a stability perspective. The same earthquake scale factor was used (0.125), which the approximate numerical simulation predicted would give a peak displacement of 7.21mm. The displacement response produced by the hybrid simulation is given in Figure 5.35, which gave a peak of 7.42mm. A very good match is obtained between the target and achieved BRB displacements, as shown by the displacement error in Figure 5.36, which gave an NRMS error of 0.543%. Figure 5.37 shows the mATS coefficients. As for the previous test, a reduction is seen in a_1 when displacements are large due to the reduction in stiffness caused by yielding. However, in this case, an offset is also seen to occur in a_0, which was not seen in the previous test. In the previous test, the elastic stiffness from the numerical substructure promoted

relatively symmetrical yielding, leaving virtually no residual displacement in the BRB (less than 0.1mm). In this test, however, without the additional restoring force from the numerical substructure, the yielding is less symmetrical causing the equilibrium point about which oscillations occur to shift from zero. Shifts in the mean position due to yielding coincide with the shifts in the mean value of a_0. This suggests the compensator adapting to the new equilibrium position, which seems to cause no issue with the performance of the delay compensation. Without the restoring force from the numerical substructure, a larger residual displacement of 0.575mm remained at the end of the test. Figure 5.38 shows the hysteresis curve, again showing a notable amount of stable yielding and energy dissipation, and again the force response from the stiffness matches the measured force very closely.

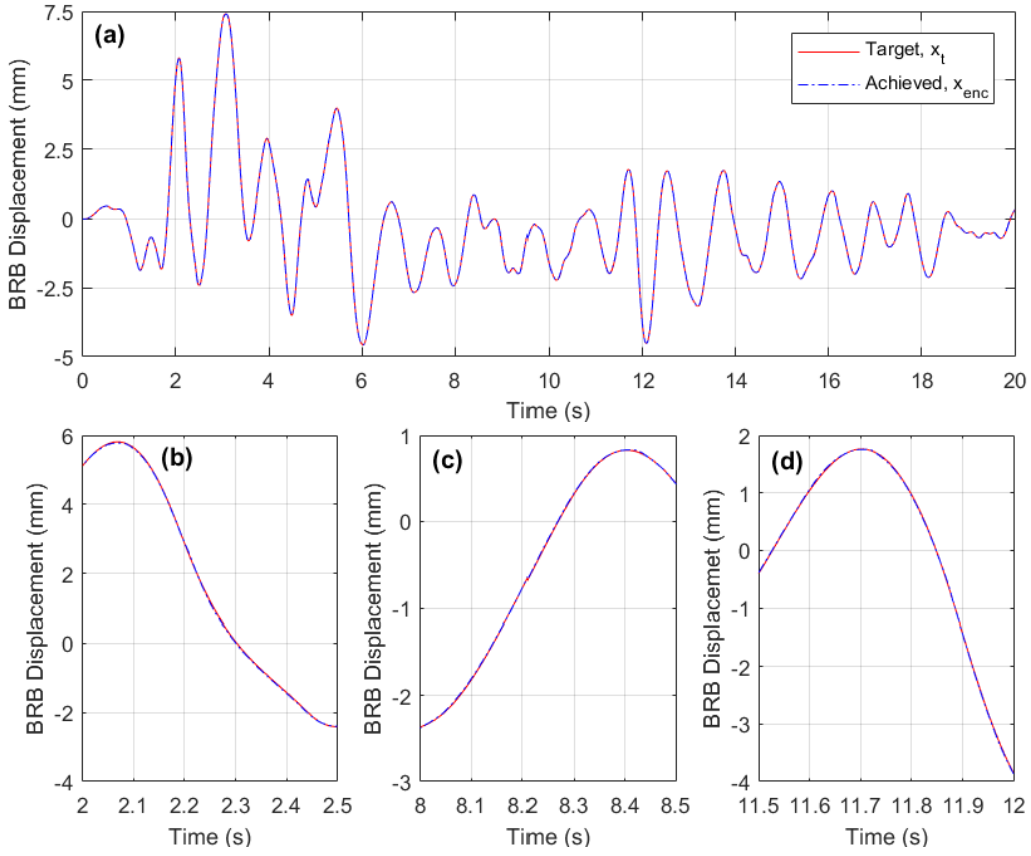

Figure 5.35 – Displacement applied to BRB during RTHS of 1Hz structure with 2% damping and no stiffness from numerical substructure: (a) full test, (b)-(d) close-ups of representative locations

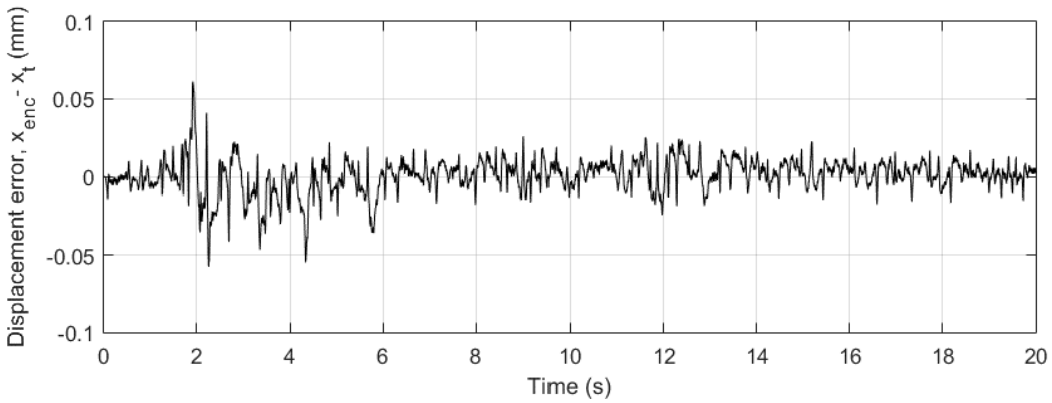

Figure 5.36 – Displacement error for RTHS of 1Hz structure with 2% damping and no stiffness from numerical substructure

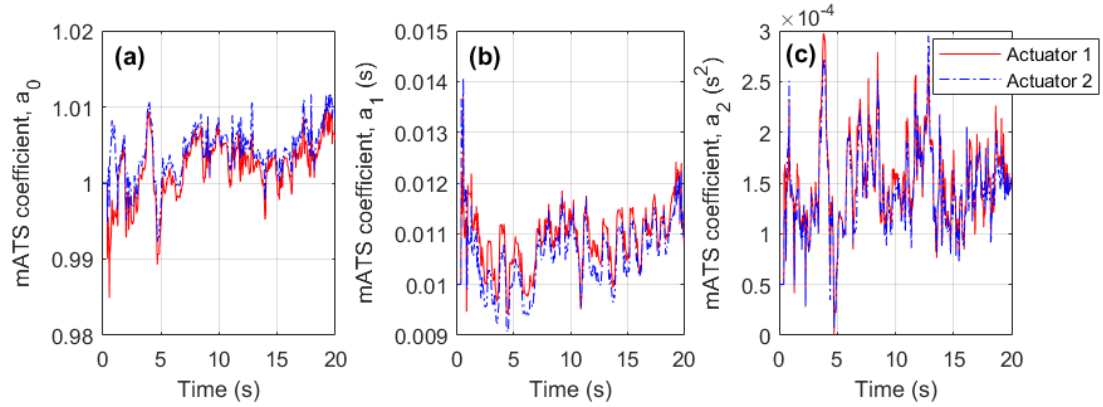

Figure 5.37 – Coefficients of mATS compensator during 1Hz RTHS test: (a) a_0, (b) a_1, and (c) a_2

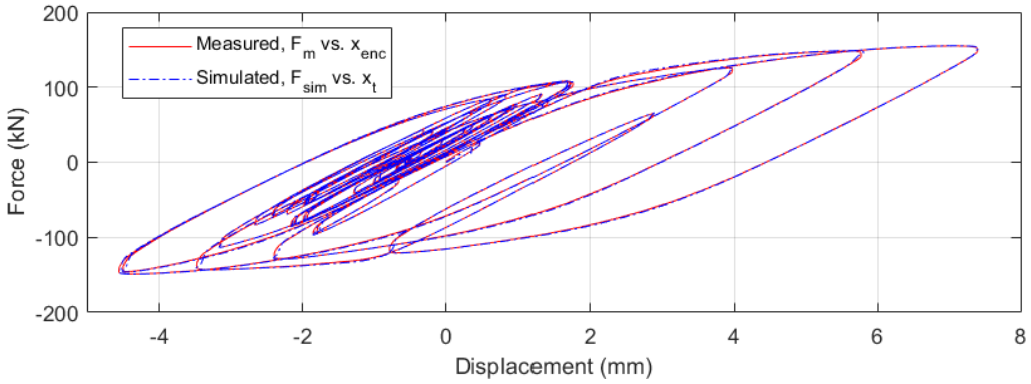

Figure 5.38 – BRB Hysteresis curve for RTHS of 1Hz structure with 2% damping and no stiffness from numerical substructure

5.7.3. RTHS of a 4Hz SDOF Structure

The RTHS tests presented above used a 1Hz SDOF structure since this is representative of the likely fundamental frequency of a BRBF structure. For reference, the five storey BRBF designed in Chapter 6

has a fundamental frequency of 1.17Hz. Of course, the response of a multistorey building will also contain contributions from higher frequency oscillations. Chapter 6 presents the results of RTHS testing of MDOF structures. However, it is informative to assess the performance at individual frequencies prior to applying the system to a MDOF structure, so tests were performed at a number of frequencies above the fundamental frequency. The results presented here are for a SDOF structure with a 4Hz natural frequency. For reference, the five storey BRBF designed in Chapter 6 has second and third mode frequencies of 2.88Hz and 4.60Hz, respectively. As for the previous test, all of the stiffness comes from the BRB ($C_k = 1$) to give the most onerous control situation, and the inherent damping remains at 2%. The El Centro ground motion was again used as the input ground acceleration, but this time with the scale factor increased to 0.75 to achieve the desired level of displacement – giving a sufficient amount of yielding to verify the performance under non-linear physical behaviour while preserving the BRB for later testing and staying within the velocity limits of the actuators.

Figure 5.39(a) shows the displacement response applied to the BRB, which has a peak of 4.6mm. The close-ups of Figure 5.39(a) in Figure 5.39(b)-(d) show an excellent match between the target and achieved BRB displacements. This is confirmed by Figure 5.40 which shows that the error between the target and achieved displacements remains small, with a maximum disparity of 0.12mm and an error of 0.86% at the peak displacement. The resulting NRMS error between x_{enc} and x_t is 1.68%. For comparison, the NRMS error between x_{enc} and u_c (the mean of the command signals generated by the two mATS compensators) is 5.17%, which gives an indication of the magnitude of error that would be produced if the same displacement was applied to the BRB in a system without delay compensation, but with correction for rig flexibility. The NRMS error between x_{enc} and $u_c + d_{rig}$ (the input to the PID controllers) is 17.87%, which gives an indication of the magnitude of error that would be produced if the same displacement was applied to the BRB in a system without delay compensation or correction for rig flexibility. Of course, in reality, in these situations the displacement response would differ due to the negative damping introduced by the delay and the lower apparent stiffness of the BRB due to

flexure of the rig, but the values give an indication of the improvement provided by the mATS compensator with rig flexibility correction.

Figure 5.41 shows the force response of the BRB as well as the output from the stiffness simulator, indicating that the stiffness simulator performs well in the presence of a reasonable amount of yielding. The parameters of the stiffness simulator were not changed for this higher frequency test, still using the values determined in Sections 5.4.3 and 5.4.4 ($\lambda = 12.5\text{ms}$ and $\beta = 0.5$). This is because, in a MDOF test, the stiffness simulator must operate on a response having multiple frequency components, so the same λ is used in all SDOF tests to match the value that will be used in the MDOF tests.

Figure 5.42 shows the coefficients of the mATS compensator which behave as expected with the a_1 coefficient reducing during yielding due to a reduction in delay, and a shift occurring in the a_0 coefficient after each yielding event.

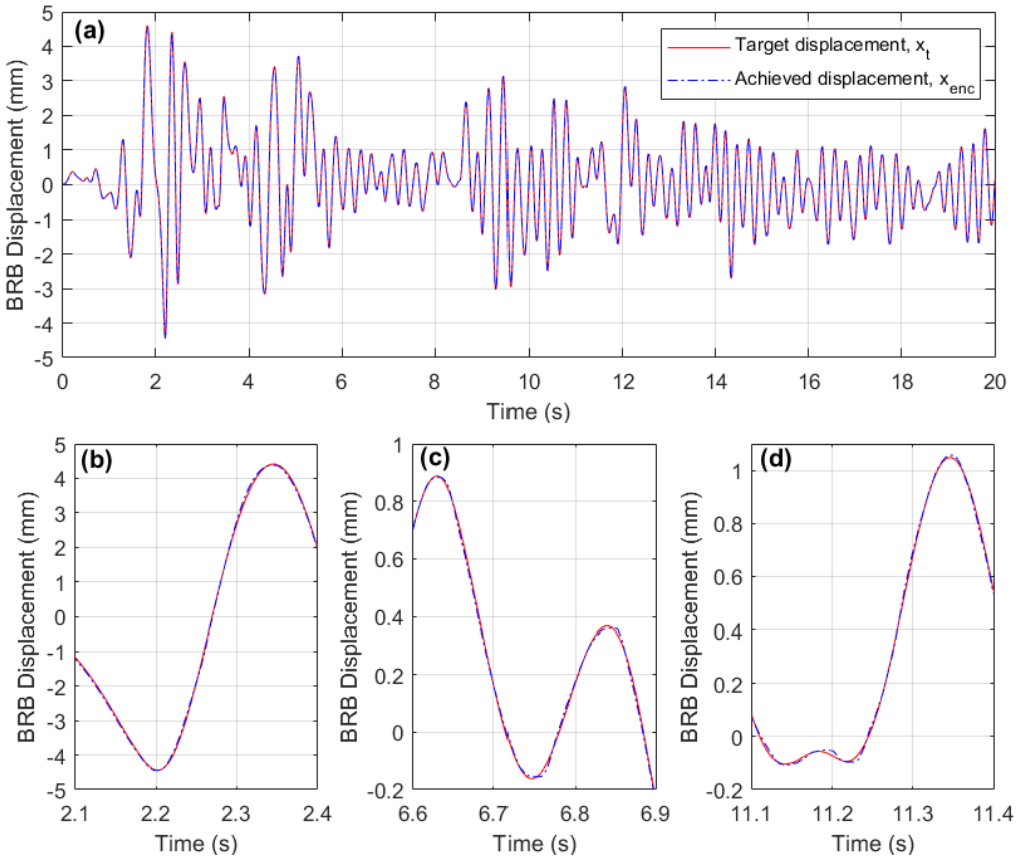

Figure 5.39 – Displacement applied to BRB during RTHS of 4Hz structure with 2% damping and no stiffness from numerical substructure: (a) full test, (b)-(d) close-ups of representative locations

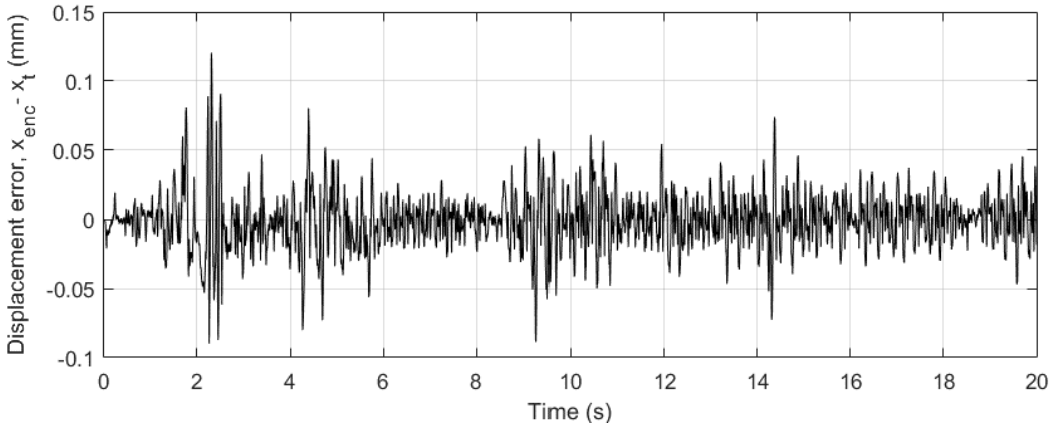

Figure 5.40 – Displacement error for RTHS of 4Hz structure with 2% damping and no stiffness from numerical substructure

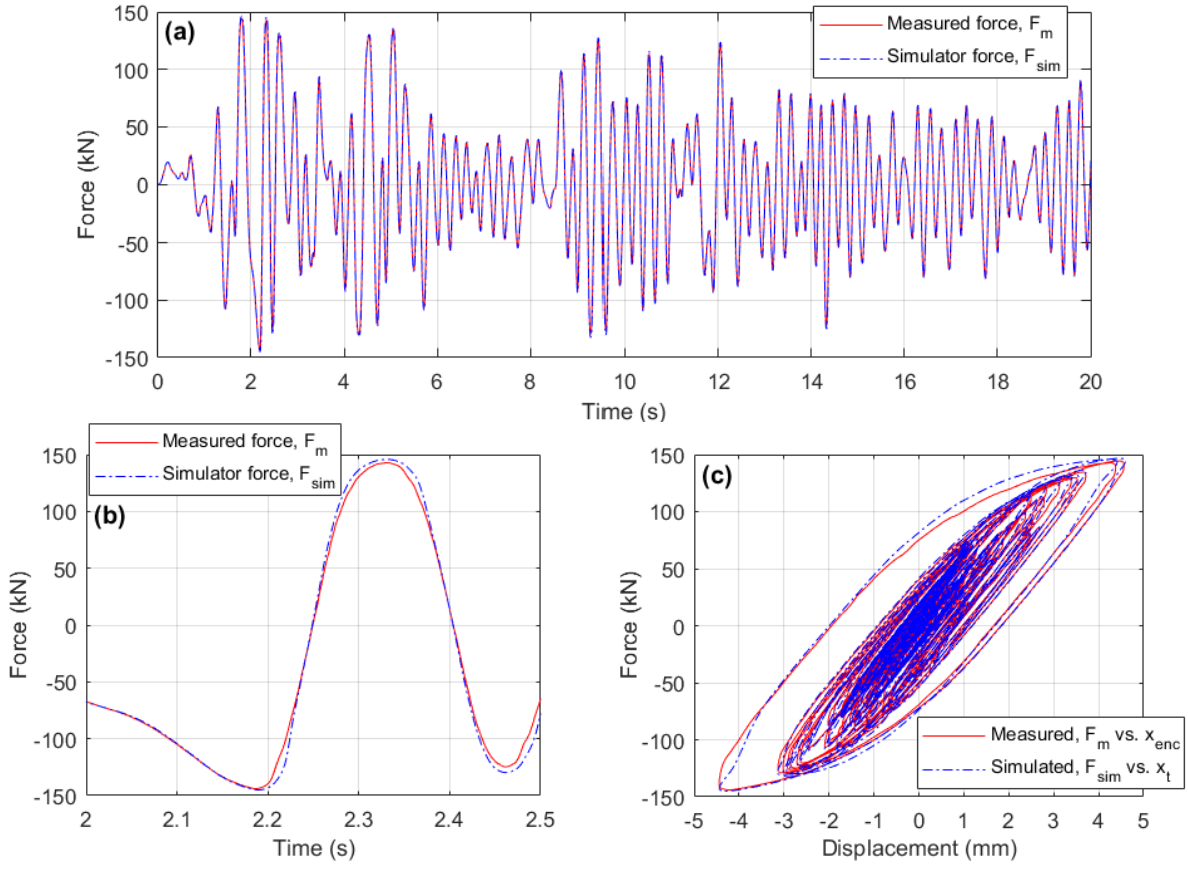

Figure 5.41 – BRB Force response for RTHS of 4Hz structure with 2% damping and no stiffness from numerical substructure: (a) full test, (b) close-up at peak, and (c) hysteresis curve

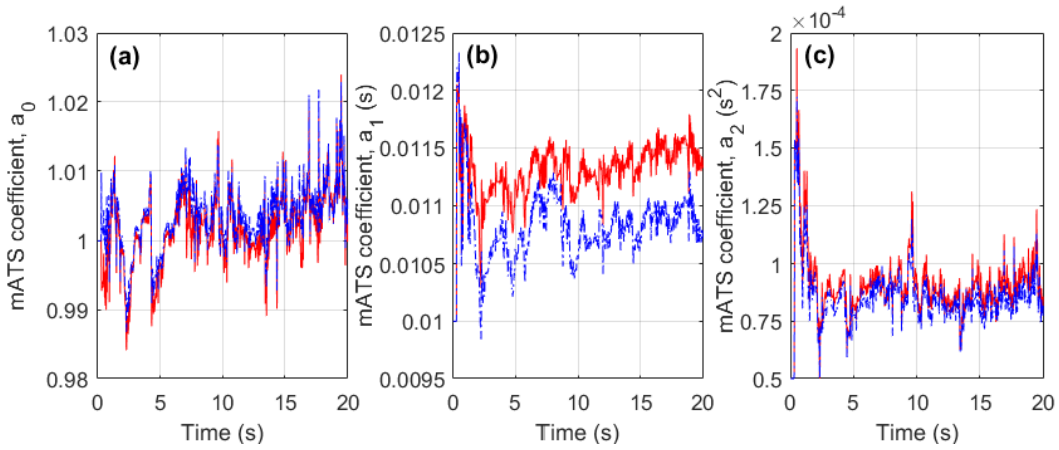

Figure 5.42 - Coefficients of mATS compensator during 4Hz RTHS test: (a) a_0, (b) a_1, and (c) a_2

5.8. Maximum Displacement SDOF Hybrid Simulations

A final set of SDOF hybrid tests were carried out, one for each earthquake, taking the BRB up to around its maximum displacement. Note that these were carried out after the MDOF testing in Chapter 6 due to the risk of damaging the BRB. At the start of each test, there was a residual displacement in the BRB due to yielding in the previous tests. For consistency, the displacement is plotted relative to the original BRB length, meaning plots start from non-zero displacement. Note that the mATS compensator took the displacement at the start of the hybrid simulation as zero, since this is the equilibrium position. The direction of the applied loading for each test was selected so that the residual displacements caused by the test would be in the opposite direction to those at the start of the test to avoid the residual displacements accumulating and allowing more tests to be performed. For these tests, the natural frequency of the structure was set to 0.5Hz to ensure the actuator rate limits were not exceeded at these large displacements. The damping ratio was also reduced to 1.655% to ensure the actual damping experienced did not exceed 5% (due to the reduction in effective stiffness of the BRB). The stiffness factor, C_K, was set to 1.0 so that, again, all of the stiffness came from the BRB.

5.8.1. Northridge

Figure 5.43 shows the displacement given by RTHS of the 0.5Hz SDOF structure in response to the Northridge ground motion scaled to 21.75%, which gave an NRMS error of 0.23% between x_{enc} and

x_t. At the start of the test there was a residual deformation in the BRB of -4.0mm, while a significant residual deformation of 16.3mm remained at the end of the test. The resulting force is shown in Figure 5.44 and the corresponding hysteresis curve in Figure 5.45, showing many cycles with significant yielding. The coefficients of the mATS compensator are shown in Figure 5.46.

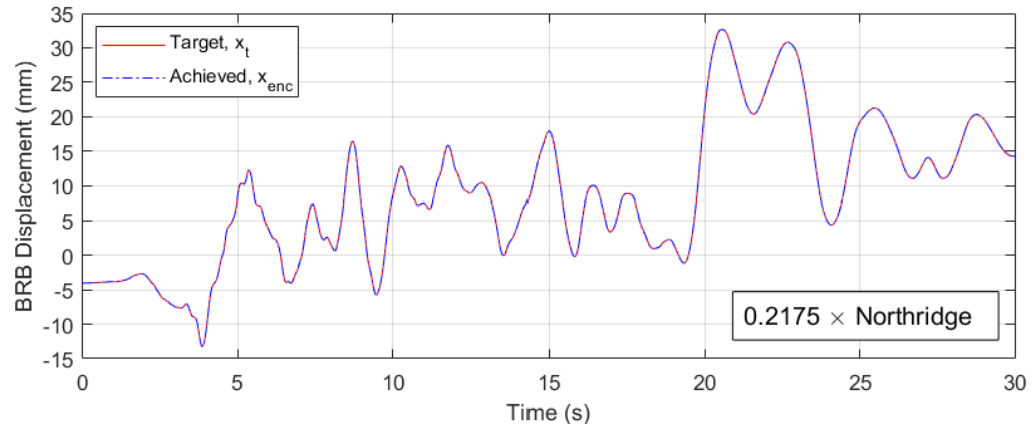

Figure 5.43 – Displacement applied to BRB during large displacement RTHS of 0.5Hz structure (Northridge)

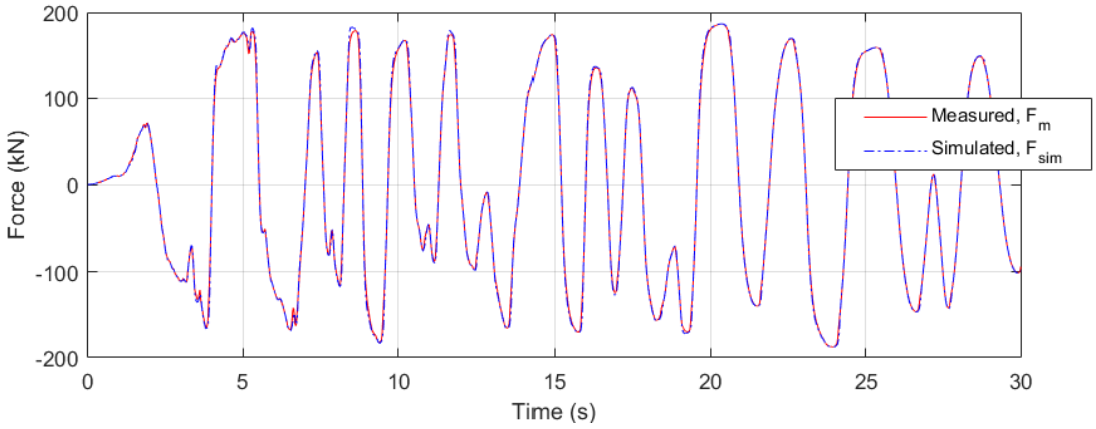

Figure 5.44 – BRB Force response for large displacement RTHS of 0.5Hz structure (Northridge)

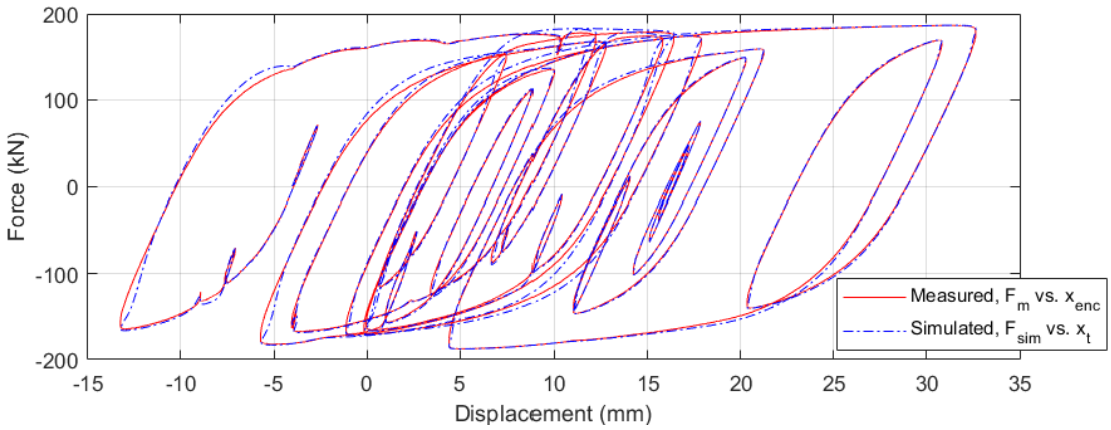

Figure 5.45 – BRB Hysteresis curve for large displacement RTHS of 0.5Hz structure (Northridge)

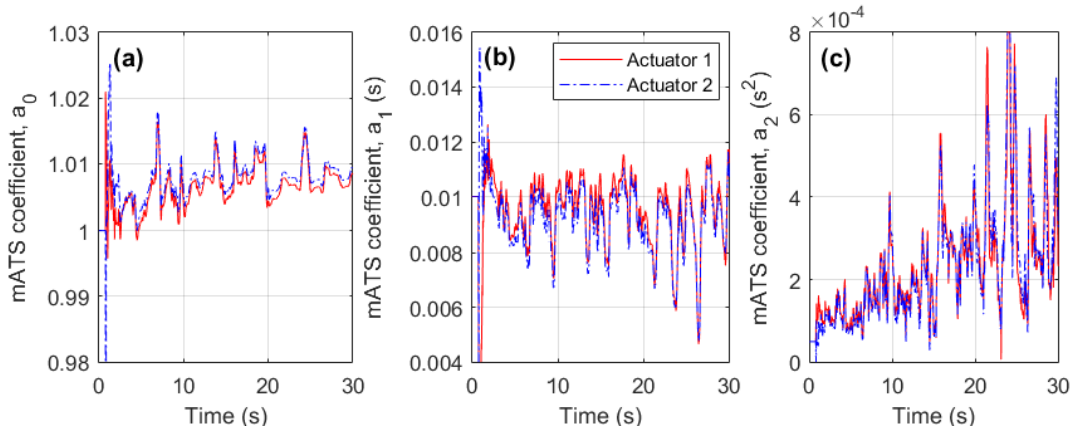

Figure 5.46 – Coefficients of mATS compensator for large displacement RTHS of 0.5Hz structure (Northridge): (a) a_0, (b) a_1, and (c) a_2

5.8.2. El Centro

Figure 5.47 shows the displacement given by RTHS of the 0.5Hz SDOF structure in response to the El Centro ground motion scaled to 31%, which gave an NRMS error of 0.29% between x_{enc} and x_t. At the start of the test there was a residual deformation in the BRB of 16mm, which by the end of the test was increased to 21mm. The resulting force is shown in Figure 5.48 and the corresponding hysteresis curve in Figure 5.49, showing many cycles with significant yielding. The coefficients of the mATS compensator are shown in Figure 5.50.

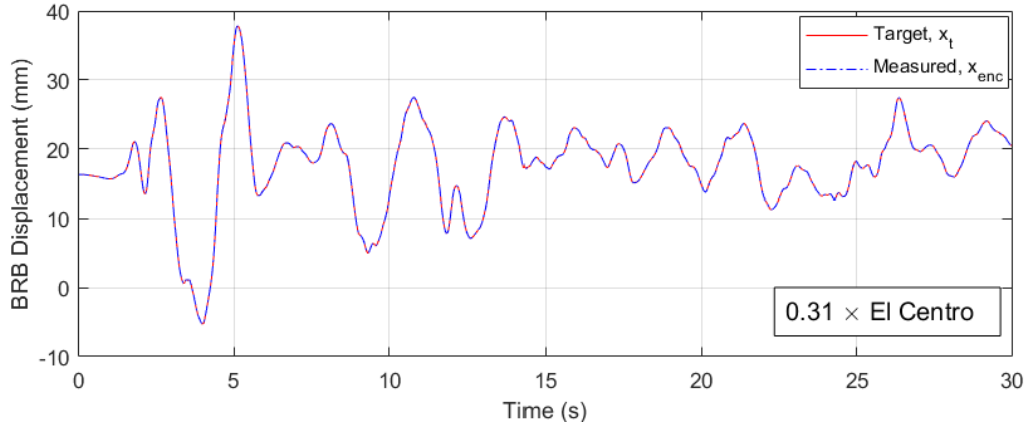

Figure 5.47 – Displacement applied to BRB during large displacement RTHS of 0.5Hz structure (El Centro)

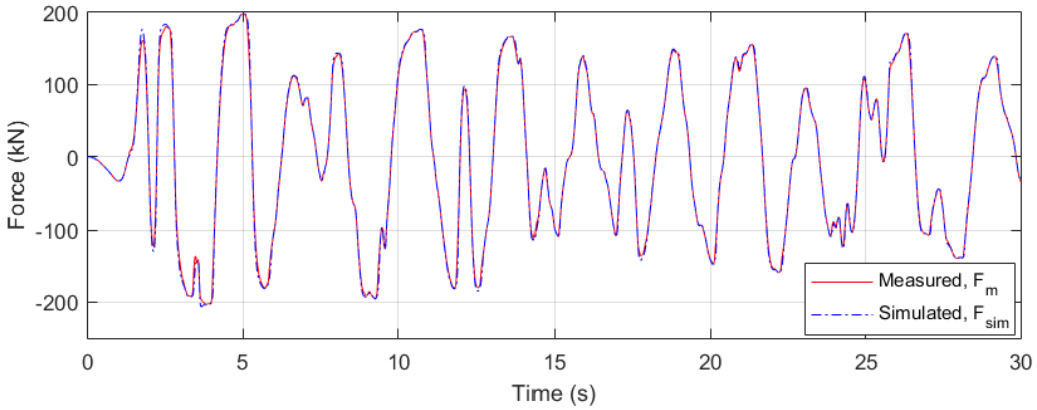

Figure 5.48 – BRB Force response for large displacement RTHS of 0.5Hz structure (El Centro)

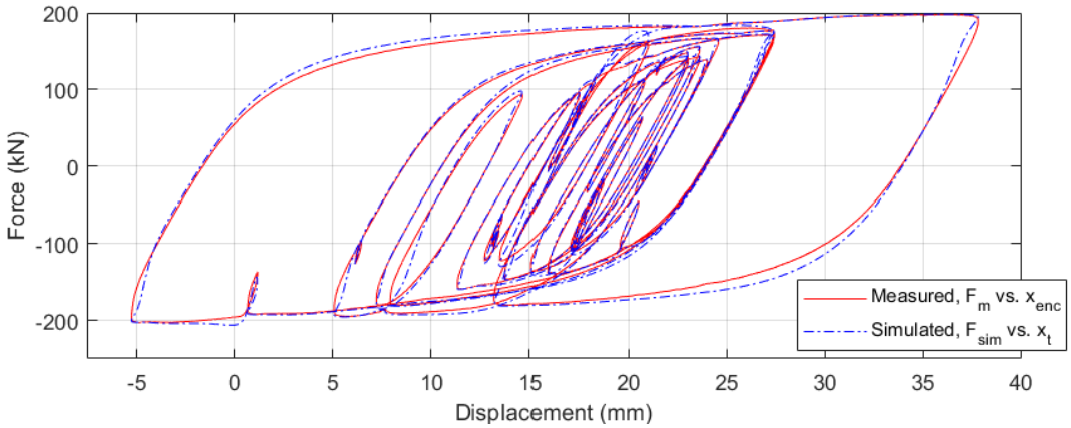

Figure 5.49 – BRB Hysteresis curve for large displacement RTHS of 0.5Hz structure (El Centro)

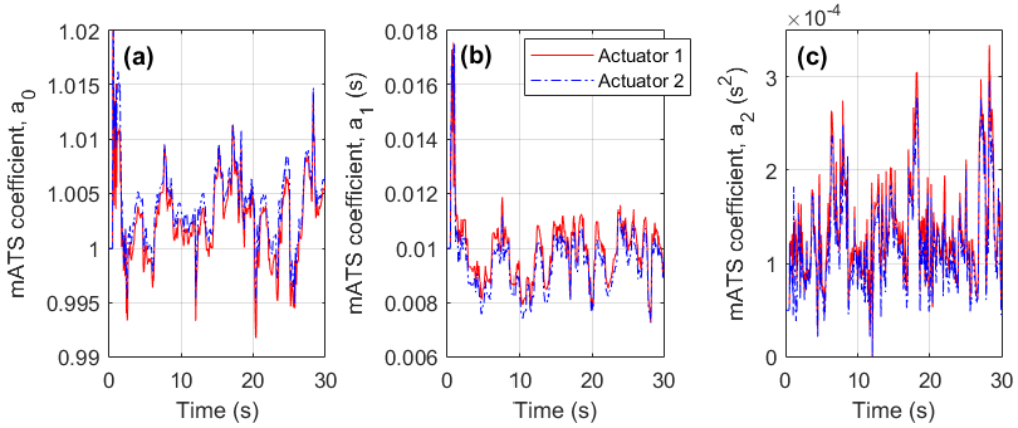

Figure 5.50 – Coefficients of mATS compensator for large displacement RTHS of 0.5Hz structure (El Centro): (a) a_0, (b) a_1, and (c) a_2

5.8.3. Kalamata

Figure 5.51 shows the displacement given by RTHS of the 0.5Hz SDOF structure in response to the Kalamata ground motion scaled to 0.53%, which gave an NRMS error of 0.39% between x_{enc} and x_t. At the start of the test there was a residual deformation in the BRB of 21mm, which by the end of the test was reduced to 12mm (the direction of the ground motion being chosen so as to reduce the residual deformation). The resulting force is shown in Figure 5.52 and the corresponding hysteresis curve in Figure 5.53, showing that the Kalamata ground motion produces one very significant yielding event. The coefficients of the mATS compensator are shown in Figure 5.54. Due to large offset of the equilibrium position due to the significant yielding at the start of the hybrid simulation, the offset caused in the a_0 coefficient of the mATS compensator, mentioned previously, is very pronounced.

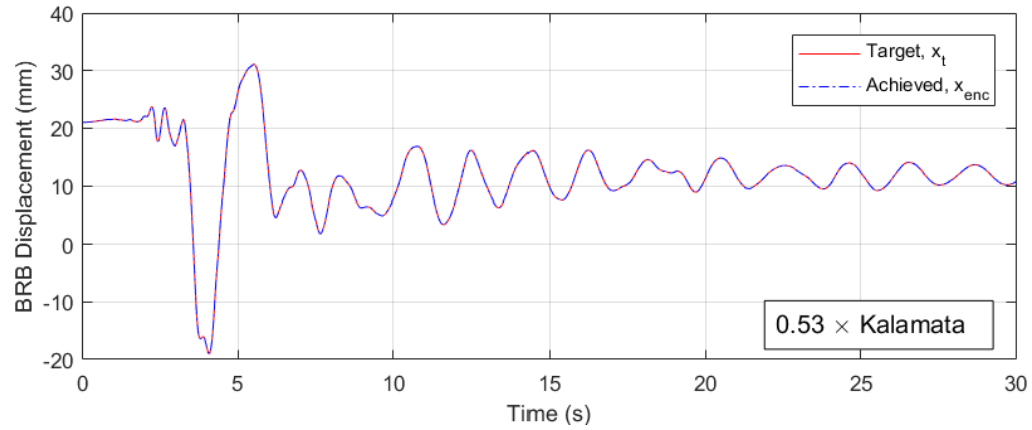

Figure 5.51 – Displacement applied to BRB during large displacement RTHS of 0.5Hz structure (Kalamata)

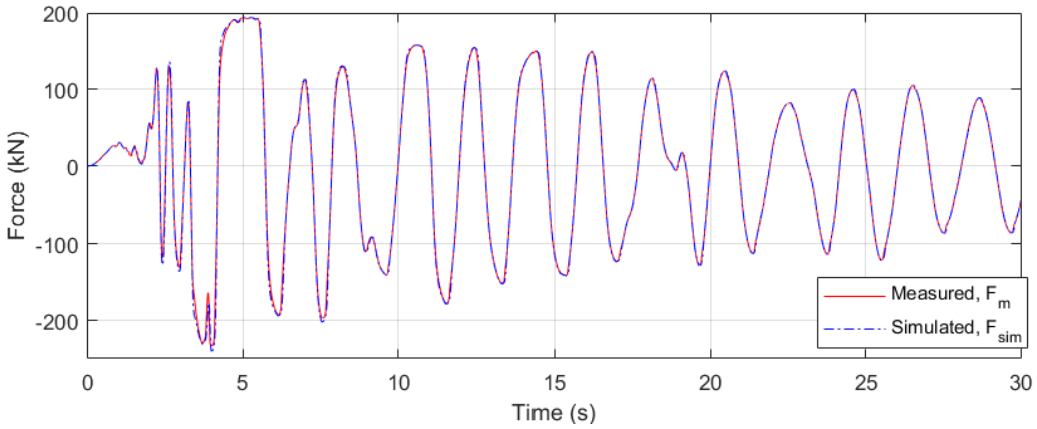

Figure 5.52 – BRB Force response for large displacement RTHS of 0.5Hz structure (Kalamata)

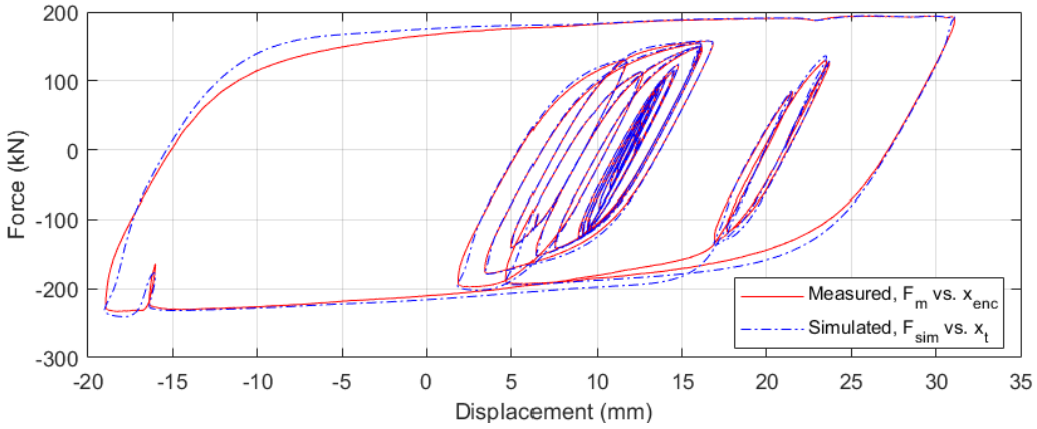

Figure 5.53 – BRB Hysteresis curve for large displacement RTHS of 0.5Hz structure (Kalamata)

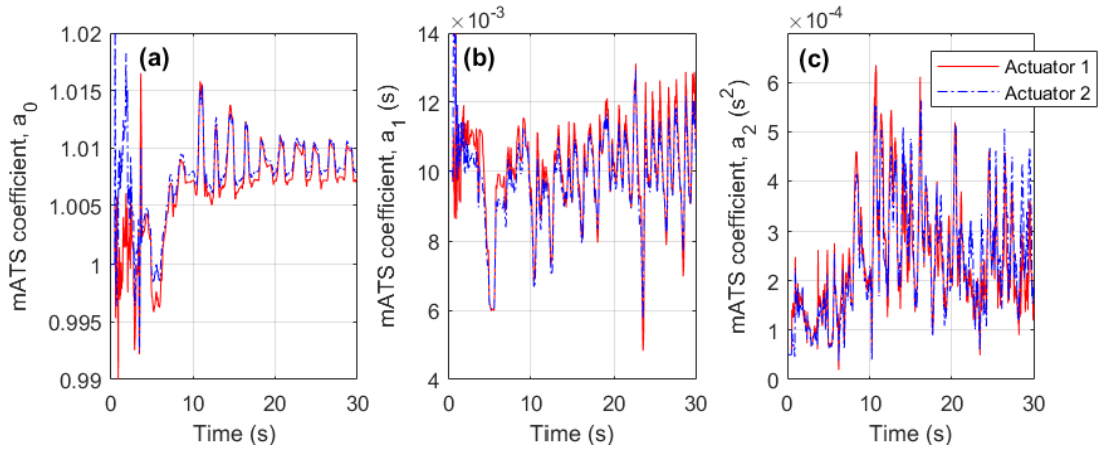

Figure 5.54 – Coefficients of mATS compensator for large displacement RTHS of 0.5Hz structure (Kalamata): (a) a_0, (b) a_1, and (c) a_2

5.9. Conclusion

In this chapter, a system for performing RTHS of a SDOF structure installed with a BRB, which forms the physical substructure, has been presented. Control of the actuator displacements at the interface going from the numerical substructure to the physical substructure has been achieved using the control system developed in Chapter 4, which includes the mATS compensator. An additional component has been developed called the stiffness simulator, which acts at the interface going from the physical substructure back to the numerical substructure. The stiffness simulator ensures continuous stable force feedback by using a model of the BRB stiffness which is continually updated based on the most recent measurements. The is an improvement on previous systems which extrapolated about the current measured force. An efficient method for fitting the coefficients of the stiffness simulator was also presented and tested. Testing showed that the stiffness simulator performed well and was used to select an appropriate value for the simulator time-constant. This combined RTHS system was then applied to the RTHS of structures of various natural frequencies at a variety of displacement amplitudes, with and without stiffness being contributed by the numerical substructure. Testing of the free response of the simulated structure to an initial excitation confirmed that the system accurately simulates the target properties of the structure and showed the small amount of frictional damping provided by the BRB in its elastic range. RTHS tests were performed at high frequencies (up to 15Hz) showing that the hybrid simulation not only remains stable but also retains quite good accuracy. Larger displacement tests were then carried out which demonstrated the performance of the hybrid simulation with significant nonlinearity in the physical substructure due to yielding of the BRB. Tests were also run at a dilated time scale, which showed excellent agreement with the results of the real-time tests. Finally, the system was applied to very large displacement hybrid tests which pushed the BRB right up to the maximum design displacement. The BRBs showed stable yielding under multiple cycles, dissipating significant amounts of energy and demonstrated large reserves of ductility.

6. Multi-Degree-of-Freedom Hybrid Testing

In this chapter, the real-time hybrid simulation (RTHS) system demonstrated in Chapter 5 is applied to the simulation of multi-degree-of-freedom (MDOF) structures. The physical part of the system and the interfaces between the substructures (actuator controllers and stiffness simulator) remain the same, but the numerical substructure is changed. Two structures were simulated to cover the two different design contexts in which BRBs can be used: one where the BRBs act as supplemental dampers and one where the BRBs form the main lateral load resisting system. These were designed in accordance with the Eurocode requirements presented in Chapter 2 to give realistic structures. A modal approach was then used to simulate these efficiently in the numerical substructure.

6.1. Numerical Modelling of BRBs

A realistic multi-storey building would be fitted with multiple BRBs. In the most likely configuration, the BRBs in a given storey would be arranged in opposed pairs placed close to the outside of the structure to maximise the resistance of the structure to torsion about its vertical axis. To achieve structural uniformity and prevent torsion being introduced by asymmetrical stiffness, this arrangement would be mirrored on the other side of the structure. This arrangement would be repeated in the other principal direction, and through all storeys of the structure. The cross-sectional areas of all BRBs in a given storey, acting in a given principal direction, are likely to be the same, but they may differ to those in the other principal horizontal direction and to those in other storeys. However, with the laboratory facilities available, only one BRB could be physically tested at a time. Therefore, one BRB from the simulated structure was tested as the physical substructure while the remainder were modelled numerically within the numerical substructure. This section investigates numerical models to simulate BRBs and the fitting of the parameters of the models to the measured BRB behaviour.

6.1.1. Candidate BRB Models

BRBs operate through axial yielding of the steel core in tension and compression, so potential models have been selected which replicate this nonlinear hysteretic force-displacement response of steel under uniaxial cyclic loading. The following five nonlinear models, which have been widely used for modelling the behaviour of steel under cyclic loading, have been selected for further investigation:

1. Bilinear model
2. Multilinear model
3. Menegotto-Pinto model
4. Ramberg-Osgood model
5. Bouc-Wen model

The mathematical formulation of each method will be given, and suitable parameters chosen by comparison to the experimentally measured force-displacement response of the BRB. Since the selected model is to be used in the RTHS feedback loop, the computational efficiency of the model and its effect on the stability of the integration will be of interest, in addition to its accuracy.

6.1.2. Optimisation of Model Parameters

The parameters of the BRB models were selected by comparing the model output to the recorded data from the open-loop cyclic test presented in Section 4.7. This had a peak displacement of $\pm$17.5mm which is seven times the yield displacement and slightly more than half the estimated maximum allowable displacement. The displacement profile used is shown in Figure 6.1(a), the resulting force in Figure 6.1(b) and the hysteresis curve in Figure 6.1(c). This shows stable hysteresis over multiple cycles with significant post-yield strain hardening. Also shown in Figure 6.1(c) (dotted line) is the hysteresis curve rotated 180^o about the origin to highlight the level of asymmetry in the BRB response. This asymmetry, with higher forces being reached in compression than in tension, is a property found in all BRBs which can be quantified by the compression strength adjustment factor, β, taken as the ratio of

the maximum compressive force to the maximum tensile force. This test at a design displacement of 17.5mm gives $\beta = 206/185 = 1.11$.

Each model requires a number of coefficients to define its behaviour. In some cases, these relate to well-defined physical properties, like stiffness or yield displacement, which can be estimated directly from the force-displacement plot that is being fitted. In other cases, however, these fitting parameters cannot be directly related to observable properties and must be determined by a trial-and-error approach (for example, the shape parameters in the Menegotto-Pinto and Bouc-Wen models). To compare the performance of models with different parameters, the NRMS force error e_{NRMS} is used as a measure of accuracy, defined as:

$$e_{NRMS} = \sqrt{\frac{\int (F - F_m)^2 \, dt}{\int F_m^2 \, dt}} \qquad 6\text{-}1$$

where F_m is the measured force from the cyclic test in response to the imposed displacement, x, and F is the force produced by the model in response to the same displacement input, x. The Matlab® optimisation function *fmincon* was used to automate the optimisation of the parameters in order to minimise e_{NRMS}. This is a nonlinear programming solver for constrained multivariable problems [102].

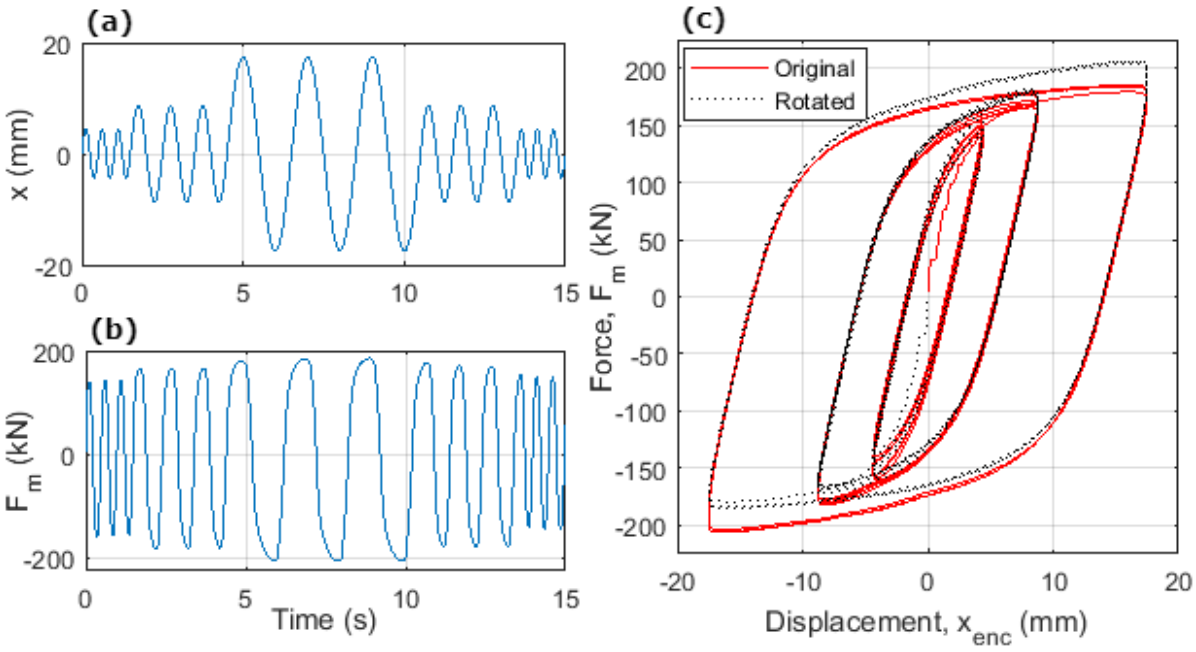

Figure 6.1 – Large displacement cyclic test: (a) applied displacement; (b) measured force; and (c) hysteresis curve

6.1.3. Model 1 – Bilinear Model

The behaviour of steel under uniaxial loading is characterised by elastic behaviour at pre-yield strains followed by plastic behaviour in the post-yield regime. A simple model that captures these properties is the bilinear model illustrated in Figure 6.2, consisting of an elastic-perfectly plastic model in parallel with a linear spring which accounts for kinematic hardening (the tendency for force to continue to increase with displacement in the post-yield regime). The model is defined by three parameters: the initial stiffness, K; the strain hardening ratio, a, which is the ratio of post-yield stiffness to initial stiffness; and the yield displacement, x_y, where the two lines intersect at the yield force, $F_y = Kx_y$.

The force, F_1, from the linear-elastic component of the model, shown in Figure 6.2(a), is simply:

$$F_1 = aKx \tag{6-2}$$

while the force, F_2, from the elastic-perfectly plastic component, shown in Figure 6.2(b), is given by:

$$F_2 = \begin{cases} (1-a)K(x-x_0) & \text{if } |x-x_0| \leq x_y \\ (1-a)Kx_y \text{sgn}(x-x_0) & \text{if } |x-x_0| > x_y \end{cases} \tag{6-3}$$

where x_0 represents a horizontal shift of the origin of the elastic-perfectly plastic model used to account for plastic deformation that has previously occurred. The following rule is applied to update x_0 each time plastic deformation occurs:

$$\text{if } |x-x_0| > x_y \text{ then set } x_0 = x - x_y \text{sgn}(x-x_0) \tag{6-4}$$

The combined response, shown in Figure 6.2(c), is then $F = F_1 + F_2$. Asymmetry of the force-displacement response can be accounted for in an approximate way by modifying eqs. 6-3 and 6-4 to have a different yield displacement in tension,x_{yT}, and compression, x_{yC}, increasing the number of fitting parameters to four.

Figure 6.3 shows the fit given by $K = 47.2kN/mm$, $a = 0.049$, $x_{yT} = 3.1mm$ and $x_{yC} = 3.7mm$, which gives an NRMS error, e_{NRMS}, of 14.7%. The popularity of the bilinear model stems from its simplicity, requiring only three or four parameters to define the model, all of which relate to physical properties that can be estimated manually from an experimental force-displacement plot. The

symmetric version of this model is implemented in OpenSees as the *Steel01* uniaxial material. The asymmetric version can be implemented by using the *Parallel* material object to combine an *Elastic* material with an *ElasticPP* (elastic-perfectly plastic) material. The downside to this model is that it assumes an abrupt transition from the pre-yield stiffness to the post-yield (strain hardening) stiffness. In reality, the tangent stiffness varies gradually as the steel passes from the elastic to the plastic regime, limiting the ability of the bilinear model to capture the true behaviour. For example, the model shown in Figure 6.3 can match the force at peak displacements in each direction, and to give a good approximation to the initial elastic stiffness, but the discrepancy in force at intermediate displacement values can be large. The remaining models improve the accuracy by fitting the gradual change in stiffness more closely but at the expense of increased complexity.

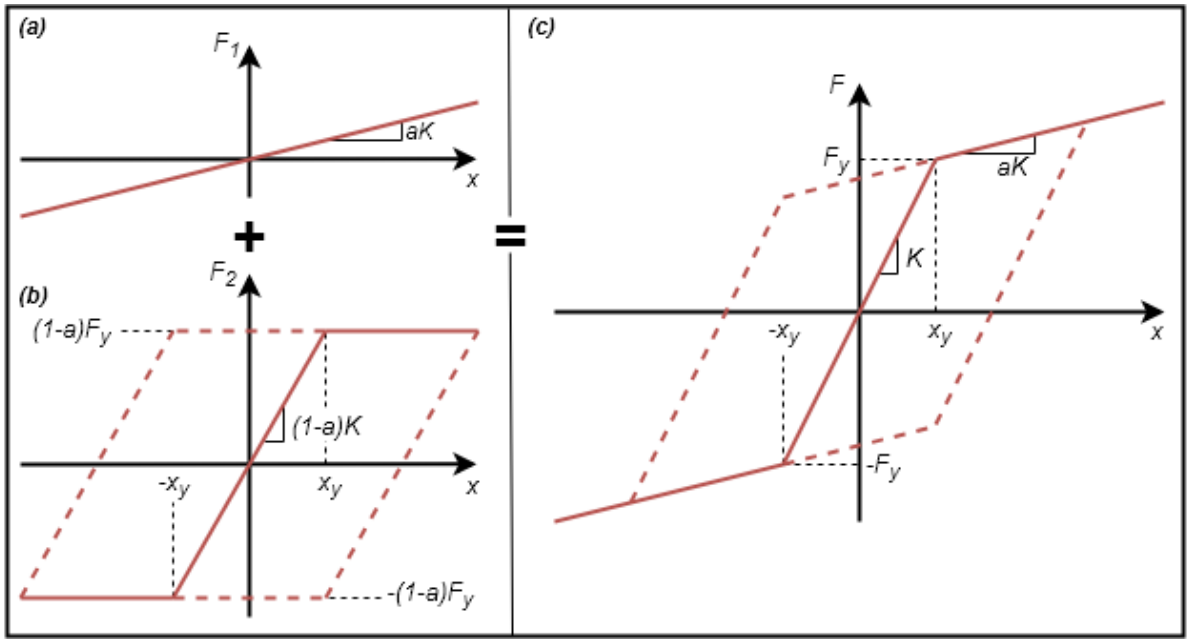

Figure 6.2 – The bilinear model

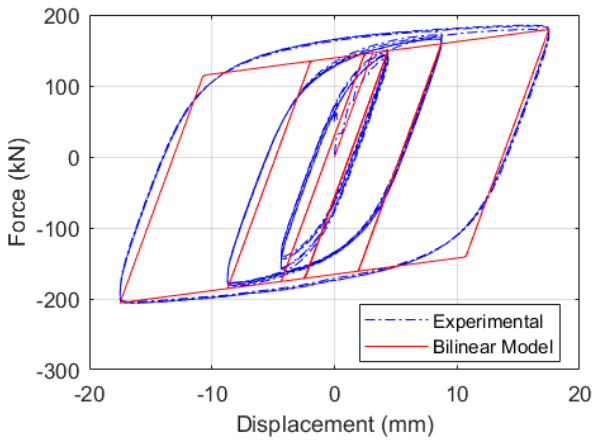

Figure 6.3 – Fit of bilinear model to experimental result

6.1.4. Model 2 – Multilinear Model

It is relatively straightforward to extend the bilinear model by adding multiple elastic-perfectly plastic models in parallel. If each has a different yield displacement, $x_{y,i}$, then the gradient of the force-displacement curve can be varied at multiple locations to give a closer fit to the experimental curve. This gives the multilinear model illustrated in Figure 6.4.

A multilinear model consisting of n line segments in each direction requires $n-1$ elastic-perfectly plastic components and one linear-elastic component. The forces due to each of the elastic-perfectly plastic components ($i = 1,2,\dots,n-1$) will be given by:

$$F_i = \begin{cases} r_i(x - x_{0,i}) & \text{for } |x - x_{0,i}| \leq x_{y,i} \\ r_i x_y \operatorname{sgn}(x - x_{0,i}) & \text{for } |x - x_{0,i}| > x_{y,i} \end{cases} \quad 6\text{-}5$$

where $r_i = K_i - K_{i+1}$ and K_i is the tangent stiffness of the i^{th} branch as shown in Figure 6.4. While the linear-elastic force component is simply:

$$F_n = K_n x \quad 6\text{-}6$$

The total force is then given by:

$$F = \sum_{i=1}^{n} F_i \quad 6\text{-}7$$

In addition, the origin shift, $x_{0,i}$, of each of the $n-1$ elastic-perfectly plastic components must be kept track of, which can be done by applying the following rule for $i = 1,2,\dots,n-1$:

$$\text{if } |x - x_{0,i}| > x_{y,i} \text{ then set } x_{0,i} = x - x_{y,i}\operatorname{sgn}(x - x_{0,i}) \quad 6\text{-}8$$

where $x_{y,i}$ is the yield displacement of the i^{th} elastic-perfectly plastic component. As for the bilinear case, asymmetry can be incorporated by adapting eqs. 6-5 and 6-8 to allow for different yield displacements in tension, $x_{yT,i}$, and in compression, $x_{yC,i}$.

To define the model, the n stiffnesses, K_i, and the $n-1$ or, if incorporating asymmetry, $2(n-1)$ displacement breakpoints, $x_{y,i}$, must be specified. This can be done by inspection – manually selecting the breakpoints $(x_{y,i}, F_{y,i})$ to fit a backbone curve to the data – but to obtain a better fit the coefficients

were optimised using the *fmincon* optimiser. To prevent the redundancy in the model from causing problems with the optimiser, the yield displacements, $x_{y,i}$, were initially set to reasonable values and the optimiser used to select the stiffness values, K_i, resulting in a symmetrical model. The optimisation was then re-run with the stiffnesses fixed at these values and the yield displacements in tension, x_{yT}, and in compression, x_{yC}, varied to minimise e_{NRMS}, resulting in an asymmetric model. Five stiffness components were used as a compromise between accuracy and complexity. The use of more components can allow a closer fit to the experimental hysteresis curve to be obtained but increases the complexity of the model and the complexity of the parameter fitting process. It is also likely that the improvement in accuracy achieved by increasing the number of components will diminish as the number of components increases. The coefficients given by this process are listed in Table 6.1 and a comparison to the experimental data shown in Figure 6.5. This gave an e_{NRMS} value of 5.50% – a vast improvement over what can be achieved with the bilinear model. Moreover, it gives a close fit to the experimental curve over the whole displacement range unlike the bilinear model for which the most appropriate coefficients are highly dependent on the magnitude of the displacement to be applied. This is an issue for dynamic analysis as the earthquake response will consist of multiple cycles at different amplitudes, the size of which will not be known in advance.

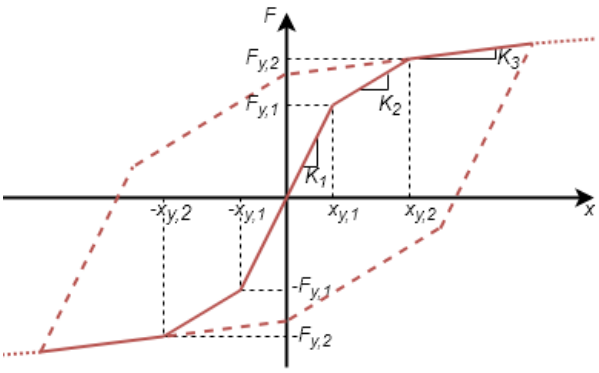

Figure 6.4 – The multilinear model

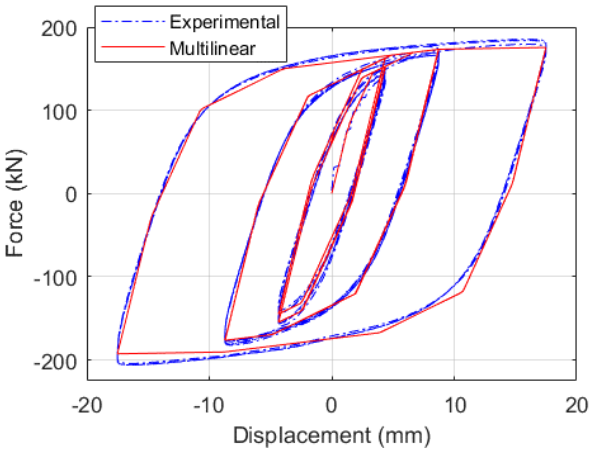

Figure 6.5 – Fit of multilinear model to experimental result

The first yield point in this model happens at 1.17mm in tension and 1.54mm in compression, which seems to disagree with the tests which showed that yielding does not occur until around 2.5mm. However, it is seen from Figure 6.5 that this is essentially accounting for the energy dissipated by friction. This is preferable to modelling the very high stiffness which occurs due to friction at a reversal of direction due to potential issues with the stability of the integration algorithm.

Component	Component Stiffness, r_i (kN/mm)	Yield Displacement in Tension, x_{yT} (mm)	Yield Displacement in Compression, x_{yC} (mm)
1	27.607	1.175	1.538
2	24.867	3.320	3.320
3	5.395	7.250	7.023
4	1.585	12.516	15.255
5 (elastic)	0.250	-	-

Table 6.1 – Coefficients of multilinear model

6.1.5. Model 3 – Menegotto-Pinto Model

The Menegotto-Pinto model is based on the model proposed by Guiffré and Pinto [103] in 1970 and enhanced by Menegotto and Pinto [104] in 1973 to incorporate kinematic hardening and to improve the definitions for calculating normalised stress and strain. The model is included in OpenSees in the materials *Steel02* and *Steel MPF*. The authors described the model in terms of normalised stress, σ^*, and normalised strain, ϵ^*, but here it is written in terms of normalised force, F^*, and normalised displacement, x^*.

The first step in defining the model is to specify a bilinear backbone with first branch stiffness K_0 and second branch stiffness bK_0, where b is the strain hardening ratio, intersecting at the point (x_y, F_y), as shown in Figure 6.6. This is similar to the bilinear model, except that the tangent lines should act as an envelope so that the experimental curve lies entirely within them. At each reversal in the direction of motion the values defining the next loading envelope are defined. These are the point at which the last displacement reversal occurred, $P_r(x_r, F_r)$, (the starting point for the new envelope) and the point

where the asymptotes of the next loading envelope meet, $P_0(x_0, F_0)$. The normalised force and displacement are then defined in terms of these values as:

$$F^* = \frac{F - F_r}{F_0 - F_r} \text{ and } x^* = \frac{x - x_r}{x_0 - x_r} \quad 6\text{-}9$$

The following function is then used to produce a smooth transition between initial asymptote of gradient K_0 and the final asymptote of gradient bK_0:

$$F^* = bx^* + \frac{(1-b)x^*}{(1 + x^{*R})^{1/R}} \quad 6\text{-}10$$

where the coefficient R determines the smoothness of the transition and is assumed to depend upon the plastic excursion, ξ, of the previous loading path using the formula:

$$R = R_0 - \frac{a_1 \xi}{a_2 + \xi} \quad 6\text{-}11$$

where the constants R_0, a_1 and a_2 must be chosen using parameter identification techniques.

Since the envelope of the loading curve under consideration is defined at each displacement reversal, it is straightforward to account for asymmetry by specifying a different yield displacement in tension, x_{yT}, and compression, x_{yC}. Further improvements can be made to the fit by allowing different values of R_0, a_1 and a_2 in tension and compression.

Figure 6.7 shows the fit given by the model defined by the coefficients listed in Table 6.2. First the parameters of the envelope (x_y, K_0, b) were chosen manually, with the value of x_y in tension being multiplied by the compression overstrength factor of 1.112 to give the value in compression. The *fmincon* optimiser was then used to determine the remaining parameters (R_0, a_1, a_2) in tension and compression so as to minimise e_{NRMS}, resulting in an NRMS error of 5.75%.

	x_y (mm)	K_0 (kN/mm)	b	R_0	a_1	a_2
Value in Tension	3	57.333	0.0093	2.5957	0.0959	9.9972
Value in Compression	3.336	57.333	0.0093	30.6949	28.6758	0.0294

Table 6.2 – Coefficients of Menegotto-Pinto model

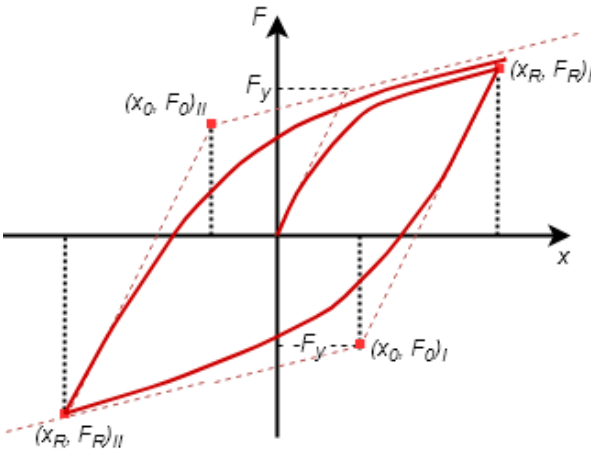

Figure 6.6 – The Menegotto-Pinto model

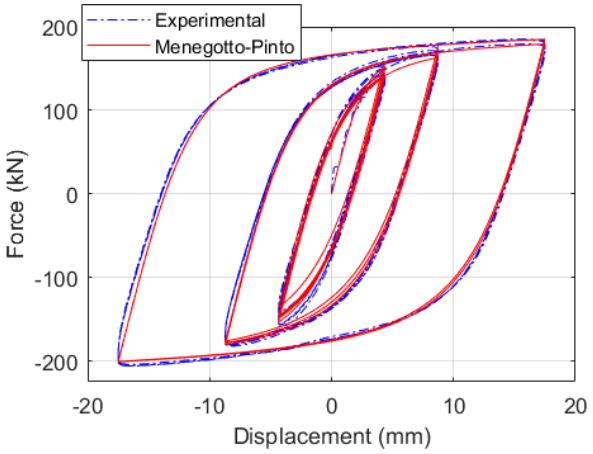

Figure 6.7 – Fit of Menegotto-Pinto model to experimental result

6.1.6. Model 4 – Ramberg-Osgood Model

The Ramberg-Osgood model proposed by Ramberg and Osgood in 1943 [105] is mentioned for completeness as it is another material model used to model the yielding behaviour of steel. It is included in OpenSees as the *RambergOsgoodSteel* material. Unlike the other models considered, which give force, F, as a function of displacement, x, this model gives displacement as a function of force:

$$x = \frac{F}{K}\left(1 + \alpha \left|\frac{F}{F_y}\right|^{n-1}\right) \qquad 6\text{-}12$$

where the nature of the model is defined by the elastic stiffness, K, and the parameters α and $n > 1$. Since the hybrid system has been set up to operate under displacement control, a nonlinear equation would have to be solved to obtain F for a given x, which would complicate the implementation in the RTHS system, so this model was not considered further.

6.1.7. Model 5 – Bouc-Wen Model

The Bouc-Wen model is a differential model of hysteresis proposed by Bouc [106] and extended by Wen [107] which is used extensively for modelling nonlinear hysteretic behaviour in dynamically excited mechanical or structural systems [108]. The original form of the model is functionally redundant [109] meaning multiple sets of coefficients can describe the same behaviour. Different authors have

reformulated the equations in various ways in order to eliminate this redundancy. The formulation here is based on that used by Black et al. [7]:

$$F(t) = \alpha K x(t) + (1-\alpha) K x_y z(t) \tag{6-13}$$

$$\dot{z}(t) = \frac{\dot{x}(t)}{x_y}\left\{1 - |z(t)|^n\left[1 + \beta\left(\mathrm{sgn}\left(\dot{x}(t)z(t)\right) - 1\right)\right]\right\} \tag{6-14}$$

where it can be seen that the force, F, can be split into an elastic component $\alpha K x(t)$, which provides the post-yield stiffness, and a hysteretic component $(1-\alpha)Kx_y z(t)$ dependent on the non-observable hysteretic parameter, $z(t)$, which is found by integrating Eq. 6-14. The model is defined by the five parameters K, α, x_y, β and n, whose meanings are listed in Table 6.3 along with constraints ensuring a physically meaningful hysteretic model on the basis of stability, passivity and thermodynamic admissibility [110].

Wang and Wen [111] modified the Bouc-Wen model to incorporate asymmetry by including an additional parameter ϕ so that Eq. 6-14 becomes:

$$\dot{z}(t) = \frac{\dot{x}(t)}{x_y}\left\{1 - |z(t)|^n\left[1 + \beta\left(\mathrm{sgn}\left(\dot{x}(t)z(t)\right) - 1\right) + \phi\left(\mathrm{sgn}\left(\dot{x}(t)\right) + \mathrm{sgn}\left(z(t)\right)\right)\right]\right\} \tag{6-15}$$

where the additional component, $\phi\left(\mathrm{sgn}\left(\dot{x}(t)\right) + \mathrm{sgn}\left(z(t)\right)\right)$, can take the value -2ϕ, 0 or 2ϕ depending on the region of the hysteretic loop the system is in. The *fmincon* optimiser was used to select the parameters which minimise e_{NRMS} for both versions of the model. The optimised parameters are given in Table 6.4, with the symmetric model giving an e_{NRMS} of 5.82% while the asymmetric model improved this to 5.02%. The resulting fit for the asymmetric model is shown in Figure 6.8.

Parameter	Interpretation	Constraints
K	Initial elastic stiffness (kN)	$K > 0$
α	Strain hardening ratio (post-yield stiffness over pre-yield stiffness)	$0 \leq \alpha < 1$
x_y	Yield displacement (mm)	$x_y > 0$
β	Dimensionless shape control parameter	$\beta \geq 0.5$
n	Dimensionless parameter controlling sharpness of yield	$n \geq 1$

Table 6.3 – Coefficients of Bouc-Wen model

	K (kN/mm)	α	x_y (mm)	β	n	ϕ
Symmetric model	42.659157	0.0333592	4.0297602	1.003897	1.3630119	-
Asymmetric model	41.975799	0.0359580	4.0682390	1.0661749	1.4517588	0.0242038

Table 6.4 – Optimised coefficients of Bouc-Wen model

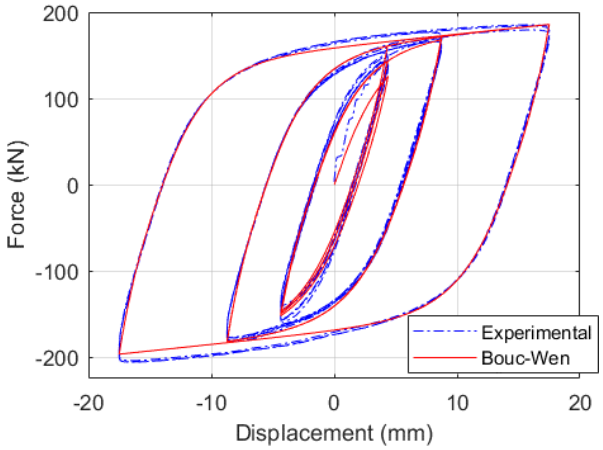

Figure 6.8 – Fit of Bouc-Wen model to experimental result

6.1.8. Comparison of Models

The NRMS errors between the experimentally measured force from the cyclic test and the forces given by the fitted models are listed in Table 6.5. The accuracy of the simple bilinear model is deemed insufficient for dynamic simulation, while the Ramberg-Osgood model is impractical to implement in the displacement-controlled system. The remaining models (multilinear, Menegotto-Pinto and Bouc-Wen) all exhibited comparable accuracy. The need to constrain out the redundancy in the multilinear and Menegotto-Pinto models during the parameter fitting process means that more optimal solutions are likely to exist for these models, but the ones obtained are sufficiently close.

The accuracies given above were calculated relative to the experimental result from which the model coefficients were derived. It is therefore prudent to verify the performance in response to a different displacement history. While the cyclic test results used above were convenient for fitting of the model coefficients, the displacement experienced in an earthquake will be far less uniform. Figure 6.9(a)

Model:	Bilinear	Multilinear	Menegotto-Pinto	Bouc-Wen
NRMS Force Error (%):	14.7	5.50	5.75	5.02

Table 6.5 – Accuracy of numerical BRB models under cyclic displacement

shows a more realistic displacement history which a BRB might be subjected to during an earthquake. This displacement was applied experimentally to the BRB, and also numerically to the multilinear, Bouc-Wen and Menegotto-Pinto models derived above, giving the force responses shown in Figure 6.9(b). The occurrence of partial unloading followed by reloading – where the direction of motion reverses before full yield has occurred in that direction – is seen to be an issue for some of the models. Figure 6.10 compares the hysteresis curves given by each of the models to the experimental result for the final part of the displacement history, indicated by the bold line in Figure 6.9(a), which includes a partial unloading event. All three models give a good match to the experimental result as unloading occurs, but when the direction reverses the models respond very differently. The Bouc-Wen model underestimates the force during reloading while the Menegotto-Pinto model overestimates it – this non-physical effect is illustrated in Figure 6.11. Only the multilinear model reproduces the behaviour realistically: reloading up to the previous loading curve before continuing along the curve that would have been produced if partial unloading had not occurred. The NRMS force errors for the section of the test plotted in Figure 6.9 are given in Table 6.6 and confirm that the multilinear model gives notably better performance than the other two methods during a partial unloading/reloading event. Table 6.6 also shows the ratio of the energy dissipated by each model over the cycle shown in Figure 6.10 to that dissipated by the experimentally tested BRB. This confirms that the Bouc-Wen model underestimates the energy dissipation after partial unloading while the Menegotto-Pinto model overestimates it, and that the multilinear model gives the best match with an error of less than 1%.

The problem of partial unloading and reloading in the Menegotto-Pinto model was noted by Filippou et al. in 1983 [112] but the error was not deemed particularly significant for their application: modelling the reinforcing steel in reinforced concrete. They noted that the issue could be prevented if the model contained a memory of all previous loading branches so that the model could retrace previous

Model:	Multilinear	Menegotto-Pinto	Bouc-Wen
NRMS Force Error (%):	7.71	13.37	12.02
Energy dissipation ratio:	0.992	1.022	0.941

Table 6.6 – Accuracy of numerical BRB models during partial unloading

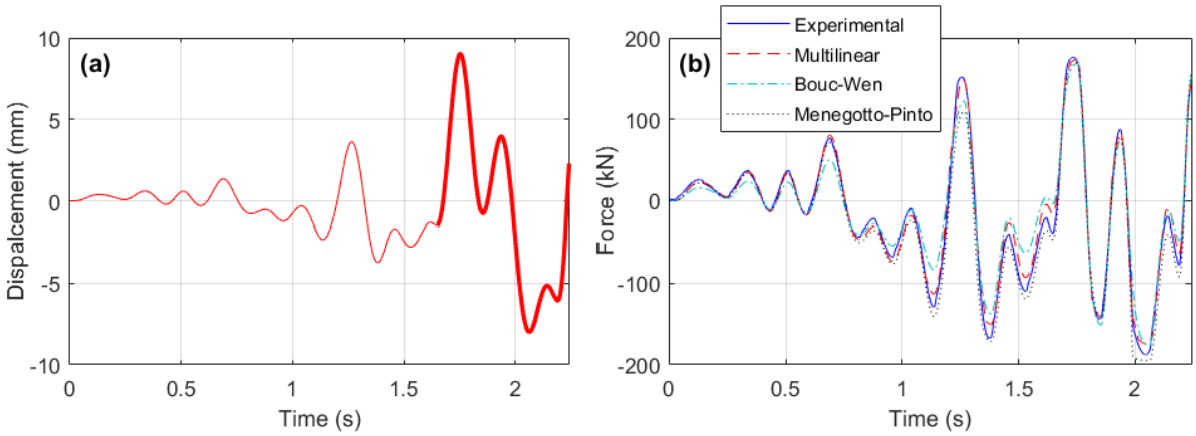

Figure 6.9 – (a) Earthquake displacement time history and (b) resulting force response

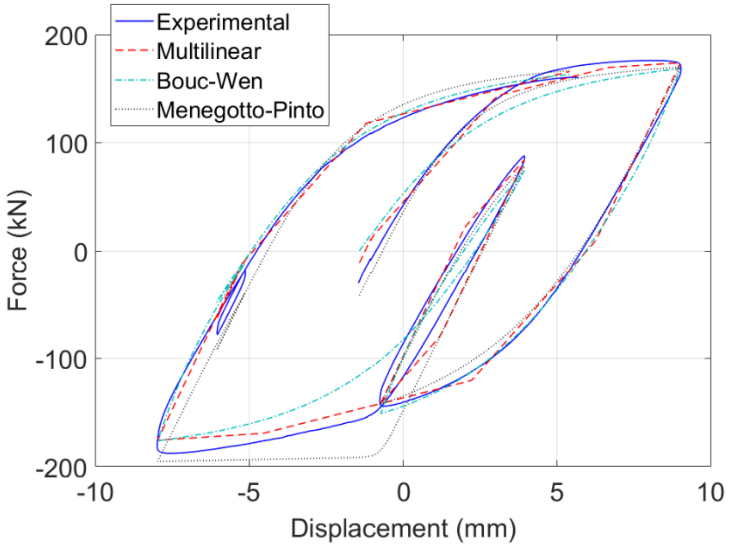

Figure 6.10 – Comparison of hysteresis curves, including partial unloading and reloading event

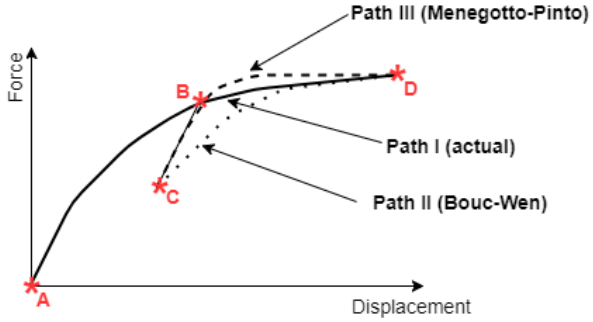

Figure 6.11 – Loading paths during reloading (C→D) after partial unloading (B→C)

incomplete loading curves. This has been implemented by Kolozvari et al. [113] and forms the *SteelMPF* model in OpenSees. A new modification recently proposed by Bosco et al. [114] avoids the need to store all previous loading curves. A key part of the modification is redefining the point $P_0(x_0, F_0)$ from being the intersection of the asymptotes of the loading envelope to being the intersection of the first

asymptote with the previous loading curve. This is more complicated to compute because of the nonlinearity of Eq. 6-10, so the solution must be found by iteration. This is difficult for RTHS where it is necessary to ensure that the solution will be available within a fixed number of computations.

A modification to the Bouc-Wen model has also been proposed [115] which introduces a stiffening factor into Eq. 6-14 which is activated when reloading after partial unloading is detected. To implement this properly the location of multiple reversal points must be recorded from which a set of "active" reversal points which tell the system when the original Bouc-Wen model would underestimate the force, and therefore when the stiffening factor should be applied.

The method chosen for modelling the BRBs in this project is the multilinear model since it is the most straightforward model capable of faithfully simulating the BRB response. It can be made to match the BRB response closely for cycles of various amplitudes, can incorporate asymmetry, and produces the true physical behaviour during reloading after a partial unloading event without requiring an iterative process or a large amount of computational memory. Model coefficients can easily be selected manually by comparison to the backbone curve from experimental data or can be optimised numerically, and the complexity of the model can be controlled by increasing or decreasing the number of segments used to form the curve. Finally, it is straightforward to modify the model to accommodate other considerations, such as limiting the initial gradient of the backbone curve to avoid numerical stability in the integration algorithm.

6.1.9. Scaling of BRB Model

In the building designed for the MDOF hybrid simulation, the required length of the BRBs depends on the geometry of the frame while the required cross-sectional area of the core depends on the stiffness and strength requirements of the structure. To adapt the multilinear model derived for the tested BRB to model BRBs with different core areas, it is assumed that the areas of each section of the core (the elastic zones, transition zones and yielding zone) are scaled in proportion. Each stiffness component, r_i, in the multilinear model is then simply multiplied by the area factor:

$$f_A = \frac{A_{design}}{A_c} \quad \text{6-16}$$

where A_c is the cross-sectional area of the yielding core of the tested BRB (525mm^2) and A_{design} is that of the BRB being simulated. Similarly, to adapt the model for BRBs of different length it is assumed that the lengths of each section of the core are scaled in proportion. Each stiffness component r_i is then divided by the length factor:

$$f_L = \frac{L_{design}}{L_c} \quad \text{6-17}$$

where L_c is the overall length of the tested BRB (2570mm) and L_{design} is that of the BRB being modelled. Meanwhile, the yield displacements, $x_{y,i}$, of each component of the model must be multiplied by f_L to approximate those of the design BRB.

Alternatively, the multilinear model fitted to the tested BRB can be used in its current form but with the input displacement scaled by $1/f_L$ and the output force scaled by f_A/f_L. This is the approach used to allow the tested BRB forming the physical substructure to simulate a BRB of different dimensions.

In a real design situation, it would be necessary to consult the BRB manufacturer to obtain the actual stiffness properties of the BRBs having the cross-sectional areas determined from initial design. The design would then need to be verified for these updated properties, and further design iterations might be necessary if the actual BRB characteristics differ significantly from the assumed values. It is unlikely that the lengths of all sections would be scaled in proportion to the overall length, or that the cross-sectional area of the elastic and transition zones would be scaled in proportion to that of the yielding zone. For example, the three sample BRBs provided for testing by Star Seismic Europe have different yielding cross-sectional areas but the dimensions of the elastic zones are the same for all three. However, this gives a sufficient approximation for the structure assumed in this project since it results in plausible BRB properties and, since the BRB stiffness is predominantly determined by the flexibility of the yielding length of the core, it is unlikely to be far off the properties of a real BRB.

6.2. Design of Numerical Substructures

6.2.1. Structural form

Two Eurocode compliant MDOF structures are simulated using RTHS in this chapter. Both consist of five-storey steel frame structures with the layout and dimensions shown in Figure 6.12 in which the members in bold are assumed to form the lateral load resisting systems, while the rest of the frame is classed as secondary members which carry only gravity loads [3]. For simplicity, only the design of the frame resisting lateral loads in the X-direction (the front frame in Figure 6.12), since the numerical substructures implemented in the RTHS testing later in the chapter are limited to a two-dimensional model, and the structure is assumed to be symmetrical.

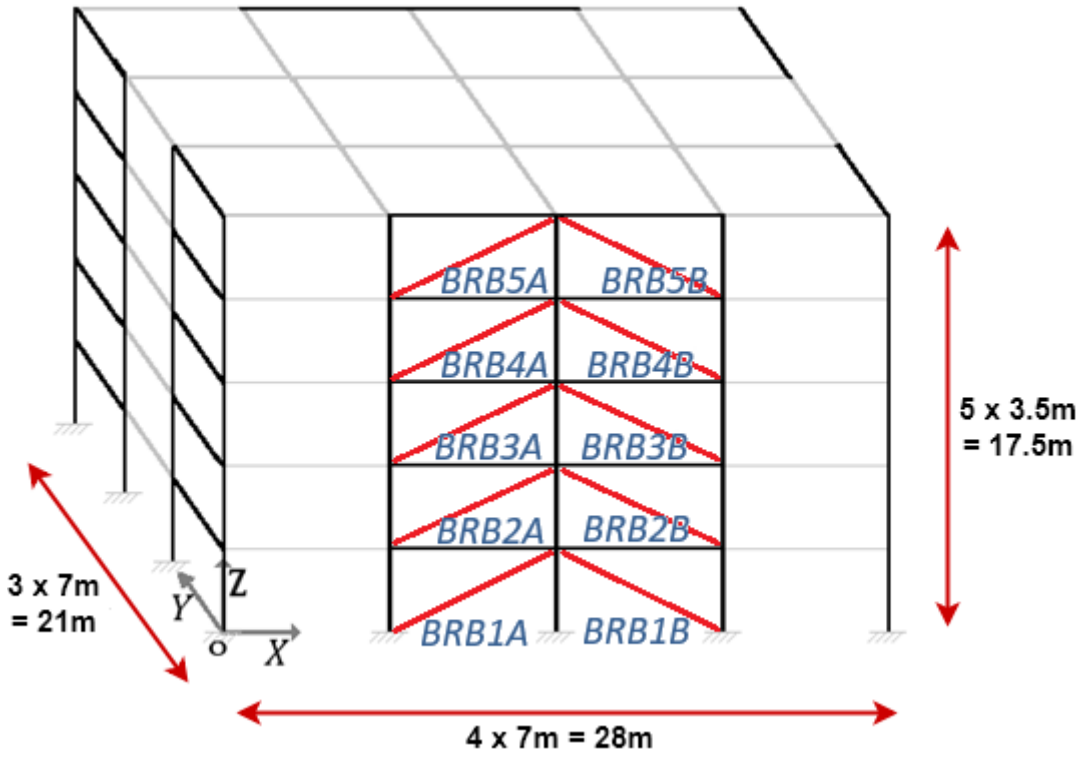

Figure 6.12 – Layout of structures designed for RTHS

6.2.2. MRF-BRBF Dual Structure

Here a Eurocode 8 compliant moment-resisting frame (MRF) is designed. BRBs will be added for RTHS to form a dual MRF-BRBF structure, but the design here is performed for the bare MRF.

6.2.3.1. Seismic Mass

The actions on the structure depend on its seismic mass which is determined from the load comination given in Eq. 2-7, where $\psi_{E,i}$ is 0.24 for imposed loads, except at roof level where it is zero. For determining the imposed loads, it has been assumed that the building is used for offices. The resulting seismic masses are 477 tonnes at floors 1 to 4 and 380 tonnes at roof level giving a total seismic mass of 2288 tonnes.

6.2.3.2. Modal Analysis

After a number of iterations, the member sizes chosen were UKB 533x312x219 for the beams and UKC 356x406x467 for the columns, which are assumed to be the same throughout the height of the building. These members satisfy the "weak beam / strong column" requirement of Eq. 2-5. A modal analysis performed in OpenSees using these member sizes and the above seismic masses gave natural frequencies of 1.075s, 0.325s, 0.168s, 0.105s and 0.077s in the modes in the horizontal direction of interest.

6.2.3.3. Lateral Force Method of Analysis

Assuming a behaviour factor, q, of 4, as specified for MRFs of ductility class medium, the ductility reduced design acceleration from Figure 2.4 is:

$$S_d(T_1) = a_g S \frac{2.5}{q}\left[\frac{T_c}{T_1}\right] = 0.24 \times 9.81 \times 1.2 \times \frac{2.5}{4} \times \left[\frac{0.5}{1.075}\right] = 0.821 m/s^2 \qquad 6\text{-}18$$

leading to a design base shear, from Eq. 2-9, of:

$$F_b = S_d(T_1) m \lambda = 0.851 \times 2288 \times 1.0 = 1946 kN \qquad 6\text{-}19$$

This is distributed between the floors in accordance with Eq. 2-11 assuming a linear fundamental mode shape. The forces, F_j, to be applied to each floor level, and the resulting storey shears, V_j, are given in Table 6.7.

Floor	m_j (tonnes)	z_j	$m_j z_j$ (tonne-m)	F_j (kN)	V_j (kN)
5 (roof)	380	17.5	6650	554	554
4	477	14	6678	557	1111
3	477	10.5	5009	418	1529
2	477	7	3339	278	1807
1	477	3.5	1670	139	1946
	$\sum m_j = 2288\ (= m)$		$\sum m_j s_j = 23346$	$\sum F_j = 1946\ (= F_b)$	

Table 6.7 – Horizontal seismic actions for MRF using Lateral Force Method

Applying these loads to an elastic model of the structure in Simulink gives a maximum beam moment of 750kNm, which is less than the plastic resistance of 1620kNm. It is verified that the shear force at the formation of plastic hinges satisfies $V_{Ed} \leq 0.5V_{pl,Rd}$, and that the columns satisfy the overstrength requirements of Eq. 2-4 as well as being checked against buckling. The interstorey drifts (IDRs) from the elastic model are multiplied by q (=4) to obtain the ULS design IDRs, which are halved to obtain the damage limitation IDRs, since it is assumed that the design response spectrum of the damage limitation earthquake is simply ν times the ULS spectrum, where ν is 0.5 in this case. This gives the design drifts in Table 6.8. It is verified that P-Δ effects can be neglected in this case, although torsion about the vertical axis caused by accidental eccentricity must be taken into account. This is done by offsetting the loads relative to the centre of stiffness of each floor. These IDRs satisfy the limits for the damage limitation state (Section 2.1.2) provided the structure has ductile non-structural elements (IDRs less than 0.75%) which will be assumed to be the case.

Storey	Design IDR without torsion (%)		Design IDR with torsion (%)	
	Damage limitation	ULS	Damage limitation	ULS
5 (roof)	0.29	0.58	0.32	0.64
4	0.455	0.91	0.5	1.00
3	0.59	1.18	0.655	1.31
2	0.62	1.24	0.685	1.37
1	0.355	0.71	0.395	0.79

Table 6.8 – Design IDRs from equivalent linear analysis

6.2.3. BRBF Structure

The BRBF structure designed here is assumed to have continuous columns which are pinned to the top of a rigid foundation with the beams pinned to the columns. Since Eurocode 8 does not provide a behaviour factor, q, or specific rules for BRBFs, the design must be verified through nonlinear analysis. However, for initial design the lateral force method is applied using an assumed value of q and reasonable rules extrapolated from those for CBFs. This is informed by the treatment of BRBFs in the American *ASCE 7-16* code [16], the design guidance of the BRB manufacturer [116], the results of BRB testing [48] and recommendations from the literature [38] [84]. This design is then verified using NLTH analysis.

6.2.3.1. Lateral Force Method Actions

Eurocode 8 allows the fundamental period, T_1, for CBFs, EBFs and MRFs to be estimated from Eq. 2-10 using values of C_t of 0.05, 0.075 and 0.085, respectively. The increased ductility provided by BRBs will generally allow smaller cross-sections to be used than for the braces in a conventional CBF, suggesting the value of C_t for BRBFs should be higher than that for CBFs. *ASCE 7-16* [16], which uses an approximation of the same form as Eq. 2-10, ascribes BRBFs the same C_t value as for EBFs (0.0731). For this design the initial estimate of natural period is therefore obtained using the Eurocode 8 specificed value of C_t for EBFs (0.075), which is the approach taken in the BRB manufacturer's initial design example [116]. This gives:

$$T_1 \approx 0.075 \times 17.5^{3/4} = 0.642s \qquad 6\text{-}20$$

Assuming a behaviour factor, q, of 7, as suggested by Vigh et al. [54] and the BRB manufacturer [116], the ductility reduced design acceleration from Figure 2.4 is:

$$S_d(T_1) = a_g S \frac{2.5}{q}\left[\frac{T_c}{T_1}\right] = 0.24 \times 9.81 \times 1.2 \times \frac{2.5}{7} \times \left[\frac{0.5}{0.642}\right] = 0.786 m/s^2 \qquad 6\text{-}21$$

which results in a design base shear, from Eq. 2-9, of:

$$F_b = S_d(T_1) m \lambda = 0.786 \times 2288 \times 0.85 = 1529 kN \qquad 6\text{-}22$$

This is distributed between the floors in accordance with Eq. 2-11 assuming a linear fundamental mode shape. The forces, F_j, to be applied to each floor level, and the resulting storey shears, V_j, are given in Table 6.9.

Floor	m_j (tonnes)	z_j	$m_j z_j$ (tonne-m)	F_j (kN)	V_j (kN)
5 (roof)	380	17.5	6650	436	436
4	477	14	6678	438	874
3	477	10.5	5009	329	1203
2	477	7	3339	219	1422
1	477	3.5	1670	110	1532
	$\sum m_j = 2288\ (= m)$		$\sum m_j s_j = 23346$	$\sum F_j = 1532\ (\approx F_b)$	

Table 6.9 – Horizontal seismic actions for BRBF using Lateral Force Method

6.2.3.2. Equivalent BRB Element

Design is performed on the basis of a nominal yield strength, $f_{y,nom}$, of 235N/mm^2 for the BRB core [48]. Since there are four BRBs operating in each principal direction, all inclined at an angle, θ, to the horizontal, initial estimates of the BRB yielding areas, $A_{req,j}$, required in each storey, j, were obtained from the strength requirement:

$$A_{req,j} \approx \frac{V_j}{4 f_{y,nom} cos\theta}$$

Using these initial values, a linear elastic finite element model was created in OpenSees. While the strength of the BRB depends only on the area of the yielding section of the core, the stiffness is slightly more complicated to compute as BRBs are non-prismatic, having a cross-sectional area which varies along the length. In addition, the BRB does not span the entire workpoint-to-workpoint length of the frame due to the dimension of the members and connections. For simplicity, in initial design using equivalent linear analysis it is common to use an equivalent prismatic brace to represent the BRB, with a stiffness factor applied to obtain the correct stiffness [118]. The stiffness factor will depend on many factors, including the dimensioning of the BRB, the connection type and the orientation in the frame. In a real design situation, the engineer would consult with the BRB manufacturer to obtain appropriate stiffness factors. For the purposes of this design, a suitable stiffness factor is estimated based on the properties of the tested BRB and will be assumed to be the same for the BRBs in all storeys. The tested

BRB has a yielding core area, A_c, of 525mm^2 and a length, L_0, of 2570mm. The experimentally determined elastic stiffness of the BRB, K_{BRB}, is 53.8kN/mm, while a prismatic member of the same length with a constant cross-sectional area of A_c would have a stiffness, K_p, of:

$$K_p = \frac{E_s A_c}{L_0} = \frac{210 \times 525}{2570} = 42.9 kN/mm$$

where $E_s = 210 kN/mm^2$ is the Young's modulus of steel. Hence, the stiffness of the equivalent prismatic brace must be increased by a factor of $53.8/42.9 = 1.25$. Similarly, the workpoint-to-workpoint length, L_{wp-wp}, in the model is 7826mm, while based on likely sizes of members and connections a likely BRB length would be around 4696mm. Treating the connection lengths as rigid, the stiffness of the brace of length L_{wp-wp} in the model would need to be increased by a factor of $7826/4696 = 1.67$ to give the correct stiffness. Hence the overall stiffness factor is given by $1.25 \times 1.67 = 2.09$ which was applied in OpenSees by setting the Young's modulus for the brace, E_b, to $E_b = 2.09 E_s$.

6.2.3.3. Design

The lateral forces from Table 6.9 were applied to the linear elastic OpenSees model with the BRBs modelled as above and the BRB forces and elastic interstorey drifts extracted. The elastic interstorey drifts are then multiplied by $q = 7$ to obtain the design interstorey drifts. This process was repeated with the BRB core areas in each storey varied until the overstrength ratio (the ratio of the design resistance to the design action) exceeded 1.0 in all floors, while aiming to minimise the variation in overstrength ratios between floors to give an even distribution of ductility through the height of the structure, as is the aim of Eq. 2-6. The BRB areas for the final design are listed in Table 6.10 along with the resulting overstrength ratios and design IDRs (the IDRs from the elastic analysis multiplied by the behaviour factor of 7).

The ability to freely select the BRB core areas, rather than being restricted to standard sections as for conventional bracing, has allowed the overstrength ratios to be closely matched between stories, with just 1.64% difference between the maximum and minimum values. This is well within the 25% range

allowed for CBFs in Eq. 2-6, as well as the more stringent 10% range recommended by Vigh et al. [54]. In turn, this results in displacements been evenly distributed between stories, with a variation of just 5.2% between the maximum and minimum IDRs. In this case P-Δ effects cannot be neglected, so they are included using the approximate formula given in Eurocode 8. These IDRs satisfy the Eurocode 8 limits for structures with ductile non-structural elements (IDRs less than 0.75%), which is assumed to be the case for this building. This design is therefore governed by strength requirements. If the structure were to have nonductile non-structural elements, the BRB areas would need to be increased to reduce IDRs below 0.5%.

Storey	BRB core area (mm^2)	Overstrength ratio	Damage limitation IDR (%)	
			Neglecting P-Δ effects	Including P-Δ effects
5 (roof)	640	1.032	0.437	0.517
4	1260	1.023	0.467	0.535
3	1710	1.016	0.479	0.544
2	2000	1.015	0.484	0.540
1	2130	1.018	0.481	0.528

Table 6.10 – BRB areas and action effects for BRBF designed using the lateral force method

The computed elastic natural periods of this structure for lateral modes in the direction resisted by the frame in question are: 0.855s, 0.347s, 0.217s, 0.155s and 0.120s. Notice that the fundamental period of 0.855s is longer than the value of 0.642s estimated from Eq. 2-10 and used in determining the seismic base shear. However, the design response spectrum (Figure 2.4) shows that a shorter period will result in a greater spectral acceleration, and hence a larger base shear, meaning the use of the shorter period is conservative.

6.2.3.4. Verification using NLTH Analysis

While the above design was carried out in accordance with the methodology of Eurocode 8, it cannot qualify as a design check since the code does not include a behaviour factor, q, or other specific rules for BRBFs. A nonlinear analysis method must therefore be performed to verify the design, for which NLTH analysis was used. This required a nonlinear BRB model for which the multilinear model described in Section 6.1.4 was used. The fitted model parameters for the tested BRB listed in Table 6.1 formed the basis of the model, while the scaling approach described in Section 6.1.9 was applied to allow the

modelling of BRBs of different length and with different cross-sectional areas. To implement the multilinear model in OpenSees, each BRB was made up of a set of five *ElasticPP* (elastic-perfectly plastic) uniaxial material objects – one for each stiffness component of the multilinear model – and these were combined into a single object using the *Parallel* material command. To account for the different BRB areas, the stiffness of each component was multiplied by the ratio of the area of the BRB being simulated (Table 6.10) to that of the tested BRB to which the multilinear model was simulated (525mm^2). To account for the difference in length between the BRBs in the simulation and the tested BRB, the yield displacements of each component was multiplied by the ratio of the assumed length of the BRBs in the simulation to the length of the tested BRB, which gave $L/L_{BRB} = 1.827$.

Eurocode 8 specifies 5% inherent damping be assumed. This was implemented in OpenSees using Rayleigh damping but, as explained in Section 2.2.3, care must be taken when using Rayleigh damping with yielding systems to avoid unintentionally high damping levels. The peak interstorey drift given by the linear method for the ULS loadcase was 37.3mm. Based on the geometry of the frame, the BRBs are inclined at 26.6° to the horizontal, so this would cause a BRB extension of 33.4mm. This is equivalent to an extension of the tested BRB of $33.4/1.827 = 18.3mm$. From the results of previous testing, the secant stiffness at this level of yielding is approximately 10.1kN/mm, or 18.8% of the initial stiffness. Repeating the modal analysis with the BRB stiffnesses reduced to 18.8% of their elastic values results in a fundamental period of 1.912s. This is taken as an estimate of the upper limit on the effective periods in the structure. The values of α and β were therefore selected (Eq. 2-24) to set the damping to 5% at 1.912s and 0.217s (the period of the third mode with the elastic stiffness). This ensured that the actual damping experienced would be less than or equal to 5% in the first three modes. This gave $\alpha = 0.2951$ and $\beta = 0.003102$.

NLTH analyses were run using the scaled recorded accelerograms for each of the three earthquakes from the Eurocode 8 compliant suite described in Table 2.1 at both the damage limitation (DL) and ULS scale factors (the DL ground motion being 50% of the ULS). The resulting IDRs are listed in Table 6.11.

To allow comparison between methods, P-Δ effects have not been included in Table 6.11 since they are treated in an approximate way in the linear analysis which would reduce the ability to compare the two methods.

As three ground motions have been used, the worst effects from the three cases must be taken. The maximum IDR at the damage limitation (DL) state is 0.486%, while the maximum at the ULS is 0.981%. The maximum IDR at the DL state from the lateral force method was 0.484%, while the ULS value would simply be double this, 0.968%.

Even when adjusted for P-Δ effects, the peak DL IDR is less than 0.75%, so the damage limitation requirement is satisfied. The BRB extension corresponding to the peak ULS IDR is also within the proven range (assuming the BRB scaling method holds) so the ULS requirement is also satisfied.

Limit State	Ground motion	Accelerogram Scale factor	Peak IDR (%)				
			1	2	3	4	5 (roof)
Damage Limitation State (DL)	El Centro	0.5×1.02	0.365	0.269	0.273	0.374	0.426
	Kalamata	0.5×1.18	0.245	0.215	0.291	0.379	0.474
	Northridge	0.5×0.87	0.250	0.277	0.300	0.311	0.486
Ultimate Limit State (ULS)	El Centro	1.02	0.779	0.570	0.547	0.608	0.736
	Kalamata	1.18	0.781	0.649	0.427	0.407	0.669
	Northridge	0.87	0.981	0.797	0.582	0.509	0.823

Table 6.11 – Peak IDRs given by NLTH analysis of BRBF (P-Δ effects neglected)

6.3. Numerical Substructure

6.3.1. MDOF Model

In the NLTH analyses above, the structural equations of motion were integrated directly using an unconditionally stable implicit algorithm (the Newmark CAAM method). However, direct integration with the full finite element model could not be implemented within the timestep of 1ms. As an alternative to using a sub-stepping procedure to allow a longer integration timestep to be used, a modal decomposition approach was used to reduce the number of DOFs of the system to a number that could be integrated within the 1ms timestep. This is based on the modal approach for linear elastic structures described in Section 2.2.2, and the adaptation of the approach to the nonlinear simulation is described below. First, it will be convenient to write the equation of motion as:

$$M\ddot{\boldsymbol{x}} + C\dot{\boldsymbol{x}} + K\boldsymbol{x} = -M\{\mathbf{1}\}\ddot{x}_g - \boldsymbol{r} \qquad 6\text{-}23$$

where K is the stiffness provided by the frame which is assumed to remain elastic (this will be significant for the MRF but minimal for the BRBF) and $\boldsymbol{r}$ is a vector containing the forces provided by the BRBs (one of which will come from the physical substructure).

6.3.2. Modal Model of MRF-BRBF Dual Structure

In the MRF-BRBF dual structure, most of the stiffness comes from the frame. Here it will be assumed that BRBs with quite a small cross-sectional area are installed to act predominantly as dampers rather than bracing. For this purpose, the same BRB size is used in every storey and they are modelled as having the cross-section of the tested specimen, but with the length scaled to fit the structure (the length multiplied by 1.827). Given that most of the stiffness comes from the MRF, and the BRBs are distributed uniformly through the height, it is assumed that the mode shapes of the BRB braced structure are the same as those of the bare MRF. The modal decomposition is performed for the MRF to obtain the mode shape matrix, Φ, and natural frequencies, ω_i, of the frame without BRBs. This gives the modal model as:

$$\ddot{\boldsymbol{q}} + \mathrm{B}\dot{\boldsymbol{q}} + \Lambda \boldsymbol{q} = -\boldsymbol{\Gamma}\ddot{x}_g + \Phi^T \boldsymbol{r} \qquad 6\text{-}24$$

where $\boldsymbol{\Gamma} = \Phi^T M\{\mathbf{1}\}$, with Φ is scaled so that $\Phi^T M \Phi = I$, and the values of ω_i in B and Λ are those for the bare MRF. This approach is based on the assumption that the mode shapes of the combined structure are close to those of the bare MRF, which is reasonable given most of the stiffness comes from the MRF. The resulting mode shapes and natural frequencies are given in Figure 6.13.

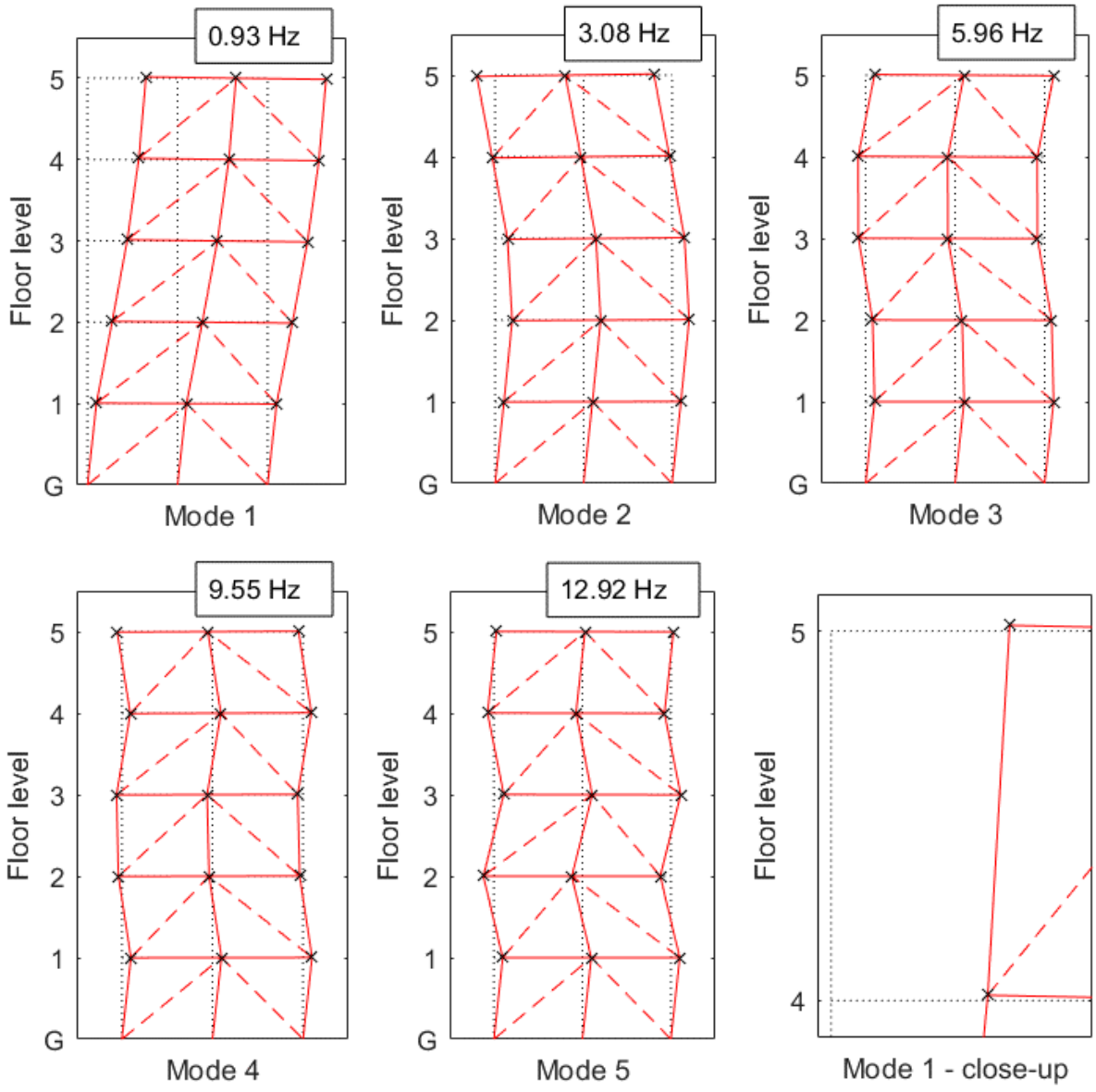

Figure 6.13 – Mode shapes of unbraced MRF used in model

6.3.3. Modal Model of BRBF Structure

A different approach is required for the BRBF since very little stiffness is provided by the frame. In this case the modal decomposition was performed on the combined structure with the BRB stiffnesses taken as their secant values at the design displacement, taken as 20% of the initial stiffness. The resulting mode shapes, along with natural frequencies given with the initial elastic stiffness of the BRBs, are shown in Figure 6.14. The main difference made to the mode shapes by using the secant rather than initial stiffnesses is a reduced vertical component in the nodes at the outer columns since this causes a smaller force in the column for a given lateral displacement. Since the frame contributes little to the stiffness of the structure, one option would be to set Λ to a matrix of zeros in Eq. 6-24 so that the stiffness contribution of the frame is neglected – equivalent to assuming all connections are pinned. However, here the small stiffness contribution that the continuous column adds to the higher modes is included. The assumption that the columns are pinned at the base means that this gives zero stiffness to the fundamental mode since, without the braces, the frame would form a mechanism. Meanwhile, the natural frequencies used to construct B must be those of the combined structure, $\omega_{comb,i}$, to give the correct damping, so now $\mathrm{B} = \mathrm{diag}(2\zeta_{i,}\omega_{comb,i})$.

These five modes are sufficient to capture the *global* behaviour of the structure which affects the displacement of the BRBs. The damping is set to 2% in all modes to ensure that its effective value, due to the period elongation associated with yielding, does not exceed 5%.

6.3.4. Integration algorithm

With the numerical substructure defined as above, the same integration procedure can be employed as for the SDOF system. It just requires an extra step to multiply the modal displacements, $\boldsymbol{q}$, by Φ to retrieve the actual displacement, $\boldsymbol{x}$, before they leave the numerical substructure, and another to multiply the nodal forces, $\boldsymbol{f}$, by Φ^T to produce the modal forces.

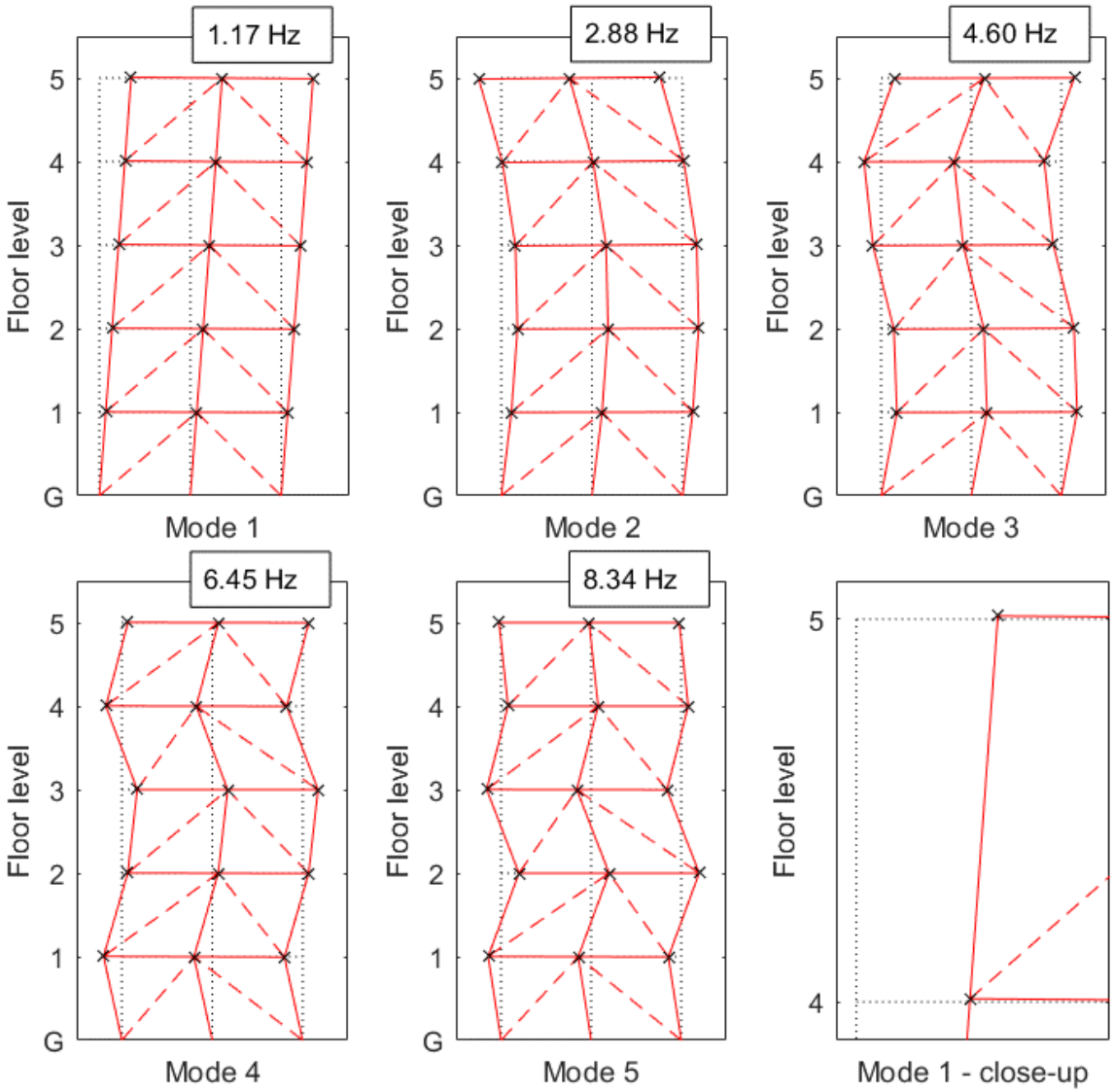

Figure 6.14 – Mode shapes of BRBF used in model

6.3.5. Coordinate Transformation

The principal directions of the coordinate system used in the numerical substructure are the horizontal direction, X, and vertical direction, Y. A coordinate transformation is therefore required to obtain the resulting extension, $\boldsymbol{e}$, occurring across the BRBs. This transformation is defined as:

$$\boldsymbol{e} = H\boldsymbol{x} \qquad 6\text{-}25$$

where the vector $\boldsymbol{e}$ is comprised of the extensions of the BRBs, the vector $\boldsymbol{x}$ is comprised of the displacements of each node of the frame, and the matrix H is the transformation matrix. Similarly, the node forces, $\boldsymbol{f}$, in the principal co-ordinate system can be obtain from the BRB forces, $\boldsymbol{F_{BRB}}$, using:

$$\boldsymbol{f} = H^T \boldsymbol{F_{BRB}} \qquad 6\text{-}26$$

6.4. Hybrid Simulation of Dual MRF-BRBF Structure

6.4.1. Description of tests

Real-time hybrid simulations were performed with the Dual MRF-BRBF structure for each of the three ground motions selected in Table 2.1 – these are listed in Table 6.12. Two tests were performed for each ground motion, one with the left-hand BRB in the first storey forming the physical substructure and one with the left-hand BRB in the second storey forming the physical substructure, since the largest interstorey drifts occurred in the second storey as a result of the columns being modelled as being fixed at the base. The scale factors applied to the Northridge and Kalamata ground motions were those associated with the *ultimate limit state (ULS)* – 0.87 and 1.18, respectively. For the El Centro ground motion, numerical simulations predicted much larger displacements at the ULS scale factor of 1.02, so a reduced scale factor of 0.78 was used to give peak displacements similar to the other two ground motions so as to preserve the BRB for later tests. Note that, in the following, the displacements given are those of the physically tested BRB. The displacements assumed in the simulation will be 1.827 times these vales.

6.4.2. Results

There is very good agreement between the peak displacements predicted by purely numerical simulation and those obtained from hybrid simulation, with a maximum discrepancy of 0.62%. Despite significant amounts of yielding, the residual deformation remaining in the BRB after each test was minimal due to the significant elastic restoring force provided by the MRF in the numerical substructure, with just 0.13mm of residual deformation being accumulated over the six tests.

Figure 6.15 shows the displacement response to the El Centro ground motion for the hybrid simulation with the physical BRB in the first storey. It shows a good match between the target and achieved displacements, which also match the displacement given by the purely numerical simulation with the physical BRB replaced with numerical model. Also shown is the response obtained with the BRBs

removed, showing that despite the small stiffness contribution of the BRBs they reduce the peak response by a notable amount. Figure 6.16 shows the mATS coefficients which behave as expected with a_1 reducing when yielding occurs and a_0 remaining close to 1.0, since the elastic restoring force from the MRF prevents a significant shift in the equilibrium position from occurring, except during the significant yielding event near the start of the simulation. The force response is shown in Figure 6.17 which shows a good match with the force from the simulator.

Figure 6.18 and Figure 6.19 show the displacement and force response, respectively, for the case where the physical BRB is located in the second storey (still with the El Centro ground motion). The corresponding hysteresis curve is shown in Figure 6.20, which shows a good match with the simulator and also shows that the multilinear numerical BRB model fits well to the observed response.

Earthquake:		El Centro		Northridge		Kalamata	
Scale:		0.78 (0.76×ULS)		0.87 (ULS)		1.18 (ULS)	
BRB storey:		1	2	1	2	1	2
Peak displacement [min, max] (mm):	Bare MRF:	-7.540, 8.790	-12.348, 15.559	-10.302, 10.153	-17.038, 17.530	-7.504, 9.892	-12.754, 15.136
	Predicted, x_p:	-6.491, 7.331	-10.720, 11.851	-6.355, 6.288	-9.581, 10.456	-6.082, 7.025	-9.786, 11.246
	Actual, x_t:	-6.501, 7.342	-10.695, 11.856	-6.358, 6.285	-9.574, 10.415	-6.093, 7.032	-9.802, 11.244
	Actual, x_{enc}:	-6.468, 7.320	-10.650, 11.803	-6.314, 6.246	-9.541, 10.369	-6.026, 7.014	-9.743, 11.193
Peak displacement error (%):		-0.31	-0.45	-0.68	-0.45	-1.10	-0.60
Residual displacement (mm):		-0.025	-0.055	-0.006	-0.033	-0.004	-0.004
NRMS error (%):		0.739	0.648	0.669	0.614	0.739	0.645
Mean mATS coefficients:	a_0:	0.9996	0.9988	0.9997	0.9989	0.9995	1.0000
	a_1 (ms):	11.177	10.782	10.948	10.488	11.563	11.227
	a_2 (ms^2):	104.62	99.12	103.26	99.74	113.93	105.91

Table 6.12 – Real-time hybrid tests of dual MRF+BRBF structure

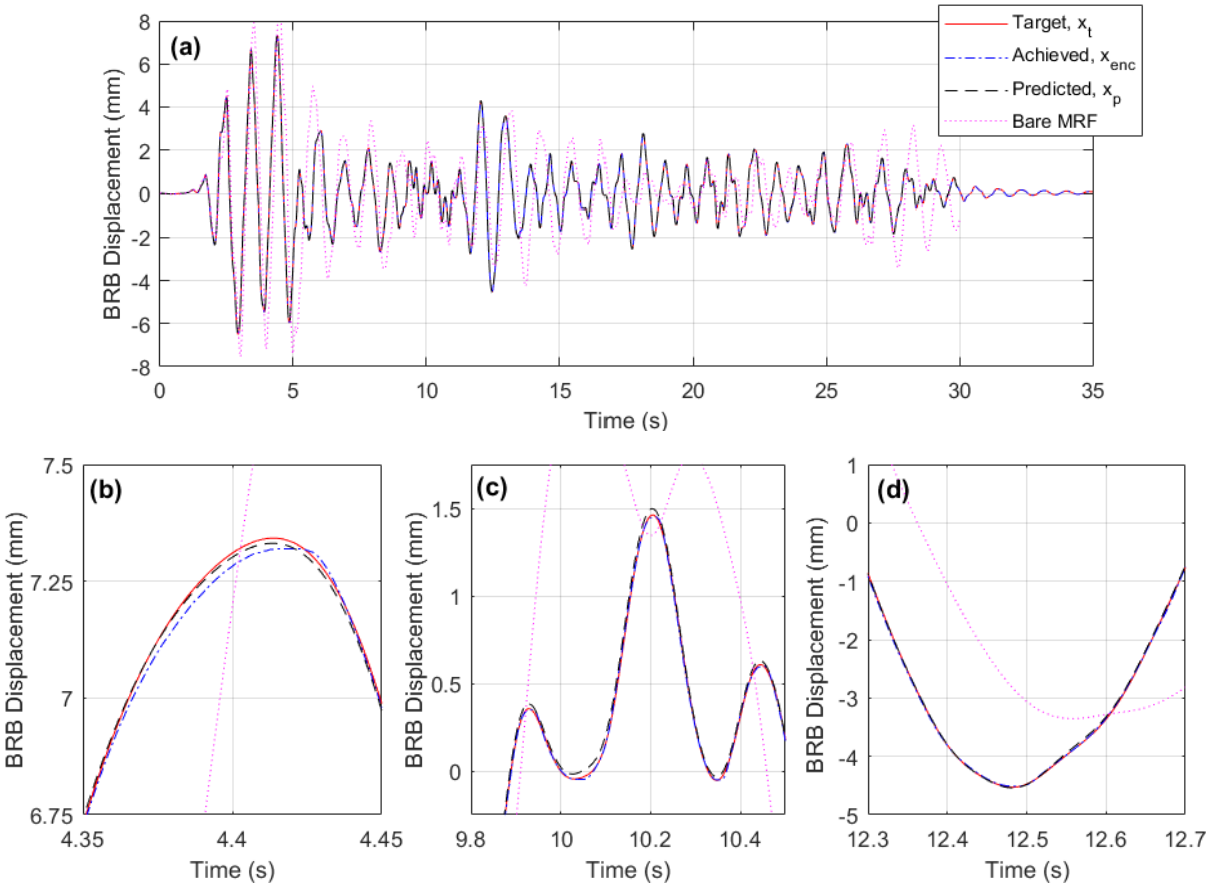

Figure 6.15 – Displacement response of BRB (physical substructure) in first storey of 5-storey MRF-BRBF dual structure subjected to El Centro ground motion with scale factor of 0.78

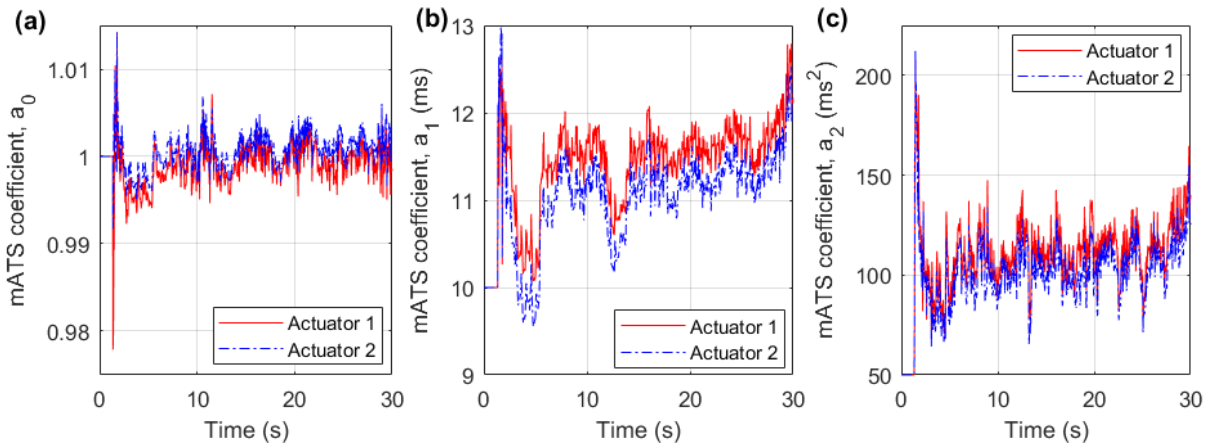

Figure 6.16 - mATS coefficients during RTHS of MRF-BRBF dual structure subjected to El Centro ground motion: (a) a_0, (b) a_1, and (c) a_2

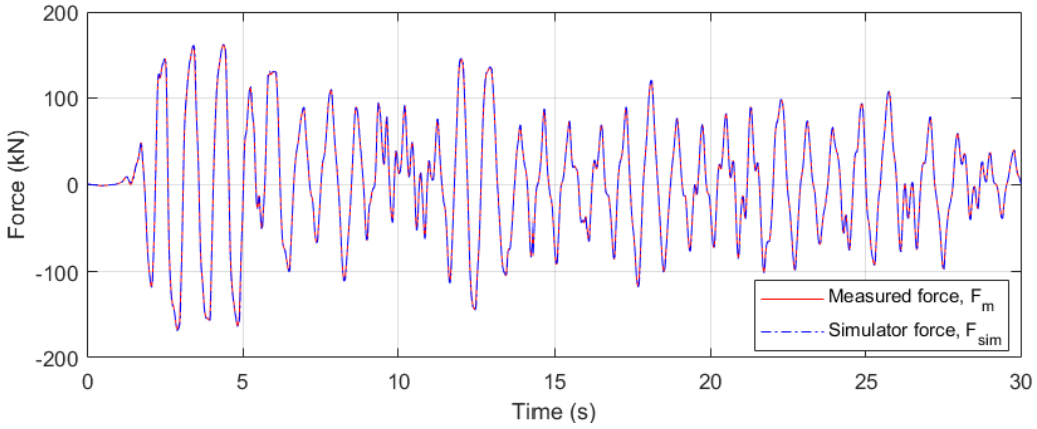

Figure 6.17 – Force response of BRB (physical substructure) in first storey of 5-storey MRF-BRBF dual structure subjected to El Centro ground motion with scale factor of 0.78

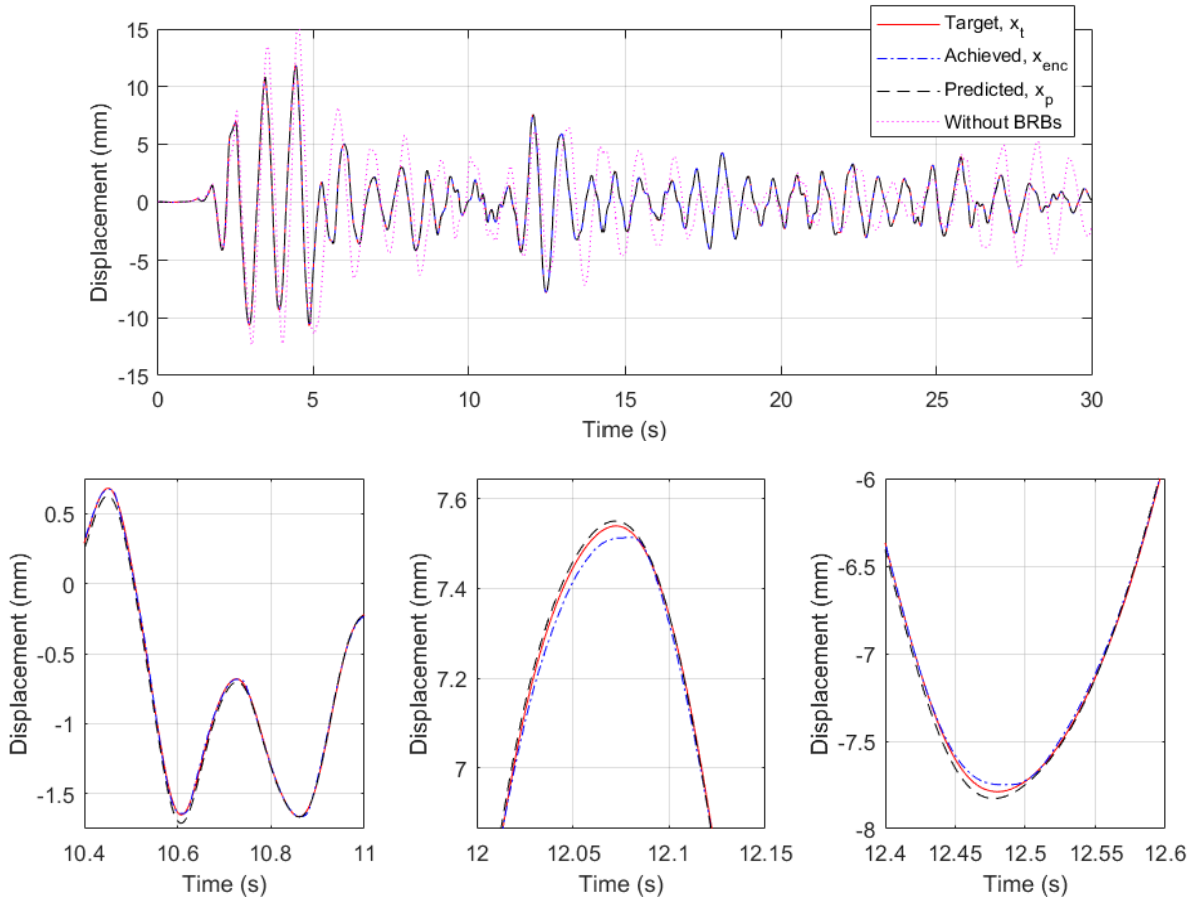

Figure 6.18 – Displacement response of BRB (physical substructure) in second storey of 5-storey MRF-BRBF dual structure subjected to El Centro ground motion with scale factor of 0.78

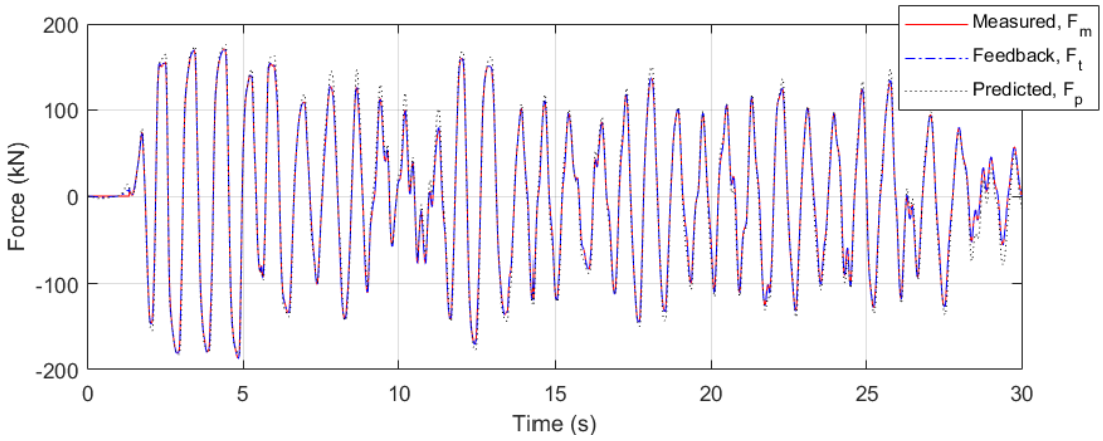

Figure 6.19 – Force response of BRB (physical substructure) in second storey of 5-storey MRF-BRBF dual structure subjected to El Centro ground motion with scale factor of 0.78

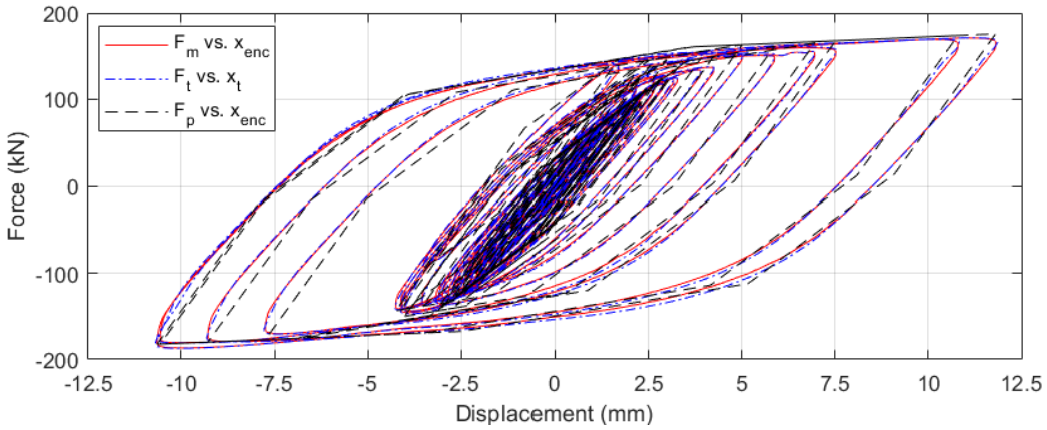

Figure 6.20 – Hysteresis curves for BRB (physical substructure) in second storey of 5-storey MRF-BRBF dual structure subjected to El Centro ground motion with scale factor of 0.78

6.5. Large Displacement Hybrid Simulation of BRBF Structure

6.5.1. Description of tests

Real-time hybrid simulations were performed with the BRBF structure for each of the three ground motions making up the suite described in Table 2.1 (ground motion time histories and response spectra shown in Appendix A). As described in Section 2.1.6.6, these were chosen to produce a Eurocode 8 compliant suite of realistic ground motions for the structure being simulated, allowing the system to be tested under three quite different ground motions. These tests are listed in Table 6.13. Two tests were performed for each ground motion, one at the damage limitation (DL) level and one at the

ultimate limit state (ULS) level, with the physical BRB being located in the first storey, where interstorey drifts are greatest. The BRBF represents a much more onerous case for the control of the hybrid simulation as much more of the stiffness comes from the physical substructure than in the MRF-BRBF dual structure. Here the physical BRB provides 50% of the stiffness in the first storey (the rest being from the opposing BRB which is modelled numerically).

6.5.2. Results

From Table 6.13 it is seen that excellent accuracy is maintained between the target and achieved displacements. The displacement responses are shown in Figure 6.21 along with the coefficients of the mATS compensator in Figure 6.22. Notice that significant offsets appear in the a_0 coefficients for the El Centro and Kalamata earthquakes (Figure 6.22(a) and (c)) due to yielding resulting in a significant offset of the equilibrium position. The hysteresis curve for the BRB during the ULS Northridge ground motion is shown in Figure 6.23 as this produced the largest peak displacement in the BRB (corresponding to Figure 6.21(b)). This highlights the significant nonlinearity being experienced, as well as demonstrating the performance of the stiffness simulator.

Earthquake:		El Centro		Northridge		Kalamata	
Limit state:		DL	ULS	DL	ULS	DL	ULS
Scale factor		0.5×1.02	1.02	0.5×0.87	0.87	0.5×1.18	1.18
Peak displacement [min, max] (mm):	Predicted, x_p:	-5.21, 5.91	-10.76, 12.44	-2.86, 5.04	-8.04, 16.26	-4.27, 2.68	-12.76, 6.81
	Actual, x_t:	-5.56 5.85	-11.15, 12.48	-2.91, 5.06	-8.52, 14.86	-4.68, 2.52	-12.61, 6.81
	Actual, x_{enc}:	-5.53, 5.84	-11.10, 12.44	-2.88, 5.03	-8.44, 14.82	-4.64, 2.52	-12.54, 6.81
Peak displacement error (%):		0.33	0.32	0.60	0.96	0.73	0.56
Residual displacement (mm):		0.41	4.02	0.18	0.52	-0.656	1.03
NRMS error (%):		0.805	0.692	0.872	0.668	1.02	0.675
Mean mATS coefficients:	a_0:	1.003	1.006	1.006	1.003	1.007	1.006
	a_1 (ms):	11.47	10.97	11.49	11.37	11.51	11.35
	a_2 (ms^2):	119.3	124.9	115.2	131.5	163.6	146.42

Table 6.13 – Real-time hybrid tests of BRBF structure

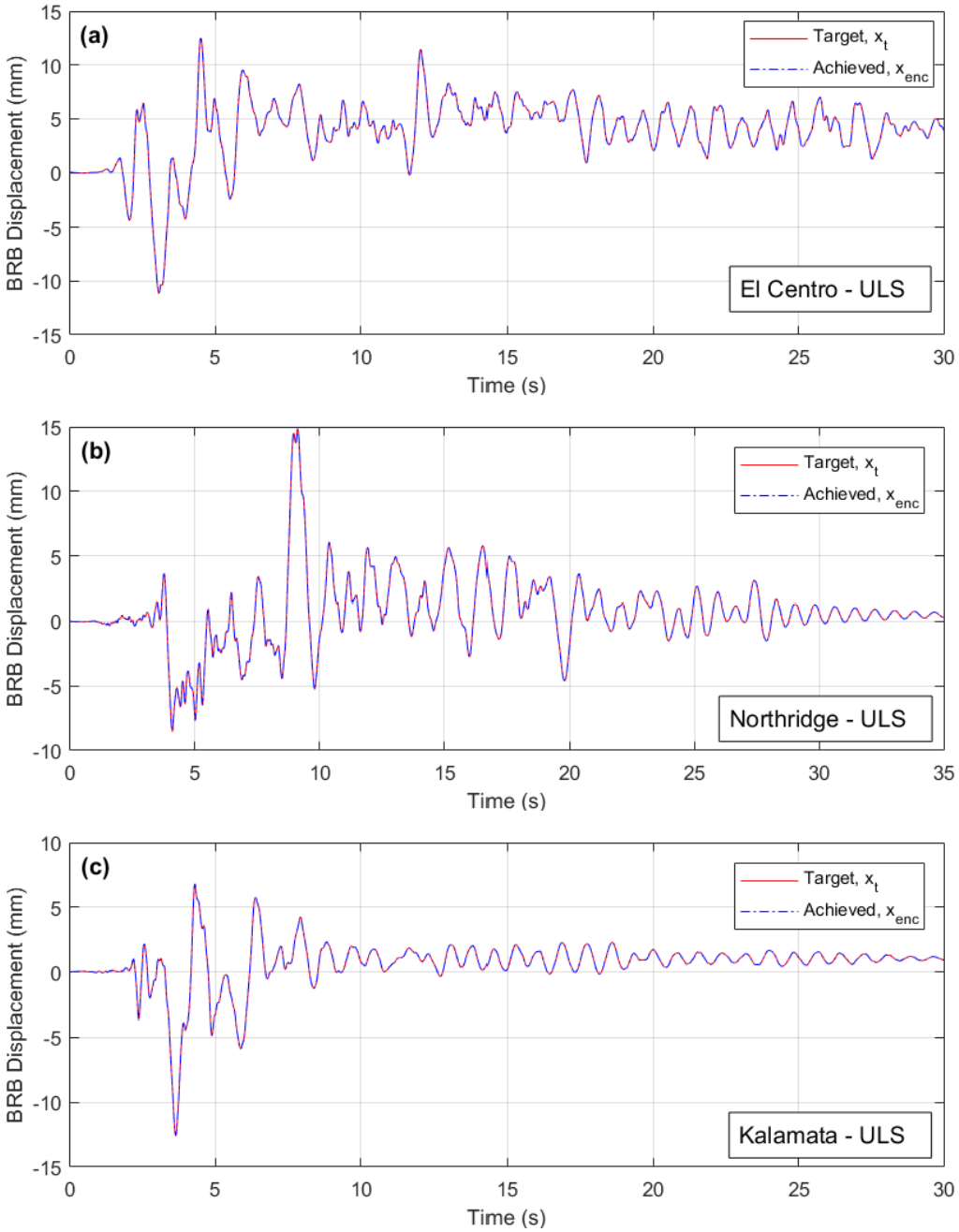

Figure 6.21 – ULS displacement applied to BRB during RTHS of BRBF (BRB in first storey): (a) El Centro, (b) Northridge, and (c) Kalamata

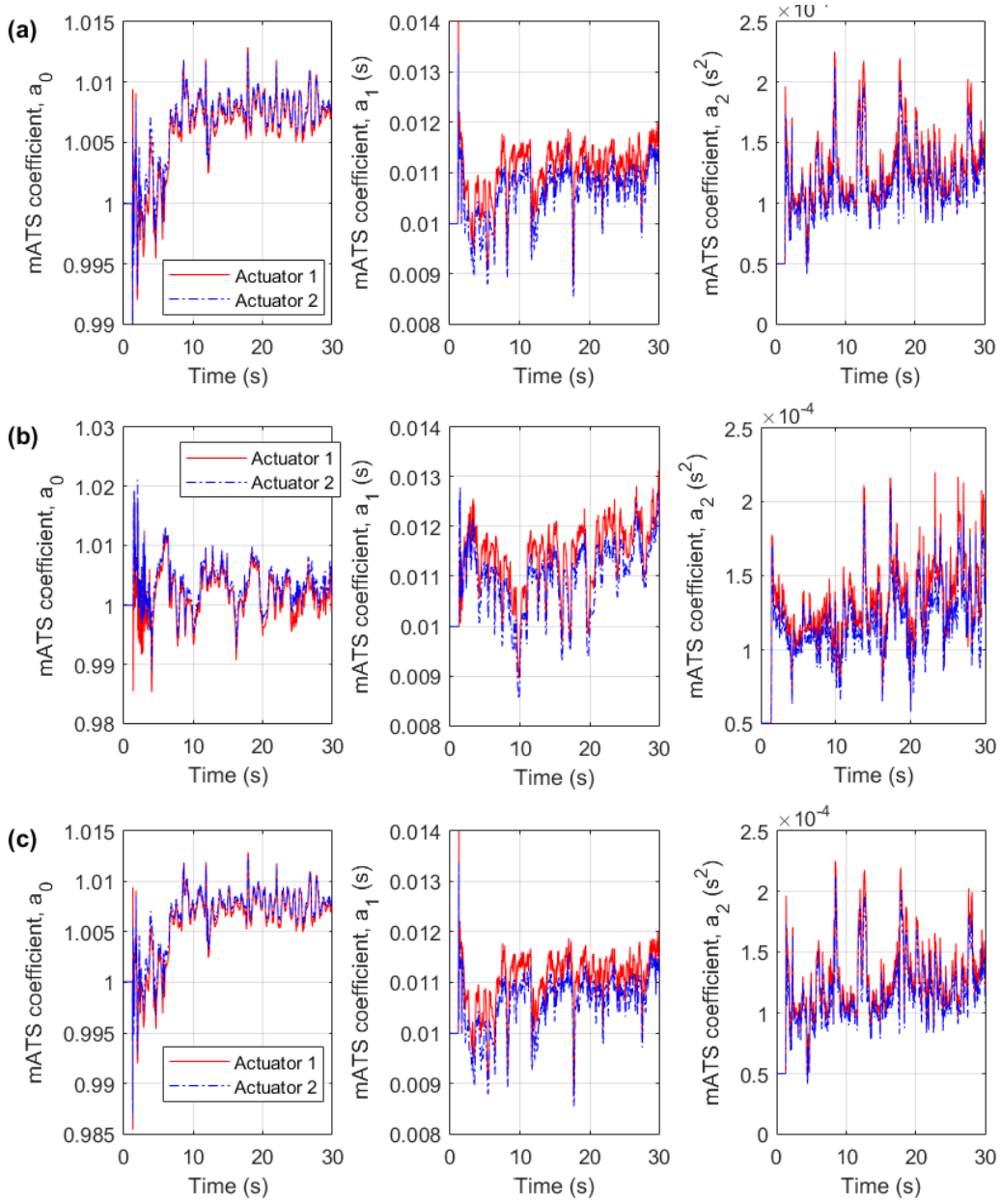

Figure 6.22 – Coefficients of mATS compensator during RTHS of BRBF: (a) El Centro, (b) Northridge, and (c) Kalamata

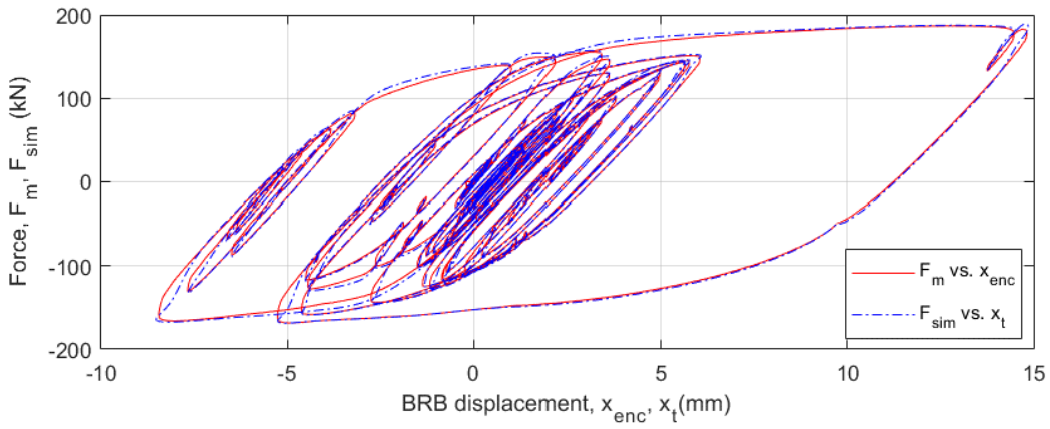

Figure 6.23 – BRB hysteresis curve during RTHS of BRBF (BRB in first storey): Northridge ULS

6.5. Hybrid Simulation with Viscoelastic Damper

6.5.1. Application to Other Physical Substructures

It has been the intention to produce a RTHS system that is not only capable of testing BRBs but a wide variety of physical substructures, as well as being used with different rig setups and actuation systems. This should allow more rapid implementation of future RTHS testing. This is facilitated by the use of adaptive delay compensation which automatically adapts to the properties of a new system without needing accurate modelling of the system dynamics or tuning of empirical parameters. A major advantage of the ATS and mATS methods is that the coefficients can be directly related to the system properties of amplitude ratio, A, and delay, δ, so that only an estimate of the initial values of these two quantities is needed to implement the system, and even if these are far from the true values the system will quickly adapt to the correct values. Similarly, using the displacement measured across the physical substructure by the encoder as the feedback to the PID controller of the actuator, rather than the displacement of the piston measured by the LVDT, will correct for the flexure of the rig without needing modification for the stiffness properties of a particular rig and physical specimen. To demonstrate the adaptability of the system, it was applied to a different physical substructure in a different test rig. In the Structural Dynamics Laboratory where the BRB testing was carried out, testing was also being performed on a viscoelastic (VE) damper by Basagiannis [119] who applied the system designed in this project to perform RTHS with the VE damper as the physical substructure. This used the same computer system, Instron® controller and hydraulic power supply, but with a different test rig, actuator and physical substructure. The only modifications that were necessary to adapt the system to the new physical setup were simplifications due to the rig only using one actuator and the stiffness simulator not being required.

6.5.2. Viscoelastic Test Setup

The VE damper tested by Basagiannis was built up from two of the dampers shown in Figure 6.24(a) which consisted of two steel plates bonded together by a 17.5mm thick layer of VE polymer. One plate

of each of these dampers was connected to either side of a central steel block which was connected to the actuator via a load cell. The outer plates were then bolted to steel plates fixed to a stiff reaction wall so that movement of the actuator would cause the VE polymer layers to deform in shear. This configuration is shown from above in Figure 6.24(b) with the actuator to the left and the fixed reaction wall to the right. The full rig is shown from the side in Figure 6.24(c) where the actuator and damper are connected in series between two reaction walls. As for the BRB test rig, the displacement, x_m, of the actuator piston is measured by a LVDT within the actuator body and the force, F_m, applied by the actuator is measured by a load cell connected to the end of the actuator piston. A displacement encoder, the same type as used for the BRB testing, measures the displacement, x_{enc}, between the central steel block of the damper and the right-hand reaction wall to give a more accurate measurement of the deformation of the damper than given by the LVDT. The rig is powered by the same hydraulic system and controlled by the same control system as for the BRB testing but uses a smaller Instron® actuator with a dynamic load rating of 100kN. The compensation for flexure of the rig is simpler than for the BRB rig since only a single actuator is used. The displacement, x_{enc}, measured across the damper is used as the feedback to mATS compensator, and the measured rig deflection, $d_{rig} = x_m - x_{enc}$, is added to the command signal, u_c, from the delay compensator before it is sent to the PID controller. As mentioned previously, this is equivalent to replacing the PID feedback with x_{enc} (instead of x_m) but is easier to implement with the Instron® controller. The resulting RTHS system is shown in Figure 6.25. The initial values of the mATS coefficients, a_0, a_1 and a_2, were set to 1.00515, 10.7ms and 9.45ms^2, respectively, based on the mean values of the coefficients from previous open-loop tests.

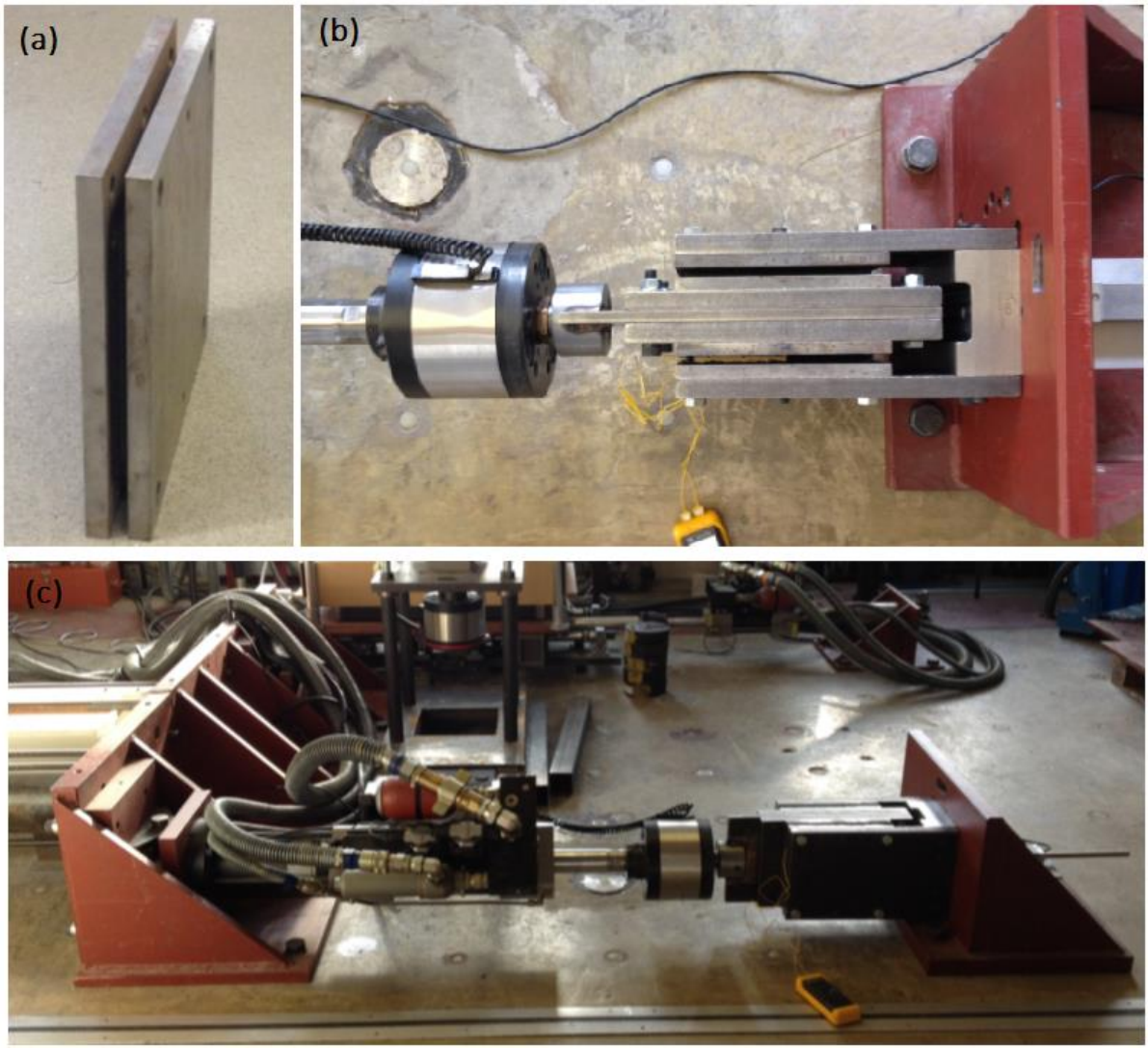

Figure 6.24 – VE damper testing setup: (a) single VE damper, (b) built-up VE damper installed in rig, and (c) full test rig

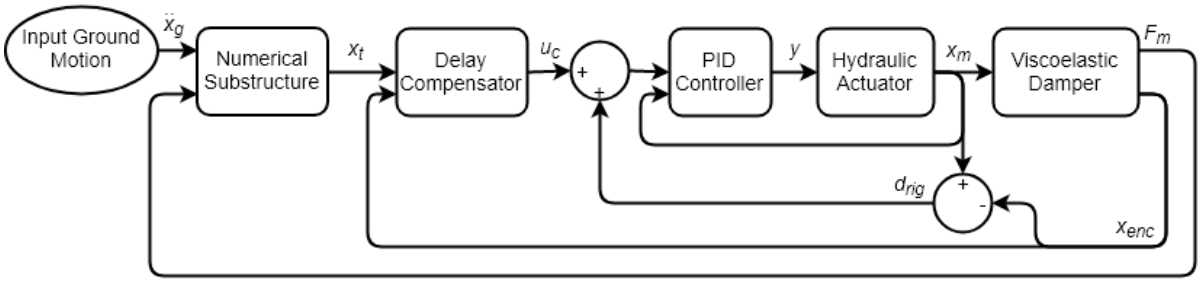

Figure 6.25 – RTHS system used with VE damper

The simulated structure consisted of a SDOF portal frame, which formed the numerical substructure, fitted with a viscoelastic damper, which formed the physical substructure. The damper was assumed to be horizontal with one end connected to the top of the frame and the other connected to the top of rigid chevron bracing which coupled it to the ground. The numerical substructure was given an elastic

stiffness, k_{num}, of 22.6kN/mm and a mass, m, of 143.3t to give the bare frame a natural frequency, f_{num}, of 2Hz; with the inherent damping, ζ, set to 2%. The El Centro earthquake record used previously formed the input ground motion and was scaled by a factor of 0.18 to prevent the shear strain amplitude from exceeding 50%.

The force-displacement response of the viscoelastic device can be approximated by an elastic stiffness, K, acting in parallel with a viscous damper with coefficient, C, as described by Eq. 2-31. However, K and C vary depending on the frequency and amplitude of oscillation, and on the temperature of the damper, all of which will vary during an earthquake motion. From open-loop characterisation tests at a frequency of 2Hz, shear strain amplitude of 30% (corresponding to a peak displacement of around 3.5mm) and temperature of 20°C, Basagiannis computed an effective stiffness of 4.35kN/mm which can be considered a representative value for this hybrid simulation. Including this stiffness contribution from the damper gives a natural frequency, f, of 2.18Hz for the combined structure.

6.5.3. Viscoelastic Test Results

The displacement response of the RTHS with the VE damper are shown in Figure 6.26. The mATS delay compensator is effective, with the achieved displacement, x_{enc}, closely matching the target displacement, x_t. The difference between the two is shown in Figure 6.27. It remains relatively small throughout the test, resulting in an NRMS displacement error of less than 1.6%. The NRMS error between the command, u_c, from the delay compensator and x_{enc} is 14.7%, which gives an estimate of what the error would be if delay compensation were not applied, showing a significant improvement is achieved. The maximum amplitude error at peaks was less than 0.4%, demonstrating the effectiveness of the amplitude correction from the delay compensator in combination with the correction for rig flexure. The mean delay in the system prior to delay compensation, measured as the delay between u_c and x_{enc} at zero-crossings, is 11.3ms. After delay compensation, the mean delay, measured as the delay between x_t and x_{enc} at zero-crossings, is virtually zero, at -0.00075ms. The mean of the absolute values of time between zero-crossings is 0.75ms. This indicates that the very small amount of error remaining

at zero-crossings is not skewed towards being a delay or an advance (which, by Eq. 4-7, would affect the apparent damping of the system). Figure 6.28 shows the measured force-displacement response, F_m vs. x_{enc}, as well as the response as it appears in the simulation, F_m vs. x_t. It shows a good match between the two indicating good accuracy in the hybrid simulation. This was then used to validate a numerical model of the damper response, which had been fitted to the results of cyclic testing, by comparing the response of a numerical simulation using the model to that of the RTHS, allowing the accuracy of the model to be evaluated under realistic dynamic conditions.

The coefficients of the mATS compensator are shown in Figure 6.29. The mean value of a_0 is 1.006, indicating that on average there is a very slight overshoot in the inner control loop. The mean value of a_1 is 11.3ms which is in agreement with the mean delay prior to compensation measured at zero-crossings. As was seen in the BRB testing, the value of a_1 varies over each half-cycle, tending to increase to a maximum value just after each peak and then reducing to its minimum value by the time of the next peak in the opposite direction. The mean value about which this variation occurs also appears to vary with the amplitude of oscillation, increasing as the amplitude decreases, indicating an increase in the delay for smaller amplitudes. While the coefficients a_0 and a_1 behave as expected, it is apparent from Figure 6.29© that there is an issue with the a_2 coefficient. The rate of variation of a_2 was much larger than expected, so the limit set on the allowable rate of change was set too low causing the rate to saturate multiple times during the test, leading to the sawtooth shape seen in Figure 6.29(c). In fact, the rate limiter is also active on a_1 but only momentarily so that it is not apparent from Figure 6.29(b). Rate limits on the variation of the ATS coefficients were recommended by Chae et al. [12], along with limits on maximum and minimum values, as a guard against potential issues due to ill-conditioning of the matrix, $X_m^T X_m$, which must be inverted to determine the ATS coefficients. However, it is not desirable for these limits to be active over a significant portion of the hybrid simulation as this delays the coefficients in reaching their correct values. The limits applied in the hybrid simulations with the BRB were much higher, so that they were not active during the simulation except for immediately after the compensator kicks in and the coefficients jump from their initial values to their fitted values – the

size of the jump depending on the appropriateness of the initial values. It is likely that a further improvement in performance could be achieved by relaxing the rate limits to allow the coefficients to vary more freely. However, as the VE testing had concluded, it was not possible to repeat the test to verify this. If there is concern that the rate of variation of the coefficients is too large, it may be preferable to reduce it by increasing the size of the effective time-window of the fit since this will reduce the rate of change of all three coefficients commensurately. In spite of this, the performance of the delay compensator remains very good.

The performance of the system was further validated through RTHS of a simple MDOF model of an elastic three-storey frame building with a VE damper in the first storey, which formed the physical substructure. The numerical substructure had natural frequencies of 1.03Hz, 2.70Hz and 3.64Hz with Rayleigh damping used to set the damping to 2% in the first and third modes, while the inclusion of the damper would increase the natural frequencies to around 1.08Hz, 2.78Hz and 3.67Hz. This, again, showed excellent accuracy with an NRMS error of 1.17% and a peak amplitude error of less than 0.1%. Moreover, the ease of modifying the RTHS system derived during the BRB testing shows the versatility of the RTHS control system, thanks to its ability to automatically adapt to the properties of the physical systems. This allowed RTHS of the VE damper to be carried out in just a fraction of the time taken to develop the system from scratch.

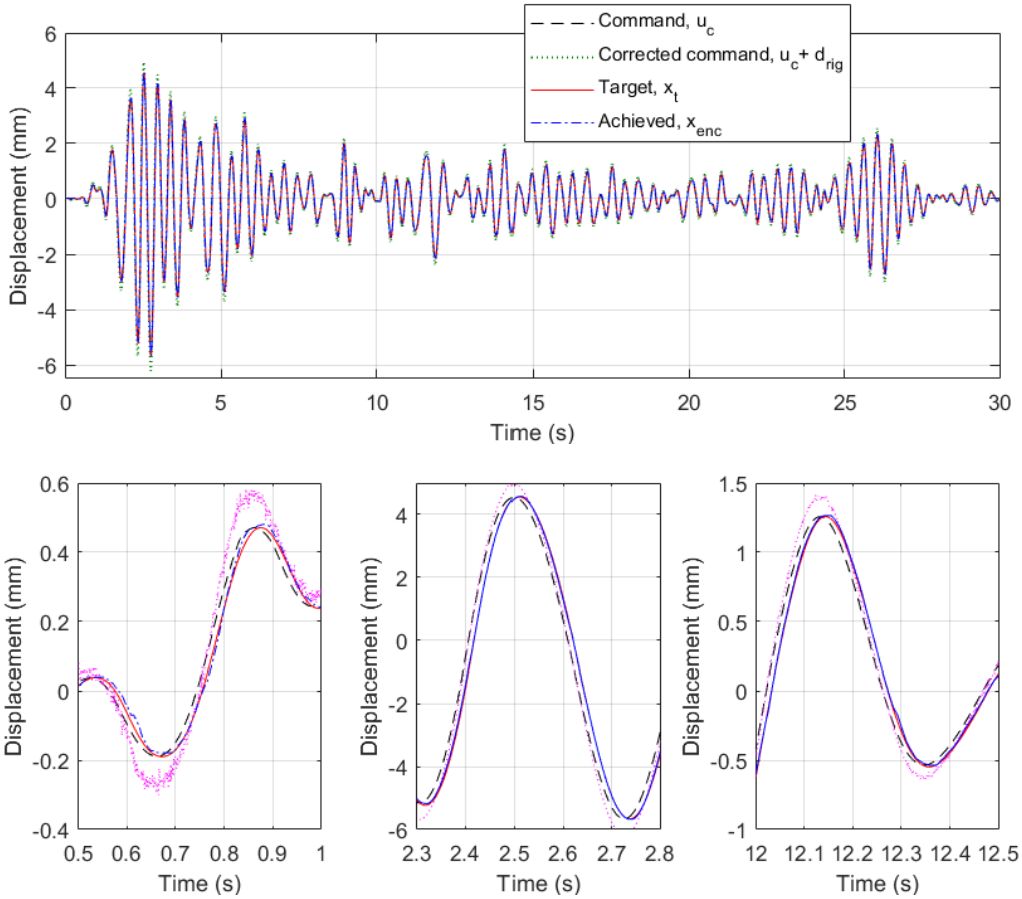

Figure 6.26 – Displacement response of VE damper in RTHS

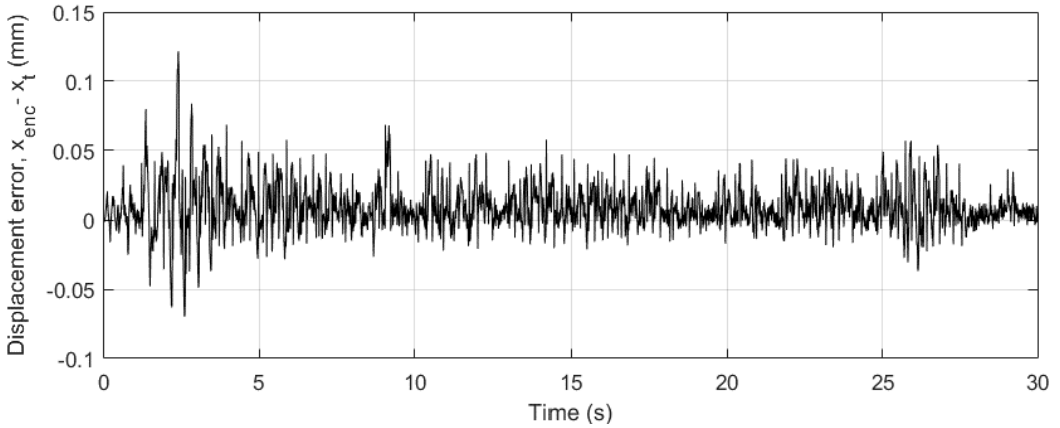

Figure 6.27 – Displacement error in RTHS with VE damper

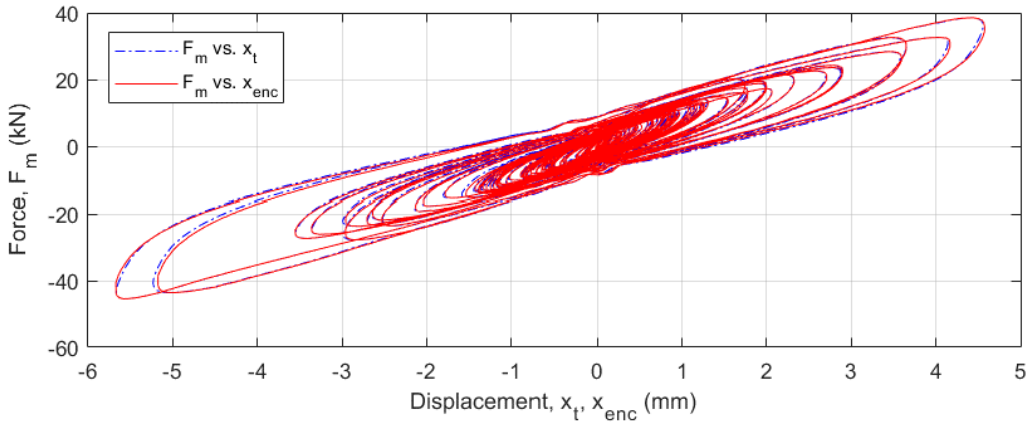

Figure 6.28 – Hysteresis curve for VE damper in RTHS

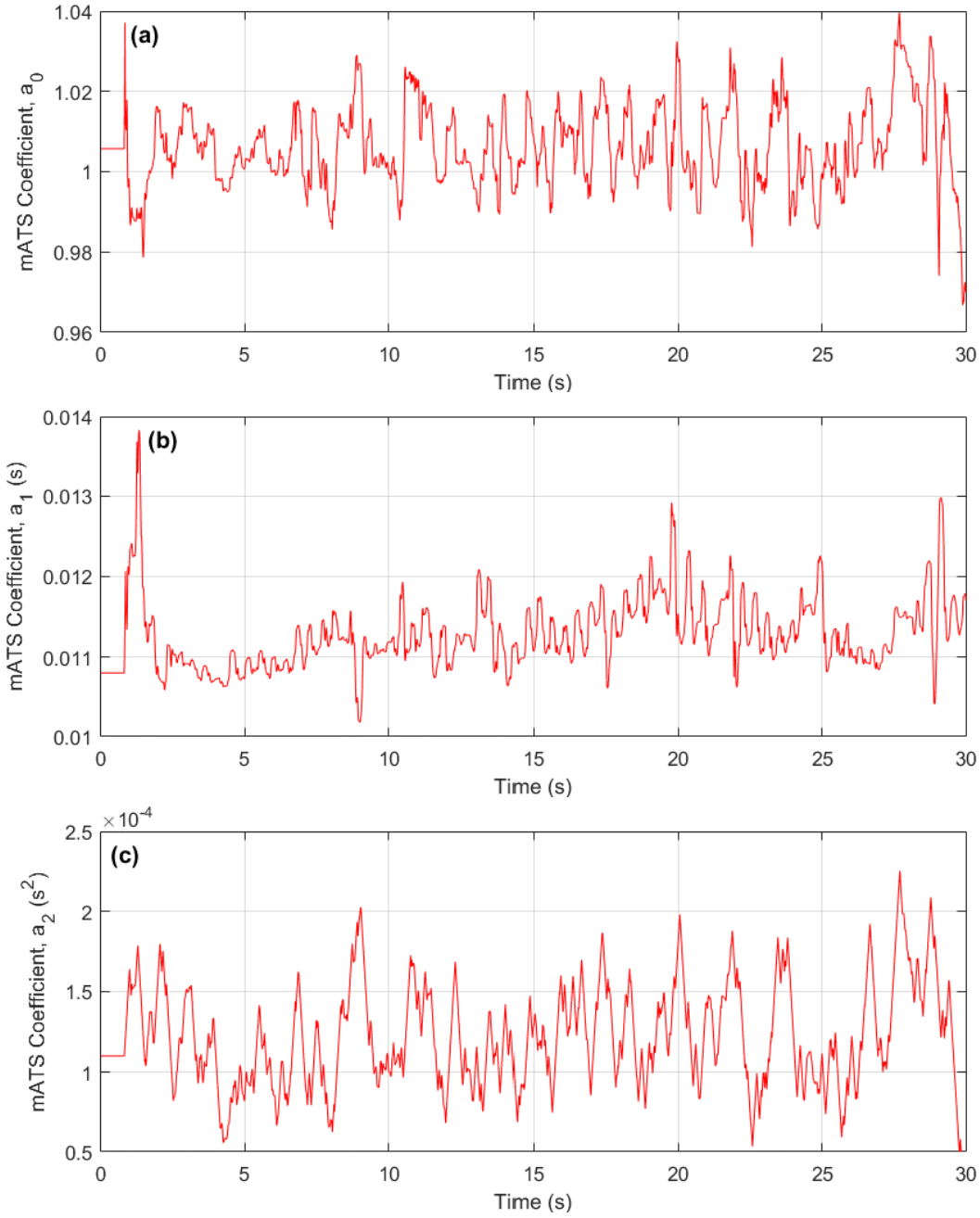

Figure 6.29 – Coefficients of mATS compensator in RTHS with VE damper: (a) a_0, (b) a_1, and (c) a_2

6.6. Conclusion

In this chapter, the RTHS system developed and tested in Chapter 5 has been extended to simulate MDOF structures. Suitable numerical substructure models were designed in accordance with Eurocode 8 to allow testing of the BRB under realistic conditions. A modal approach was used to reduce the number of DOFs to a level which could be integrated within the timestep of 1ms. This was applied to RTHS of both a MRF-BRBF dual structure and a BRBF structure. Since a multi-storey structure would be fitted with multiple BRBs, numerical models for modelling the BRB response were investigated, and a multilinear model was shown to provide a close fit to the experimental data and provide the correct physical response. This model was used to simulate the BRBs in the MDOF structure with the exception of the one forming the physical substructure. The control system performed well, even in the presence of higher mode response, and stable, accurate RTHS was achieved. As a demonstration of the versatility of the RTHS control system developed in this project, the system was applied to RTHS with a viscoelastic damper. The system worked very effectively, providing very good accuracy of actuation, and required minimal modification to apply it to the different system.

7. Conclusion

7.1. Outcomes

This project has investigated the components required to form stable, accurate real-time hybrid simulation (RTHS). A RTHS system has been developed and tested in a large number of hybrid simulations using a buckling-restrained brace (BRB) as the physical substructure. Key outcomes of this project include:

1. The development of an improved version of the Adaptive Time Series (ATS) compensator:

   The inevitable delay in the response of servo-hydraulic actuation systems is known to have a destabilising effect on the RTHS feedback loop, preventing hybrid simulations from being carried out successfully in real-time without a delay compensation procedure being employed. The modification to the ATS compensator developed in this project (the mATS compensator) significantly reduces its computational demand by formulating the fitting equations so that a recurrence relation can be used. This is significant in RTHS since reducing the amount of computation can allow the calculations to be computed in less time so that a smaller timestep can be used. Alternatively, it can free up processing power for implementing more complex numerical substructures. The mATS compensator also increases robustness by removing the need for down-sampling of the fitting data. Extensive open-loop testing has shown it to provide excellent actuation quality and to adapt well to changes in actuation delay which have been shown to occur due to nonlinearity of the physical substructure. When tested as part of a RTHS system it not only provides stability, but also a high degree of accuracy, which is greatly helped by its ability to compensate for amplitude errors in addition to delays.

2. The development of a system for compensating for rig deflection:

   The inevitable deflection occurring in the components of the test rig causes an error in the amplitude of the applied displacements when the actuation system is controlled using

feedback of actuator displacement rather than the deformation of the physical substructure. A method for correcting for rig deflection using direct measurement of the physical specimen deformation using an encoder has been proposed and shown to be effective. It requires no tuning and integrates well with the mATS compensator. This system has been adapted to enforce the specific requirement of the two-actuator test rig that the displacements of the actuators be constrained to be the same.

3. The development of an online stiffness simulator for stable force feedback:

   The stiffness simulator ensures continuous stable force feedback by using a model of the BRB stiffness which is continually updated based on the most recent measurements. This provides stability to the system by applying a correction for the force error that will occur due to imperfect actuation while maximising accuracy by fitting closely to the varying stiffness of the BRB. This improves on previous systems which extrapolated about the current measured force. An efficient method for fitting the coefficients of the stiffness simulator was also presented. Testing showed that the stiffness simulator performed well and an appropriate value for the simulator time-constant was selected.

4. Fitting numerical models to BRB response:

   Potential numerical models for modelling BRB behaviour were reviewed and parameters of the model fitted to the BRB behaviour. This provided a nonlinear model which could be implemented in the numerical substructure for RTHS of a BRBF.

The above components have been combined with both SDOF and MDOF numerical substructures where they have provided robust, stable performance. The system also provides excellent accuracy. This is demonstrated by the small size of the errors between the target and achieved displacement across the BRB, by the very good agreement between real-time and time-dilated hybrid system, and by comparison with numerical models.

7.2. Future Work

While the RTHS components developed and investigated in this project have been tested using a BRB as the physical substructure, it has been intended that it should be possible to apply the system to other types of RTHS with minimal effort. The versatility of the system has been demonstrated by applying it to RTHS with a VE damper, which required virtually no modification to the control system other than adjusting it to operate on a single actuator rather than two in parallel. It is therefore hoped that the RTHS procedure developed in this project can be applied to RTHS with other physical specimens. This is facilitated by the system having minimal dependence on empirically tuned parameters. For example, the mATS compensator has been shown to give comparable performance for a wide range of effective time windows and it adapts readily to different conditions without requiring testing to determine specific properties of the actuation system. It is hoped that making use of the system provided here could greatly accelerate the implementation of RTHS testing of other devices compared to developing a new system from scratch.

8. References

[1] A. R. Kolbe *et al.*, "Mortality, crime and access to basic needs before and after the Haiti earthquake: a random survey of Port-au-Prince households," *Med. Confl. Surviv.*, vol. 26, no. 4, pp. 281–297, 2010.

[2] E. Miranda, G. Mosqueda, R. Retamales, and G. Pekcan, "Performance of nonstructural components during the 27 February 2010 Chile earthquake," *Earthq. Spectra*, vol. 28, no. SUPPL.1, 2012.

[3] CEN, *Eurocode 8: Design of structures for earthquake resistance — Part 1: General rules, seismic actions and rules for buildings*, no. February. 2004.

[4] International Code Council, *International Building Code*. 2018.

[5] M. D. Symans *et al.*, "Energy Dissipation Systems for Seismic Applications: Current Practice and Recent Developments," *J. Struct. Eng.*, vol. 134, no. 1, pp. 3–21, 2008.

[6] M. C. Constantinou and M. . D. Symans, "Seismic Response of Structures With Supplemental Damping," *Struct. Des. Tall Spec. Build.*, vol. 2, no. January, pp. 77–92, 1993.

[7] C. J. Black, N. Makris, and I. D. Aiken, "Component Testing, Seismic Evaluation and Characterization of Buckling-Restrained Braces," *J. Struct. Eng.*, vol. 130, no. 6, pp. 880–894, 2004.

[8] K. Takanashi and M. Nakashima, "Japanese Activities on On-Line Testing," *J. Eng. Mech.*, vol. 113, no. 7, pp. 1014–1032, 1987.

[9] T. Horiuchi, M. Inoue, T. Konno, and Y. Namita, "Real-time hybrid experimental system with actuator delay compensation and its application to a piping system with energy absorber," *Earthq. Eng. Struct. Dyn.*, vol. 28, no. 10, pp. 1121–1141, 1999.

[10] C. Chen, "Development and numerical simulation of hybrid effective force testing method," Ph.D Dissertation, Department of of Civil and Environmental Engineering, Lehigh University, Bethlehem, PA, 2007.

[11] A. P. Darby, M. S. Williams, and A. Blakeborough, "Stability and delay compensation for real-time substructure testing," *J. Eng. Mech.*, vol. 128, no. 12, pp. 1276–1284, 2002.

[12] Y. Chae, K. Kazemibidokhti, and J. M. Ricles, "Adaptive time series compensator for delay compensation of servo-hydraulic actuator systems for real-time hybrid simulation," *Earthq. Eng. Struct. Dyn.*, vol. 42, no. 11, pp. 1697–1715, 2013.

[13] CEN, "Eurocode: Basis of structural design," *Eur. Comm. Stand. Brussels, Belgium*, 2002.

[14] CEN, "Eurocode 1: Actions on Structures. Part 1-1. General Actions; Densities, Self-weight, Imposed Loads for Buildings," *Eur. Comm. Stand. Brussels, Belgium*, 2002.

[15] CEN, *Eurocode 3: Design of steel structures - Part 1-1: General rules and rules for buildings*. 2005.

[16] ASCE, *Minimum design loads for buildings and other structures*. 2016, p. 608.

[17] R. D. Hanson and T. T. Soong, *Seismic Design with Supplemental Energy Dissipation Devices, Monograph No. 8, EERI Oakland, Calif.* 2001.

[18] Pacific Earthquake Engineering Research Center, "PEER Ground Motion Database," 2013. [Online]. Available: http://peer.berkeley.edu/peer_ground_motion_database/spectras/21713/unscaled_searches/new. [Accessed: 13-May-2015].

[19] R. Darragh, W. J. Silva, and N. Gregor, "Strong Motion Record Processing for the PEER Center," in *Proceedings of COSMOS Invited Workshop on Strong-Motion Record Processing*, 2004, pp. 1–12.

[20] V. Grazier, "Determination of the true ground displacement by using strong motion records," *Izvestiya Academy of Sciences, USSR, Physics of the Solid Earth*, vol. 15, no. 12. pp. 875–885, 1979.

[21] OpenSees, "Open System for Earthquake Engineering Simulation," *University of California, Berkeley*, 2012. [Online]. Available: http://opensees.berkeley.edu/. [Accessed: 12-May-2015].

[22] S. Mazzoni and F. McKenna, "OpenSees command language manual," *… Engineering …*, 2006. [Online]. Available: http://opensees.berkeley.edu/OpenSees/manuals/usermanual/OpenSeesCommandLanguageManual.pdf. [Accessed: 12-May-2015].

[23] B. Stroustrup, *The C++ Programming language*. Pearson Education, 2013.

[24] B. B. Welch, K. Jones, and J. Hobbs, *Practical Programming in Tcl and Tk*, 4th ed. 2003.

[25] M. Nakashima, "Development, potential, and limitations of real-time online (pseudo-dynamic) testing," *Philos. Trans. R. Soc. A Math. Phys. Eng. Sci.*, vol. 359, no. 1786, pp. 1851–1867, 2001.

[26] J. F. Hall, "Problems encountered from the use (or misuse) of Rayleigh damping," *Earthq. Eng. Struct. Dyn.*, no. 35, pp. 525–545, 2006.

[27] F. A. Charney, "Unintended Consequences of Modeling Damping in Structures," *J. Struct. Eng.*, pp. 581–592, 2008.

[28] E. L. Wilson and J. Penzien, "Evaluation of orthogonal damping matrices," *Int. J. Numer. Methods Eng.*, vol. 4, no. December 1970, pp. 5–10, 1972.

[29] A. K. Chopra and F. Mckenna, "Modeling viscous damping in nonlinear response history analysis of buildings for earthquake excitation," no. September 2015, pp. 193–211, 2016.

[30] D. Lee and D. P. Taylor, "Viscous damper development and future trends," *Struct. Des. Tall Build.*, vol. 10, no. 5, pp. 311–320, 2001.

[31] BSI, "BS EN 15129:2009: Anti-seismic devices," *BSI, London, UK.*, 2009.

[32] C. E. Grigorian, T. S. Yang, and E. P. Popov, "Slotted Bolted Connection Energy Dissipator," *Earthq. Spectra*, vol. 9, no. 3, pp. 491–504, 1993.

[33] T. T. Soong and G. F. Dargush, "Passive energy dissipation systems in structural engineering," *John Wiley Sons Chichester*, vol. 6, no. 1, pp. 172–172, Jun. 1997.

[34] A. S. Pall and C. Marsh, "Response of Friction Damped Braced Frames," *J. Struct. Div. Proc. Am. Soc. Civ. Eng.*, vol. 108, no. June, 1982.

[35] A. Filiatrault, R. Tremblay, and R. Kar, “PERFORMANCE EVALUATION OF FRICTION SPRING SEISMIC DAMPER,” *J. Struct. Eng.*, vol. 126, no. 4, pp. 491–499, 2000.

[36] A. S. Whittaker, V. V. Bertero, C. L. Thompson, and L. J. Alonso, “Seismic Testing of Steel Plate Energy Dissipation Devices,” *Earthq. Spectra*, vol. 7, no. 4, pp. 563–604, 1991.

[37] N. Hoveidae and B. Rafezy, “Overall buckling behavior of all-steel buckling restrained braces,” *J. Constr. Steel Res.*, vol. 79, pp. 151–158, 2012.

[38] Star Seismic Europe Ltd., “Star Seismic - BRBF system.” [Online]. Available: http://www.starseismic.eu/BRBF_system. [Accessed: 03-Oct-2018].

[39] M. Wakabayashi, T. Nakamura, A. Katagihara, H. Yokoyama, and T. Morizono, “Experimental Studies on Elastic-Plastic Hysteretic Behavior of Flat Bar Braces Cased in Concrete Wall without Bound, Part 1, Preliminary Tests,” in *Proc. of Annual Convention of Kiniki Section of AIJ*, 1973, pp. 121–124.

[40] M. Wakabayashi, T. Nakamura, and N. Yoshida, “Experimental Studies on the Elastic-Plastic Behavior of Braced Frames under Repeated Horizontal Loading: Part 1,” *Bull. Disaster Prev. Res. Inst.*, vol. 27, no. 3, pp. 121–154, 1977.

[41] M. Wakabayashi, T. Nakamura, and N. Yoshida, “Experimental Studies on the Elastic-Plastic Behavior of Braced Frames under Repeated Horizontal Loading: Part 2,” *Bull. Disaster Prev. Res. Inst.*, vol. 29, no. 4, pp. 143–164, 1980.

[42] C. Field and E. Ko, “Connection Performance of Buckling Restrained Braced Frames,” in *13th World Conference on Earthquake Engineering*, 2004, no. 1321.

[43] American Institute of Steel Construction, “Seismic Provisions for Structural Steel Buildings AISC 341-10,” *Seism. Provisions Struct. Steel Build.*, 2010.

[44] Nippon Steel, “Unbonded Brace,” 2017. [Online]. Available: http://www.unbondedbrace.com/. [Accessed: 04-Jan-2017].

[45] CoreBrace, “CoreBrace,” 2017. [Online]. Available: http://www.corebrace.com/. [Accessed: 04-Jan-2017].

[46] “Star Seismic Europe Ltd.” [Online]. Available: http://starseismic.eu. [Accessed: 06-Dec-2016].

[47] Star Seismic Europe Ltd., “Star Seismic - Projects.” [Online]. Available: http://www.starseismic.eu/projects. [Accessed: 03-Oct-2018].

[48] L. Dunai, “Type Testing of Buckling Restrained Braces According To EN 15129,” p. 34, 2011.

[49] ECCS, *Recommended Testing Procedure for Assessing the Behaviour of Steel Elements under Cyclic Loads*. 1986.

[50] “FEMA 450 2003 Edition - NEHRP Recommended Provisions For Seismic Regulations For New Buildings And Other Structures: Part 1 - Provisions - fema450_1.pdf.” [Online]. Available: https://www.wbdg.org/ccb/DHS/fema450_1.pdf. [Accessed: 17-Oct-2014].

[51] Ministry of Regional Development and Public Administration (Romania), *P100-1/2013 “Code for earthquake resistant design. Design provisions for buildings” (in Romanian)*. 2013.

[52] Y. H. Huang, A. Wada, H. Sugihara, N. M., T. Takeuchi, and M. Iwata, “Seismic performance of moment-resistant steel frame with hysteretic damper,” in *Behavior of steel structures in*

seismic areas, Proceedings of the 3rd International Conference STESSA 2000, 2000, pp. 403–409.

[53] M. Iwata, T. Kato, and A. Wada, "Performance evaluation of buckling-restrained braces in damage-controlled structures," in *4th International Conference on Behaviour of Steel Structures in Seismic Areas (Stessa 2003)*, 2003, pp. 37–43.

[54] L. G. Vigh, Á. Zsarnóczay, and T. Balogh, "Eurocode conforming design of BRBF – Part I: Proposal for codification," *J. Constr. Steel Res.*, vol. 135, no. April, pp. 265–276, 2017.

[55] S. Hussain, P. Van Benschoten, M. Al Satari, and S. Lin, "Buckling Restrained Braced Frame (BRBF) Structures: Analysis, Design and Approvals Issues," 2006.

[56] A. Blakeborough, M. S. Williams, A. Darby, and D. M. Williams, "The development of real-time substructure testing," *Philos. Trans. R. Soc. A Math. Phys. Eng. Sci.*, vol. 359, no. 1786, pp. 1869–1891, Sep. 2001.

[57] A. R. Plummer, "Model-in-the-Loop Testing," *Proc. Inst. Mech. Eng. Part I J. Syst. Control Eng.*, vol. 220, no. 3, pp. 183–199, May 2006.

[58] J. A. Carlson and W. Staehlin, "Shake Table Testing," *ASHRAE Trans.*, vol. 110, pp. 339–343, 2004.

[59] C. W. French, J. Timm, and C. K. Shield, "IMPLEMENTATION OF EFFECTIVE FORCE TESTING: METHOD OF SEISMIC SIMULATION FOR STRUCTURAL TESTING," in *12WCEE2000*, 2000, pp. 1–8.

[60] S. Petry and K. Beyer, "Testing unreinforced masonry structures at reduced scale," *15th World Conf. Earthq. Eng.*, p. 9, 2012.

[61] D. M. Williams, M. S. Williams, and A. Blakeborough, "Numerical modeling of a servohydraulic testing system for structures," *J. Eng. Mech.*, vol. 127, no. 8, pp. 816–827, 2001.

[62] M. Hakuno, M. Shidawara, and T. Hara, "Dynamic destructive test of a cantilever beam, controlled by an analog-computer," *Proc. Japan Soc. Civ. Eng.*, vol. 1969, no. 171, pp. 1–9, 1969.

[63] K. Takanashi, K. Udagawa, M. Seki, and H. Tanaka, "Seismic failure analysis of structures by computer-pulsator on-line system," *J. Inst. Ind. Sci.*, vol. 26, no. 11, pp. 13–25, 1974.

[64] S. A. Mahin, P.-S. B. Shing, C. R. Thewalt, and R. D. Hanson, "Pseudodynamic Test Method - Current Status and Future Directions," *J. Struct. Eng.*, vol. 115, no. 8, pp. 2113–2128, 1989.

[65] P.-S. B. Shing and S. A. Mahin, "EXPERIMENTAL ERROR PROPAGATION IN PSEUDODYNAMIC TESTING," 1983.

[66] M. Nakashima, H. Kato, and E. Takaoka, "Development of real-time pseudo dynamic testing," *Earthq. Eng. Struct. Dyn.*, vol. 21, no. 1, pp. 79–92, 1992.

[67] K. Takanashi and K. Ohi, "Earthquake response analysis of steel structures by rapid computer-actuator on-line system, (1) a progress report, trial system and dynamic response of steel beams," *Bull. Earthq. Resist. Struct. Res. Cent.*, vol. 16, pp. 103–109, 1983.

[68] P. A. Bonnet, M. S. Williams, and A. Blakeborough, "Evaluation of numerical time-integration schemes for real-time hybrid testing," *Earthq. Eng. Struct. Dyn.*, vol. 37, no. 13, pp. 1467–1490, 2008.

[69] M. Ojaghi, I. L. Martínez, M. S. Dietz, M. S. Williams, and A. Blakeborough, “Geographically distributed hybrid testing & collaboration between geotechnical centrifuge and structures laboratories,” vol. 17, no. 1, pp. 53–71, 2018.

[70] Instron, “Labtronic 8800 structural test control system computer interface: reference manual.” IST Systems Limited, 1998.

[71] MathWorks, “Simulink Documentation,” 2017. [Online]. Available: http://uk.mathworks.com/help/simulink/index.html. [Accessed: 21-Feb-2018].

[72] dSpace, *dSpace - Solutions for Control - User Guide*. dSpace Ltd., 2002.

[73] P. A. Bonnet, “The Development of Multi-axis Real-time Substructure Testing,” University of Oxford, 2006.

[74] M. Ojaghi, “The Development of Real-Time Distributed Hybrid Testing for Earthquake Engineering,” Department of Engineering Science, University of Oxford, 2010.

[75] T. Horiuchi, M. Nakagawa, M. Sugano, and T. Konno, “Development of a Real-time Hybrid Experimental System with Actuator Delay Compensation,” *Proc. of 11th World Conf. Earthquake Engineering*. 1996.

[76] T. Horiuchi and T. Konno, “A new method for compensating actuator delay in real-time hybrid experiments,” *Philos. Trans. R. Soc. A Math. Phys. Eng. Sci.*, vol. 359, no. 1786, pp. 1893–1909, 2001.

[77] J. Zhao, C. French, C. Shield, and T. Posbergh, “Considerations for the development of real-time dynamic testing using servo-hydraulic actuation,” vol. 1794, no. March 2002, pp. 1773–1794, 2003.

[78] M. Wallace, J. Sieber, S. Neild, D. Wagg, and B. Krauskopf, “Stability analysis of real-time dynamic substructuring using delay differential equation models,” 2005.

[79] N. M. Newmark, “A Method of Computation for Structural Dynamics,” *Journal of the Engineering Mechanics Division*, 1959. [Online]. Available: http://cobweb.ecn.purdue.edu/~ce573/. [Accessed: 24-Oct-2014].

[80] R. Jung, P. B. Shing, E. Stauffer, and B. Thoen, “Performance of a real-time pseudodynamic test system considering nonlinear structural response,” no. June, pp. 1785–1809, 2007.

[81] P. A. Bonnet, M. S. Williams, and A. Blakeborough, “Compensation of actuator dynamics in real-time hybrid tests,” *J. Syst. Control Eng.*, vol. 221, no. 2, pp. 251–264, 2007.

[82] C. Chen and J. M. Ricles, “Tracking Error-Based Servohydraulic Actuator Adaptive Compensation for Real-Time Hybrid Simulation,” *J. Struct. Eng.*, vol. 136, no. 4, pp. 432–440, 2010.

[83] O. Mercan, “Analytical and experimental studies on large scale, real-time pseudodynamic testing,” Ph.D. dissertation, Dept. of Civil and Environmental Engineering, Lehigh Univ., Bethlehem, Pa., 2007.

[84] B. Dong, R. Sause, and J. M. Ricles, “Accurate real-time hybrid earthquake simulations on large-scale MDOF steel structure with nonlinear viscous dampers,” *Earthq. Eng. Struct. Dyn.*, 2015.

[85] B. Dong, R. Sause, and J. M. Ricles, “Seismic Response and Performance of a Steel MRF

Building with Nonlinear Viscous Dampers under DBE and MCE," *J. Struct. Eng.*, vol. 142, no. 6, pp. 1–16, 2016.

[86] a P. Darby, A. Blakeborough, and M. S. Williams, "Improved control algorithm for real-time substructure testing," *Earthq. Eng. Struct. Dyn.*, no. July 2000, pp. 431–448, 2001.

[87] P.-S. B. Shing and S. A. Mahin, "COMPUTATIONAL ASPECTS OF A SEISMIC PERFORMANCE TEST METHOD USING ON-LINE COMPUTER CONTROL," *Earthq. Eng. Struct. Dyn.*, vol. 13, no. January, pp. 507–526, 1985.

[88] S.-Y. Chang, "Explicit Pseudodynamic Algorithm with Unconditional Stability," *J. Eng. Mech.*, vol. 128, pp. 935–947, 2002.

[89] S.-Y. Chang and S. A. Mahin, "Two new implicit algorithms of pseudodynamic test methods," *J. Chinese Inst. Eng.*, vol. 16, no. 5, pp. 651–664, 1993.

[90] C. Chen and J. M. Ricles, "Development of Direct Integration Algorithms for Structural Dynamics Using Discrete Control Theory," *J. Eng. Mech.*, vol. 134, no. 8, pp. 676–683, 2008.

[91] M. Nakashima and N. Masaoka, "Real-time on-line test for MDOF systems," *Earthq. Eng. Struct. Dyn.*, vol. 28, no. 4, pp. 393–420, 1999.

[92] N. M. Newmark, "Computation of Dynamic Structural Response in the Range Approaching Failure," *Symp. Earthq. Blast Eff. Struct. Los Angeles*, 1952.

[93] H. M. Hilber, T. J. R. Hughes, and R. L. Taylor, "Improved numerical dissipation for time integration algorithms in structural dynamics," *Earthq. Eng. Struct. Dyn.*, vol. 5, no. June 1976, pp. 283–292, 1977.

[94] W. H. Algaard, "Integrated Implementation System for Pseudodynamic Testing," Department of Civil Engineering, Glasgow University, 2001.

[95] L. F. Shampine and M. W. Reichelt, "The MATLAB ODE Suite," *SIAM J. Sci. Comput.*, vol. 18, no. 1, pp. 1–22, 1997.

[96] A. Raltson, *A First Course in Numerical Analysis*. New York: McGraw-Hill, 1965.

[97] P. Bogacki and L. F. Shampine, "A 3(2) Pair of Runge-Kutta Formulas," *Appl Math Lett*, vol. 2, no. 4, pp. 321–325, 1989.

[98] C. Kolay and J. M. Ricles, "Development of a family of unconditionally stable explicit direct integration algorithms with controllable numerical energy dissipation," *Earthq. Eng. Struct. Dyn.*, vol. 43, pp. 1361–1380, 2014.

[99] R. Y. Jung and P. B. Shing, "Performance evaluation of a real-time pseudodynamic test system," *Earthq. Eng. Struct. Dyn.*, vol. 35, no. 7, pp. 789–810, 2006.

[100] Chen and Tsai, "A Combined Phase and Force Compensation Method for Real-time Hybrid Testing," *15th World Conf. Earthq. Eng.*, 2012.

[101] S. Starosielec and D. Hägele, "Discrete-time windows with minimal RMS bandwidth for given RMS temporal width," *Signal Processing*, vol. 102, pp. 240–246, 2014.

[102] MathWorks, "MathWorks fmincon - Find minimum of constrained nonlinear multivariable function - MATLAB," 2018. [Online]. Available: http://www.mathworks.se/help/optim/ug/fmincon.html. [Accessed: 30-Sep-2018].

[103] A. Giuffrè and P. E. Pinto, “Il comportamento del cemento armato per sollecitazioni cicliche di forte intensità,” *G. del Genio Civ.*, vol. 5, no. 1, pp. 391–408, 1970.

[104] M. Menegotto and P. E. Pinto, “Method of Analysis for Cyclically Loaded R. C. Plane Frames Including Changes in Geometry and Non-Elastic Behavior of Elements under Combined Normal Force and Bending,” *Proc. IABSE Symp. Resist. Ultim. Deform. Struct. Acted by Well Defin. Loads*, vol. 13, pp. 15–22, 1973.

[105] Ramberg, W. and W. R. Osgood, “Description of stress–strain curves by three parameters,” *Tech. Note No. 902, Natl. Advis. Comm. Aeronaut. Washingt. DC.*, 1943.

[106] R. Bouc, “Forced vibration of mechanical systems with hysteresis,” in *4th Conference on Nonlinear Oscillations*, 1967, p. 315.

[107] Y.-K. Wen, “Method for random vibration of hysteretic systems,” *J. Eng. Mech. Div.*, vol. 102, no. 2, pp. 249–263, 1976.

[108] M. Ismail, F. Ikhouane, and J. Rodellar, “The hysteresis Bouc-Wen model, a survey,” *Arch. Comput. Methods Eng.*, vol. 16, no. 2, pp. 161–188, 2009.

[109] F. Ma, H. Zhang, A. Bockstedte, G. C. Foliente, and P. Paevere, “Parameter Analysis of the Differential Model of Hysteresis,” *J. Appl. Mech.*, vol. 71, no. 3, pp. 342–349, 2004.

[110] F. Ikhouane, V. Mañosa, and J. Rodellar, “Dynamic properties of the hysteretic Bouc-Wen model,” *Syst. Control Lett.*, vol. 56, no. 3, pp. 197–205, 2007.

[111] C.-H. Wang and Y. Wen, “Evaluation of pre-Northridge low-rise steel buildings—part I, modeling.,” *J. Struct. Eng. ASCE*, 2000.

[112] F. C. Filippou, E. P. Popov, and V. V. Bertero, “Effects of Bond Deterioration on Hysteretic Behaviour of Reinforced Concrete Joints. Report to the National Science Foundation,” *Earthq. Eng. Res. Cent.*, no. August, pp. 1–212, 1983.

[113] K. Kolozvari *et al.*, “Shear-Flexure Interaction Modeling for Reinforced Concrete Structural Walls and Columns under Reversed Cyclic Loading,” *October*, no. PEER 2015/12, 2015.

[114] M. Bosco, E. Ferrara, A. Ghersi, E. M. Marino, and P. P. Rossi, “Improvement of the model proposed by Menegotto and Pinto for steel,” *Eng. Struct.*, vol. 124, pp. 442–456, 2016.

[115] A. E. Charalampakis and V. K. Koumousis, “A Bouc-Wen model compatible with plasticity postulates,” *J. Sound Vib.*, vol. 322, no. 4–5, pp. 954–968, 2009.

[116] Star Seismic Europe Ltd., “Preliminary design of a BRBF system - Use of equivalent force method.” [Online]. Available: http://admin.starseismic.net-solutions.hu/downloads/Preliminary design of BRBF system - Use of equivalent force method.pdf. [Accessed: 30-Sep-2018].

[117] Á. Zsarnóczay and L. G. Vigh, “Eurocode conforming design of BRBF – Part II: Design procedure evaluation,” *J. Constr. Steel Res.*, vol. 135, no. May 2016, pp. 253–264, 2017.

[118] K. S. Robinson, “Advances in design requirements for Buckling Restrained Braced frames,” in *NZSEE Conference*, 2014, pp. 1–8.

[119] C. A. Basagiannis, “SEISMIC DESIGN AND EVALUATION OF MOMENT RESISTING FRAMES USING ELASTOMERIC DAMPERS,” Department of Engineering Science, University of Oxford, 2018.

Appendix A – Ground Motion Records

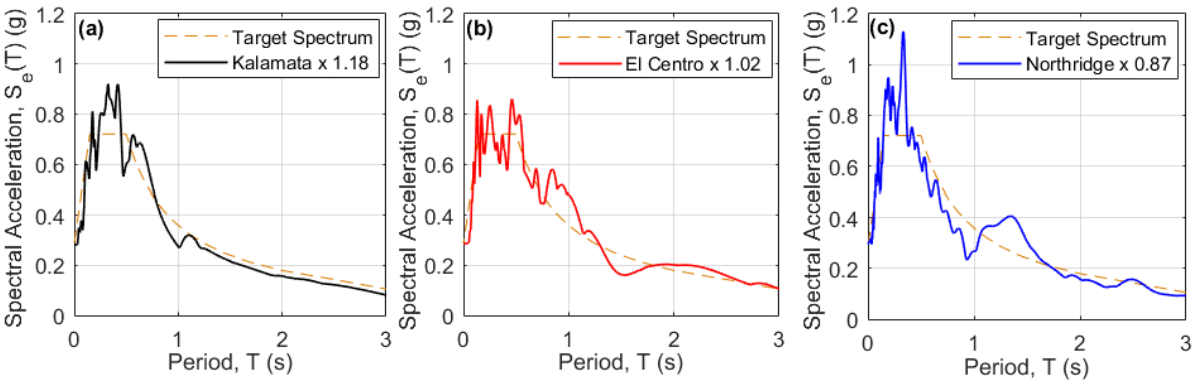

Figure A.1 – Elastic response spectra of Eurocode 8 compliant scaled ground motion suite:
(a) Kalamata (scale factor: 1.18), (b) El Centro (scale factor: 1.02), (c) Northridge (scale factor: 0.87)

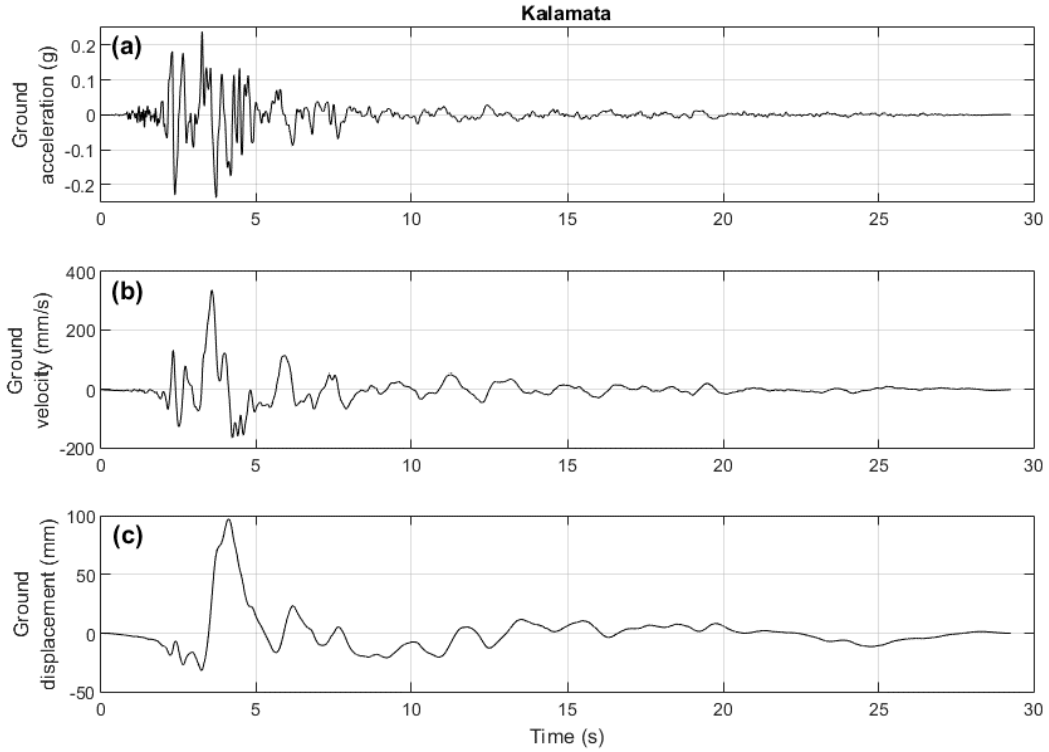

Figure A.2 – Kalamata ground motion (unscaled): (a) acceleration, (b) velocity, (c) displacement

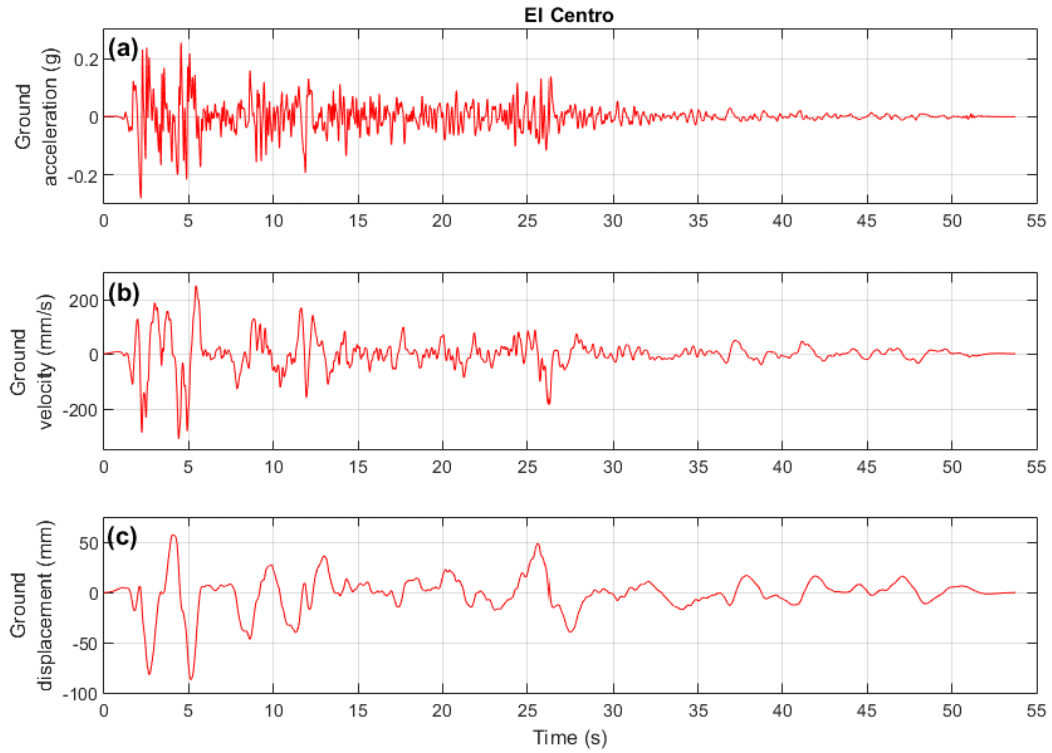

Figure A.3 – El Centro ground motion (unscaled): (a) acceleration, (b) velocity, (c) displacement

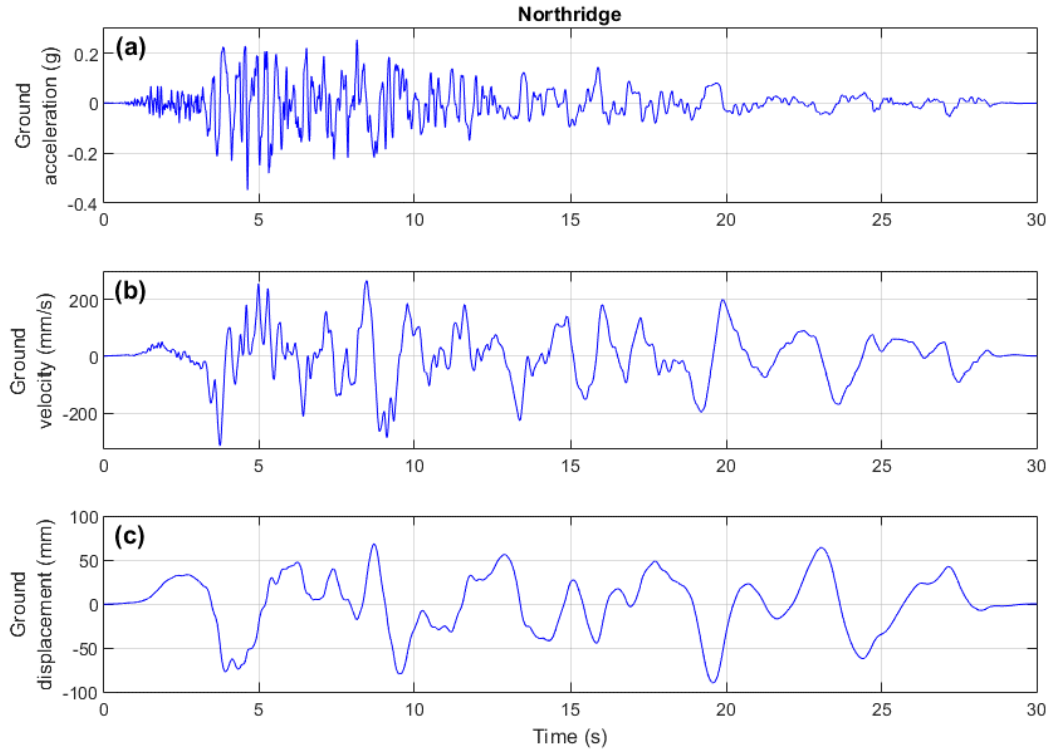

Figure A.4 – Northridge ground motion (unscaled): (a) acceleration, (b) velocity, (c) displacement